

Rotating Spiral Prototype Contactor: Design and Demonstration

A thesis submitted to
The University of Sheffield

By
Mohamed K. S. Zambri

For the degree of
Doctor of Philosophy

Supervisor:

Dr. Jordan M. MacInnes

Department of Chemical and Biological Engineering
The University of Sheffield
UK

September 2014

Abstract

Continuous counter-current flow of two phases in a rotating spiral channel is reported for the first time. In the rotating spiral channel, centrifugal force is much greater than gravity and is used to overcome surface forces to produce a nearly flat uniform interface. The position of the phase interface and the flow rate ratio of the phases are under full control by changing the rotation rate and the pressure gradient.

The work in this research has been divided into two main parts. First is the design of the rotating spiral apparatus using the existing wide channel model to decide the spiral channel dimensions and to size the various other passages. Second is using the apparatus to investigate the effect of operating conditions and physical properties of the phases. Most of the experiments were performed for the air-water system, although tests using liquids representing a range of viscosity and a case of liquid-liquid contacting are also included. The tests have shown that the apparatus has the ability, as expected, to handle a wide range of phase flow rate ratio, rotation rate, range of operating pressure and liquid viscosity for gas-liquid contacting. For the liquid-liquid system (octanol-water) equal success was found, although the range of tests was limited. This shows that the same spiral channel can be used for both gas-liquid and liquid-liquid applications.

High accuracy measurements of liquid layer thickness are achieved over the full range of tests. These show that good agreement with the wide channel model is achieved for larger rotation rates and layer thicknesses where interface meniscus effects are less significant. Liquid layer as thin as 17 μm were recorded although measurements at different positions along the channel showed that layer thickness varied by around 20% and this is due to the offset of the spiral centre from the axis of rotation for this device.

Declaration

This is to declare that this thesis is an account of the authors work carried out and completed at the University of Sheffield, UK, except where acknowledgements are made. This work has not been submitted for any other degrees.

Mohamed K. S. Zambri

Acknowledgments

All praise due to Allah the Great, the most Gracious and Merciful for his support and help by giving me the strength, health and patience to finish my study.

I would like to express my deepest gratitude, honour and sincere appreciation to my supervisor Dr. Jordan MacInnes for his invaluable guidance, encouragement, constructive suggestions throughout the whole research endeavour. A great thanks and special appreciation to all members of my family in Libya but in particular my parents and my sister Aisha who looked after my children during the last two years of my study. Also, I would like to acknowledge the following individuals for their support and help during my journey of study:

- Dr. George Dowson
- Dr. Dmitriy Kuvshinov
- Mrs. Maria Soto
- Team of technical services in the department
- Finally, my gratitude to the Libyan government for the funding

Publications

MACINNES, J. M. & ZAMBRI, M. K., Hydrodynamic Characteristics of a Rotating Spiral Fluid-Phase Contactor, submitted to *Chemical Engineering Science*, Sept. 2014.

Nomenclature

Symbol	Definition
A	Area, m^2
a	Interface surface area, m^2/m^3
C	Constant
D	Diffusivity, m^2/s
d	Droplet/bubble diameter, m
d_c	Column diameter, m
Eö	Eötvös number
F_{LV}	Flooding factor
f'	Slope of the equilibrium function $Y_v = f(Y_L)$
F_p	Packing factor
Fr	Froude number
g	Gravitational acceleration, m/s^2
H	Transfer unit height, m
h	Channel height, m
h_L	Height of liquid layer, m
h_m	Meniscus height, m
K	Overall mass transfer coefficient, $kmol/m^2/s$
k	Mass transfer coefficient, $kmol/m^2/s$
l	Diffusion distance, m
l_e	The length of one equilibrium stage, m
N	Number of equilibrium stages
n	Molar density, $kmol/m^3$
P	Pressure, Pa
Q	Volumetric flow rate, m^3/s

q	Volume flow rate ratio
q_n	Molar flow rate ratio
R	Radius, m
Re	Reynolds number
Sc	Schmidt number
T	Temperature, °C
t	Space between channel revolutions, m
u	Velocity, m/s
We	Weber number
w	Channel width, m
x	Coordinate direction along the channel
Y	Mole fraction
y	Coordinate direction across the channel

Greek symbols

Definition

Φ	Specific throughput, s ⁻¹
ρ	Mass density, kg/m ³
n	Molar density, kmol/m ³
μ	Viscosity, Pa s
σ	Surface tension, N/m
Ω	Rotation rate, rad/s or rpm
ξ	Fraction of channel occupied by heavy phase
α	Spiral angle, radians or degrees
τ	Diffusion time scale, s
δ	Capillary height, m

Subscripts

<i>B</i>	Bulk value (velocity, concentration)
<i>C</i>	Critical / corner
<i>e</i>	Equilibrium (state)
<i>G</i>	Glass surface value
<i>I</i>	Interface
<i>i</i>	Inner side
<i>L</i>	Liquid (heavy phase)
<i>o</i>	Outer side
<i>R</i>	Refraction
<i>s</i>	Spiral value
<i>V</i>	Vapour (light phase)

Definition

Superscripts

*	Non - dimensional variables
---	-----------------------------

Definition

Contents

Contents	viii
List of Tables	xiii
List of Figures	xiv
Chapter 1	1
1. Introduction.....	1
1.1 Rotating spiral approach	2
1.2 Structure of the thesis	4
Chapter 2	6
2. Background	6
2.1 Principles of fluid-phase contacting.....	8
2.1.1 Flow rate ratio	8
2.1.2 Relative diffusion lengths	10
2.1.3 Specific throughput	12
2.2 Gas-liquid contacting	13
2.2.1 Spray tower	13
2.2.2 Bubble column	15
2.2.3 Packed bed column	16
2.2.4 Wetted walls column.....	19
2.3 Liquid-liquid contacting	21
2.3.1 Spray column	21
2.3.2 Rotating disk contactor (RDC)	22
2.3.3 Karr reciprocating plate column.....	24

2.4	Centrifugally-forced contacting	25
2.4.1	Rotating packed bed (RPB).....	25
2.4.2	Rotating spiral contactor	28
2.4.3	Spinning cone column.....	31
2.4.4	Thin film spinning disc reactor	33
2.4.5	Rotor-Stator spinning disk reactor	35
2.4.6	Coil planet centrifuge (CPC).....	37
Chapter 3	39
3.	Wide Channel Model.....	39
3.1	Flow model	40
3.2	Solute model	42
3.3	Predicted hydrodynamic behaviour	44
3.4	Mass transfer performance	47
3.5	Further design considerations.....	51
Chapter 4	55
4.	Rotating spiral apparatus	55
4.1	Rotating spiral unit	57
4.1.1	The seal unit	58
4.1.2	The spiral element.....	61
4.1.3	The rotating shaft	63
4.2	The electric motor	65
4.3	Flow and pressure control instruments.....	65
4.3.1	Adjusting the pressure in spiral.....	66
4.3.2	Monitoring and controlling liquid outlet reservoir level.....	68
4.4	Typical operating procedure	69

4.5	Liquid supply with syringes.....	69
4.6	Typical contacting network	73
Chapter 5		75
5.	Liquid layer measurement	75
5.1	Imaging setup and method	76
5.2	Interface imaging.....	78
5.2.1	Different background materials.....	79
5.2.2	Different colour backgrounds in the spiral channel	85
5.3	Camera alignment	89
5.3.1	Interface parallel to the side wall	89
5.3.2	Interface affected by menisci and tilt	92
5.4	Image analysis.....	95
5.5	Interface model	100
5.6	Contact angle and surface tension measurements.....	106
5.7	Minimum liquid layer thickness	109
5.8	Interface model verification	111
Chapter 6		114
6.	Results and Discussion	114
6.1	Water and air	115
6.1.1	Variation of Q_V	115
6.1.2	Variation of Q_L	126
6.1.3	Effect of pressure	132
6.2	Radial position test	133
6.3	Other phase systems	139
6.3.1	Viscous liquids and air	140

6.3.2	A liquid-liquid system.....	142
Chapter 7	146
7. Conclusion	146
7.1	Tests conducted.....	146
7.2	General behaviour.....	147
7.3	Wide channel model prediction.....	147
7.4	Future work.....	148
7.4.1	Experimental work.....	148
7.4.2	Different applications.....	149
7.4.3	Device development.....	150
References	152
Appendices	161
Appendix A	161
A. Counter Current Phase Contacting	161
A1	Equations for Bulk compositions.....	161
A2	Mass Transfer Coefficients.....	163
A3	Mass Transfer Effectiveness.....	164
Appendix B	167
Network Modelling	167
B 1 Developed flow in tube	167
B 1.1	Major losses.....	167
B 1.2	Minor losses.....	168
B 2 Energy equations	169
B 3 Phase properties in the spiral channel	170
B 4 Applications of network model	171

B 4.1 Pressure drop estimation	171
B 4.2 Spiral pressure and the selection of network tubing	172
B 4.3 Calculation example.....	173
B 4.4 Spiral temperature	175
Appendix C: Technical drawings	180
C1 Seal case assembly views.....	181
C2 Seal Case.....	183
C3 Shaft.....	185
C4 Internal Parts.....	187
Appendix D: Further channel photographs at additional conditions	193
D1 Influence of Q_L at different rpm	193
D2 Radial position test	196
D3 Images for different phase systems at similar h_L.....	199

List of Tables

Table 3.1 Spiral Channel Dimensions.....	45
Table 4.1: Syringe pump settings for different syringes size.....	70
Table 4.2: Passage and tubing diameters used in the apparatus network tubing.	74
Table 5.1: Dynamic parameters for the computed interface profiles (MacInnes and Zambri, 2014).....	104
Table 5.2: Summary of measured contact angles for the experimental liquids and solid surfaces.....	108
Table 6.1: Rotation rate values and back pressure.....	115
Table 6.2: Radial positions values.	134
Table B.1: Calculations of static segments.	173
Table B.2: Calculations of rotating nodes.....	174
Table B.3: Values of pressure drop in each segment in the flow system.....	174
Table B.4: Values of pressure at each point in the flow system.	175

List of Figures

Figure 1.1: Counter-Current flow in rotating spiral channel.	1
Figure 1.2: Rotating spiral coordinate system and phase flow consideration (MacInnes et al. 2012).....	3
Figure 2.1: Illustrative diagram of a light dispersed phase ‘ V ’ (vapour) in a heavy continuous phase ‘ L ’ (Liquid).	7
Figure 2.2: Illustrative diagram for phase and solute balance.	9
Figure 2.3: Length scales in fluid phase contacting.....	12
Figure 2.4: Flow issues in spray tower (McCabe et al., 1985).....	14
Figure 2.5: Flow pattern in bubble column (McCabe, 1985).....	15
Figure 2.6: Schematic of packed bed column.	17
Figure 2.7: Generalised pressure drop correlation to find out the flooding point based on the flooding factor, phase properties, and packing characteristics (Coulson, 1991).....	18
Figure 2.8: Flooding and entrainment in wetted walls column.....	21
Figure 2.9: Overview of rotating disk contactor (Internet-2).....	23
Figure 2.10: Flow pattern in rotating disk contactor (AL-aswad, 1982).	23
Figure 2.11: Karr reciprocating plate column; different plates types (Internet-3).....	25
Figure 2.12: Overview and flow pattern of rotating packed beds (Internet-1).	26
Figure 2.13: Coordinate system and computational domain (right hand diagram). R is the radial position to the centre of the channel, α is the local angle of inclination of the spiral and Ω is the rotation vector (Ortiz-Osorio et al., 2009).	28
Figure 2.14: Overview of rotating spiral apparatus and the glass chip of spiral micro channel (MacInnes et al., 2010).	29
Figure 2.15: Fluid and heat transfer systems in rotating unit (MacInnes et al., 2010). ...	30
Figure 2.16: Overview and flow pattern of spinning cone column (Makarytchev et al., 1998).	33
Figure 2.17: Spinning disc reactor schematic (Hetherington, 2006).	34
Figure 2.18: Flow pattern in rotor-stator spinning disk reactor (Meeuwse, 2011).	36

Figure 2.19: The planetary motion in coil planet centrifuge contactor (Ito and Bowman, 1977).	37
Figure 3.1 Nomenclature and geometry for two-phase parallel flow in rotating spiral channel of infinite width.	40
Figure 3.2: Liquid layer thickness variation with liquid flow rate. Conditions are $Q_V = 3.54$ NL/min, $P_S = 2.1$ bar absolute and different rotation rate.	46
Figure 3.3: Liquid layer thickness variation with vapour flow rate. Conditions are $Q_L = 3.25$ mL/min, $P_S = 2.1$ bar absolute and different rotation rate.	46
Figure 3.4: Optimum non-dimensional throughput for air-water absorption system.	50
Figure 3.5: Optimum liquid layer thickness and specific throughput for standard air-water system as flow rate ratio is varied.	51
Figure 3.6: Stability envelope plot for pressure difference over channel length; standard air-water system.	54
Figure 4.1: Rotating Spiral Apparatus.	56
Figure 4.2: Section view of rotating spiral unit.....	58
Figure 4.3: Lip seal connections.	59
Figure 4.4: Seal unit components; (a) seal unit, (b) spacers and seal-pair channel, (c) case and seal unit, and (d) lip seal.....	60
Figure 4.5: Spiral element design.	62
Figure 4.6: The components of attaching the spiral element to the head of the shaft.....	63
Figure 4.7: Rotating shaft passages.....	64
Figure 4.8: Flow and pressure instruments in rotating spiral apparatus for air and water system.....	67
Figure 4.9: Monitoring of liquid outlet reservoir.....	68
Figure 4.10: Flow and pressure instruments for viscous liquids contacting with air.....	71
Figure 4.11: Flow and pressure instruments for liquid-liquid phase system.	72
Figure 4.12: Schematic diagram of flow network of rotating spiral device.....	73
Figure 5.1: Photography setup and alignment position.....	76
Figure 5.2: Difference in interface line for different depth of focus settings.	77
Figure 5.3: Identification of the liquid interface using a glass vial and different backgrounds colours.....	78

Figure 5.4: Photographs of the interface (in the vial) for different background materials: silver tape (a), PEEK (b), matt black paper (c), white paper (d) and reflecting aluminium (e).	79
Figure 5.5: Analysis profile line used for the tests.	80
Figure 5.6: Imaging the liquid interface in glass vial for different backgrounds materials.	81
Figure 5.7: Intensity profiles for different background materials.	82
Figure 5.8: Photographs of the gravity interface (in glass vial) for different distances between the background and the liquid interface.....	83
Figure 5.9: Identification of liquid interface for different distances.	84
Figure 5.10: Photographs of the interface (in the vial) for the (a) silver (b) yellow (c) white (d) red (e) green (f) blue and (g) PEEK backgrounds.	86
Figure 5.11: Intensity profiles (red intensity) for the interface test using different backgrounds colours.....	87
Figure 5.12: Photographs using different colour backgrounds (tape applied to the channel bottom).....	88
Figure 5.13: The interface is parallel to the wall and camera position is outward from the outer channel wall.	90
Figure 5.14: The interface is parallel to the wall and camera position too far inward the channel wall.	91
Figure 5.15: The interface affected by meniscus and gravity with the camera position too far outward.	92
Figure 5.16: The interface is affected by meniscus and gravity and camera position is too far inward.	93
Figure 5.17: The interface is affected by meniscus and gravity and the camera position too far inward	94
Figure 5.18: Image details and profile lines for air-water contact system.	97
Figure 5.19: Example print-out showing location of positions of maximum central differences of monochrome intensity.....	99
Figure 5.20: Identified positions on image associated with light paths.	100

Figure 5.21: Geometry of the interface. R_o is the radial distance from the rotation axis to the outer channel wall. θ_w is the contact angle at the channel wall surface and represents either θ_G at the glass wall surface or θ_p at the plastic wall surface (PEEK or yellow tape) (MacInnes and Zambri, 2014)..... 102

Figure 5.22: Computed interface profiles at various values of rotation rate for conditions typical of the experiments. $z = 0$ corresponds to the plastic surface and $z = 4$ mm to the glass surface. The conditions are as follows: $\theta_G = 15^\circ$, $\theta_p = 75^\circ$; $\rho_L = 995 \text{ kg/m}^3$, $\rho_V = 2.4 \text{ kg/m}^3$ and $\sigma = 0.07 \text{ N/m}$; $h = 1.5 \text{ mm}$, $w = 4.0 \text{ mm}$ and $R_o = 34 \text{ mm}$. The inset plot shows the same curves with an expanded y coordinate scale, revealing both the simple tilting of the interface in the central region at high rotation rate and full penetration of the menisci regions at low rotation rate (MacInnes and Zambri, 2014). 105

Figure 5.23: Contact angle measurements for one droplet of water on (a) hydrophilic surface and (b) hydrophobic surface. 106

Figure 5.24: Contact angle measurements using (a) Digital camera using 1X magnification and (b) FTA200 Dynamic contact angle analyser. 107

Figure 5.25: The calculated differences between y_c and y_L relative to liquid layer thickness as a function of rotation rate and layer thickness for $R_o = 34 \text{ mm}$ (MacInnes and Zambri, 2014)..... 111

Figure 5.26: Comparison between the calculated and measured height parameters as functions of the capillary height using two values of contact angles on the glass ($\theta_G = 15^\circ$ and $\theta_G = 30^\circ$) and the measured value for the PEEK ($\theta_p = 75^\circ$) (MacInnes and Zambri, 2014)..... 113

Figure 6.1: The comparison results between liquid layer measurements and wide channel model for varying Q_v at constant $Q_L = 9.6 \text{ mL/min}$ at range of rotation rates..... 116

Figure 6.2: Liquid layer thickness variation with gas flow rate, meniscus size remains approximately constant. Conditions are $Q_L = 9.6 \text{ mL/min}$, $P_s = 2.1 \text{ bar absolute}$ and 3840 rpm 118

Figure 6.3: Liquid layer thickness variation with gas flow rate meniscus size remains approximately constant. Conditions are $Q_L = 9.6$ mL/min, $P_S = 2.1$ bar absolute and 1480 rpm.	119
Figure 6.4: The results of meniscus height measurement for varying Q_L at constant $Q_V = 3.54$ NL/min and several rotation rate values over the range.	119
Figure 6.5: Shape of liquid layer for infinite (left) and finite (right) width channel.....	120
Figure 6.6: The effect of reducing the liquid flow rate on the meniscus size.	121
Figure 6.7: The effect of increasing the rotation rate on the meniscus size.....	121
Figure 6.8: The results of liquid layer measurements compared with wide channel model for varying Q_V at constant $Q_L = 3.49$ mL/min at range of rotation rates.....	123
Figure 6.9: The results of liquid layer measurements compared with wide channel model for varying Q_V at constant $Q_L = 1.10$ mL/min at range of rotation rates.....	124
Figure 6.10: Thick liquid layer at liquid inlet due to low rotation rate and high vapour flow rate.	124
Figure 6.11: Interface position and shape at liquid inlet for different liquid layer thickness (rotation rate). Conditions are $Q_V = 3.54$ NL/min, $Q_L = 3.49$ mL/min and $P_S = 2.1$ bar absolute.	125
Figure 6.12: The results of liquid layer measurements compared with wide channel model for varying Q_L at constant $Q_V = 3.54$ NL/min at range of rotation rates.....	127
Figure 6.13: Liquid layer thickness variation with liquid flow rate. The meniscus size remains approximately constant. Conditions are $Q_V = 3.54$ NL/min, $P_S = 2.1$ bar absolute and 3840 rpm.	128
Figure 6.14: The results of liquid layer measurements compared to the wide channel model when a surfactant solution is added to water flow; $Q_V = 3.54$ NL/min.	129
Figure 6.15: A comparison for the liquid layer measurements with and without surfactant at 1480 rpm.....	129
Figure 6.16: Effect of surfactant on liquid layer thickness and meniscus size. Conditions are $Q_V = 3.54$ NL/min, $Q_L = 1.10$ mL/min, $P_S = 2.1$ bar absolute and 1480 rpm.	130

Figure 6.17: Effect of rotation rate on liquid layer thickness and meniscus size. Conditions are $Q_V = 1.71$ NL/min, $Q_L = 9.6$ mL/min and $P_S = 2.1$ bar absolute.	131
Figure 6.18: The results of liquid layer measurements compared with the wide channel model for variation of spiral pressure at several values of rotation rate.	133
Figure 6.19: Selected radial positions along the spiral channel.	135
Figure 6.20: Liquid layer measurements along the spiral channel compared to the wide channel model. Conditions are 1920 rpm, $Q_V = 3.54$ NL/min, and range of Q_L	136
Figure 6.21: Liquid layer variation and meniscus size with the effect of radial position. Conditions are $Q_V = 3.54$ NL/min, $Q_L = 3.49$ mL/min, and 1920 rpm.	137
Figure 6.22: Liquid layer measurements (relative to the average) for range of rotation rate and range of liquid flow rate compared to the model results when offset is included.	139
Figure 6.23: Liquid layer measurements for viscous liquids and water contacting with air and compared to the wide channel model. Conditions are: $Q_V = 1.15$ NL/min, 3200 rpm, and $P_S = 1.81$ bar absolute.	142
Figure 6.24: Liquid layer measurements compared to the wide channel model for octanol-water contact system. Conditions include a range of water flow rate but fixed octanol flow rate ($Q_V = 0.23$ mL/min); all are at a rotation rate of 3200 rpm.	144
Figure 6.25: Liquid layer thickness variation with water flow rate for water-octanol contact system. Conditions are as for Figure 6.23.	145
Figure 7.1: Stacking of channels to increase the throughput.	151

Chapter 1

1. Introduction

Separation processes are widespread in the chemical industries and commonly involve fluid phases. Fluid phase contacting involves bringing two or more fluids into close contact so the diffusion rate is high and molecular species can be transferred rapidly. The method of achieving this close contact differs from approach to approach. Some of the conventional methods (whether using rotation or not) have tried to control the droplet and bubble size to be as small as possible and others tried to control the thickness of a liquid layer. Even though such approaches are in wide commercial use they have many limitations related to allowed flow rates and purification level that can be obtained. Rotating spiral contacting is a novel approach proposed by MacInnes et al. (2005) which solves the operating issues in the conventional methods. This approach avoids the phase mixing by allowing the fluids to flow counter-currently through a spiral channel in separate and parallel layers (Figure 1.1).

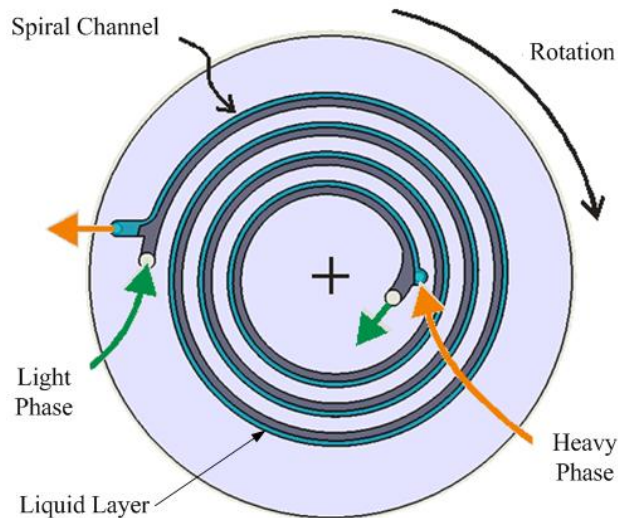


Figure 1.1: Counter-Current flow in rotating spiral channel.

1.1 Rotating spiral approach

Rotating spiral technology has simplified the way of fluid phases contact one another by employing centrifugal acceleration in an organised way. This novel method allows the fluid phases to flow side by side in two separate and parallel layers without mixing using the effect of the rotation to overcome both gravity and surfaces forces. The phase flow rates and the liquid layer thickness are completely controlled by the rotation rate and pressure gradient in the spiral channel. For any effective separation process using counter-current flow the most important factors that need to be considered are the liquid layer thickness and the flow rate ratio. These factors in the rotating spiral technology are under a high level of control, so by adjusting the rotation rate and the pressure gradient, the liquid layer thickness and the phase velocities can be changed and fixed to achieve any desired operating condition. This flexibility of operation allows control of the mass transfer rate to be constant along an entire length of the spiral channel in the two phases.

The rotating spiral approach has been experimentally demonstrated in MacInnes et al. (2010) where successful implementation of batch distillation in a spiral micro channel was presented. It was very important to extend the research on this new technology to be applied in larger scale and continuous operation.

The work in this research is based on the wide channel model proposed by MacInnes et al. (2012). This model considers a spiral channel of infinite width rotating about its axis (Figure 1.2). The spiral channel has the height, h , spiral angle, α , and the fraction of liquid layer thickness, ξ .

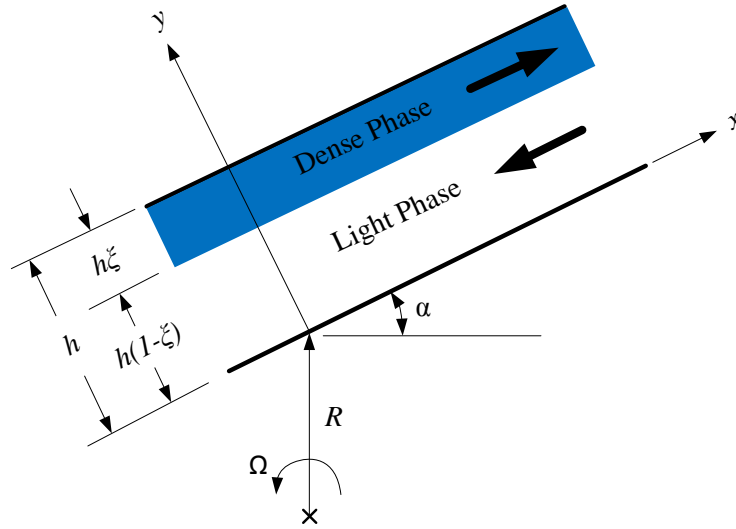


Figure 1.2: Rotating spiral coordinate system and phase flow consideration (MacInnes et al. 2012).

The wide channel model has the ability to provide the limits of operating conditions and also the important characteristics of spiral channel design. This model has been used in this research to design a prototype rotating spiral contactor to produce a continuous counter-current flow in the spiral channel. In addition, the calculations of the model have given the limits of the operating conditions for a specific design of spiral channel and contact system. The flow is introduced to the rotating spiral channel by using rotating lip seals riding on a rotating shaft that has passages connecting the fluids to the ends of the spiral.

Most experiments have been performed using tap water and lab compressed air that is the air-water system. One of the aims of this research is to compare the measurements of liquid layer thickness with the prediction of the wide channel model for the designed spiral channel and the different contacting systems used. Other calculations carried out by MacInnes (2014) have shown that the rotating spiral technology is flexible in use for wide range of operating conditions and the same spiral channel can be used for both gas-liquid and liquid-liquid contacting although for the same channel length gives far lower purification for liquid-liquid contacting. Thus, another aim was testing the designed

apparatus for a wide range of flow rate ratio, spiral pressure, liquid viscosity and for liquid-liquid contacting using the same spiral channel.

The objectives of this work can be summarized in the following points:

- 1- Design, construct and develop a continuous counter-current flow test apparatus.
- 2- Obtain measurements of the liquid layer thickness and compare these measurements with the expectation of the wide channel model.
- 3- Verify that the rotating spiral apparatus is flexible and can be used over a wide range of operating conditions (flow rates, operating pressure – gas density, and liquid viscosity).
- 4- Verify that the same design of spiral channel can handle both kinds of phase contacting (gas-liquid and liquid-liquid).

1.2 Structure of the thesis

The structure of the thesis comprises seven chapters which describe step by step the work that has been done to achieve the research objectives. A general idea about the rotating spiral contacting approach and the considerations of counter-current flow in this technology has been presented in Chapter 1. There is a brief background in Chapter 2 related to some of existing approaches of contacting (rotating and non-rotating) to address some of the operating issues affecting the process of fluid phase contacting and how the rotating spiral method overcomes these issues. The wide channel model equations are presented in Chapter 3 and some of the expected results of the measurements of the liquid layer thickness are also included in this chapter based on the operating conditions and the designed spiral channel. Chapter 4 presents the design of rotating spiral apparatus and explains the importance of each individual part and unit and the method of transferring the fluids to and from the rotating spiral channel. The methodology of imaging the interface and the analysis method used to determine the liquid layer thickness can be found in Chapter 5. The comparison of these measurements

with the expectations of the wide channel model for all experiments performed in this research is presented in Chapter 6. Finally, the conclusion of these comparisons and some suggestions for future work are presented in Chapter 7.

The thesis also includes four appendices (A, B, C, and D) providing supporting information for different chapters. Appendix A presents the general equations of counter-current fluid phase contacting. These equations are applicable for the rotating spiral contacting approach and all other contacting methods. Area of different passage sizes was involved in the flow network of the apparatus and selection of these sizes was based on network calculations of flow rates and pressures throughout the system. The equations used in these calculations are presented in Appendix B. The technical drawings for the apparatus are presented in Appendix C. Finally, further photographs of the channel layers not included in the text showing the variation of the liquid layer thickness at different operating conditions are given in Appendix D.

Chapter 2

2. Background

Separation of molecular species from multi-component fluid mixtures can be achieved by contacting with a second immiscible fluid phase. The degree of separation depends on the length and manner of contacting occurring between the two phases. Co-current flow can be used when just one equilibrium stage provides acceptable purification (Reiss, 1967) but counter-current flow allows separation to any desired purity due to the multiple stages of contacting achieved. Thus, counter-current contacting of fluid phases is commonly used. In practice controlling counter-current flow is difficult because the phases tend to form into discrete elements due to interfacial surface tension leaving a situation such as that depicted in Figure 2.1. In the case shown, the light phase has formed into droplets or bubbles that rise through a falling continuum of the denser liquid phase. Equally, it could be the denser liquid phase that is divided into droplets in a continuum of light phase, either gas or immiscible liquid. Often a solid packing is used in the contacting space to help control the size and form of the elements of phase material. Sometimes the denser liquid phase flows as a film or as rivulets over the surface of the packing, as well as breaking away from solid surfaces to form droplets. These complex flows and spatial configurations of the phases depend both on the relative flow rates of the phases and on the physical properties of the fluids and interface.

The effectiveness of the mass transfer depends on the size and velocity of the phase elements (the scales ℓ_V, u_V, ℓ_L and u_L in Figure 2.1) with particular optimum values of relative size and velocity associated with a given phase and solute system. But when one phase is dispersed within the other, the size, shape and velocity are determined dynamically by the relative flow of the phases. This is unfortunate because the optimum

ratio of the phase flow rates is fixed by the equilibrium characteristics of the transferring of solute molecule in the two phases and in achieving this ratio of flow rates the dynamics of the phase flows together with the packing geometry determine the characteristic size of elements. Thus, either the correct relative size of the phase elements or the correct relative flow rates can be produced, but not the two at the same time. The rotating spiral, as will be seen, allows both the scales and the flow rates to be controlled simultaneously.

A further problem with dispersing one phase into the other is that the drag force is relatively high for the un-streamlined passage shape for flow of the continuous phase around the discrete elements of the other phase and through the packing. A consequence is a limitation on allowed levels of flow rate before the inter-phase drag force results in either the continuous phase carrying the discrete phase out of the contacting volume or the discrete phase doing the same thing with the continuous phase. For example, in packed columns discretely-flowing liquid can be prevented from falling down the column by a gas flow that is too large. The liquid accumulates and overflows into the gas outlet, which is termed flooding. Alternatively, a gas flow that is too small may lead to the down-flowing liquid carrying the gas out the liquid outlet, termed entrainment. In the rotating spiral, the phases flow in parallel streams and therefore only friction and not form drag is involved so such phase ejection problems are more straightforward to prevent (Coulson et al., 2002b, Treybal, 1981b, McCabe et al., 1985).

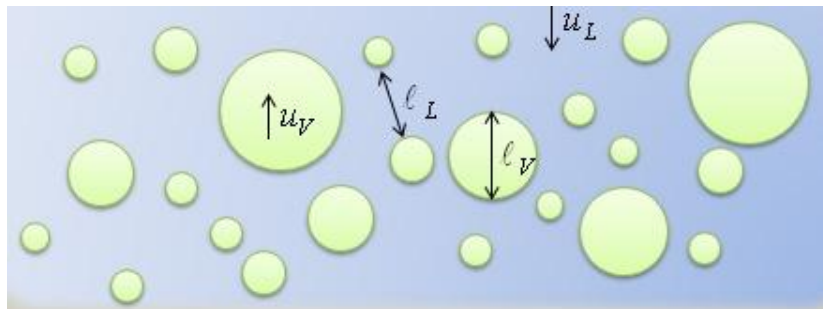


Figure 2.1: Illustrative diagram of a light dispersed phase 'V' (vapour) in a heavy continuous phase 'L' (Liquid).

Before considering in some detail different approaches to counter-current contacting and current areas of work, it is helpful to develop some fundamental principles that provide a framework for discussion.

2.1 Principles of fluid-phase contacting

The analytical model developed in MacInnes et al. (2012) for flow and mass transfer in the rotating spiral has highlighted the essential principles of counter-current phase contacting. Here a more general but also simplified presentation will help to clarify the important issues in contacting and to highlight key advantages of the rotating spiral approach. In the presentation the scales ℓ_V and ℓ_L will be viewed as representing the effective diffusion length in the phases and restrictions on their relative size and on the ratio of phase flow rates will be developed. These scales correspond directly to the physical size of phase elements for laminar flow but may represent viscous sublayer thickness or other appropriate convective scale in the case of turbulent flow or complex laminar flow.

2.1.1 Flow rate ratio

The first principle of counter-current contacting arises simply from mass balance on the transferring solute species. The schematic diagram in Figure 2.2 represents the principal variables involved in the balance and indicates the situation appropriate to an absorption process: the solute is transferred from the light phase to the heavy phase. The light phase (variables with a subscript V) enters with some initial solute concentration and leaves with a lower concentration, the excess having been transferred to the heavy phase (subscript L variables). The heavy phase has no solute at inlet, as indicated, which is the usual situation in practice.

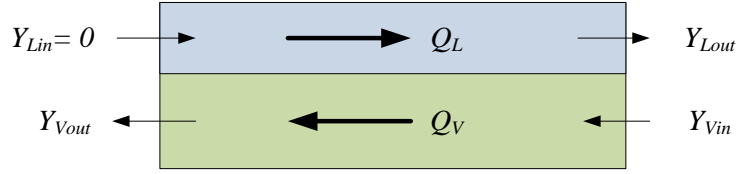


Figure 2.2: Illustrative diagram for phase and solute balance.

Applying a balance on solute gives:

$$Y_{Lout}n_LQ_L + Y_{Vout}n_VQ_V = Y_{Vin}n_VQ_V \quad (2.1)$$

Q_V , Y_V and n_V are the volume flow rate, solute mole fraction and molar density in the light phase and Q_L , Y_L and n_L are the volume flow rate, solute mole fraction and molar density in the heavy phase.

Dividing by n_LQ_L gives a relation between mole fractions in terms of the single parameter q_n which is the ratio of light to heavy molar flow rates:

$$Y_{Lout} + Y_{Vout}q_n = Y_{Vin}q_n \quad (2.2)$$

Now the highest possible level of Y_{Lout} is achieved when the exiting heavy phase has come to perfect equilibrium with the entering light phase and this occurs only for an infinite length of contacting. If the equilibrium function is $Y_V = f(Y_L)$ for a given temperature and pressure of operation then assuming dilute solute concentration, we can write $Y_V = f'Y_L$ where f' is the constant slope of the equilibrium curve. In this dilute case the heavy phase outlet solute mole fraction can be expressed in terms of the inlet light phase solute mole fraction as follows:

$$Y_{Lout} < \frac{Y_{Vin}}{f'}$$

Using this to eliminate Y_{Lout} in equation 2.2 and solving for q_n gives:

$$q_n < \frac{Y_{vin}}{f'(Y_{vin} - Y_{vout})} \quad (2.3)$$

This is a standard result found in mass transfer text books (McCabe et al., 1985, Kohl, 1997) and shows that to achieve a given separation, i.e. Y_{vout}/Y_{vin} the flow of heavy phase must exceed a minimum value and this value depends on the equilibrium characteristics (f') of the solute in the two phases. But also, as the heavy phase flow rate increases the cost of regeneration or supply of that phase increases and so there will be an optimum for the flow rate ratio. Such a relation can be derived for each type of contacting, from distillation to liquid-liquid extraction to reactive separation. So the dependence of flow rate ratio on the phase and solute properties and on the level of separation that is required for optimum contacting conditions is a fundamental and general principle of counter-current phase contacting.

2.1.2 Relative diffusion lengths

The second principle of fluid phase contacting is that neither phase should restrict the transfer of the solute more than the other. If one phase 'limits' the mass transfer then it must be possible to adjust the relative size scale of the phases such that the mass transfer coefficient is increased in the limiting phase (and decreased in the other phase) such that the overall mass transfer coefficient is increased. Increasing the overall mass transfer coefficient means the same separation is produced in a shorter length along the direction of contacting. The optimum ratio of characteristic size, ℓ , in the phases can be determined by considering the order of magnitude of the length, L_e , along the contacting direction required for diffusion to transmit solute over the characteristic size. The diffusion time scale is given in terms of this size and the diffusion coefficient, D , by:

$$\tau = \frac{\ell^2}{D} \quad (2.4)$$

The distance travelled in the diffusion time depends on the average velocity, u , which in turn depends on flow rate and the section area available. The general expression between section area and the characteristic diffusion size is complex. However, for the geometry of the rotating spiral flow (Figure 2.3) in which the phases flow in layers of thickness ℓ and width w , the flow length can be expressed as follows:

$$L_e = u\tau = \tau \frac{Q}{\ell w} = \frac{\ell^2}{D} \frac{Q}{\ell w}$$

So

$$L_e = \frac{\ell Q}{Dw} \quad (2.5)$$

Requiring the length L_e to be the same in each phase produces the restriction on phase size scales.

$$L_{eV} = \frac{\ell_V Q_V}{D_V w} = \frac{\ell_L Q_L}{D_L w} = L_{eL}$$

Rearranging leads to a relation between relative size and relative flow rate and diffusion coefficient in the two contacting phases.

$$\frac{\ell_L}{\ell_V} = \frac{Q_V}{Q_L} \frac{D_L}{D_V} \quad (2.6)$$

As might be expected, the phase with the smallest diffusion coefficient should also be formed into element sizes that are smaller than for the other phase. Also though, the phase with the larger volume flow rate (the ratio imposed by the first principle, 2.1.1) must have the smaller element size according to equation 2.6. This is the case since the velocity increases in inverse proportion to ℓ , but the diffusion time is decreased in proportion to ℓ^2 . Thus, the diffusion time is decreased more than the flow time is increased as size decreases and the length L_e is shortened.

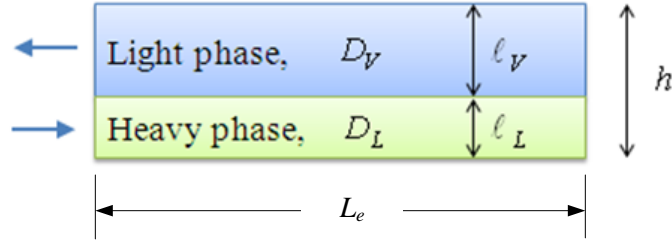


Figure 2.3: Length scales in fluid phase contacting.

2.1.3 Specific throughput

A final principle concerns the effect of phase element size on the effectiveness of contacting. As might be expected, reducing the element size allows the same mass transfer to be completed in a smaller volume in a shorter time. The volume throughput per unit volume of a device conveniently measures the effect of element size. With the unit of volume taken as the passage volume associated with a single equilibrium stage, the device volume is then approximately the number of required stages multiplied by this volume. The volume of an equilibrium stage is $V = L_e A$ and the volume throughput is uA giving the specific throughput Φ in simple terms as:

$$\Phi = \frac{Q}{V} = \frac{u}{L_e} \quad (2.7)$$

But since $L_e = u\tau$ the specific throughput is inversely proportional to the diffusion time scale and thus, can be expressed as

$$\Phi = \frac{D}{\ell^2} \quad (2.8)$$

Therefore, for a given phase and solute system, device size (volume) and processing time scale are proportional to ℓ^2 . Thus, reduction in contacting size, ℓ , results in a device that is smaller in size and has processing time that is similarly reduced.

2.2 Gas-liquid contacting

2.2.1 Spray tower

Spray towers are used in the case of gas-liquid contacting where the gas enters at the bottom of the tower while liquid is introduced by a series of sprays at the top of the tower. In this approach the intention is to decrease the diffusion distance, ℓ , to increase the mass transfer rate. The diffusion lengths can be decreased by controlling the droplet size to be small and the inter-drop distance also to be small so the ratio of length scale remains appropriate. But this kind of contacting approach is considered to have poor performance due to significant coalescence of the droplets after they have fallen just a few meters from the top of the tower (Coulson et al., 2002a). Thus the ratio of relative distances cannot remain optimum, and hence the approach fails in the second principle of fluid phase contacting (principle 2.1.2). The interfacial surface area thereby seriously decreased due to the droplets coalescence and also unequal resistance to mass transfer is expected as a result of the ratio of scales for the contacting phases is not correct.

This technique can be effective when the volume fraction of the dispersed phase needs to be as small as possible, i.e. where f' is small and so the flow rate ratio is high ($Q_V > Q_L$). Because coalescence is important in this approach, increasing the amount of gas phase flow through the tower needs to be under high level of control because any extra amount of the light phase will cause flooding. Issues such as these commonly occur during the operation of these techniques and cause limitations of the flow rates and as a result, this method cannot produce a constant flow rate ratio in attempt to control the droplet size (Akita and Yoshida, 1974, Coulson et al., 2002b, McCabe et al., 1985). Also, different diffusion time along the tower occurs because the flow can push the spray to one side (Figure 2.4) and then the droplets are much closer together in some regions than others, resulting in more effective diffusion in some places relative to others. In addition, the coalescence rate will be greater where the droplets spacing is smaller and hence droplet size will vary even more than otherwise, which also means a variation in the effectiveness of diffusion in the droplet phase.

Experiments on the hydrodynamic characteristics in the spray tower with modified geometry to improve the mass transfer using an aeration process have been carried out (Ochowiak and Broniarz-Press, 2011). In this experiment different designs of the light-phase suppliers are used to provide a circulating flow in order to decrease the coalescence rate. The results showed that there was a significant decrease in the flow resistance with the modified system.

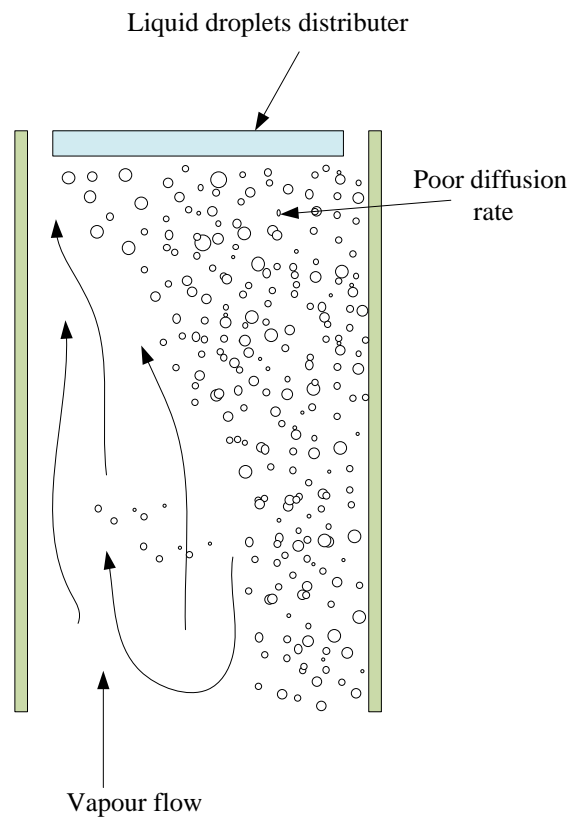


Figure 2.4: Flow issues in spray tower (McCabe et al., 1985).

2.2.2 Bubble column

This approach is similar to the spray tower and the difference between them is that the dispersed phase in this case is the light phase. The light phase enters the column at the bottom and bubbles through the liquid (continuous) phase. The same limitations mentioned for spray towers can be considered to apply. Bubble coalescence can occur and lead to a poor mass transfer rate and phase ejection (Coulson et al., 2002b, McCabe et al., 1985). Many studies have been performed on this kind of contacting to determine the flow patterns in different designs in order to seek ways of reducing bubble coalescence and hence increasing the mass transfer rate. The bubble columns can have circular, rectangular or square cross sectional area. In general it can be described as a container of the continuous phase (liquid) with bubbles of the dispersed phase introduced at the bottom (Figure 2.5).

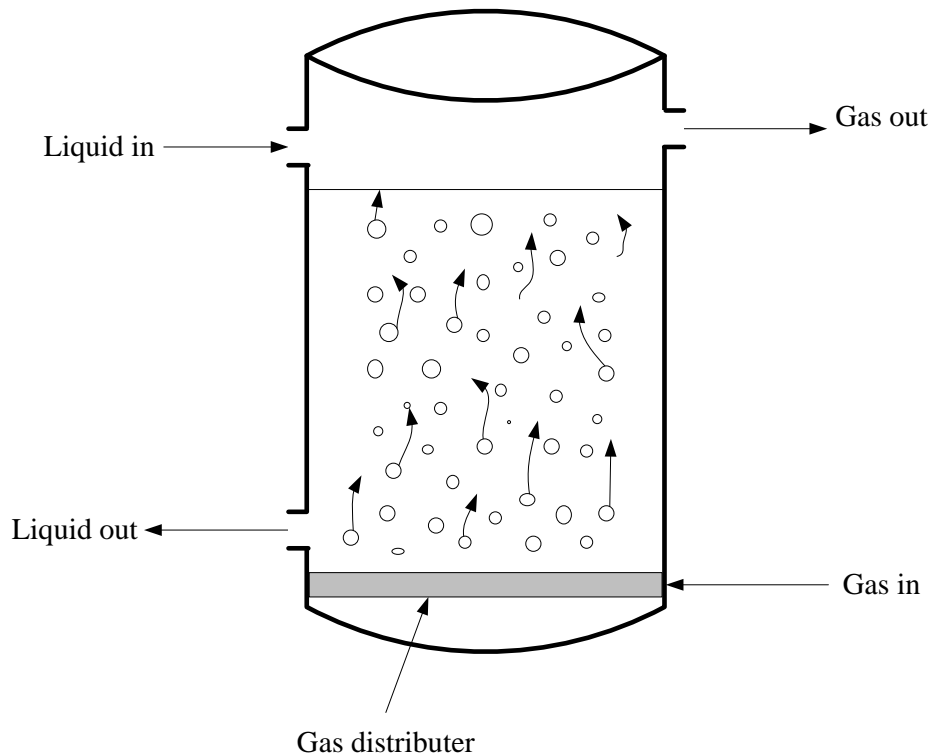


Figure 2.5: Flow pattern in bubble column (McCabe, 1985).

Similar to other contacting technologies experimental work has continued to search for ways of increasing the effectiveness of contacting. Research on the gas holdup, bubble size distribution and the bubble mean diameter for oxygen micro-bubbles in an air-water system has been carried out recently (Muroyama et al., 2013). An improvement in the absorption effectiveness was observed in using micro-bubbles in comparison with millimetre bubbles where the interfacial area was greater and the bubble diameter was very uniform (and around 65 μm). This improvement is expected due to the reduced gas phase size but the liquid phase size is unlikely to be variable in practice and hence mass transfer can be optimum only for particular phase and solute systems where the achievable relative scale is correct.

2.2.3 Packed bed column

The packed column is commonly used in the chemical industries for separation purposes (e.g. gas–liquid absorption). In this case, the phases flow counter-currently where the light phase (continuous) enters at the bottom while the dense phase is driven down by gravity through a random or structured packing in the form of trickle film or droplets as shown in Figure 2.6 (Jerzy, 2010). Different types of packing are used for different phase and solute systems in an attempt to achieve a flow rate ratio near to the optimum for each system. This approach has limitations regarding allowed phase velocities and relative sizes (diffusion distances) and still suffers from several issues (e.g. flooding) during operation process but nevertheless is widely used in chemical industries.

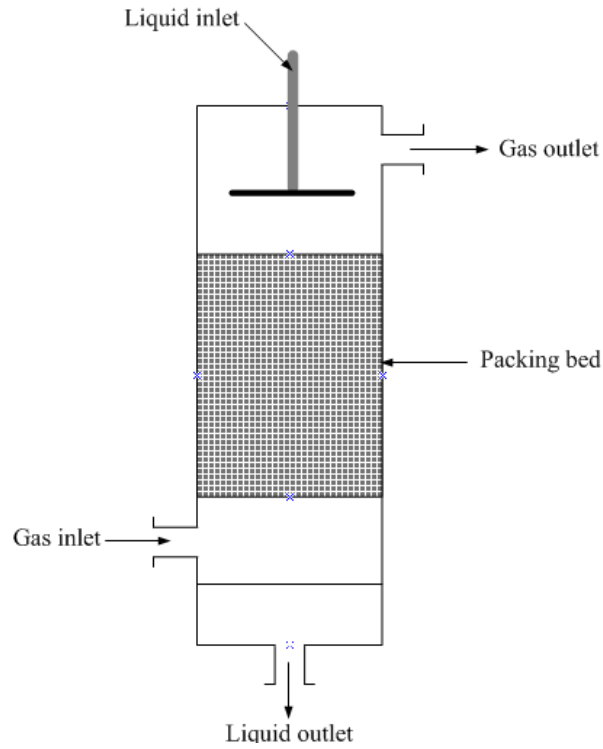


Figure 2.6: Schematic of packed bed column.

Many correlations have been proposed to calculate the flooding point and these correlations depend on the properties of the phases and the packing characteristics. Coulson et al. (1991) presented a correlation to find out the flooding point based on the pressure drop over the packing height. The method starts by calculating the primary flooding factor, F_{LV} , from phase densities and the superficial velocities of the two phases:

$$F_{LV} = \frac{m_L^{\bullet}}{m_V^{\bullet}} \sqrt{\frac{\rho_V}{\rho_L}} \quad (2.9)$$

Where m_V^{\bullet} and m_L^{\bullet} are the phase mass flow rates per unit column cross-sectional area, $\text{kg/m}^2\text{s}$.

The same author presented a chart (Figure 2.7) for determining the flooding point in packed bed columns. This chart shows the relation between the flooding factor calculated from Eq. 2.9 and the constant K_4 at different values of pressure drop presented as lines on the chart. At this value of flooding factor and with the line of a chosen value of pressure drop, the term of K_4 can be read on the chart and then the superficial velocity can be calculated from the relation below (Coulson, 1991):

$$K_4 = \frac{(m_V \dot{\bullet})^2 F_p [(\mu_L / \mu_w)(\rho_w / \rho_L)]^{0.1}}{\rho_V (\rho_L - \rho_V) g} \quad (2.10)$$

Where F_p packing factor characteristic of the size and type of packing, μ_w and ρ_w are the viscosity and density of water at 293k.

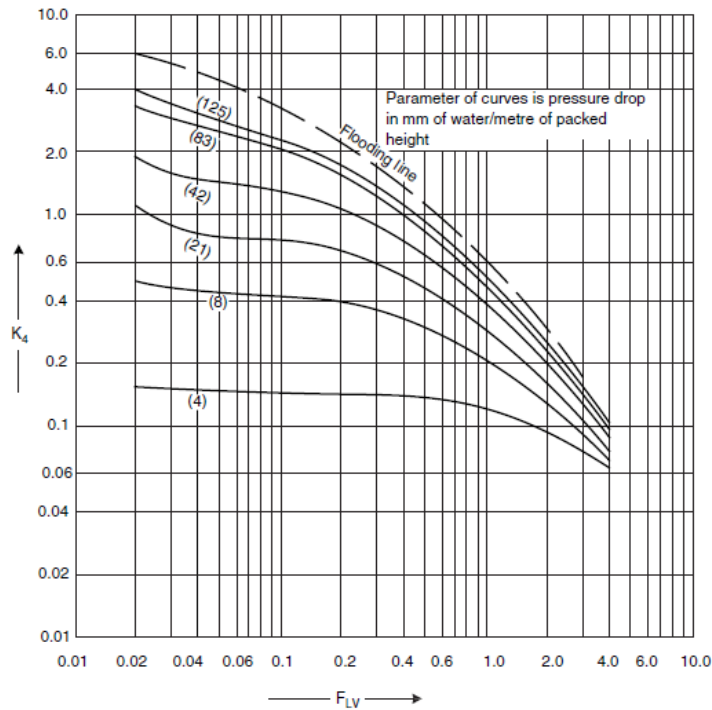


Figure 2.7: Generalised pressure drop correlation to find out the flooding point based on the flooding factor, phase properties, and packing characteristics (Coulson, 1991).

For a given flow rate ratio and phase system, K_4 is determined when it is decided how close to the flooding point the column is to operate. From the definition of K_4 it can be seen that certain dependencies on density and viscosity of the phases and as the body force increases the allowed velocity goes up to a limited point before the flooding to occur (note g here can be replaced in rotating systems by $R\Omega^2$). There is an increasing restriction on the allowed velocity with increasing F_{LV} value, i.e. with decreasing flow rate ratio. Thus, for phase and solute systems requiring small flow rate ratio the packed column may be impractical. Moreover, from the definition of K_4 it can be seen that there is another dependency from the type of packing, represented by the packing factor, F_p . Each packing has a particular value of packing factor, so once selected the allowed operating range as a function of flow rate ratio is fixed.

Concerning handling viscous liquids, the correlations presented above may not be applicable over a significant range of viscosity as they have been tested over a range spanning only a factor of three in viscosity. Thus with more viscous liquid, the liquid film size may grow to fill the gaps in the packing and the gas may force its way up the column in large bubbles. With regard to the contacting principles it can be concluded that the flow rate ratio cannot be produced regardless of the phase and solute system. Also, it is difficult to control the ratio of relative distances as the size of droplets and liquid layers is dependent on the relative flow rates of the phases.

2.2.4 Wetted walls column

In wetted wall columns gas–liquid contacting occurs via a thin layer of liquid falling down the inside surface a vertical pipe under the influence of gravity, while the gas phase flows counter-currently through the pipe centre. Occasionally co-current flow processing is performed using this technique (McCabe et al., 1985). An unstable liquid layer thickness is produced in this case and hence there is limited control of liquid layer thickness.

Many studies have been conducted in order to understand this type of phase contacting; in particular, values of the mass transfer coefficients have been determined, especially in cases of unsteady flow (Coulson et al., 2003). The unsteadiness of the flow comes from growing waves along the column during the process of maintaining the flow rate ratio associated with the body force. This comes from the fact that in the falling film using the gravity results in relatively small attainable velocities and relatively large attainable phase size that also varies along the column. The liquid layer thickness is determined by the liquid flow rate with only slight effect from the gas flow rate. Thus, the liquid flow rate will only be correct for a given pipe diameter and a particular value of f' , i.e. flow rate ratio. It is possible to change the liquid layer thickness by changing the liquid flow rate only. But also the gas flow rate needs to be changed to maintain a given flow rate ratio.

Even though wetted wall columns have the advantage of lower gas pressure drop in comparison with other conventional gas–liquid contacting devices, there are limitations for gas flow rate associated with the practical application of this technique. In some cases the orderly gas flow is disrupted by strong interaction with the liquid flow (Hughmark, 1980).

A consequence can be that large waves occasionally form on the interface and move upward in the column producing entrainment of liquid and, eventually, bridging of the liquid across the pipe section. This situation is yet another form of flooding and is illustrated in Figure 2.8 (Carvalho and Costa, 2006, Gilliland, 1934). In addition to the limitations and operation difficulties presented here considering the phase contacting principles similar results can be found regarding the relative diffusion lengths that vary along the tower and the flow waves produce different layer thickness and the flow rate ratio will vary in order to control these difficulties.

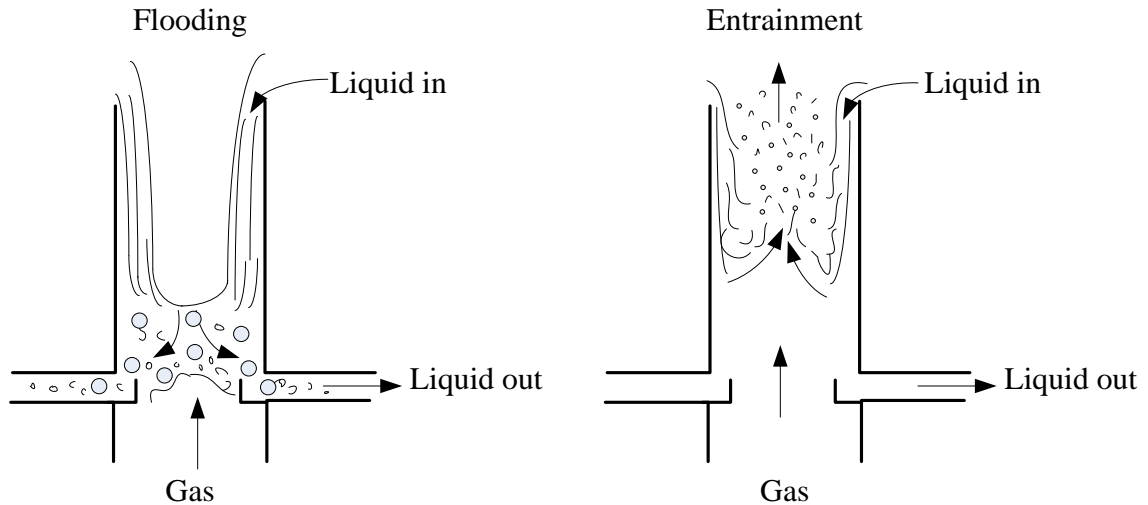


Figure 2.8: Flooding and entrainment in wetted walls column.

2.3 Liquid-liquid contacting

2.3.1 Spray column

There is only one difference between the spray column and the spray tower which is in the phases involved. Spray columns are widely used in liquid–liquid extraction processes. Typically the lighter phase is introduced as droplets at the bottom of the column and these rise through the heavier phase. Despite the fact that this equipment is simple in construction it has some drawbacks that make it limited in use. Inefficient processing due to the recirculation of the continuous phase consequently results in unsteady counter-current flow and lack of control of droplet size due to coalescence and insufficient velocity to force larger droplets to breakup into smaller-sized droplets. In such equipment one theoretical stage can be several meters in length (Coulson et al., 2002a)

Coulson et al. (2002) states that, due to the droplets falling down or rising up through the continuous phase under the effect of gravity, there will be a limitation on the amount of dispersed phase which can pass through the column for any given flow rate of

continuous phase. Therefore, any additional feed of light phase introduced at the bottom of the column will be rejected as a surplus amount, i.e. flooding will occur. As a result, the prediction of the conditions governing flooding occurrence is very important.

Many studies have been conducted to predict flooding point conditions, depending on the phase velocities and the volume fraction occupied by the dispersed phase. Sherwood et al. (1939) studied an extraction process in both spray and packed columns. Thornton, (1956) also carried out a similar study to predict the limiting holdup and flooding rates in an extraction process using a spray column. These studies concluded that the limitation of liquid holdup and flooding rate are dependent on droplet volume fraction of the dispersed phase and the flow rate ratio (Sherwood et al., 1939, Thornton, 1956). The conclusions here are similar to those for the spray tower regarding relative diffusion lengths (ℓ_L and ℓ_V) and their variation due to coalescence of droplets.

2.3.2 Rotating disk contactor (RDC)

The first introduction of the rotating disk contactor was by Reman in early 1950s where it was described as a cylindrical shell with a number of stator rings attached to the cylinder wall and a number of rotating disks driven by a shaft as shown in Figure 2.9 (AL-aswad, 1982). This type of contactor is widely used in liquid-liquid extraction (Strand et al., 1962) where the light liquid is introduced into the bottom to flow upward counter-currently with the more dense liquid which is introduced into the top of the column. The flat rotating disk was made without protrusions on the surface in order to provide uniform shearing conditions which consequently may lead to spreading the droplets as possible (Kafarov and Aleksandrovskii, 1965). The size of droplets is limited and maintained by the speed of the rotor and therefore the effect of centrifugal force is limited and includes just the droplets in direct contact with the rotor disk (Vermijs and Kramers, 1954). This type also has a limited flow rate ratio and increasing the flow rate of one of phases can lead to phase ejection due to the phases interactions. This can be seen clearly from the flow pattern for the rotating disk contactor shown in Figure 2.10 where the phases are mixed together all the time along the column.

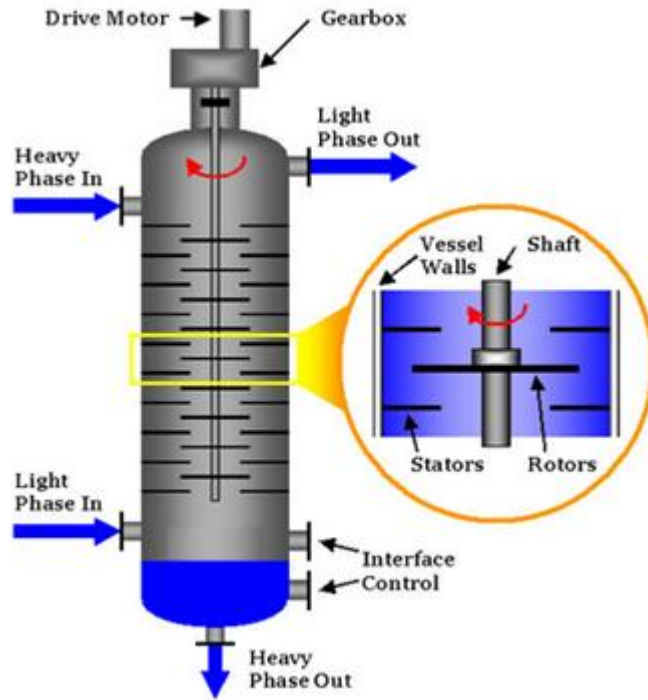


Figure 2.9: Overview of rotating disk contactor (Internet-2).

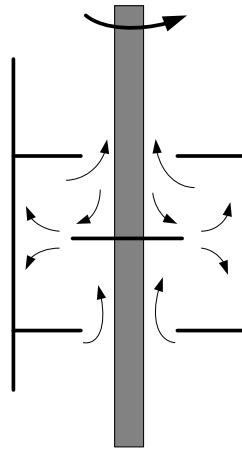


Figure 2.10: Flow pattern in rotating disk contactor (AL-aswad, 1982).

2.3.3 Karr reciprocating plate column

The Karr column uses reciprocation of disks rather than rotation to control phase element size. It has been used for liquid-liquid contacting where the less dense phase produced at the bottom of the column while the denser phase introduced at the top to flow counter-currently with the light phase. The fluids have to pass through sieved plates fixed on axial shaft moving up and down or have to pass in between partition plates fixed on the shell of the column and the vibrating plate fixed on the axial shaft (Figure 2.11). Many studies have been done on this kind of contacting approach to identify the flooding point and hold-up of liquid in the column. The flooding can happen due to formation of an emulsion layer growing from the middle of the column (Aravamudan, 1995). Also, according to Baird and Shen (1984) the movement of the plates up and down produces small droplets near the top of the tower and larger droplets near the distributor, when the droplet phase is heaviest. Thus small droplets may be carried out the top with the light phase rather than falling down the column as required. For dispersed light phase the opposite presumably will occur with small droplets carried out with the heavy phase at the column bottom. Other studies related to the performance of the reciprocating columns and which include different diameters of the sieve plates have shown that there is significant effect on the dispersed phase hold-up and the mass transfer coefficient (Smith et al., 2008, Stella et al., 2008). It can be concluded that this approach fails to produce the appropriate relative diffusion lengths uniformly over the column since droplet size varies. This difference in sizes causes the flooding velocity also to vary with that dictated by smallest size limiting overall operation.

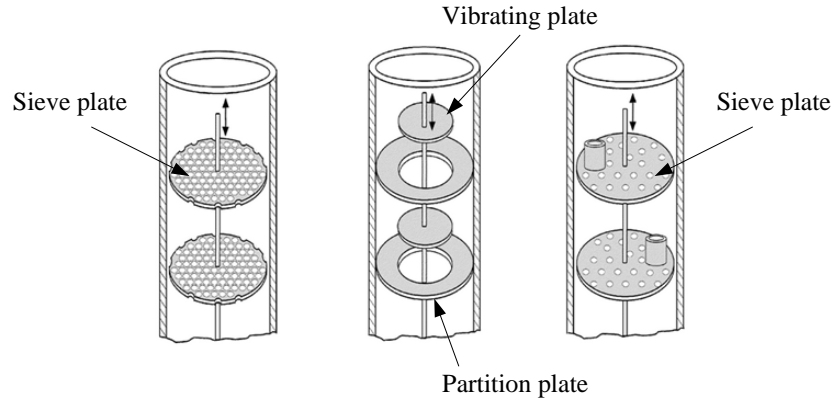


Figure 2.11: Karr reciprocating plate column; different plates types (Internet-3).

2.4 Centrifugally-forced contacting

2.4.1 Rotating packed bed (RPB)

Because of the issues arising in the conventional methods that related to phase ejection, limitation in flow rates and the limitations of purification that come from the dependency on gravity body force (Equation 2.10), researchers have tried to improve the contacting process between phases using rotation to increase the body force. There are a number of methods that use the rotation technique in the contacting process to separate the phases but they still suffer from all of the issues related to mixing of the phases. The first work on rotating packed beds was done by Podbielniak beginning in the 1930s. The original idea was using a rotating spiral tube or channel to produce gas-liquid or liquid-liquid contacting. In this approach a counter-current flow was produced and in a short time a number of improvements to the design in order to control the flows and to achieve effective separation were introduced (Podbielniak., 1935, Podbielniak., 1937, Podbielniak., 1938). The work to improve this method continued and by the 1940s instead of using a rotating spiral tube porous packing began to be used (for example precision-spaced wire packing, (Podbielniak, 1941). By the 1950s publications indicated that the Podbielniak was being applied commercially (Jacobsen and Beyer, 1956, Barson and Beyer, 1953, Kaiser, 1965) and these describe the advantages in scale-up and

reduction in unit size relative to a packed column associated with a centrifugal packed bed.

Vivian et al. (1965) studied the effect of gravity on the effectiveness of mass transfer experimentally by using a packed bed rotating in a large-scale centrifuge. The height of a liquid transfer unit was found, as expected, to decrease with increasing gravity (centrifugal acceleration). The higher body force led to the liquid phase breaking down into small droplets and hence a larger interfacial area (Vivian, 1965). But similar to all other conventional approaches, issues arising due to phase mixing remain although the higher effective g value allows higher throughput before phase ejection occurs (implied by the dependence on g in Eq. 2.10). The centrifugal body force varies with the radial position and hence flooding velocity and the ratio of relative phase sizes cannot be uniformly optimum throughout the rotating bed.

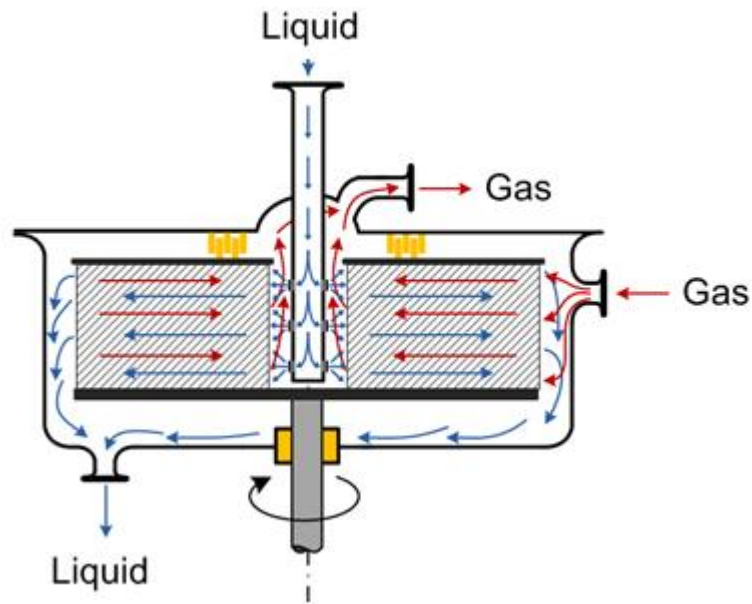


Figure 2.12: Overview and flow pattern of rotating packed beds (Internet-1).

Colin Ramshaw (1983) has presented an example of a distillation process using the HIGEE technology followed by a number of papers studying the operating characteristics of rotating beds (Munjaj et al., 1989, Keyvani, 1989, Kelleher and Fair, 1996, Guo et al., 2000, Burns et al., 2000). Other studies have been performed on the flow characteristics and application of rotating packed beds in gas-liquid contacting (Rao et al., 2004, Chandra et al., 2005). The HIGEE equipment in the recent years has started to have commercial application including carrying out absorption and desorption of carbon dioxide in organic aqueous solutions and water (Jassim et al., 2007, Sun et al., 2009). Also, some work has been done in the area to producing fine particles in gas-liquid reaction systems (Zhao et al., 2010).

Comparing these devices with the others it can be found that rotating packed beds use different beds for different types of phase contacting as the contact still depends on the droplet size and this size still depends on flow rates and phase properties. The centrifugal force is different radially along the packing bed so the velocity and dispersed phase volume fraction are not uniform. Because of phase mixing throughout the packing, the problems of lack of control of phase size and phase ejection continue to prevent optimum contacting across the range of phase and solute systems. It can be concluded that the only essential advantage is the shift in flooding velocity, minimum packing size, and the relative distances due to increased body force. And there are still problems with handling viscous liquids. The rotating spiral approach on the other hand allows adjustment of the interface position and hence relative phase size and the flow rate ratio over broad ranges of phase and solute systems simply by changing the rotation rate and the pressure gradient applied to the channel. This approach has the advantage to handle a wide range of phase and solute systems at optimum contacting conditions, including viscous liquids, and the same device can be used for both gas-liquid and liquid-liquid contact system (MacInnes et al., 2012, MacInnes, 2014).

2.4.2 Rotating spiral contactor

The first presentation of the rotating spiral technique was by MacInnes et al. (2005) who produced an initial model of spiral channel flow. Information about the effect of increasing the gravity force using rotation to overcome the surface forces and produce uniform layers of the phases were presented. In addition, the importance of channel geometry, angular velocity, pressure gradient, and the centrifugal force to control the liquid flow explored. Excellent design and operation of rotating spiral can be achieved from the successful control of the inlet and outlet streams of the phases (MacInnes, 2005, MacInnes et al., 2010).

Numerical computations related to the flow and composition for rotating spiral contacting have been presented in Ortiz-Osorio et al. (2009) and include determination of mass transfer coefficients to predict the performance for this approach by considering the two dimensional developed flow (Figure 2.13).

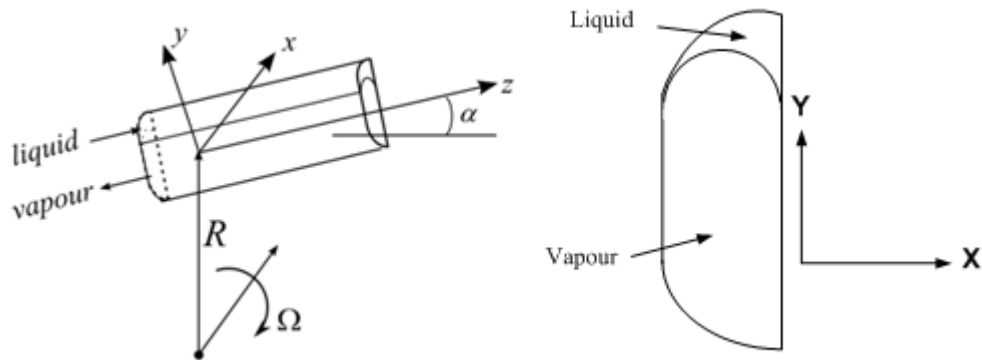


Figure 2.13: Coordinate system and computational domain (right hand diagram). R is the radial position to the centre of the channel, α is the local angle of inclination of the spiral and Ω is the rotation vector (Ortiz-Osorio et al., 2009).

The approach was first demonstrated experimentally by MacInnes et al. (2010) when counter-current gas-liquid distillation flow was produced in a rotating spiral channel to produce multistage separation of a 50:50 binary mixture of hydrocarbons. The flow was controlled by adjusting the reboiler heating rate with corresponding cooling at the inner end of the spiral to produce counter-current distillation flow. An effective separation has been achieved in this device corresponding to about seven equilibrium stages. The apparatus and the spiral channel used are shown in Figure 2.14 (MacInnes et al., 2010).

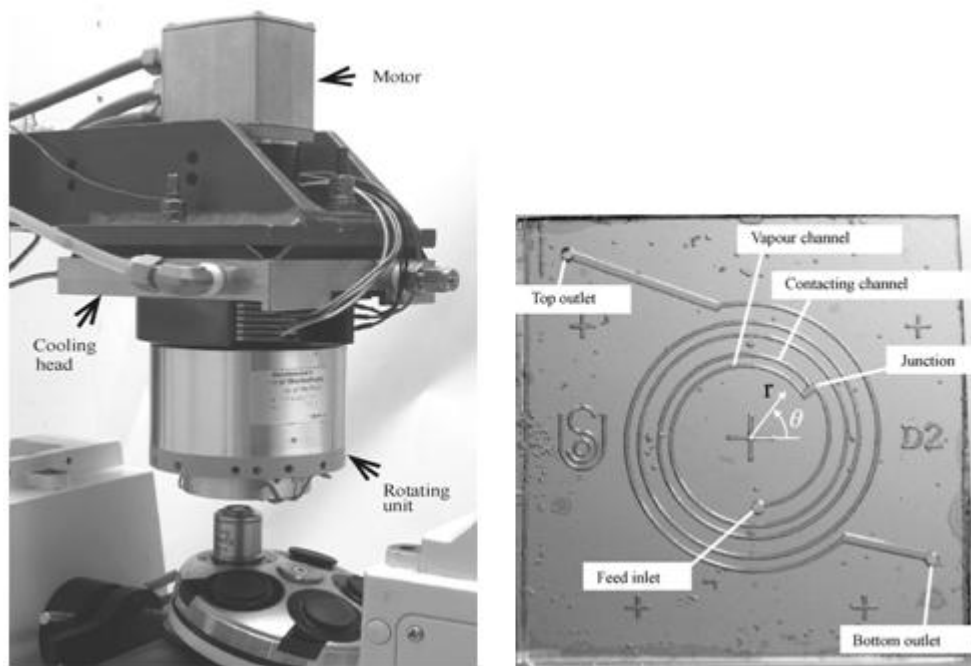


Figure 2.14: Overview of rotating spiral apparatus and the glass chip of spiral micro channel (MacInnes et al., 2010).

The apparatus was designed as a quasi-continuous process with no external flow connections: the initial mixture was charged into a reservoir at small radius and reached an approximately steady state of flow lasting for about forty minutes. Figure 2.15 shows the vent to the central supply reservoir as well as the vials used to collect the product liquids for post analysis. The device includes heating and cooling system for

boiling and condensation processes at the ends of the spiral channel. The work done on this device included a comparison with the results of other multistage distillation devices using micro scales: membrane contacting reported by (Zhang et al., 2009) and falling film contacting reported by (Tonkovich et al., 2008). To make this comparison acceptably, considerable work is required before the benefits of each approach can be fully clarified. At this stage it will be helpful to present a rough comparison with the other devices reported so far. MacInnes et al. (2010) has shown that the rotating spiral device can produce rapid distillation where the distillation time required for one stage is 0.13 seconds. The total number of stages was approximately 7 equilibrium stages and the length of one equilibrium stage was 5.3 mm. The effectiveness of contacting was shown to be about four times greater than that for the falling film and about 150 times greater than for the membrane experiment, although there were problems with the experimental consistency in the latter case. This was judged on the basis of the measured equilibrium contacting length in relation to generic scale for this length, i.e. the average velocity multiplied by the diffusion time scale. This takes into account differences due solely to differences in size and velocity.

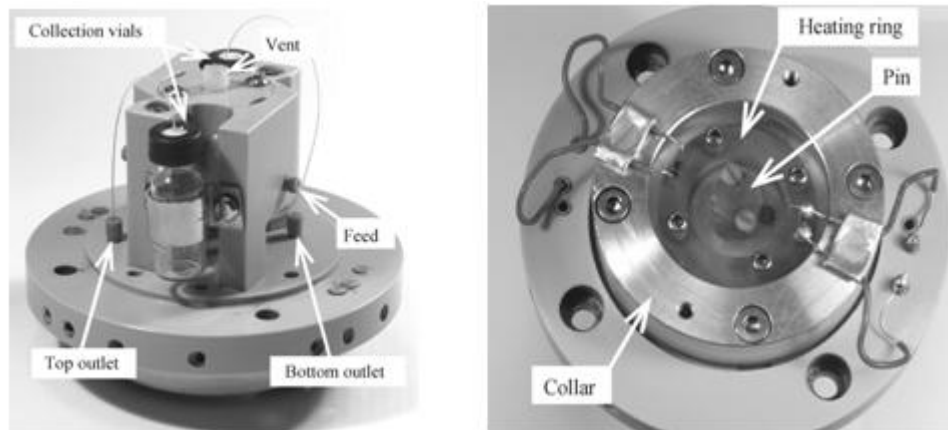


Figure 2.15: Fluid and heat transfer systems in rotating unit (MacInnes et al., 2010).

The success in controlling the flow under the most difficult circumstances of distillation processing and in such a small spiral channel (255 μm wide and 95 μm deep) gave encouragement to start the present work. It was very important to push this approach towards continuous flow processing and to examine it theoretically in a broad context of absorption, desorption and extraction including both gas-liquid and liquid-liquid contact systems. MacInnes et al. (2012) developed a model for channels with infinite width that can be used to predict the mass transfer performance quantitatively in the contacting channel. The model established a framework for deciding the appropriate geometry of the channel, the operating condition regimes and the mass transfer effectiveness for both gas-liquid and liquid-liquid contact systems (MacInnes et al., 2012). Broad application of this model was used to understand the variation in operating conditions required to handle the broadest possible range in phase and solute systems in separate work (MacInnes, 2014). The rotating spiral contacting was found to allow a wide range of phase and solute system, liquid viscosity, purification level and flow rate ratio for absorption and desorption processing using a single channel geometry and with only modest variation in rotation rate. One of the aims of this work is to test these findings experimentally and obtaining results to show that flow rate ratio and phase properties can be varied over wide ranges using a single device. A second is to use the data obtained to give a critical test allowing verification of the model hydrodynamic characteristics and critical assessment of its limitations.

2.4.3 Spinning cone column

The spinning cone column (SCC) is very similar in design to the rotating disk contactor but has been designed for gas-liquid contacting. This type of contactor is widely used in the food industry to distil the light (volatile) components from liquids and slurries (Casimir and Craig., 1990). The SCC consists of a number of cones attached to a rotating shaft receiving the fluids from fixed cones on the column shell (Figure 2.16). The first detailed description of the spinning cone column was by Huffman and Urey (1937) in the process of separation of heavy water. One of the other studies that have been performed on the spinning cone column was by Makarytchev et al. (1998) who

studied the flooding characteristics and the performance of this equipment. Computational fluid dynamics studies also have been performed to study the gas flow pattern and pressure distribution and also to achieve deeper understanding of contacting process (Makarytchev et al., 1998, Huffman and Urey, 1937, Makarytchev et al., 2005).

This type of contactor uses gravity to drive the liquid down the column over rotating and stationary cones with the light phase introduced into the bottom to produce the counter-current flow. The fluid will be transferred from the rotating cones to the stationary ones by the effect of centrifugal force that pushes the liquid up toward the top of the cone to fall down to the next stationary cone. The liquid layer thickness varies along the cone surface, i.e. thinner at the top of the cone and thicker near the centre where there is less effect from centrifugal force and smaller circumference. This variation gives a worsening mass transfer as the axis is approached and hence a variation in the relative diffusion lengths (ℓ_L/ℓ_V). The light phase must cross the liquid flow at the top of the cone and CFD analysis for one particular geometry suggests that the mass transfer is determined almost entirely by the spray droplets resulting from the process of breakup of the layer, with negligible mass transfer associated with the layer flows on the cone surfaces (Makarytchev et al., 2004).

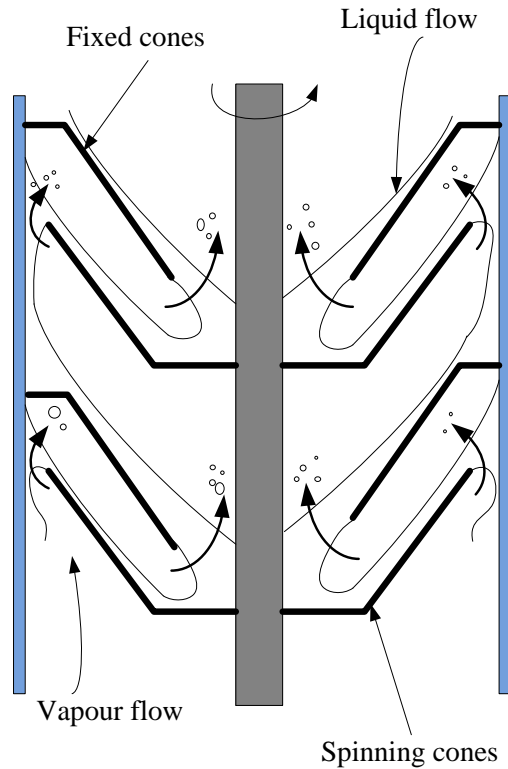


Figure 2.16: Overview and flow pattern of spinning cone column (Makarytchev et al., 1998).

2.4.4 Thin film spinning disc reactor

The description of the spinning disc reactor (SDR) is similar to rotating packed beds in the operation process except that the liquid phase is segregated from the gas phase, as in the spinning cone contactor. The spinning disc can be mounted either horizontally or vertically. The horizontal spinning disc has been used in gas-liquid, mixing and precipitation processes while the vertical orientation has been used as biological contactor for enhanced uptake of oxygen by a thin film of liquid. It has been found that the thin liquid film produced by this approach allows increased mass transfer rates in processes including absorption, stripping, mixing and reaction in comparison with non-rotating conventional approaches (Hetherington, 2006). In the horizontal spinning disc reactor, the feed (reactant stream) is introduced at a position close to the centre to flow across the surface of the spinning disc under the effect of centrifugal force. Then the

liquid is thrown toward the reactor walls to flow down where it drains away (Figure 2.17). Also, the rotating disc is designed to provide heating or cooling of the surface to control the reaction temperature.

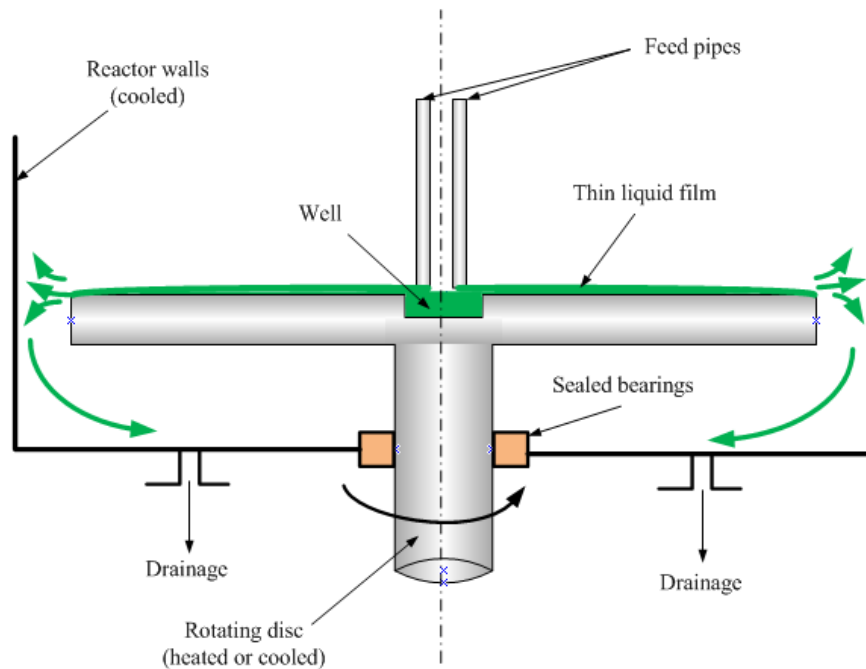


Figure 2.17: Spinning disc reactor schematic (Hetherington, 2006).

The experimental results for this approach have shown a short residence time on the disc, typically a few seconds (0.1 – 3.0 sec). The residence time and the liquid film thickness are dependent on the physical properties of the fluids, the rotation rate, and the radial position of the fluid. Measurements of the liquid film thickness have shown variation in the thickness with the radial location, with a thicker film near the centre of the disc and thinner film at the outer radius where higher centrifugal force is applied. Similar to all other contacting approaches tests and improvements of this approach have continued. An evaluation of the effectiveness of continuous thin film processing in spinning disc reactors has been performed and compared with static films. The results of this evaluation have shown that the SDR has higher overall rates of copolymerization and also an ability to produce and maintain thinner films (Dobie et al., 2013). The

spinning disc reactor has shown an obvious success in the field of mixing in comparison with the other rotating or non-rotating devices. Experimental work on a small scale spinning disc reactor has been conducted to find out the micromixing efficiency and the results compared to other approaches. The results of this work have shown that determining the micromixing efficiency in an SDR is based on the rotation rate, fluid flow rates, flow rate ratio and liquid viscosity (Boodhoo and Al-Hengari, 2012). Comparison of the micromixing efficiency of a spinning disc reactor with a rotating packed bed and a rotor-stator reactor has indicated that the performance of the SDR exceeds the operating performance of the RBP at almost double the flow and is similar to RSR at much higher flow rates, for the particular designs compared. A variation in the liquid film thickness in this approach is expected which conflicts with the ideal of optimum phase size throughout the contacting process. Thus, using the SDR for gas-liquid contacting will result in poor diffusion rate near the centre of the disc relative to that at the outer radius. In rotating spiral contacting a very thin and uniform liquid layer thickness can be produced and similar diffusion rate along the channel can be obtained.

2.4.5 Rotor-Stator spinning disk reactor

After the success achieved in the chemical industries using the rotating technology, there has been a continuous focus on improvements in these devices to make the production process safer and efficient. The most important factor to focus on was the mass transfer rate in the reaction and separation processes. Thus, for reactions involving two or more phases, increasing the mass transfer rate will lead to increasing the reaction rate and hence more production will be obtained. The rotor-stator spinning disk is one such device which is widely used in gas-liquid, liquid-liquid, and solid-liquid contacting. In gas-liquid contacting the rotor-stator spinning disc reactor consists of a rotating disc in a cylindrical housing. The distance between the rotor and the reactor wall is small, approximately 1 mm. The liquid, which is the continuous phase, is injected to the reactor from the top while the gas phase is injected through a small gas inlet in the bottom stator, near the rim of the rotor (Figure 2.18). Gas bubbles are sheared off at the gas inlet, due to the high velocity gradient, and thus shear force, between the rotor and the

stator. The gas bubble size decreases with increasing rotational disc speed. The centrifugal force causes the gas bubbles to move radially inward; the gas holdup in the rotor-stator spinning disc reactor with a single gas inlet in the bottom stator is only a few percent. The inward radial velocity decreases with decreasing bubble size; the residence time, and thus the gas holdup, increases with increasing rotational disc speed (Meeuwse, 2011).

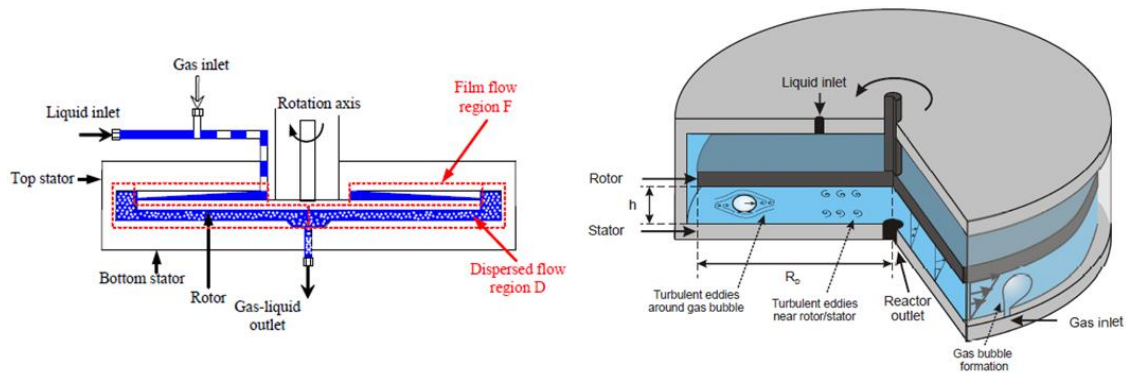


Figure 2.18: Flow pattern in rotor-stator spinning disc reactor (Meeuwse, 2011).

Even though this technology depends on phase mixing which limits the flow rate ratio it has shown a higher mass transfer rate in comparison with the conventional contacting approaches especially in the new multiphase reactor proposed by Meeuwse et al. (2010). The results showed that the volumetric mass transfer rate and the gas hold up in the spinning disc reactor increase with increasing the rotation rate. However, the average diameter of the gas bubbles decreases with increase rotation rate leading to increase the interfacial area and hence better mass transfer rate (Meeuwse et al., 2010). Because of the direct effect of the gas bubble size on the mass transfer rate, Meeuwse et al. (2011) studied the effect of rotor-stator distance and rotor radius on the rate of gas-liquid mass transfer. The results of this study have shown that the mass transfer rate for the rotor-stator with 1 mm distance is twice as high for that with 2 mm distance. On the other hand, the rotor-stator with a smaller disk radius can produce a higher volumetric gas-

liquid mass transfer coefficient than the bigger one (Meeuwse et al., 2011). It can be concluded that, despite this technology giving better performance for mass transfer processes in comparison with the conventional contacting approaches, it does not allow fluid phase contacting to be optimum. This comes from uncontrolled bubbles size which completely depends on the equipment design (rotor-stator distance and the disk radius), thus this approach does not appear to allow adjustment to optimum ratio of scales, l_L/l_V , (the usual for mixed phase contacting) and the flow is not counter-current (at least in some of the devices) and as a result reaction with separation is not possible.

2.4.6 Coil planet centrifuge (CPC)

This method is completely different from the other rotating equipment described previously in this chapter. It uses a coiled separation column in a planetary motion; in other words it rotates about its own axis and at the same time revolves around the main central axis of rotation (Cazes, 2004). This approach has been used for liquid-liquid contacting where the planetary motion used to drive the liquid together with the centrifugal effect (Ito, 1980). The first use of these devices was to produce a counter-current flow in a horizontal helical tube in a planetary motion as shown in Figure 2.19 (Ito and Bowman, 1977).

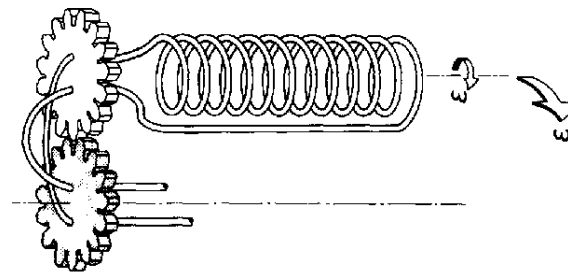


Figure 2.19: The planetary motion in coil planet centrifuge contactor (Ito and Bowman, 1977).

Different types of coil planet centrifuge have been used in separation processes and these types may be classified into categories depending on the mode of planetary motion. Thus, the first category is known as ‘synchronous’ where the rotor coil column makes one rotation on its own axis for each rotation cycle about the main axis. The second type is the ‘non-synchronous’ which gives the possibility of adjusting the rotation rates separately (Cazes, 2004). Research in coil planet centrifuges continues with most work related to medical science, e.g. separating aspirin from the hydrocarbons or producing peptides and proteins in a purification process (Ito, 2005, Knight et al., 2011). An investigation into the performance of the coil planet has been done on a compact device in order to resolve issues related to the limitation of rotation speed in the original device (Yang et al., 2010a, Yang et al., 2010b).

Like the rotating or non-rotating packed beds these devices mix the phases (in fact alternately mixing and separating the phases in each loop of the coil). The design of these devices does not include rotary seals since the planetary motion enables direct tubing connection without the tubing experiencing twisting. This can be a weakness as the tubing is still continually flexed and after a period of time the supply tubes need to be replaced due to the flexing as well as the abrasion due to contact with metal guide surfaces.

Chapter 3

3. Wide Channel Model

MacInnes et al. (2012) developed a model for the two phase flow in a rotating spiral channels of height, h , and infinite width. Figure 3.1 shows the spiral channel geometry (on the right hand side) and the notation (left hand side) that is appropriate when the channel has infinite width. The ratio of surface area to the volume for the passage is $a = 1/h$ and the inverse of this gives the length scale, i.e. h . This model allows prediction of phase flow rates, layer thickness and mass transfer coefficients (k_V and k_L) as functions of operating conditions, geometric parameters and phase properties. In the present work where hydrodynamic behaviour is studied only the flow part of the model is required to fully understand the experimental results. However, some consideration of the mass transfer aspects of the model will be considered to highlight the way hydrodynamic characteristics control the mass transfer. Chapter 2 briefly and qualitatively identified these as being the ratio of flow rates and the relative thickness of the phase layers, i.e. placement of the interface. Here, the precise relations that determine optimum values of these hydrodynamic parameters are developed. This section briefly presents the derivation of the model equations and also shows the analytical solution including the expressions for mass transfer coefficients. This is followed by illustration of the way the optimum hydrodynamic conditions are determined with the model and by demonstration of some simple effects that will be observed in the experiments, as single parameters are varied: phase flow rates and rotation rate.

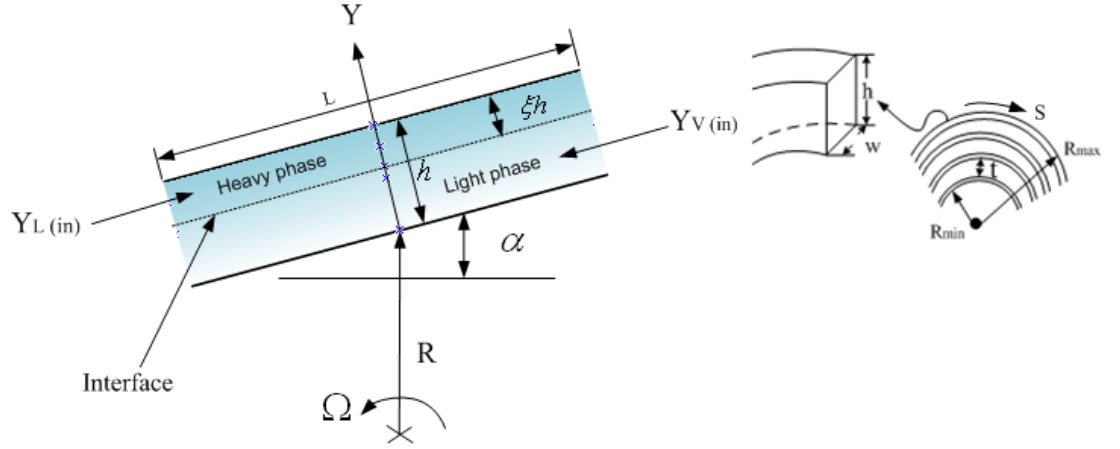


Figure 3.1 Nomenclature and geometry for two-phase parallel flow in rotating spiral channel of infinite width.

3.1 Flow model

Using the notation presented in Figure 3.1 and with the x coordinate locally tangent to the s coordinate along the spiral channel, MacInnes et al. (2012) argue for a channel of infinite width that curvature of the channel may be ignored ($R/h \gg 1$) and flow is governed by the differential equations and boundary conditions:

$$\mu_v \frac{d^2 u_v}{dy^2} = \frac{dp}{dx} - \rho_v R \Omega^2 \sin \alpha \quad (3.1)$$

$$\mu_L \frac{d^2 u_L}{dy^2} = \frac{dp}{dx} - \rho_L R \Omega^2 \sin \alpha \quad (3.2)$$

$$u_v = u_L, \quad \text{and} \quad \mu_v \frac{du_v}{dy} = \mu_L \frac{du_L}{dy} \quad \text{at} \quad y = (1 - \xi)h \quad (3.3)$$

$$u_v = 0 \quad \text{at} \quad y = 0 \quad (3.4)$$

$$u_L = 0 \quad \text{at} \quad y = h \quad (3.5)$$

Solution of these equations results in explicit relations for the velocity profile in each phase as a function of densities, viscosities, rotation rate, pressure gradient, channel height and spiral angle. The ultimate results required in this work are the expressions for volume flow rates and the ratio of these since, as argued in chapter 2, the phase flow rate ratio is fixed by the solute equilibrium characteristics and the purification required. It is helpful to express the results in terms of non-dimensional parameters and so in general dimensional quantities are normalised by values in the liquid phase. Non-dimensional density and viscosity are then expressed by the density and viscosity ratios:

$$\rho_r = \frac{\rho_v}{\rho_L} \quad \mu_r = \frac{\mu_v}{\mu_L} \quad (3.6)$$

The volume flow rates are normalised by the flow rate that would occur in the channel with the same pressure gradient but in the absence of liquid and rotation:

$$Q_o = -\frac{h^3}{12\mu_v} \frac{dp}{dx} \quad (3.7)$$

This normalising flow rate is selected since it will be near to the actual gas flow rate since the liquid layer occupies a small fraction of the channel, the liquid generally has a much smaller velocity than the gas (so is not greatly different from the fixed wall) and the gas is little affected directly by centrifugal effects. In terms of these normalisations, the solution gives for the phase volume flow rates:

$$Q_v^* = \frac{(1-\xi)^2 [3(1-\gamma)\mu_r\xi^2 + (1-\rho_r\gamma)(1-\xi)(1-\xi + 4\mu_r\xi)]}{1-(1-\mu_r)\xi} \quad (3.8)$$

$$Q_L^* = \frac{\mu_r\xi^2 [3(1-\rho_r\gamma)(1-\xi)^2 + (1-\gamma)\xi(4(1-\xi) + \mu_r\xi)]}{1-(1-\mu_r)\xi} \quad (3.9)$$

Q_v^* and Q_L^* are non-dimensional volume flow rates for vapour and liquid, respectively. Clearly, the phase flow rates depend just on the property ratios, the relative position of the interface, ξ , and the dynamic parameter, γ , which is the ratio of body and pressure forces on the liquid:

$$\gamma = \frac{\rho_L R \Omega^2 \sin \alpha}{dp/dx} \quad (3.10)$$

Eqs. 3.7, 3.8, 3.9 and 3.10 together allow solution for liquid layer thickness ($h_L = h\xi$), the ratio of forces (γ) and the pressure gradient, given the phase flow rates, the spiral channel geometry (h and $R \sin \alpha$), the rotation rate (Ω) and the phase densities and viscosities. That is, for a given experiment, where these are all known, the layer thickness can be predicted.

3.2 Solute model

Mass transfer prediction requires the second part of the model in which expressions for mass transfer coefficients are derived following a similar path to that for the flow model.

The governing equations and boundary conditions for solute mole fraction are:

$$D_v \frac{d^2 Y_v}{dy^2} = u_v \frac{dY_{vB}}{dx} \quad (3.11)$$

$$D_L \frac{d^2 Y_L}{dy^2} = u_L \frac{dY_{LB}}{dx} \quad (3.12)$$

$$Y_v = f(Y_L) \quad \text{and} \quad n_v D_v \frac{dY_v}{dy} = n_L D_L \frac{dY_L}{dy} \quad \text{at} \quad y = (1-\xi)h \quad (3.13)$$

$$\frac{dY_v}{dy} = 0 \quad Y_v = Y_{v0} \quad \text{at} \quad y = 0 \quad (3.14)$$

$$\frac{dY_L}{dy} = 0 \quad \text{at} \quad y = h \quad (3.15)$$

Where Y_V and Y_L are the mole fractions for the light and heavy phase respectively. Boundary conditions (Eqs. 3.14 and 3.15) impose zero solute flux to the channel walls and fix the level of concentration, which must be known. The gradients of bulk concentration along the channel must also be known, however only one is required as the other is then fixed by the overall balance on solute species:

$$\frac{dY_{VB}}{dx} = -\frac{n_L u_{LB} \xi}{n_V u_{VB} (1-\xi)} \frac{dY_{LB}}{dx} \quad (3.16)$$

Solution of these equations results in the relations for normalised mass transfer coefficients:

$$k_V^* = \frac{35 \left\{ 1 - \xi \left[2 - \mu_r (4 - \xi) - \xi \right] - \gamma \left[3\mu_r \xi^2 + \rho_r (1 - \xi) (1 - \xi + 4\mu_r \xi) \right] \right\}^2}{13 + 2\gamma(1 - \xi)(A + B) + \gamma^2 (1 - \xi)(C + D) + \xi(E + F)} \quad (3.17)$$

$$k_L^* = \frac{35 \left\{ \xi \left[2 + \xi (1 - \mu_r) \right] - 3 + \gamma \left[3\rho_r (1 - \xi)^2 + \xi (4 - (4 - \mu_r) \xi) \right] \right\}^2}{n_r D_r \xi \left\{ G + 2\gamma(H - I) + \gamma^2 (J + K) \right\}} \quad (3.18)$$

The variables A through K are sub-functions defined by the following equations (MacInnes et al., 2012):

$$A = 7\mu_r \xi^2 \left\{ \xi \left[8 - 13\mu_r - 4\xi(1 - \mu_r) \right] - 4 \right\}$$

$$B = \rho_r (1 - \xi) \left\{ \xi \left[39 - 82\mu_r - \xi(39 - 4\mu_r(34 - 33\mu_r)) \right] + (1 - \mu_r) (13 - 41\mu_r) \xi^2 \right\} - 13 \}$$

$$C = 63\mu_r^2 \xi^4 + 14\mu_r \rho_r (1 - \xi) \xi^2 \left[4(1 - \xi) + 13\mu_r \xi \right]$$

$$D = \rho_r^2 (1 - \xi)^2 \left\{ 13 + \xi \left[13(\xi - 2) + 2\mu_r (41(1 - \xi) + 66\mu_r \xi) \right] \right\}$$

$$E = 2\mu_r (1 - \xi)^3 (41 - 13\xi)$$

$$F = \xi(1 - \xi) \mu_r^2 \left[132 + \xi(13\xi - 82) \right] - 13 \left\{ 5 - \xi \left[10 - \xi(10 - (5 - \xi)\xi) \right] \right\}$$

$$\begin{aligned}
G &= 63 - \xi \left\{ 70 + \xi \left[36 - 56\mu_r - 30(1 - \mu_r)\xi - 13(1 - \mu_r)^2 \xi^2 \right] \right\} \\
H &= 7\rho_r(1 - \xi)^2 \left[\xi(5 + 4(1 - \mu_r)\xi) - 9 \right] \\
I &= \xi \left\{ 91 - \xi \left[141 - 28\mu_r - (9 + 26\mu_r)\xi - (1 - \mu_r)(41 - 13\mu_r)\xi^2 \right] \right\} \\
J &= 63\rho_r^2(1 - \xi)^4 + 14\rho_r(1 - \xi)^2 \xi \left[13(1 - \xi) + 4\mu_r\xi \right] \\
K &= \xi^2 \left\{ 132 + \xi \left[132(\xi - 2) + \mu_r(82(1 - \xi) + 13\mu_r\xi) \right] \right\}
\end{aligned} \tag{3.19}$$

Again non-dimensional variables have been used with the mass transfer coefficient normalised using the diffusion scale $n_v D_v / h$ and the new property ratios (for diffusion coefficient and mole density) appearing:

$$D_r = \frac{D_v}{D_L} \quad n_r = \frac{n_v}{n_L} \tag{3.20}$$

The important feature of these complicated expressions for mass transfer coefficients is that they simply depend on the same parameters as the flow solution did, i.e. geometry, rotation rate, pressure gradient, interface location, densities and viscosities, and also on the diffusion coefficients and molar densities of the phases. It is important to note that the mass transfer coefficients do not depend on the bulk gradient of concentration or on the bulk value of concentration. Also, neither the flow solution nor the mass transfer coefficients depend on Reynolds number for the infinite width channel.

3.3 Predicted hydrodynamic behaviour

In preparation for design of the experimental device, it was helpful to use the model to explore the relation between rotation rates, flow rates and interface locations. The geometry used corresponds to the eventual spiral channel used in the experiments here and water contacting with air at 2.1 bar absolute and 20 °C is considered. The air-water system became the main phase system used in the experiments. Table 3.1 lists the

geometric parameters that are used in the model calculations here (and in the experimental channel).

Table 3.1 Spiral Channel Dimensions.

Height, h (mm)	Width, w (mm)	Length, L (mm)	Space, t (mm)	Radius, R (mm)	Range for θ
1.5	4.0	910	2.0	$16.5 + 3.5\theta / \pi$	$0 < \theta < 10.98\pi$

Figures 3.2 and 3.3 show the effect on liquid layer thickness of varying water flow rate and air flow rate, respectively, while all other parameters are fixed. In each case, several values of rotation rate are calculated. First of all, in each plot increasing the rotation rate serves to reduce the liquid layer thickness since the driving body force on the liquid is then increased, resulting in the layer thinning to produce a larger countering shear stress with fixed liquid flow rate. Layer thickness increases with increasing liquid flow rate at fixed rotation rate since body force remains constant and the layer must thicken to maintain a balancing shear stress. The effect of liquid flow rate is quite strong, particularly at low flow rates where the same increment of flow rate increase produces a much greater relative change.

Figure 3.3 shows that air flow rate has little effect on layer thickness which is an indication that the shear stress exerted by the gas at the liquid interface is generally minor in relation to centrifugal and wall forces on the liquid. For the thicker layer at high gas flow rate in the case of 1480 rpm the gas has evidently become sufficiently restricted that its shear stress at the interface becomes important for the liquid.

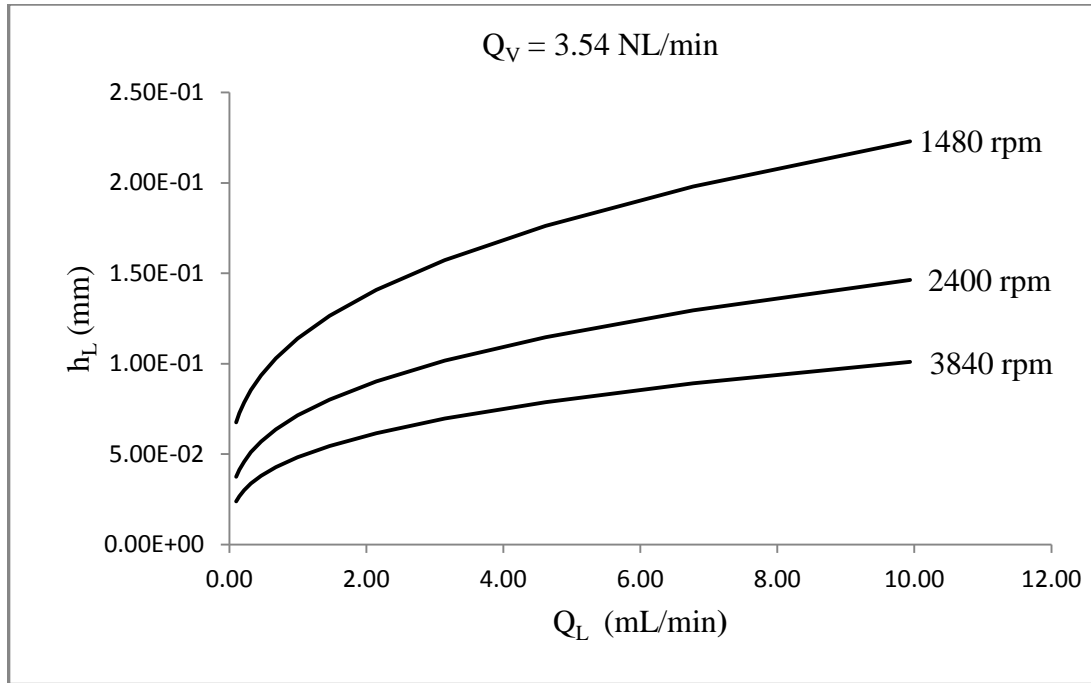


Figure 3.2: Liquid layer thickness variation with liquid flow rate. Conditions are $Q_V = 3.54 \text{ NL/min}$, $P_S = 2.1 \text{ bar absolute}$ and different rotation rate.

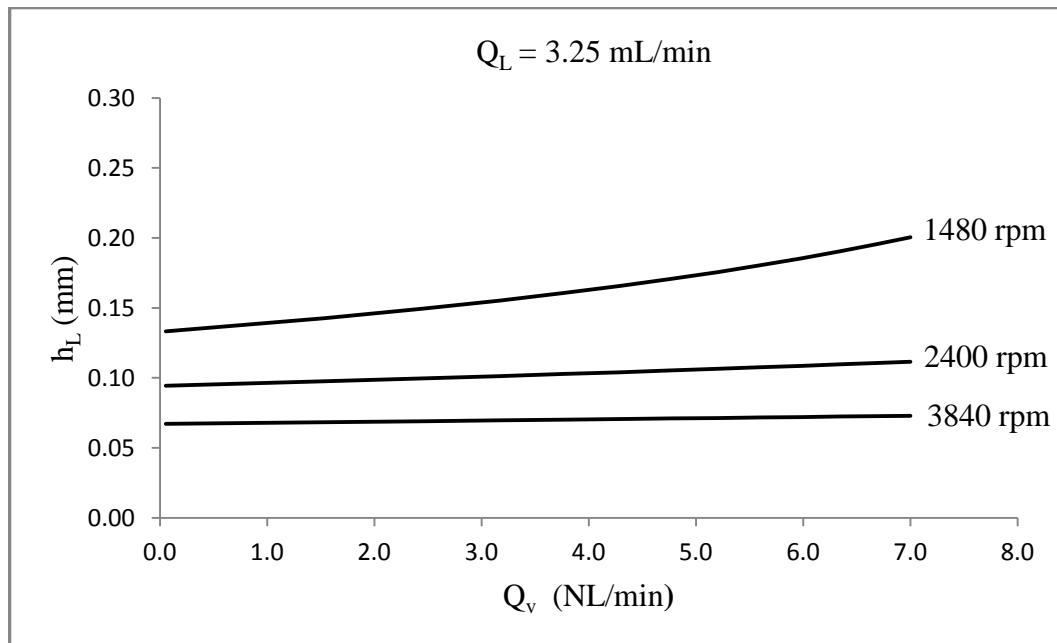


Figure 3.3: Liquid layer thickness variation with vapour flow rate. Conditions are $Q_L = 3.25 \text{ mL/min}$, $P_S = 2.1 \text{ bar absolute}$ and different rotation rate.

Over these ranges of air and water flow rate, the rotation rate required can be achieved conveniently using a standard electric motor with variable speed controller. The range of liquid layer thickness should also be accessible to measurement by means of standard macro photography. Thus, this channel geometry was adopted for the design.

3.4 Mass transfer performance

It is essential to consider the solute part of the model to ensure the design will be suited to mass transfer measurements in later work. To start with, it is helpful to give a clear definition of what is meant by ‘optimum’ contacting of the two fluid phases. The presentation here reflects the same considerations discussed at the start of chapter 2, but the specific exact relations associated with the model (MacInnes et al., 2012) are developed.

First of all, the ratio of phase flow rates is fixed by the purification to be reached and by the equilibrium characteristics of the solute. Two types of contacting will be considered, absorption and desorption, but others will have similar relations for optimum flow rate ratio in terms of purification and equilibrium characteristics. In the case of absorption (from the gas phase) of a solute with equilibrium coefficient f' and where the ratio of outlet gas solute mole fraction and the inlet value (the ‘purification ratio’) is $a_v = Y_{vout}/Y_{vin}$, conservation of solute requires:

$$-q_n > \frac{1 - f' a_L}{f' (1 - a_v)} \quad (3.21)$$

Here, q_n is the ratio of the molar flow rates of the phases which is related to the volume flow rate (appearing in the flow model) by:

$$q_n = \frac{n_v Q_v}{n_L Q_L} \quad (3.22)$$

The concentration of solute in the inlet liquid is represented in Eq. 3.21 by $a_L = Y_{Lin}/Y_{Vin}$, which is ordinarily zero. In the case of the equality of the two sides of Eq. 3.21, the liquid passes out the outlet in perfect equilibrium with the incoming gas stream which requires an infinitely long contacting length. Noting that q_n is negative for this counter-current flow, the left hand side of Eq. 3.21 is positive and satisfying the inequality corresponds to having an excess flow of liquid to achieve purification a_V , as expected. Increasing the liquid flow rate allows a decreased length of contacting and hence capital cost, but also increases liquid replenishment cost. Balancing these costs determines the optimum flow rate ratio.

Exactly the same analysis results in the restriction on desorption processes in terms of the purification $d_L = Y_{Lout}/Y_{Lin}$ and normalised inlet gas solute mole fraction $d_V = Y_{Vin}/Y_{Lin}$:

$$-q_n > \frac{1-d_L}{f'-d_V} \quad (3.23)$$

The second aspect of optimum contacting is placement of the interface at the best location for mass transfer. This location corresponds to that giving the largest value of specific throughput. Specific throughput, Φ , is defined as the throughput (volume flow rate of the processed stream) per volume required to produce a unit of separation. In the case of the wide channel model, the specific throughput may be written:

$$\Phi_V = \frac{-u_{VB}(1-\xi)}{\ell_e} \quad (3.24)$$

Where the subscript 'V' indicates gas stream throughput, u_{VB} is the (negative) bulk gas velocity and ℓ_e is the equilibrium stage length, selected to represent a unit of contacting. (Alternative lengths could be used and Appendix A gives further details of background mass transfer theory which includes alternative measures of mass transfer length.) The

equilibrium stage length may be expressed in general for a dilute solute, where f' is constant, as (e.g. Sherwood et al., 1975)

$$\ell_e = -\frac{n_v u_{VB} (1-\xi) \ln(-f' q_n)}{K_v a (1+f' q_n)} \quad (3.25)$$

Where $K_v = (1/k_v + f'/k_L)^{-1}$ is the overall mass transfer coefficient. So, finally, substituting for ℓ_e in Eq. 3.24 and specialising to the case of a wide rotating spiral channel gives the relation for specific throughput:

$$\Phi_v = -\frac{K_v (1+f' q_n)}{n_v h \ln(f' q_n)} \quad (3.26)$$

Since the relation between f' and q_n is fixed by optimum flow rate ratio, for a given phase and solute system specific throughput is maximised by maximising $K_v a = K_v/h$. Figure 3.4 shows results for the air-water system and with a solute giving $f'=1$ for different values of q_n in the range allowing full purification for absorption processing. The specific throughput is plotted as interface position (ξ) is varied. The specific throughput plotted is that for a particular number of stages, hence the division by N in the plotted specific throughput. It makes no difference to the position of the optimum plotting it this way or plotting specific throughput per volume of one equilibrium stage. For a given flow rate ratio there is a clear peak in specific throughput and this corresponds the optimum layer position. At this optimum and with the same flow of gas being processed the length of channel giving one equilibrium stage is minimised and the mass transfer is optimum for that flow ratio. It can be seen that the optimum rises rapidly at first as the flow ratio is increased from the critical value of $q_n = -1$ and then the increase in specific throughput is reduced. This point is emphasised by the plot in Figure 3.5 of specific throughput as q_n is varied in relation to the critical value corresponding the equality in Eq. 3.21. Again the system is air-water with $f'=1$ and the value of ξ plotted corresponds to the optimum interface position. As q_n moves away from the critical value, either to the right (desorption) or to the left (absorption), the specific

throughput first rises rapidly and then the increase becomes less rapid. The optimum flow ratio will be determined by the economics of both the shortening device path and the increasing regeneration cost.

An important outcome of this model calculation is the small thickness of optimum liquid layers both for absorption and desorption. From Figure 3.5, ξ ranges from about 0.002 to about 0.02, which corresponds to layer thickness for the 1.5 mm experimental channel in the range 3 to 30 μm . Such thin layers may or may not be feasible. A modest 10% reduction in specific throughput is associated with increasing these thicknesses by a factor of three to the range 10 to 100 μm which, as will be shown, is a range that is accessible.

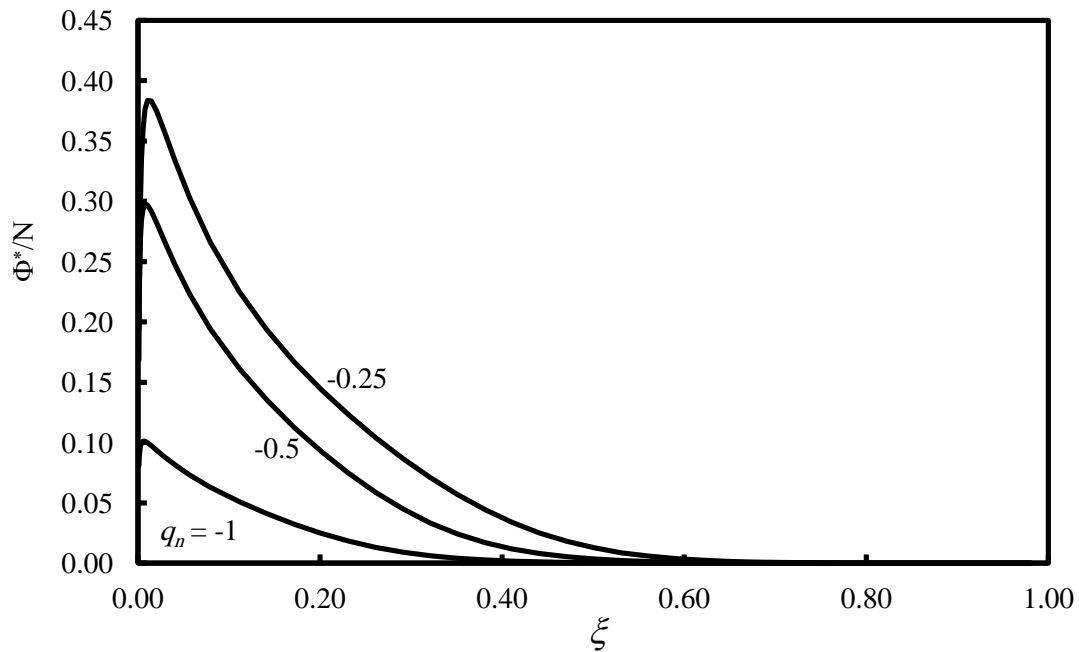


Figure 3.4: Optimum non-dimensional throughput for air-water absorption system.

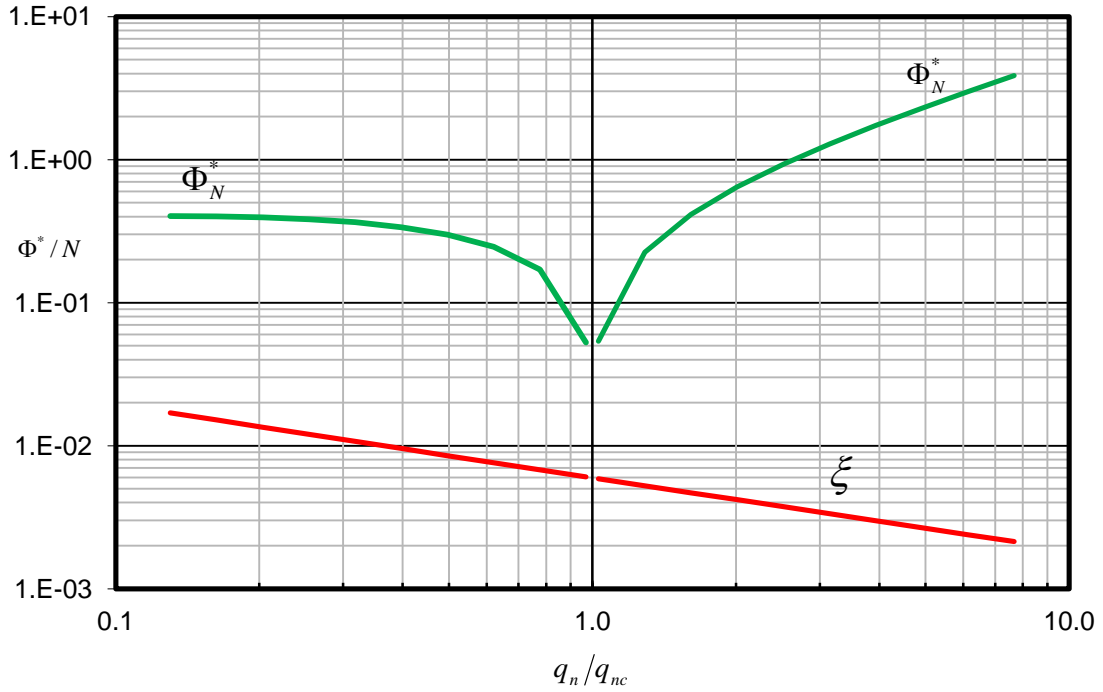


Figure 3.5: Optimum liquid layer thickness and specific throughput for standard air-water system as flow rate ratio is varied.

These results demonstrate that the capability of adjusting the phase flow rate ratio and the interface position is crucial in obtaining optimum use of a given device. Since both are hydrodynamic parameters, the present work on flow characteristics of the rotating spiral has direct implications for mass transfer.

3.5 Further design considerations

In addition to the preceding considerations of the spiral channel design, MacInnes et al. (2012) argue that the stability of the layer flows must be considered. If either of the layers becomes unstable, entering a transitional or turbulent flow state, or if the interface becomes unstable, through centrifugal or capillary waves, control of the layers and the counter-current flow may be lost. Also, in the experimental apparatus it is desirable to ensure operation such that at least from part of the range of operation, conditions are such that the approximations made in the wide channel model (infinite channel width, no

effect of gravity) are good. The criteria for these various aspects of operation are presented here.

To ensure effective contacting in the spiral channel the phase layers should remain separated and in parallel flow. However, due to either an increase in the flow velocity or the channel size, the flow will eventually become unstable and parallel flow could be disrupted. There are different causes of unstable flow but in all cases waves begin to grow without limit. The waves can be inertial waves in either phase or centrifugal or surface tension waves at the phase interface. While no reliable guidance on when this instability will develop is available, MacInnes et al. (2012) put forward rough criterion based on the Reynolds number in each phase, the Froude number and the Weber number. It is hypothesised that exceeding critical a value of any one of these should be avoided as loss of stable flow may result.

The Reynolds, Froude and Weber number conditions are as follows:

$$\text{Re}_v = \frac{h \rho_v u_{vB} (1-\xi)}{\mu_v} < \text{Re}_c \quad \text{where} \quad u_{vB} = \frac{Q_v}{h(1-\xi)} \quad (3.27)$$

$$\text{Re}_L = \frac{h \rho_L u_{LB} \xi}{\mu_L} < \text{Re}_c \quad \text{where} \quad u_{LB} = \frac{Q_L}{h\xi} \quad (3.28)$$

$$\text{Fr} = \frac{u_{LB}}{\sqrt{R \Omega^2 \xi h}} < \text{Fr}_c \quad (3.29)$$

$$\text{We} = \frac{h \xi \rho_v (u_{LB} - u_{vB})^2}{\sigma} < \text{We}_c \quad (3.30)$$

The critical values suggested are $\text{Re}_c = 500$, $\text{Fr}_c = 0.5$ and $\text{We}_c = 1.0$, which are considered to be conservative. That is, significantly higher values than these are likely to be possible without losing control of the counter-flowing phase layers.

Two further conditions are related to control of the phase interface such that the liquid layer approximates the uniform layer thickness of the wide channel model. The first

parameter is the relative importance of gravity which determines the tilting of the interface (from parallel to the channel walls). The requirement is

$$R\Omega^2/g \gg 1 \quad (3.31)$$

Finally, the centrifugal force should also be large enough to dominate the interface surface forces, both reducing meniscus size at the end walls of the finite channel and preventing pockets of gas or liquid forming within the spiral channel. The characteristic ratio of centrifugal to surface force (Eötvös number) should be much greater than unity, leading to the condition:

$$E\ddot{o} = \frac{\Delta\rho R\Omega^2 h^2}{\sigma} \gg 1 \quad (3.32)$$

Where $\Delta\rho = \rho_L - \rho_V$ and σ is the interfacial surface tension.

For a given phase and solute system, it is possible to make plots to determine the stable operating regime as a function of channel size (MacInnes et al., 2012). For example, with the air-water system and for a solute having $f' = 1$ the diagram shown in Figure 3.6 results. The dependent variable plotted is the pressure drop along the channel for fixed purification and for optimum interface location. (Similar plots result for any variable related to flow rate, i.e. flow rate of one or the other phase, rotation rate or the pressure drop as in the figure.) On such plots, the curves of constant stability parameter plot as straight lines for logarithmic axes and these straight lines then bound the region of stable layer flow. Low pressure drop requires low rotation rate and hence the surface tension and gravity conditions represent lower boundaries to stability. As pressure drop moves upward from these lower bounds, the first flow instability line reached is deemed to be the limit. So in this case, the Re_V line is reached first and disruption by turbulent flow in the gas phase flow would be expected. This important line of work is not pursued further here but this diagram does guide selection of channel size in the present work. The 1.5 mm channel height used in the experiment should allow at least two orders of magnitude range of pressure drop (and hence flow rates) to be studied for the air-water system.

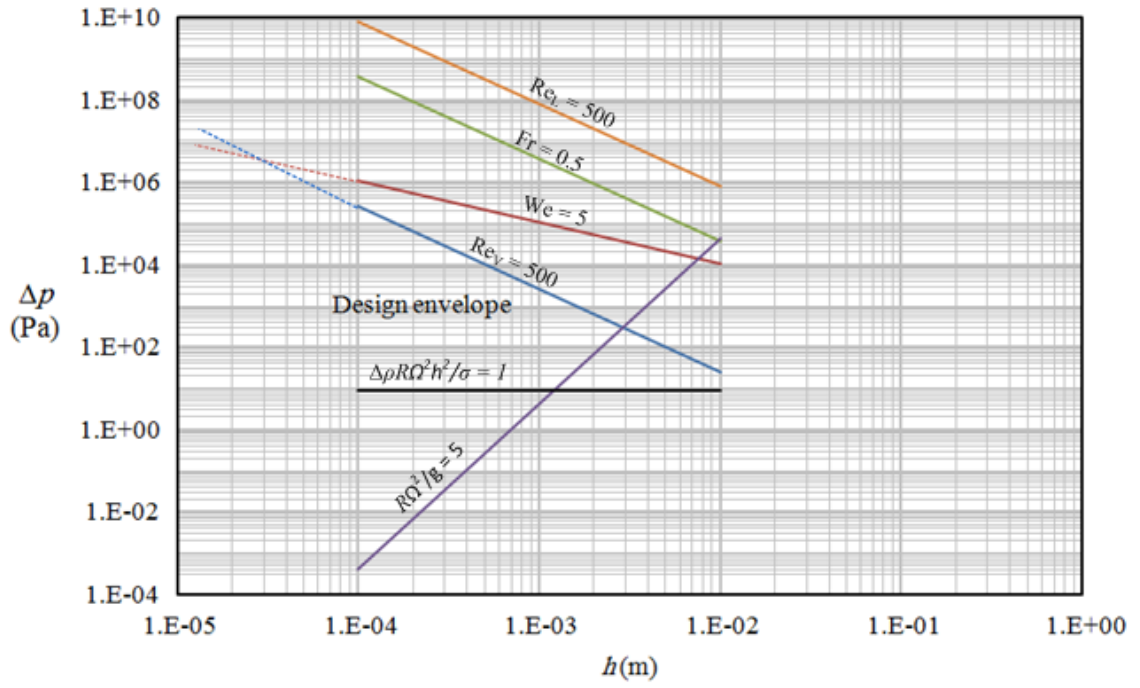


Figure 3.6: Stability envelope plot for pressure difference over channel length; standard air-water system.

Chapter 4

4. Rotating spiral apparatus

The rotating spiral device developed as part of this work is now described. Several particular technical issues needed to be resolved and details of these are presented in this chapter. One of these technical issues is making the rotating connections allowing fluids to flow in and out of the rotating unit. The description of the apparatus will be divided into two sections: the description of the main unit comprising drive motor, seal case and spiral assembly, and the auxiliary elements including the external flow system to supply, control and measure the fluid streams. The overall apparatus is pictured in Figure 4.1 with the ‘rotating spiral unit’ combining the seal housing and the spiral element assembly (shown from below in the inset). Below are two cameras; a small monitoring camera to the left allows a continuous view of the channels (in particular the liquid outlet reservoir) during operation and a digital SLR on the right for high-resolution imaging for measuring the phase interface position. Both cameras are synchronised with the rotation using a triggered strobe light.

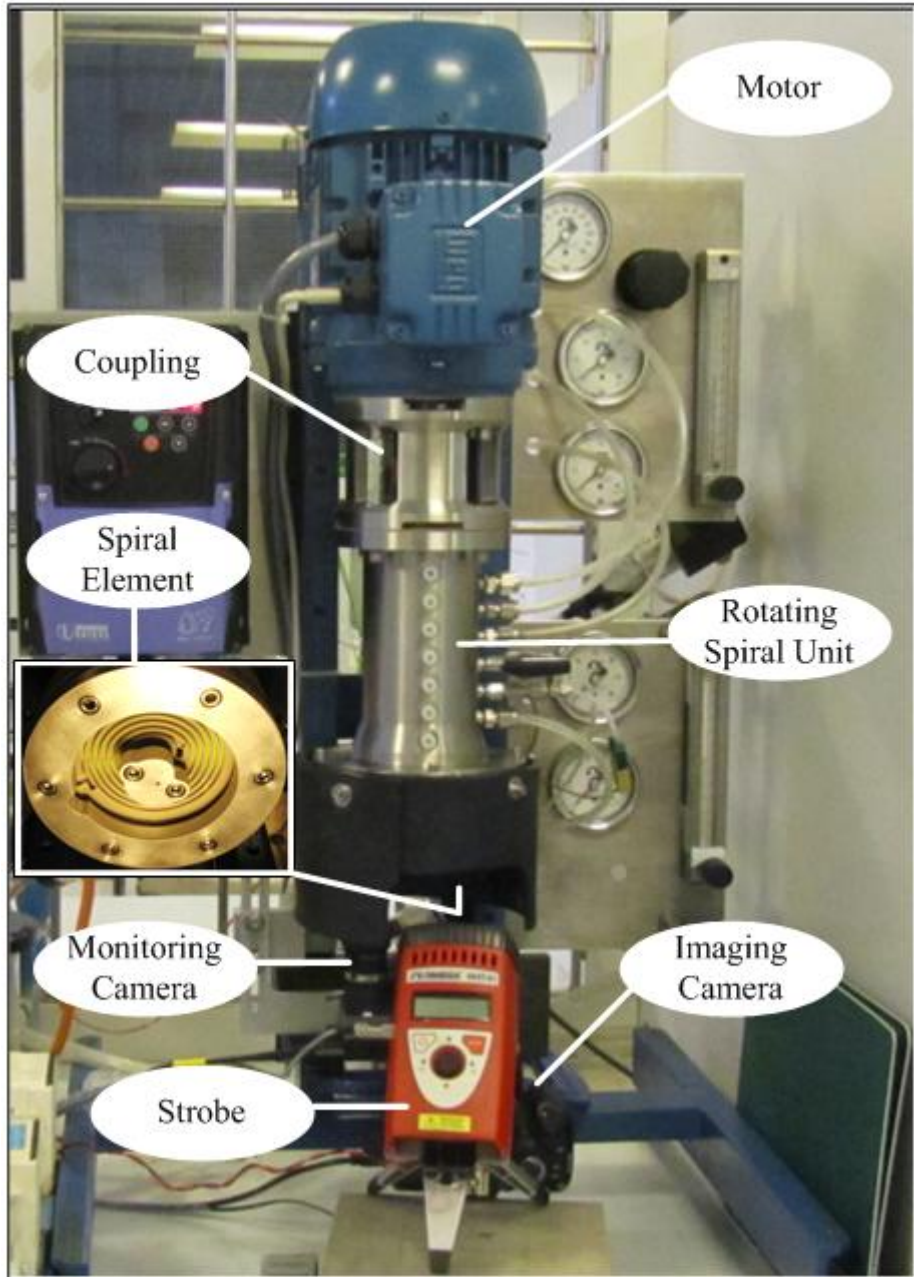


Figure 4.1: Rotating Spiral Apparatus.

4.1 Rotating spiral unit

The rotating spiral unit is shown in section view in Figure 4.2. It consists of several individual elements which serve to allow passage of the contacting fluids to and from the rotating spiral. Lip seals riding on a rotating shaft allow individual streams to be passed from static connection to the rotating unit. Due to the rotation, heat generation will occur from the ball bearings and from the friction between the lip seals and the rotating shaft surface. Thus, the design uses water cooling passages along the shaft to maintain acceptable temperature for the seals, shaft and contacting fluids. The first and last of the six lip seal connections are for the cooling water flow. The further four seal pairs give the two inlets and two outlets for the two separate fluid streams. The contacting fluids are directed along passages in the rotating shaft that lead to the spiral element that is clamped to the shaft head. The spiral channel is formed by milling into the face of the spiral element and covering with a glass window to close the channel and allow optical access for photography. The case also includes two rolling bearings to support the rotating shaft with a lock nut at the top. All the metal parts were made from 316L stainless steel. The unit measures approximately 10 cm in diameter and 20 cm in height. The complete technical drawings of the component parts are supplied in appendix C for reference.

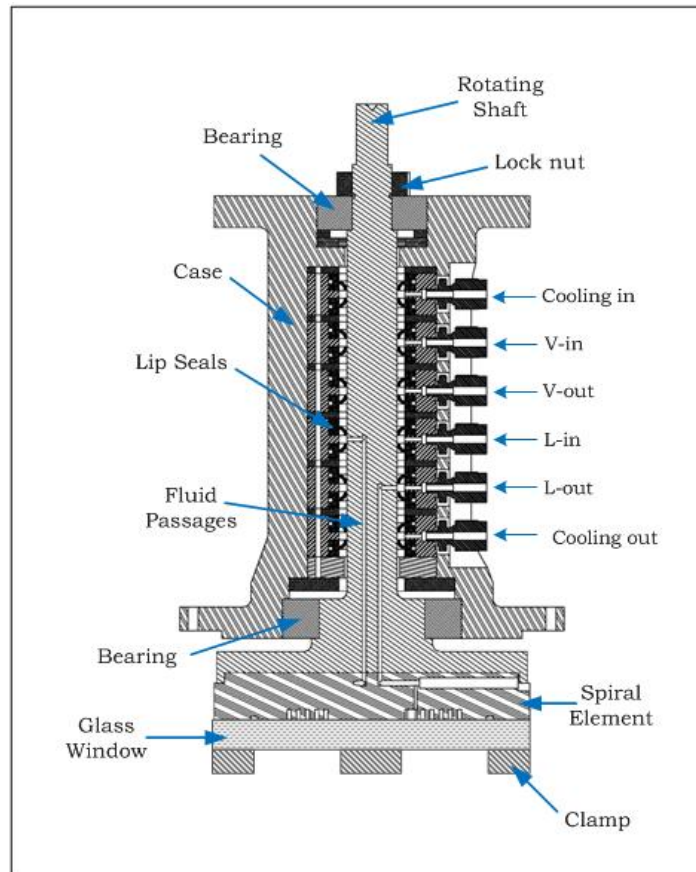


Figure 4.2: Section view of rotating spiral unit.

4.1.1 The seal unit

The purpose of the seals is to transfer the fluids to and from the spiral element via the passages in the shaft with no leakage. This involves handling one inlet and one outlet for each of three fluid streams, two contacting fluid streams and the cooling water stream. A pair of lip seals is required for each connection (Figure 4.3) and each pair is fixed in a metal T-piece to form the sealed transfer gap in between. Also there are six spacers between seal pairs to lock the seals into the T-pieces. Each spacer includes a groove to drain liquid which may accumulate in case of leakage. Figure 4.4 shows the components of the seal unit individually and in various stages of assembly.

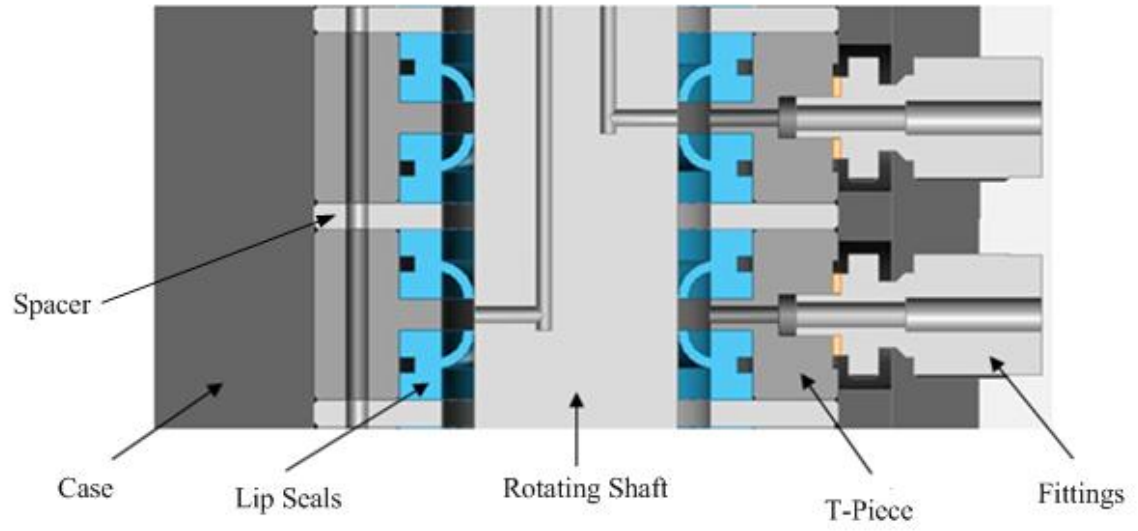


Figure 4.3: Lip seal connections.

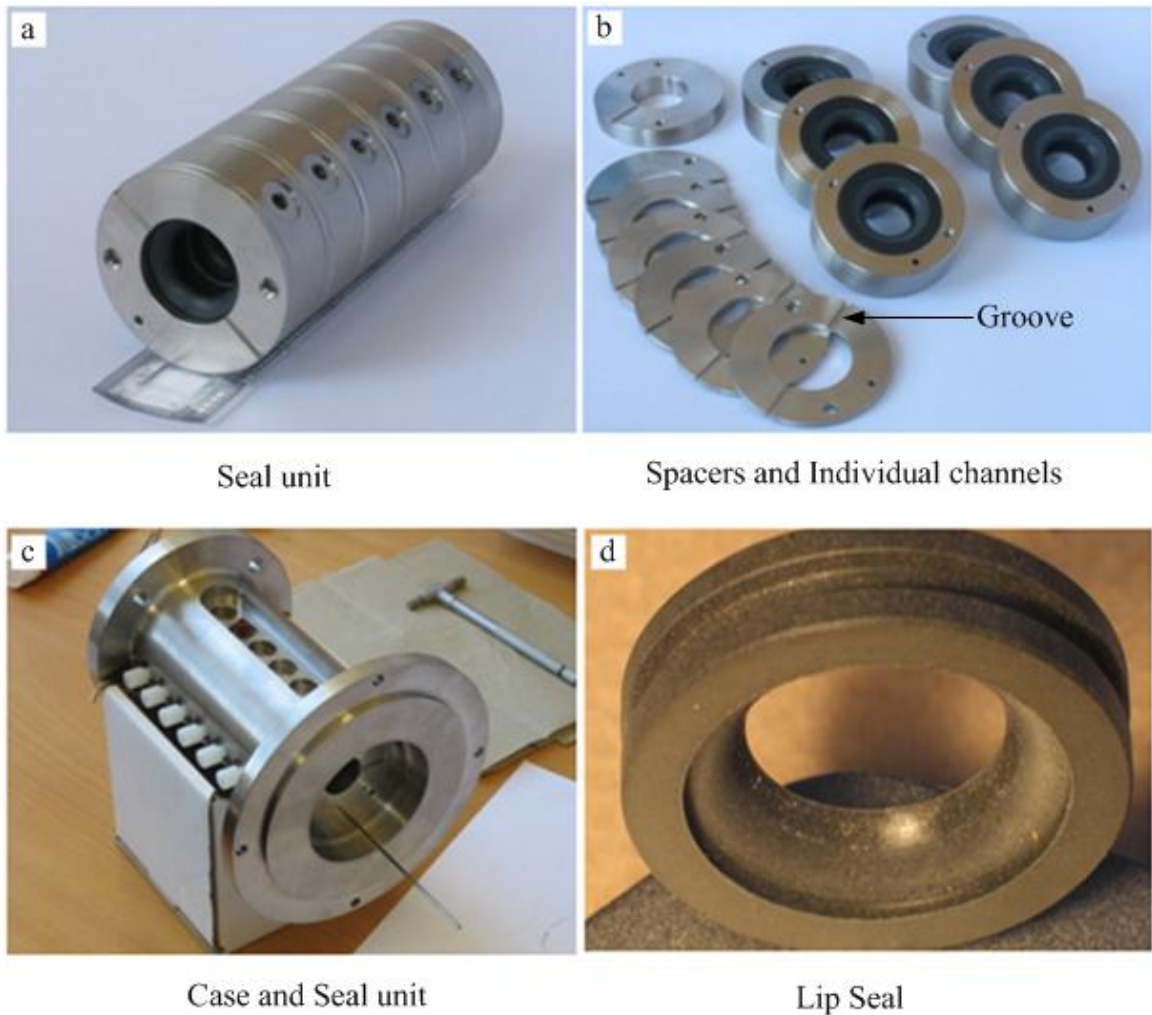


Figure 4.4: Seal unit components; (a) seal unit, (b) spacers and seal-pair channel, (c) case and seal unit, and (d) lip seal.

The lip seals were supplied by Ceetek Ltd., Bedford UK. The seals are of a standard design and made from a PTFE-carbon fibre composite material, giving the seals inertness to a wide range of contacting fluids and suitable mechanical properties both to seal and to resist wear. The maximum allowed operating pressure difference across the lip seal is indicated by the manufacturer to be 4.0 bar. The PTFE gives low friction, wide temperature range (260 – 400 °C) and dry running capabilities. Proper surface finish of the shaft is critical to ensure positive sealing and achieve long seal life in rotating applications (Parker Hannifin, 2006). The shaft surface finish was specified at less than

0.2 μm rms roughness and was hardened to nominally Rc 70. In addition care was taken to reduce shaft run-out and eccentricity to less than 40 μm and 60 μm , respectively, as recommended by the seal supplier.

4.1.2 The spiral element

The spiral element was made from PEEK (polyether ether ketone) since it is chemically inert, lower density than a metal and yet having stable structural properties. The spiral channel was milled into the face of the PEEK surface using computer-controlled machining to form a channel 0.91 m long, 4 mm deep and 1.5 mm height (the width of the cut channel). Figure 4.5 shows the cut pattern for the spiral channel, the bolt holes, an O-ring groove and the inlet and outlet holes drilled down into the spiral element. The heavy phase enters at the inner end of the spiral at A1 and leaves the channel at the outer end at A2. Flowing in the opposite direction, the light phase enters at the outer end of the spiral at B2 and leaves at the inner end at B1. Also, surrounding the region of the spiral is an O-ring to give an absolute seal between the glass window PEEK surfaces. Fluid is prevented from escaping through the inner bolt holes since there is direct pressure from the clamp there. Adjacent revolutions of the spiral channel are sealed just by the close fit between glass and PEEK surface. Figure 4.6 shows an exploded view that reveals the various components making up the spiral element assembly, including the head of rotating shaft to which this is clamped. As can be seen a PTFE gasket seals between the spiral element and the head of the shaft where the phase flows pass from one to the other.

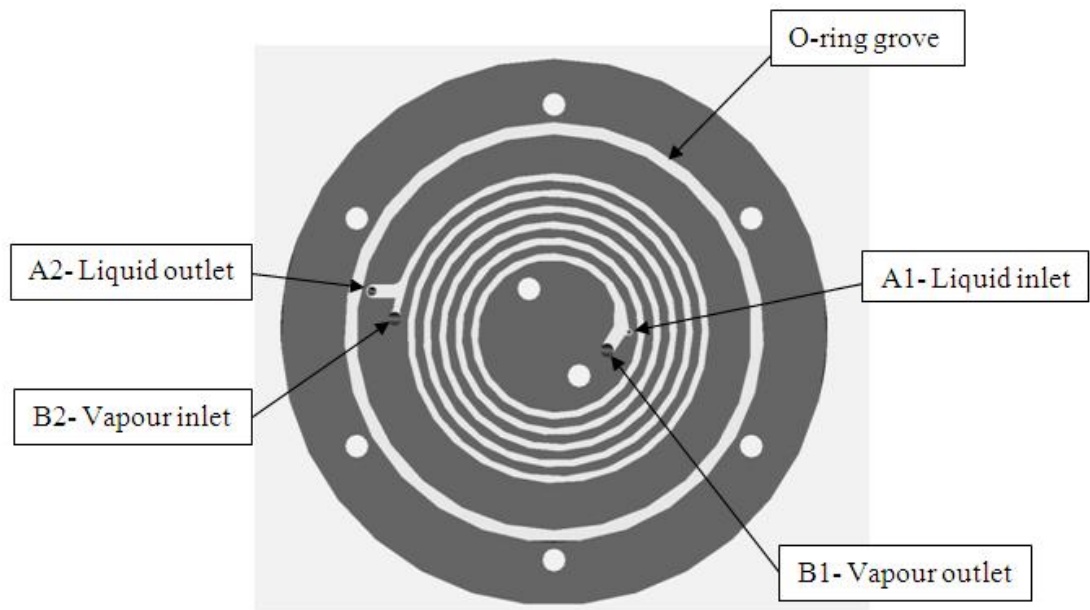


Figure 4.5: Spiral element design.

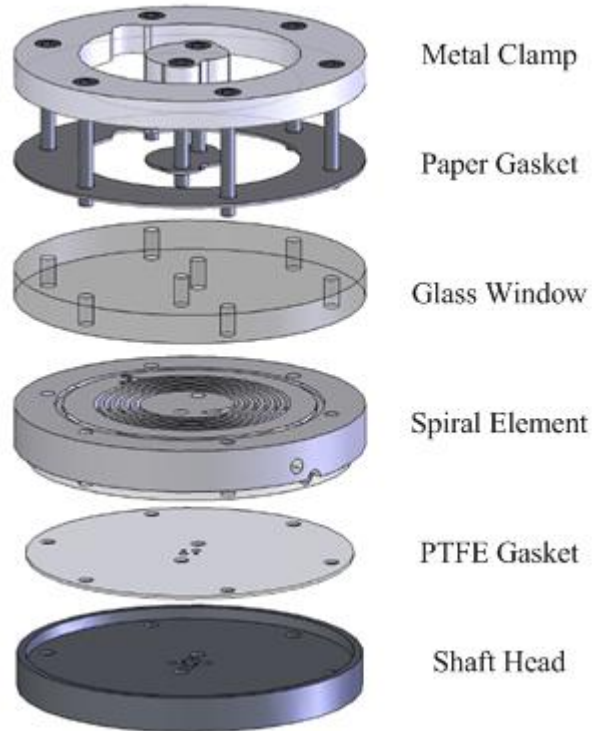


Figure 4.6: The components of attaching the spiral element to the head of the shaft.

4.1.3 The rotating shaft

This part is the structural backbone of the device, and also provides the routing passages connecting the seals to the spiral element and the cooling passages. Each shaft passage involves a radial hole leading flow to the axial hole conveying fluid along the shaft. In the case of the cooling flow, the flow is in one radial hole and along the length of the shaft to another radial hole. The contacting fluid passages, on the other hand run the full length to the head of the shaft, connecting with mating holes in the spiral element to connect in turn with the appropriate port to the spiral channel ends. So the various fluid streams do not contaminate one another other than in the spiral channel, a PTFE gasket with passage holes is used to seal around the connections at the shaft head-spiral element junction. This gasket is shown in Figure 4.6. The whole patterns for the flows within the shaft are shown in Figure 4.7. Four outer cooling water passages surround the four inner contacting fluid passages. The passages for the heavy phase flow are made 1.5 mm in

diameter and those for the light phase (typically gas) and the cooling water holes are 3 mm diameter. These sizes are estimated to give negligible pressure drop over the expected flow rate ranges for the two contacting phases.

The shaft is attached to the case using a sealed ball bearing at both the top and the bottom, with a lock nut to prevent axial movement. Rotating seal surfaces that are too soft can wear rapidly due to seal abrasion. Thus, the shaft is hardened using a low-temperature surface diffusion technique known as Kolsterising (Bodycote) which produces surface hardening without loss of corrosion resistance in the 316L stainless steel.

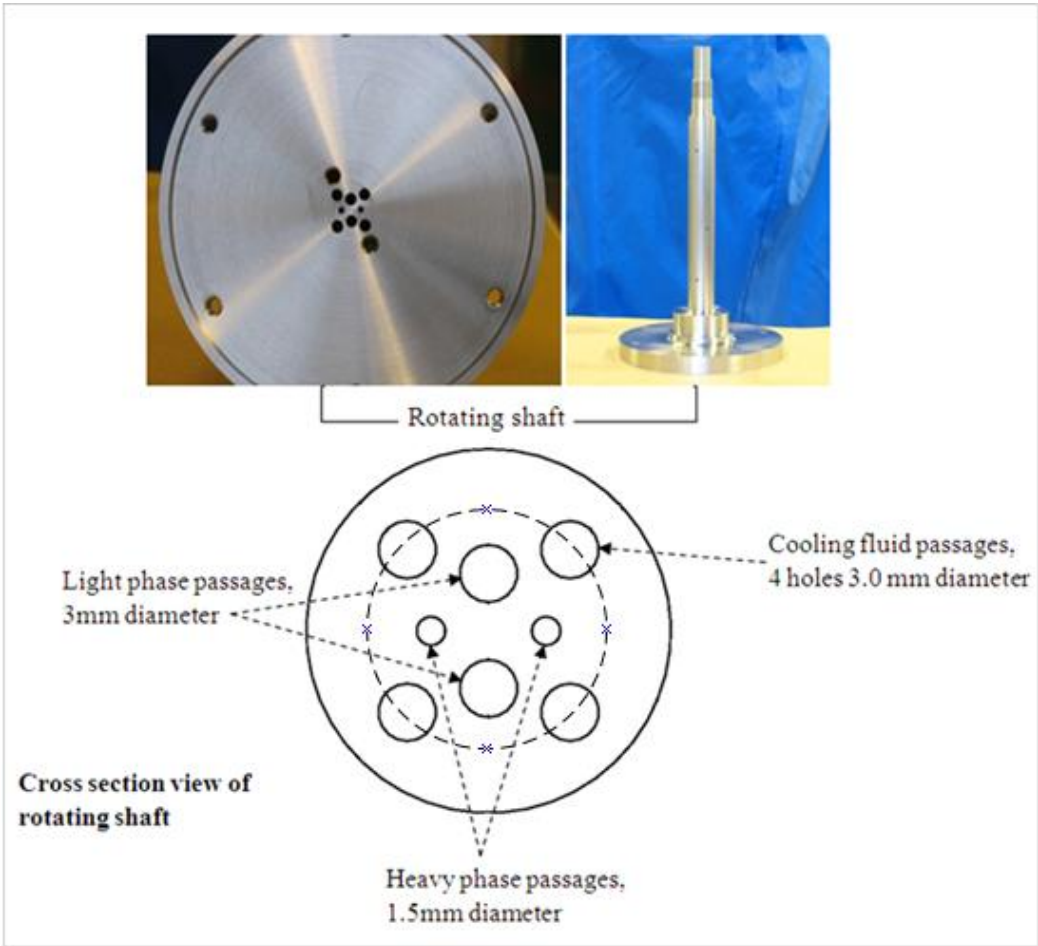


Figure 4.7: Rotating shaft passages.

4.2 The electric motor

A 750 W three-phase AC induction motor (WEG) driven by an inverter (Invertek) was used to produce rotation rates in the range 400 to 4000 rpm. The motor provides approximately double the estimated maximum power and torque required to turn the shaft against seal and bearings resistance. These maximum conditions correspond to the highest rpm and seal pressure differential. In order to select the suitable electric motor, estimates of the torque and hence power for the six pairs of seals were made.

4.3 Flow and pressure control instruments

The apparatus was designed to operate at pressures up to 4.0 bar (seal limit) and, for a gas-water system, with flow rates from 0 to about 10 NL/min (gas) and 0 to about 10 mL/min (water). These ranges are determined by the passages sizes leading to and from the spiral. So for more viscous liquids the flow rate range is more limited, but this is consistent with the reduced flow rate range that is appropriate on the spiral for more viscous liquids. The apparatus, thus, was designed to suit different contact systems including ones with viscous liquids but also, for example, liquid-liquid systems. Most of the experiments in this research have been done with gas-liquid systems, but one case of liquid-liquid contacting is also tested. In all cases the theoretical expectation is that the contacting conditions can be adjusted to produce optimum conditions, i.e. the phase flow rate ratio and the interface position can be adjusted to the particular ideal values for the particular phase and solute system. This is done by independent adjustment of the flow rates and of the position of the phase interface in the channel. Control of the phase flow rates is a matter of controlling pressures and resistances (using needle valves) while measuring the flow rates. Flow rates were measured using rotameters (Icenta, 140 mm variable area flow meters, accuracy 2% of full scale reading) in the case of air and water flows and using syringe pump drive rate for viscous liquids. The position of the interface must then be measured and the method used is based on photography and image analysis using a model for interface shape, and this will be described in chapter 5.

4.3.1 Adjusting the pressure in spiral

Figure 4.8 shows the flow diagram for the air-water system with mains water (at approximately 40 psig) entering the apparatus through a rotameter and needle valve to set the liquid flow required. There is a switching valve at the liquid inlet to direct the flow either to the device or to divert the flow to a sink. The diversion was necessary to prevent flow to the spiral until rotation was started and centrifugal force was effective. There are pressure and temperature gauges at all flow inlets and outlets and also other temperature measurements (not shown) related to bearing temperatures and ambient lab temperature.

The air flow comes from a lab compressor through a pressure regulator (REG 1) which allows regulation of upstream pressure up to 2 bar (nominal). Regulating the air inlet pressure in turn determines, with gas flow rate, the pressure in the spiral and this pressure must be set to the particular value required to balance the hydrostatic pressure rise in the liquid, due to the centrifugal body force, from the pressure at the liquid outlet. Thus, the setting of the upstream gas pressure is dependent on the rotation rate, liquid density and the downstream liquid pressure. If the gas pressure is too high in the spiral channel the liquid reservoir level will drop too low and allow gas to flow out the liquid outlet and if the pressure is too low the reservoir level will overflow into the spiral channel.

Setting a desired pressure in the spiral starts with calculating the pressure rise in the heavy phase between the outlet (the ‘pressure pot’ in Figure 4.8) of that phase and the phase interface in the reservoir at the outer end of the spiral. From the equations presented in the Appendix B, and the passage sizes and lengths leading from the pressure pot back to the reservoir, one can calculate the pressure rise for a given test. Thus, a given spiral pressure can be imposed by setting the pressure in the downstream pot using REG 2 such that the sum of this pressure and the pressure rise give the correct pressure.

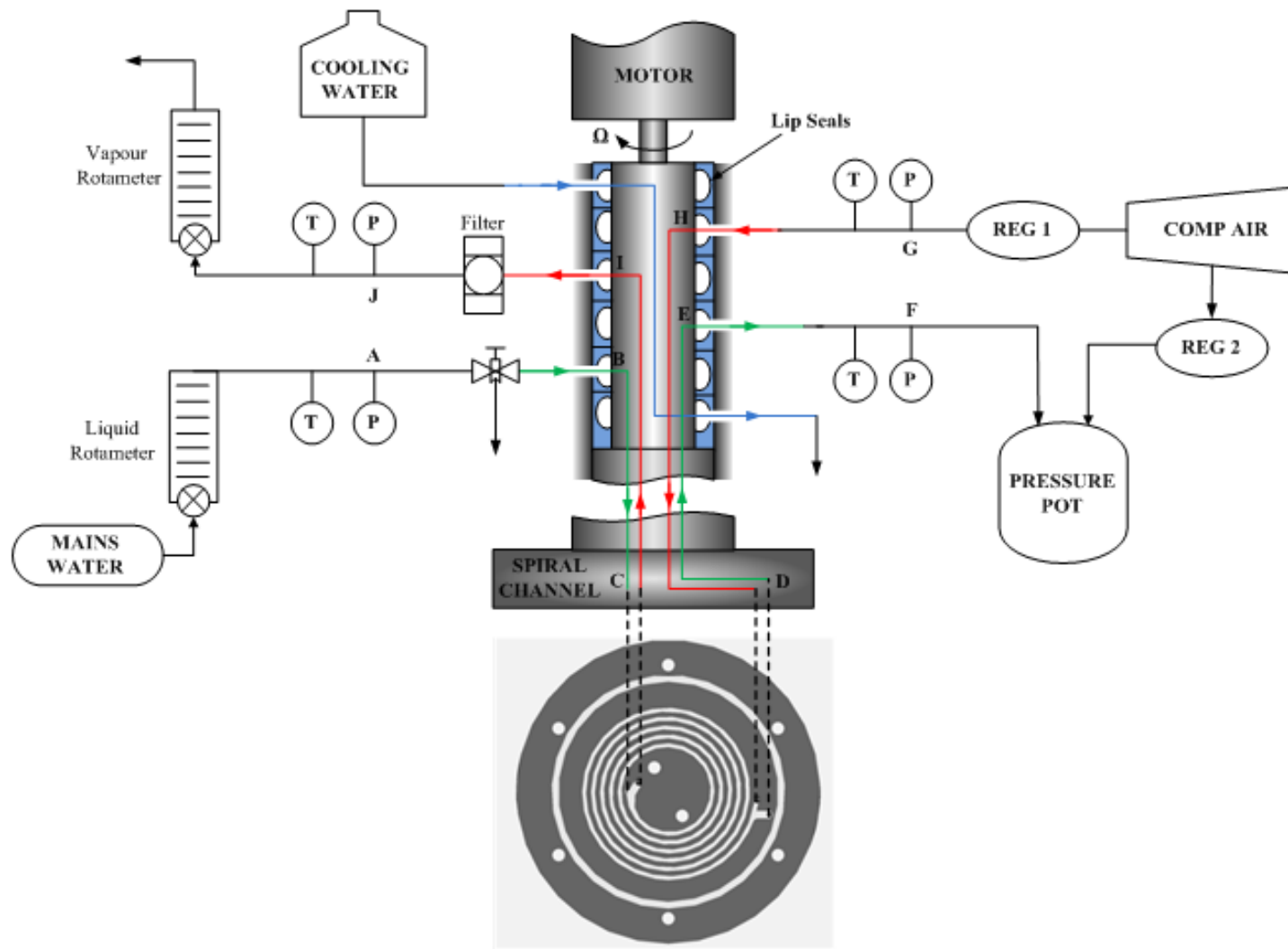


Figure 4.8: Flow and pressure instruments in rotating spiral apparatus for air and water system.

4.3.2 Monitoring and controlling liquid outlet reservoir level

Figure 4.9 shows a typical view of the reservoir during operation and a detailed view of the components involved in the monitoring. The monitor camera and strobe light are triggered using a magnet embedded in the spiral element and a Hall-effect sensor to pick up the time it passes a fixed point. This allows the camera and strobe to be synchronised with the rotation of the spiral so the same position on the spiral is recorded each revolution and a stationary image is seen. In this way the reservoir region is continuously visible and the effect of adjustment of pressures and flow rates can be monitored, enabling convenient adjustment of the reservoir level.

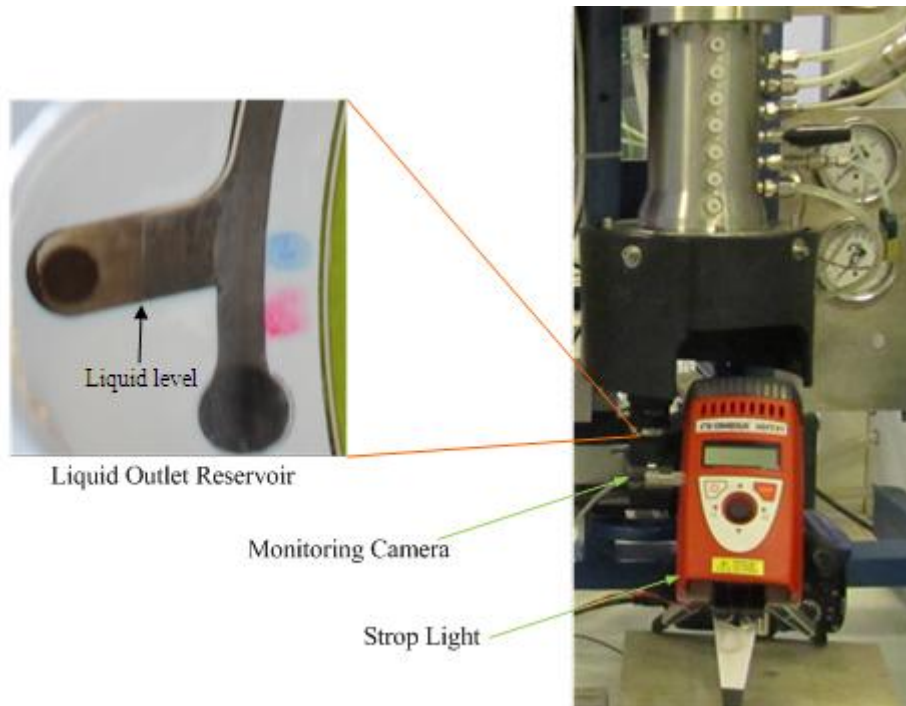


Figure 4.9: Monitoring of liquid outlet reservoir.

4.4 Typical operating procedure

The operating procedure used in the experiments is the same for all phase systems tested with slight modification for cases where a syringe pump is used to drive the fluid. The general operating procedure using the specific case of the air-water phase system can be summarized in steps as follows:

- Open the valve to start cooling water flow
- Open the valve for compressed air
- Set the back pressure using the pressure regulator on liquid outlet pressure pot (REG 2)
- Switch on the electric motor and set the rotation rate required
- Connect the monitoring camera to the computer and adjust it so the water outlet reservoir is clearly in view
- Set the air and water flows required using the rotameter needle valves
- Switch on the valve at liquid inlet to allow water flow to the spiral channel
- From the monitoring camera view, and once the water arrives at the outlet reservoir, adjust the water level in the reservoir using pressure regulation of the air inlet (REG 1)
- Using the macro camera take a picture and check if the liquid layer can be seen; if not use the bypass syringe to initiate the layer
- For any change in fluid flows or rotation rate, adjust the water reservoir level to the new condition

4.5 Liquid supply with syringes

In this research also syringes have been used to drive the viscous liquids where desired flow rates fall to low levels. The only change to the system is replacement of the mains water supply with the syringe pump instead, with the syringe drive rate rather than the rotameter used to determine flow rate. Figure 4.10 shows the flow system for tests using the syringe drive. In the case of the liquid-liquid contact system (1-octanol with water) both streams are driven with syringe pumps as a result of the low flow rate needed for each liquid (Figure 4.11). The syringe pump provides a variable linear speed with settings from 0 to 99.9 proportional to speed. From the syringe volume per length section area of the syringe, the flow rate can be calculated.

$$Q = \frac{V_s}{L_s} u_s \quad (4.1)$$

where V_s is the volume of the syringe, L_s the length of the syringe producing that volume and u_s is the syringe speed. A number of different syringe sizes were used to span the necessary range of flow rates and Table 4.1 gives the values at speed settings over the pump range for the principal syringes used. It can be seen that flow rates spanning the range from 0.01 to 1 mL/min are achieved and this, with the further range of the water rotameter represents an overall test range of three orders of magnitude.

Table 4.1: Syringe pump settings for different syringes size

Syringe volume: 20mL			10mL			5mL			3mL		
Pump Setting	Q_L mL/min	Time min	Pump Setting	Q_L mL/min	Time min	Pump Setting	Q_L mL/min	Time min	Pump Setting	Q_L mL/min	Time min
5	0.0567	353	5	0.0325	307	5	0.0239	209	5	0.0117	257
10	0.1134	176	10	0.0651	154	10	0.0478	105	10	0.0234	128
15	0.1701	118	15	0.0976	102	15	0.0717	70	15	0.0350	86
20	0.2269	88	20	0.1302	77	20	0.0957	52	20	0.0467	64
25	0.2836	71	25	0.1627	61	25	0.1196	42	25	0.0584	51
30	0.3403	59	30	0.1952	51	30	0.1435	35	30	0.0701	43
35	0.3970	50	35	0.2278	44	35	0.1674	30	35	0.0817	37
40	0.4537	44	40	0.2603	38	40	0.1913	26	40	0.0934	32
45	0.5104	39	45	0.2929	34	45	0.2152	23	45	0.1051	29
50	0.5671	35	50	0.3254	31	50	0.2392	21	50	0.1168	26
55	0.6239	32	55	0.3580	28	55	0.2631	19	55	0.1284	23
60	0.6806	29	60	0.3905	26	60	0.2870	17	60	0.1401	21
65	0.7373	27	65	0.4230	24	65	0.3109	16	65	0.1518	20
70	0.7940	25	70	0.4556	22	70	0.3348	15	70	0.1635	18
75	0.8507	24	75	0.4881	20	75	0.3587	14	75	0.1751	17
80	0.9074	22	80	0.5207	19	80	0.3827	13	80	0.1868	16
85	0.9641	21	85	0.5532	18	85	0.4066	12	85	0.1985	15
90	1.0209	20	90	0.5857	17	90	0.4305	12	90	0.2102	14
95	1.0776	19	95	0.6183	16	95	0.4544	11	95	0.2219	14

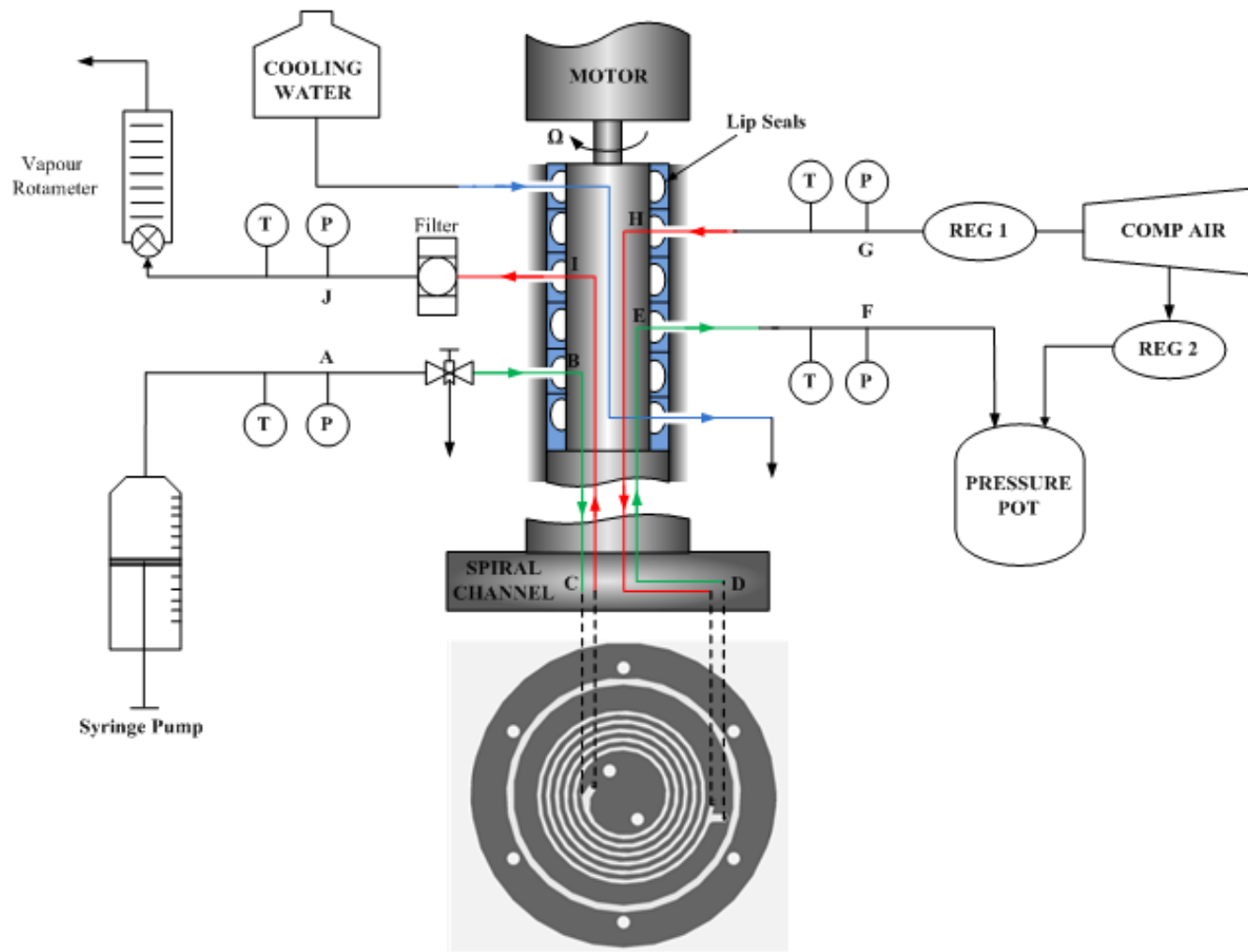


Figure 4.10: Flow and pressure instruments for viscous liquids contacting with air.

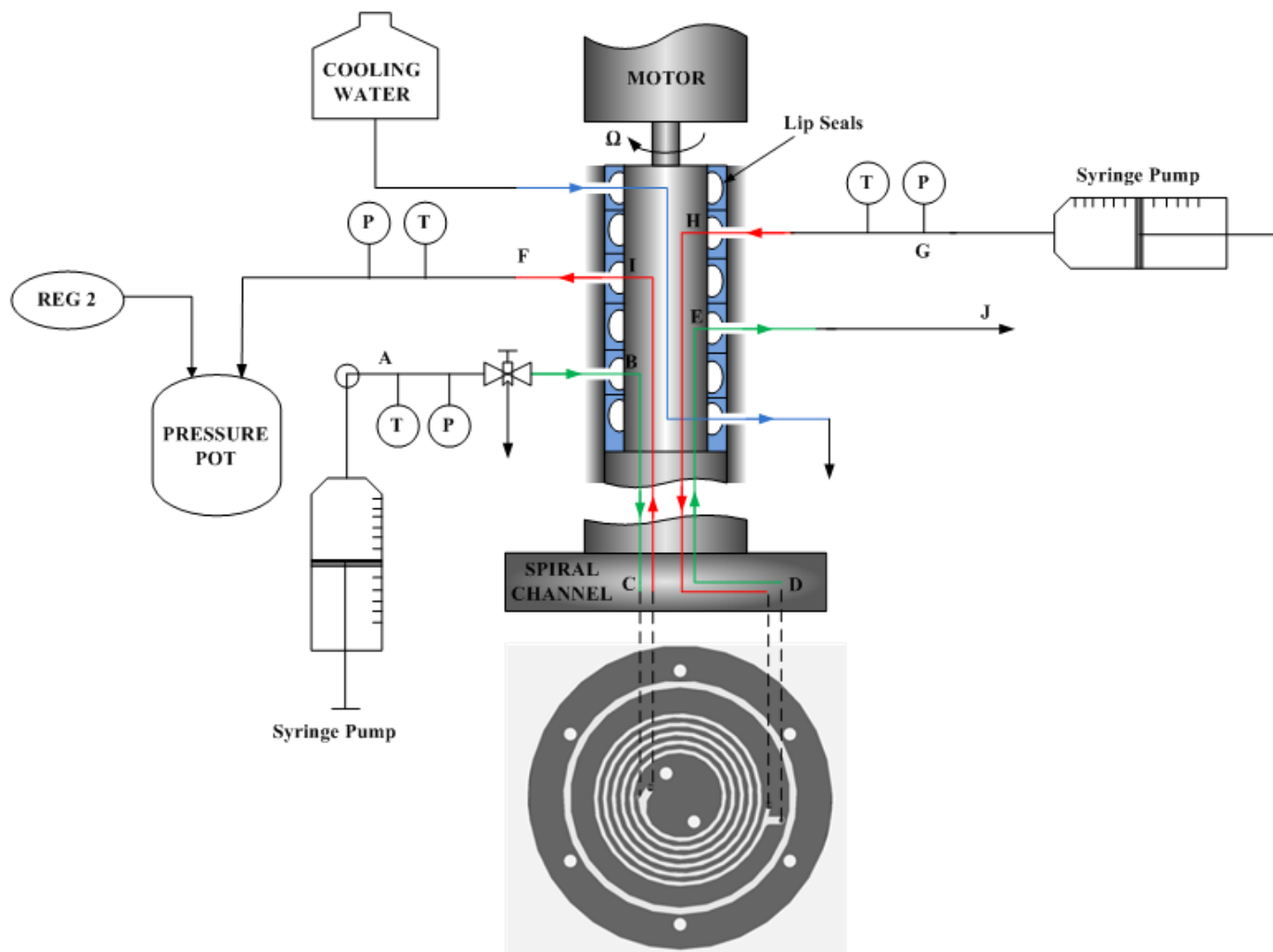


Figure 4.11: Flow and pressure instruments for liquid-liquid phase system.

4.6 Typical contacting network

In order to achieve a reliable design for experimentation and ensure operation over a wide range of conditions, pressure and flow calculations were required. Firstly, the importance of these calculations comes from the requirements of sizing auxiliary components such as pressure regulators, pressure gauges, and flow measurements devices. Secondly, design for the pressures reached within the spiral and at other locations in the flow network requires reliable information about these pressures.

This section presents the equations needed to calculate the pressures at the inlets, outlets, and junction points of the flow system in both fluid streams. The pressure and flow rates within the system can be determined using network analysis together with standard pipe flow relations and the wide channel model. Figure 4.12 gives a schematic diagram of flow network of the apparatus and identifies the main passage sections and junctions where they meet.

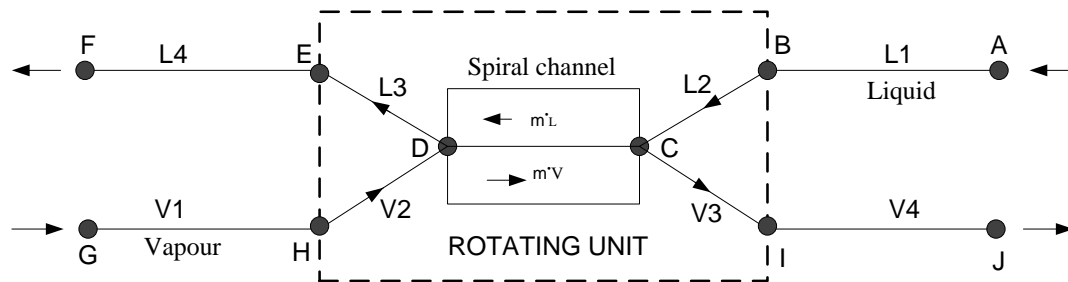


Figure 4.12: Schematic diagram of flow network of rotating spiral device.

The figure shows the heavy phase entering the flow system at point A, and flowing through ducts L1 and L2 to flow counter-currently with the light phase in the spiral channel between points C and D. It then leaves the spiral through ducts L3 and L4 to point F, the liquid outlet. The same happens in the opposite direction where the light phase enters at point G and flows through the ducts V1, V2, V3 and V4 and the spiral

channel to leave the system at point J. The dashed region indicates the ducts in the rotating unit, so ducts L2, L3, V2 and V3 are rotating and junctions H, E, B and I represent points where flow passes from stationary to rotating passages. The junctions are of course the locations of the lip seals, which support a maximum pressure of 4.0 bars. Points C and D indicate the junctions with the ends of the spiral channel.

Appendix B presents the equations of the network modelling used to calculate the pressure drop in the system and to decide the passages sizes. Also, the model shows the effective method of measuring the temperature and calculating the pressure in the spiral to allow comparisons to be made with the wide channel model, which must have the experimental gas density and liquid viscosity in the spiral flow. Table 4.2 shows the passage sizes selected for the apparatus network tubing. These were selected to produce minor pressure drop, for the expected passage lengths, in relation to that from point D to C in the spiral flow.

Table 4.2: Passage and tubing diameters used in the apparatus network tubing.

Passage	Size, mm	Fluid Type
L1	3.175 mm (1/8")	Liquid
L2	1.5 mm	Liquid
L3	1.5 mm	Liquid
L4	3.175 mm (1/8")	Liquid
V1	6.35 mm (1/4")	Vapour
V2	3.0 mm	Vapour
V3	3.0 mm	Vapour
V4	6.35 mm (1/4")	Vapour

Chapter 5

5. Liquid layer measurement

The rotating spiral apparatus was designed to operate under a wide range of operating conditions producing very thin layers of the heavy phase flowing counter currently with the light phase. It is crucial in mass transfer processes to produce a large mass transfer coefficient which means an effective absorption/extraction process can be obtained. The wide channel model of MacInnes et al. (2012) presented in chapter 3 has shown in particular the importance of adjusting the position of the phase interface in rotating spiral contacting in order to achieve optimum mass transfer. This must be done while at the same time achieving the correct ratio of flow rates to allow the separation. Thus, investigation of the dependence of the liquid layer thickness on rotation rate, flow rates and fluid properties is necessary to demonstrate variable interface positioning and to compare with the model to assess its potential usefulness for estimating optimum conditions. The flow rates and rotation rate measurements have been described, leaving the more difficult measurement of interface position. Interface position will be quantified in terms of the thickness of the heavy phase (liquid) layer. The liquid layer is not uniformly thick as a result of menisci and tilting of the interface as a result of gravity and the minimum thickness will be used as a single measure of thickness. The liquid layer thickness will be determined optically using three steps: taking a photograph of the liquid layer, analysing recorded intensities along a line of pixels across layer photograph and using a model of the interface shape to determine the actual minimum liquid layer thickness. The final step is required since the image does not record the interface minimum directly.

5.1 Imaging setup and method

In order to achieve a high quality result, a digital camera (Canon EOS D550) with macro lens (Canon MP-E 65mm, f2.8, 1-5x magnification) was fixed and aligned to the outer channel wall of the spiral (Figure 5.1). The camera was in all cases focused on the rim of the visible channel as this presented a reliable target.

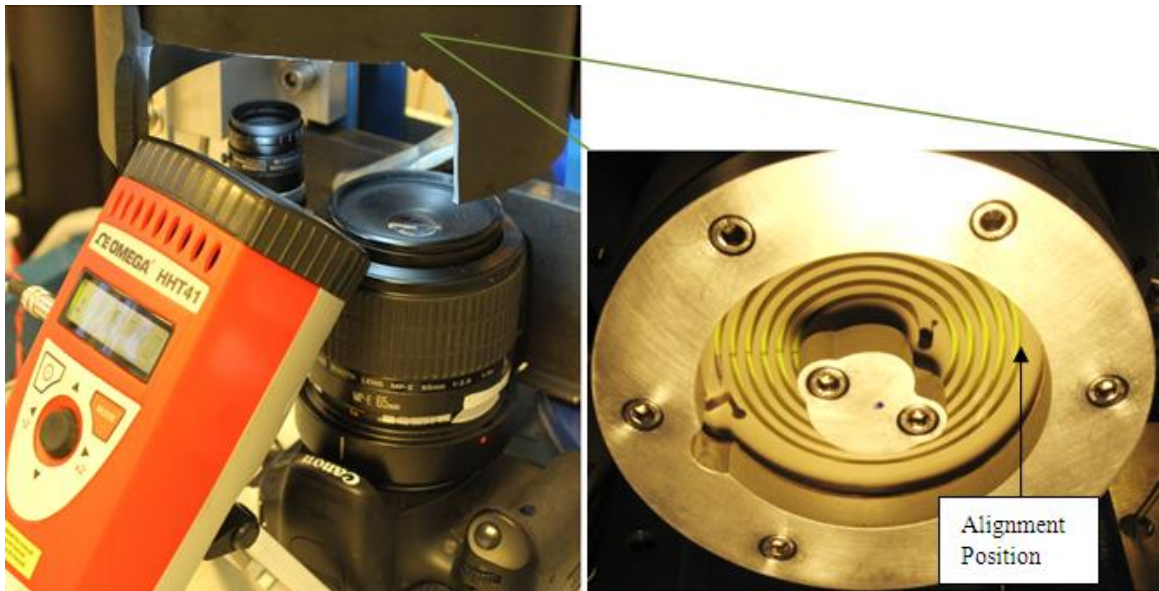


Figure 5.1: Photography setup and alignment position.

A strobe flash light was used (the same as for the monitor camera) and triggered in synchronisation with rotation to allow a single image from a single flash exposure to be produced, by using an exposure time less than the flash interval. This approach was not satisfactory because it required using a small value of aperture (f2.8) and hence with a small depth of focus. Thus, to get a clear view of the interface throughout the depth of the channel using the maximum aperture value (f16) was a priority. However, this required use of a high level of gain (ISO 6400) in order to obtain a usable image from the single strobe illumination. To overcome this problem, multiple flash exposures during around 30 consecutive rotations of the spiral were found to produce an image

with low noise and negligible blur due to variability in the combined exposures. Comparing images taken with multiple exposures and with single exposure of the same layer showed that the flow was steady and illumination was repeatable over the sequence of multiple exposures. Figure 5.2 shows example images when many individual single exposure images of the same layer were compared, the standard deviation of the channel rim positions (which were in sharp focus) was found to have a standard deviation of about $4 \mu\text{m}$.

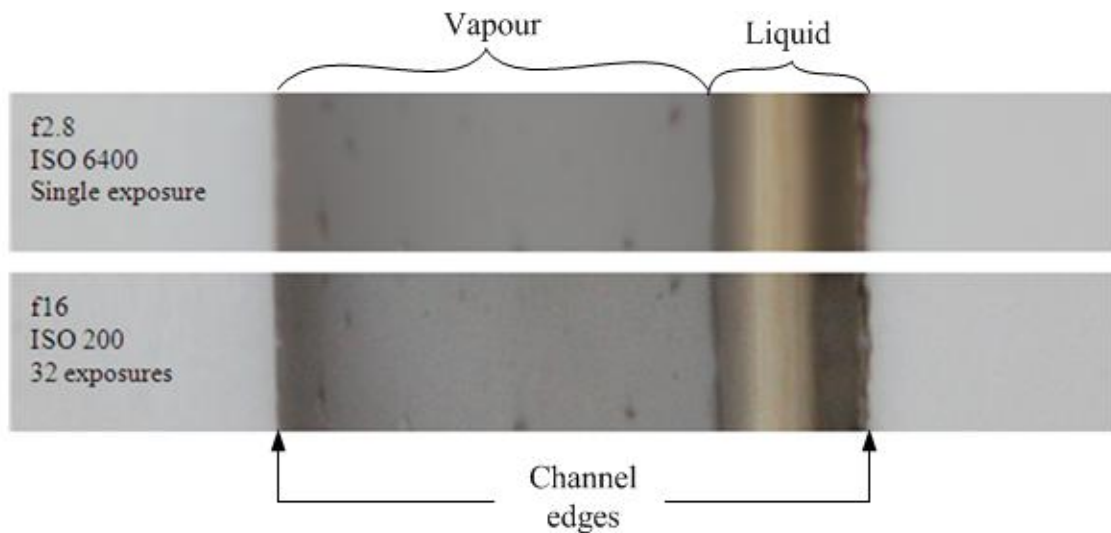


Figure 5.2: Difference in interface line for different depth of focus settings.

Before proceeding to consider layer measurement in the spiral channel a larger-scale and simpler system was investigated and the results highlight essential and common issues associated with interface identification. These are presenting in the next section before moving to the method used to measure layer properties in the actual rotating spiral.

5.2 Interface imaging

A number of questions arise concerning interface identification, such as the effect of using different background colours/materials, the effect of depth of focus and the effect of changing the distance between features in the background that affect the appearance of the interface. To address these issues a simple interface formed by a liquid partially filling a glass vial is used. The basic situation is shown in Figure 5.3 and includes the vial on a solid-colour background and the macro camera with a steady light source to the side. Alternatively, contrasting background is used as in Figure 5.6.



Figure 5.3: Identification of the liquid interface using a glass vial and different backgrounds colours.

5.2.1 Different background materials

In this test different background materials have been used to see how accurately the positions of interface line can be identified. The materials used are matt black paper, a reflecting surface (aluminium), silver tape, PEEK, and white paper. The test arrangement using water inside a glass vial with white paper for the base is shown schematically in Figure 5.6, which differs from what is shown in Figure 5.3 in that the background is formed from a horizontal white surface and a contrasting vertical surface placed at varying distances behind the vial. Figure 5.4 shows images that have been taken using different background materials.

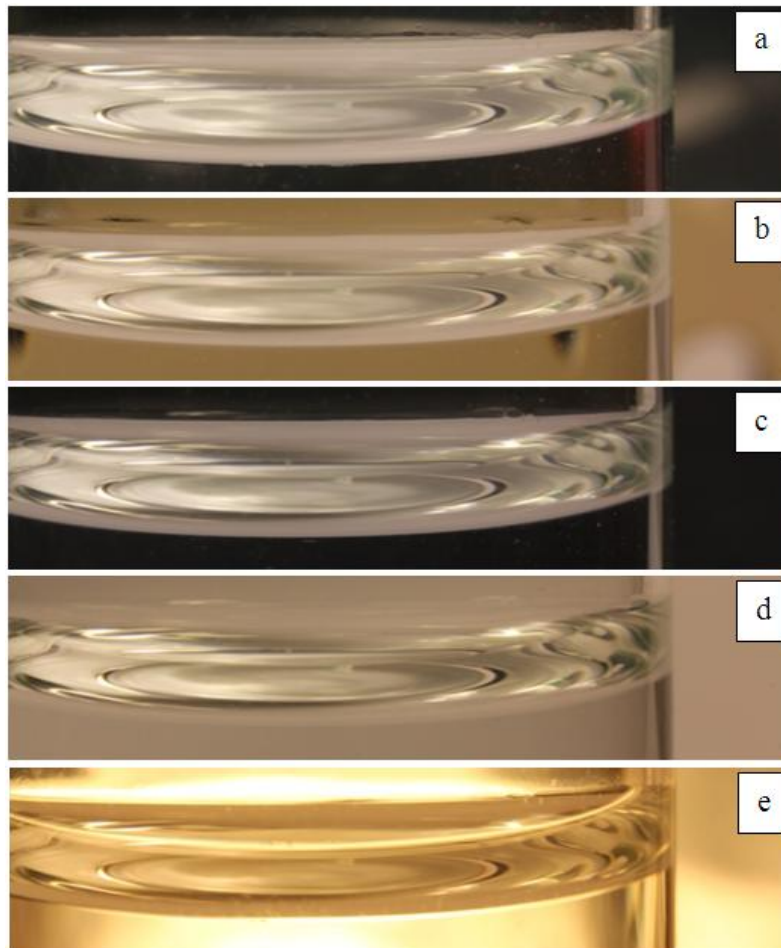


Figure 5.4: Photographs of the interface (in the vial) for different background materials: silver tape (a), PEEK (b), matt black paper (c), white paper (d) and reflecting aluminium (e).

The photographs are analysed using Mathematica software (Version 5.2). The software is used to extract lines of intensity along a line in the image. There are three intensity arrays available in the standard (jpg) format of the images stored by the camera: red, green and blue. The different colours may give intensity profiles along the selected line of differing clarity depending on the background colour. The stored images contain an array of intensity values 5184 columns by 3456 rows. Figure 5.5 below shows the position of the profile line that has been used to analyse the interface in the photos. It runs perpendicularly through the interface and near the centre where light is relatively undistorted by the curvature of the glass vial. The camera is aligned so its axis is parallel to the plane containing the contact line and at the same level as the minimum of the liquid interface (Figure 5.6).

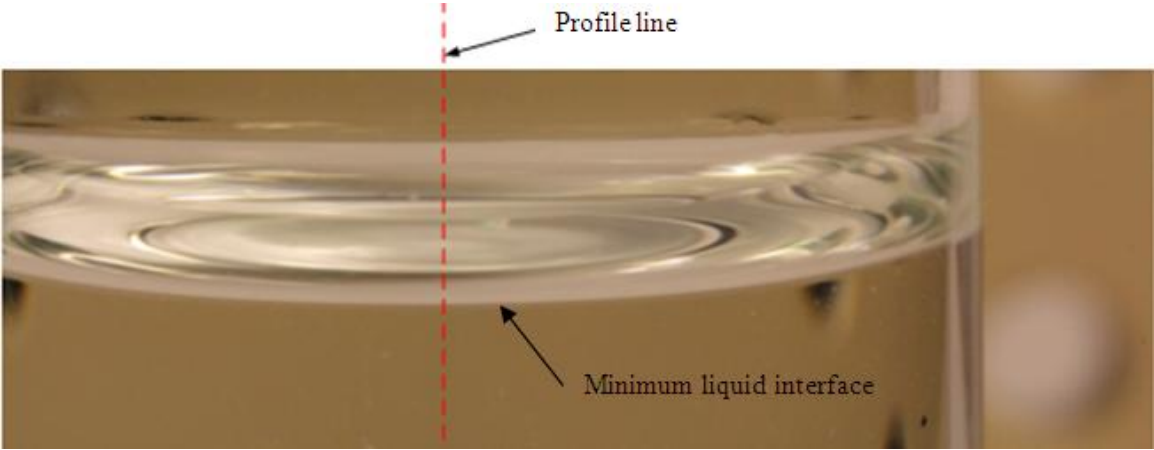


Figure 5.5: Analysis profile line used for the tests.

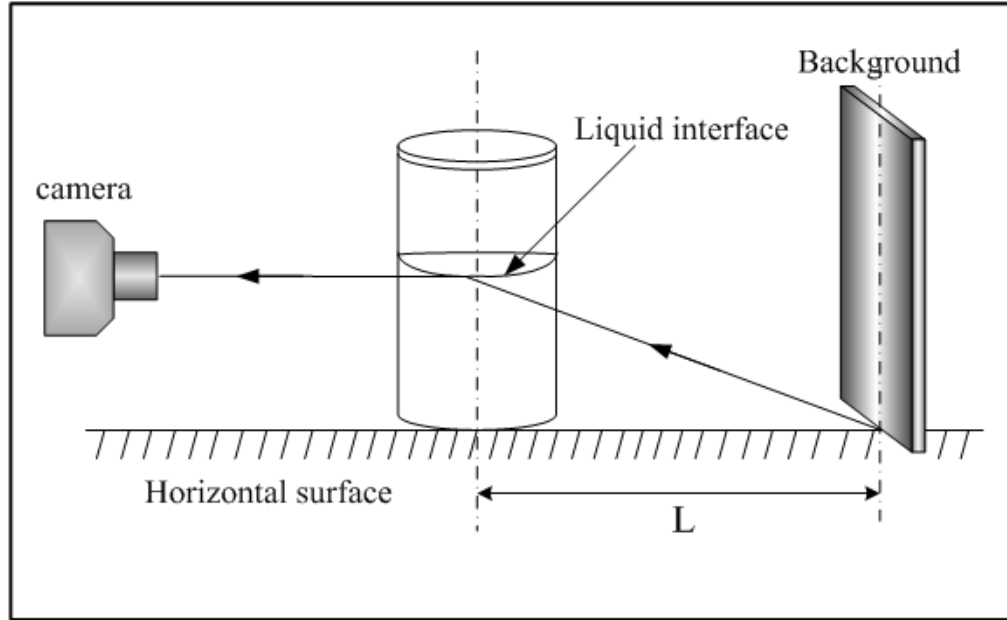


Figure 5.6: Imaging the liquid interface in glass vial for different backgrounds materials.

When the images presented in Figure 5.4 are analysed using the same vertical line and the red colour one finds the variation with background colour Shown in Figure 5.7. In the figure, left to right corresponds to moving from bottom to top in the photographs. Thus, the constant value of the intensity related to the background colour and the initial sharp change in the intensity come from the immediate change in the colour corresponding to the liquid interface position. Then the final sharp change in intensity is related to the position of the meniscus contact line on glass surface. Comparing the intensity profile for different background materials shows differences in liquid interface identification. For example, the black paper and the silver give good results by showing a clear and sharp rise in the intensity in comparison with the intensity profiles for the other materials. One of these materials was then used to study the effect of changing the distance between the liquid interface and the background material (L in Figure 5.6). Images at different distances (0, 3, 7 and 12 cm) have been taken using the silver material as background and the resulting images are shown in Figure 5.8.

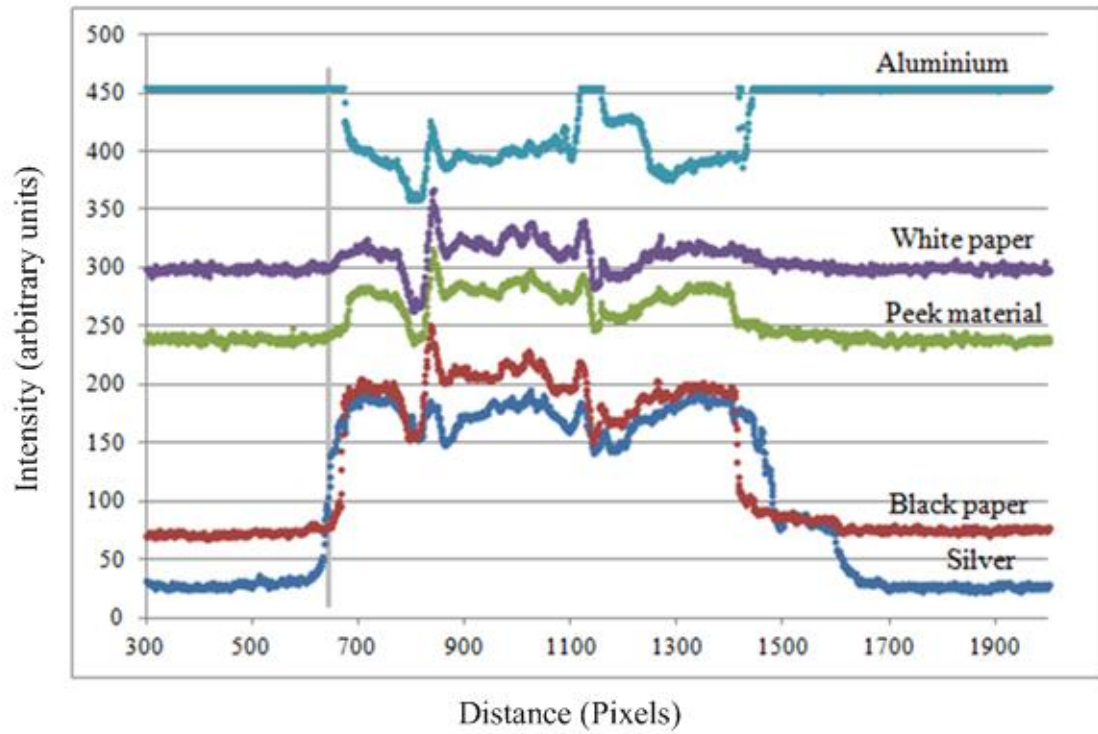


Figure 5.7: Intensity profiles for different background materials.

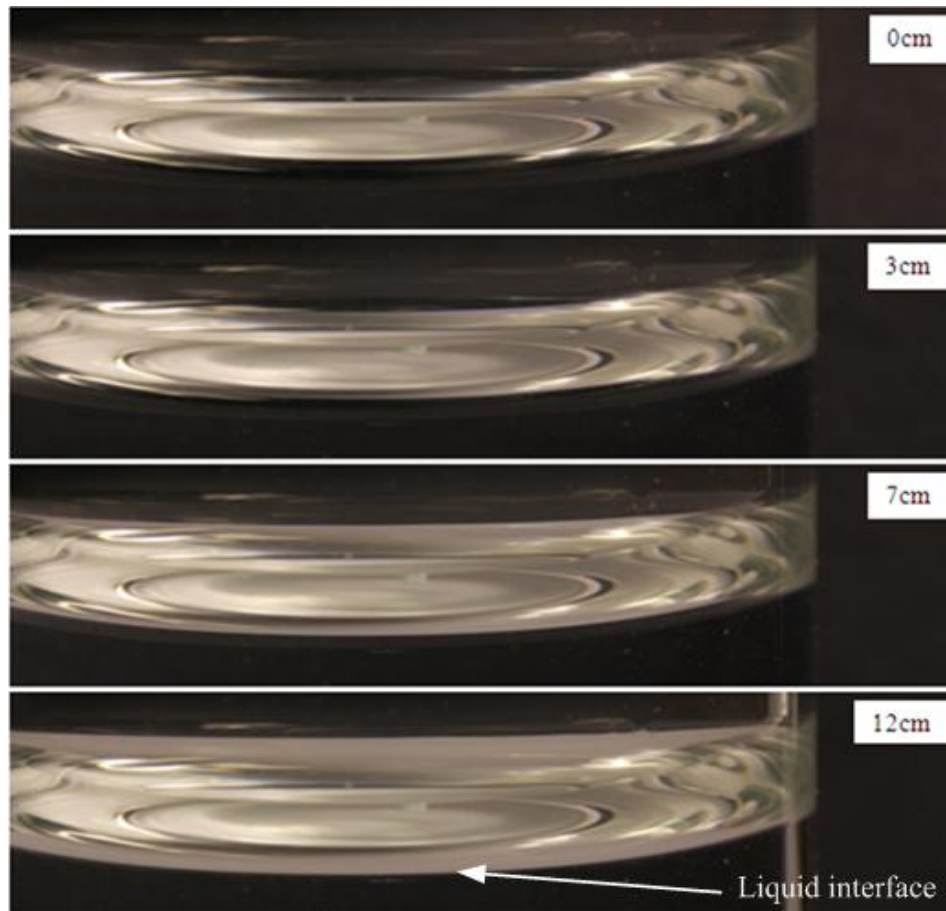


Figure 5.8: Photographs of the gravity interface (in glass vial) for different distances between the background and the liquid interface.

The silver gives a dark background since light does not reflect from it in the direction of the camera. Light from the horizontal white surface on which the vial sits does reach the camera after reflecting from the liquid interface surface, the undulating character of the resulting image being a consequence of the slightly wavy bottom of the glass vial. Thus, the interface is visible due to reflection of this light and the contrast between the relatively intense light received from white surface reflected by the interface provides a contrast with the dark background of the silver surface. On close examination Figure 5.8 however reveals that the apparent interface position is changing in relation to the fixed features of the reflection of the vial bottom. The distance between the apparent interface position and the first dark band increases as the background distance increases. This is

because this apparent interface position is only an approximation of the interface outline and is actually the reflection of the corner between the (dark) vertical background and the (bright) horizontal base plane. As the background is moved closer the vial, to point where the background corner reflects moves forward and upward along the curving interface. The images analysed as before, show clearly this effect of changing the background distance on the apparent liquid interface position (Figure 5.9). The figure shows the apparent interface position moves progressively downward as the background is moved back, with the true interface position being detected for the background moved an infinite distance away.

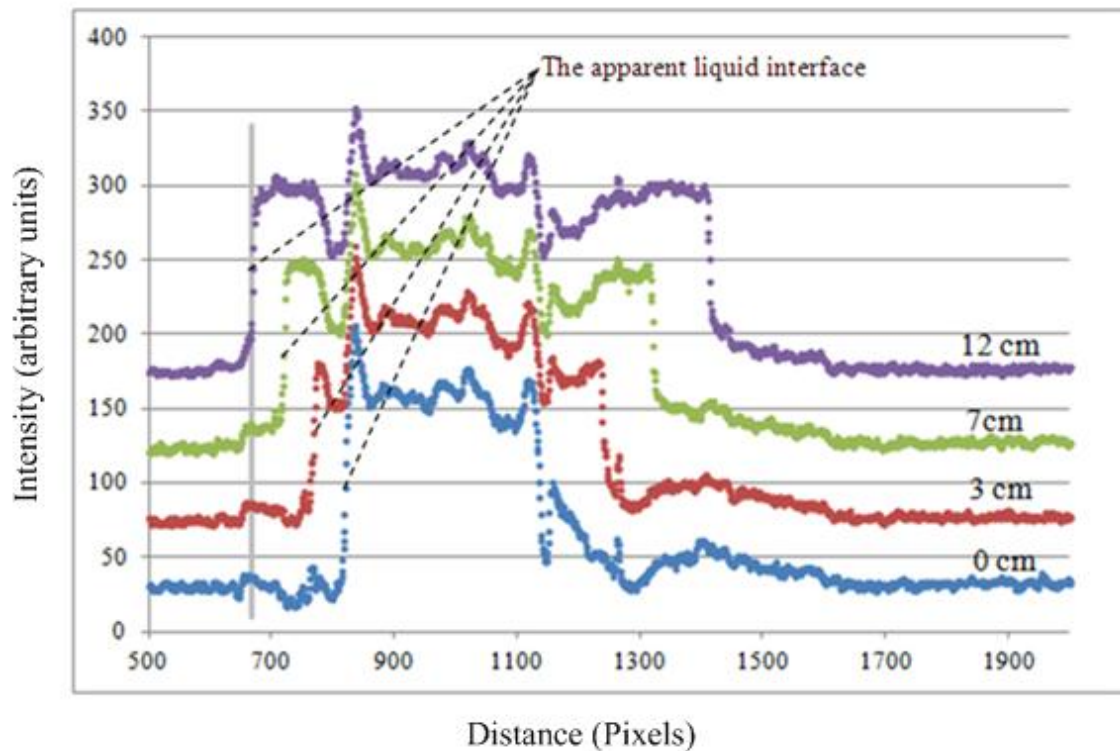


Figure 5.9: Identification of liquid interface for different distances.

5.2.2 Different colour backgrounds in the spiral channel

Imaging the liquid interface at different background distances showed that identification of the liquid interface position is directly affected. But also the choice of background colour may help with interface identification. It seemed essential therefore to test the effect of background colour in the spiral itself. It was possible to place carefully cut sections of adhesive tape on the channel bottom to provide this contrasting background and this was done for several different tape colours to determine the effect. The distance from the interface to this background is fixed by the channel geometry and where the interface minimum occurs but, due to the small scale of the channel and difficult imaging and lighting conditions under rotation, producing good contrast in the image between the reflected bottom of the channel (the background) and the side wall is crucial. Results for the liquid interface in the vial can be used to make a preliminary selection of appropriate backgrounds for use in the channel. A broad range of reflective tapes were assembled: red, green, blue, white and yellow (all of a type with glass beads incorporated) and aluminium foil tape (silver). For these different backgrounds using a distance of 12 cm produced the images and intensity profiles shown in Figure 5.10 and Figure 5.11, respectively. The intensity profiles presented in Figure 5.11 come from the analysis of the photos using the red channel.

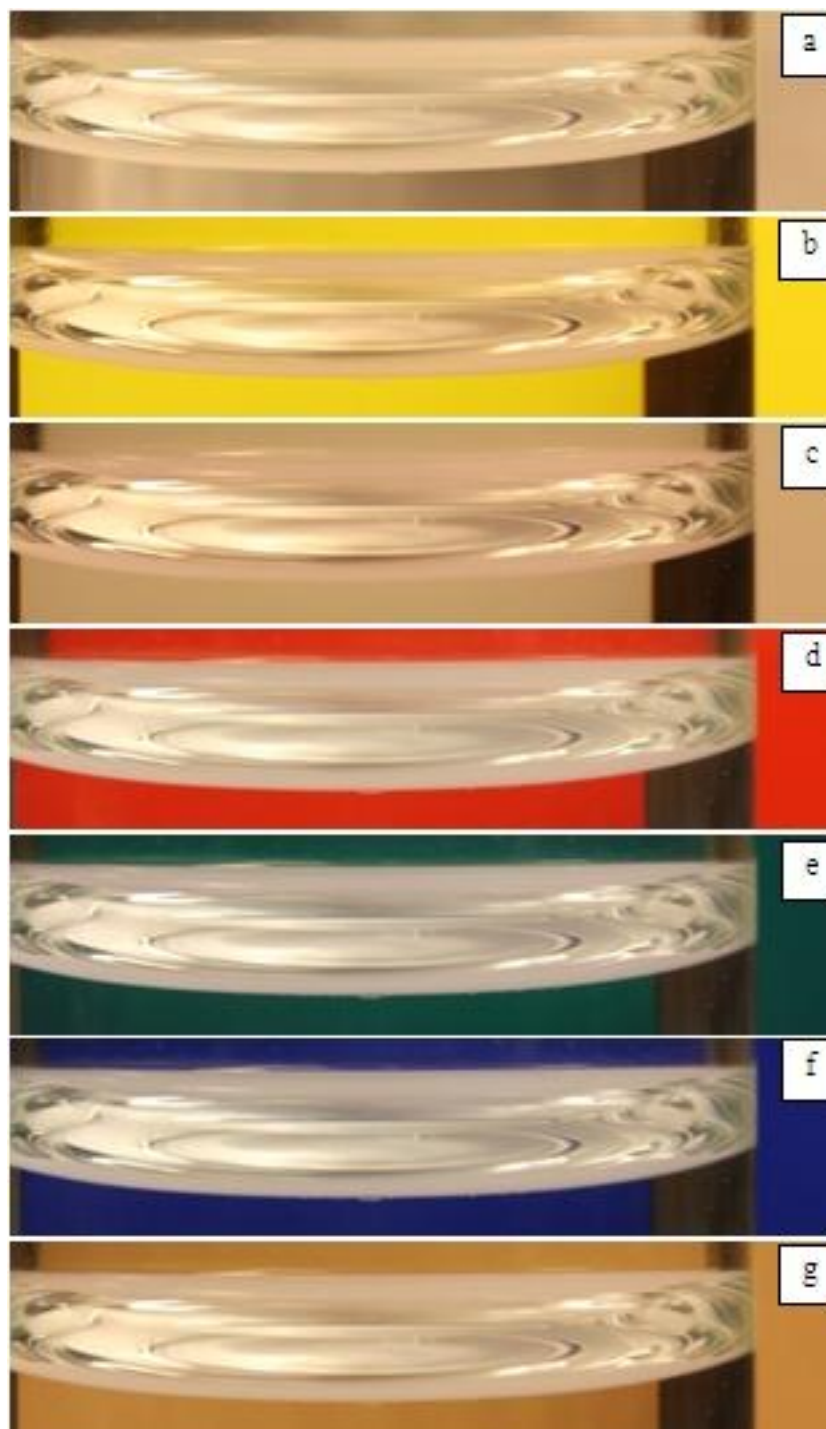


Figure 5.10: Photographs of the interface (in the vial) for the (a) silver (b) yellow (c) white (d) red (e) green (f) blue and (g) PEEK backgrounds.

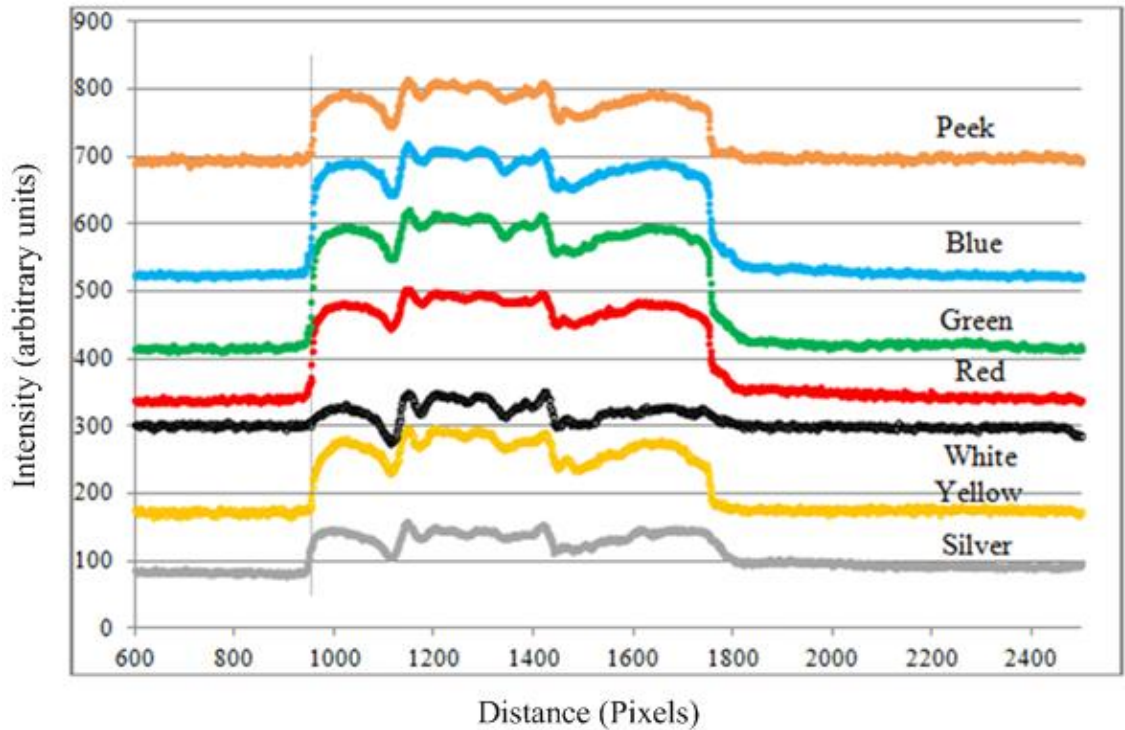


Figure 5.11: Intensity profiles (red intensity) for the interface test using different backgrounds colours.

Looking for the intensity profiles in Figure 5.11, silver, white and PEEK can be excluded from the comparison as they give lower contrast between reflected background surfaces, i.e. a smaller jump in intensity for the reflected background corner (shown with a vertical grey line on the figure). To make a final choice all of the remaining colours were tested in the rotating channel with a liquid layer present to see which one gives the best contrast in that context. Figure 5.12 shows images for 1920 rpm with air flow rate 1.71 NL/min and water flow rate 4.64 mL/min for each of the four candidate backgrounds and also with no tape on channel bottom (PEEK material).

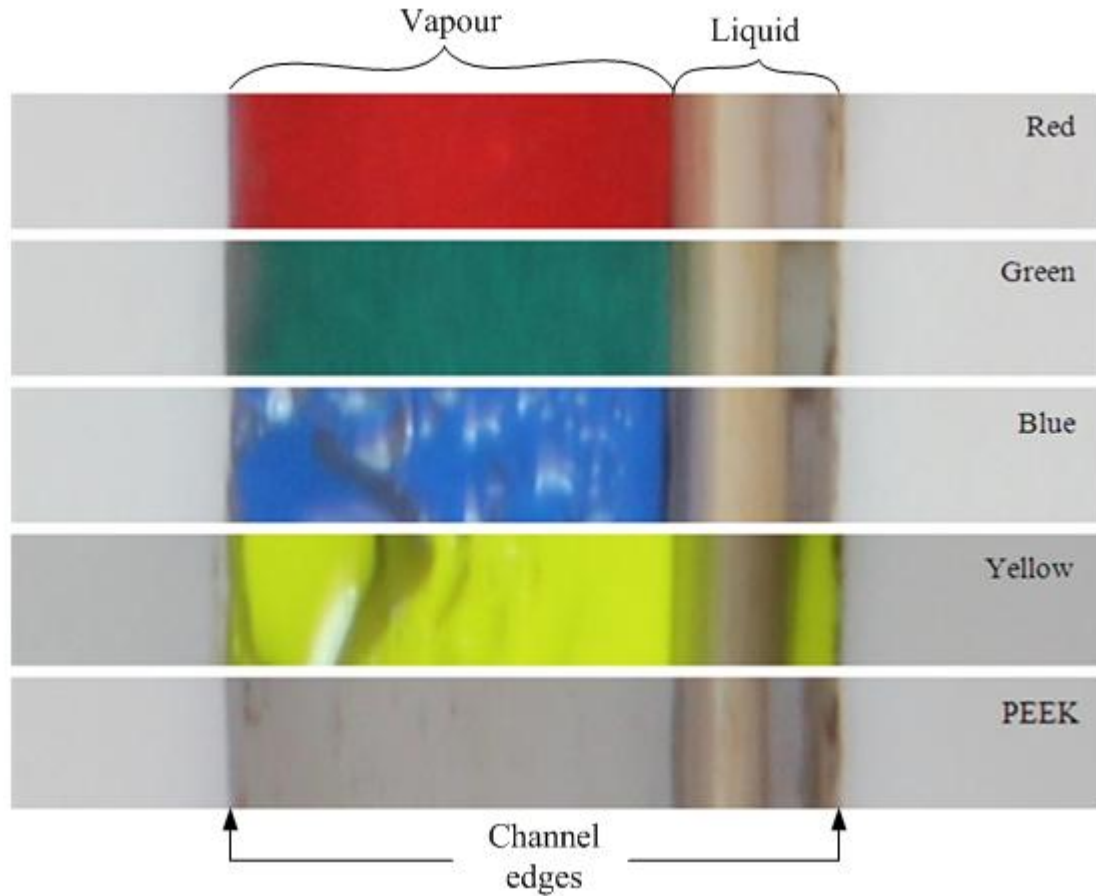


Figure 5.12: Photographs using different colour backgrounds (tape applied to the channel bottom).

It was clear by examination of the intensity profiles that both the yellow and green tape gave more distinct contrast for the corner reflection and also a more clear jump in intensity at the meniscus contact line on the glass window compared with the red, blue or PEEK backgrounds. It was decided to use the yellow tape as the background for imaging the interface in all of the subsequent experimental work.

5.3 Camera alignment

Correct alignment of the camera is crucial to allow viewing down into the liquid layer and to avoid significant error in the ultimate determination in the liquid layer thickness. The camera must view to the full depth of a liquid layer that is typically more than 40 times deeper than it is thick and for the thinnest layers the depth can reach 200 times the minimum liquid thickness. The analysis in this section will consider the errors of misalignment in two stages: first considering the simpler ideal case of a uniform thickness liquid layer and second including meniscus and tilt of the interface. For both cases the effect of camera position will be examined for the two possible directions of misalignment: outward or inward from the outer channel wall. Analysis of the effect of these camera offsets is helped by considering the ideal case of the flat interface parallel to the side wall and then including the real effect of the interface tilt due to the effect of gravity and meniscus rise due to contact with the channel end walls as a second step.

5.3.1 Interface parallel to the side wall

Misalignment of the camera refers to a deviation of the viewing direction from the line precisely parallel to and coincident with the outer channel wall. When the liquid layer is viewed at an angle instead, since the liquid layer is thin the interface may be obscured by the outer wall or by the interface itself. There are two cases to consider therefore, offset of the camera position to beyond the outer wall of the channel and offset towards the inner channel wall.

5.3.1.1 Camera position too far outward

In this case the camera is too far outward from alignment with the side wall by a distance a as shown in Figure 5.13. The apparent liquid layer thickness is detected as h'_L which differs from the true value of h_L .

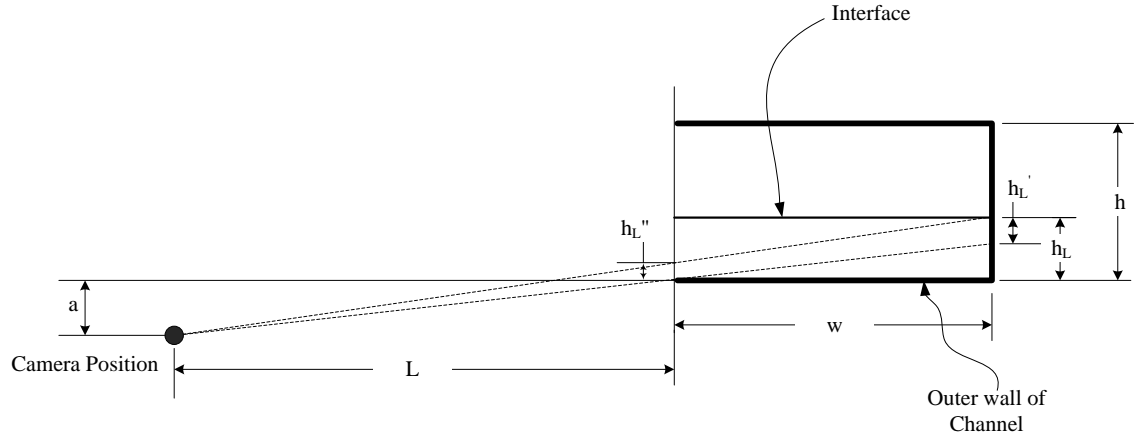


Figure 5.13: The interface is parallel to the wall and camera position is outward from the outer channel wall.

For a distance $a = 0$, the relative error in determining the liquid layer thickness, h_L in the figure, can be calculated from the geometric relation:

$$\frac{h_L' - h_L}{h_L} = -\frac{w}{L} \frac{a}{h_L} \quad (5.1)$$

The experimental spiral channel has $w = 4$ mm and camera distance of $L = 200$ mm (for 1X magnification). Thus, for example for a liquid layer thickness of $h_L = 50$ microns and an offset of $a = 0.5$ mm (one third the channel height of 1.5 mm), the h_L measured will have a relative error of -20%.

There is a further error due to projection from bottom to top of channel which is however relatively small:

$$\frac{h_L'' - h_L'}{h_L'} = -\frac{w}{L + w} = -2\% \quad (5.2)$$

Referring to Eq. (5.1) it is clear that, provided $a < h_L$, the expected relative error in measured h_L will be less than approximately 2.0%. Thus, for a given offset in the outer direction the relative error increases as layer thickness decreases.

5.3.1.2 Camera position too far inward

For offset towards the inner wall of the channel a different analysis is required. For a camera position a distance b as shown in Figure 5.14 the apparent layer thickness will be the correct distance, h_L , since it will be judged by the positions of the contact line at the glass surface and the rim of the outer wall.

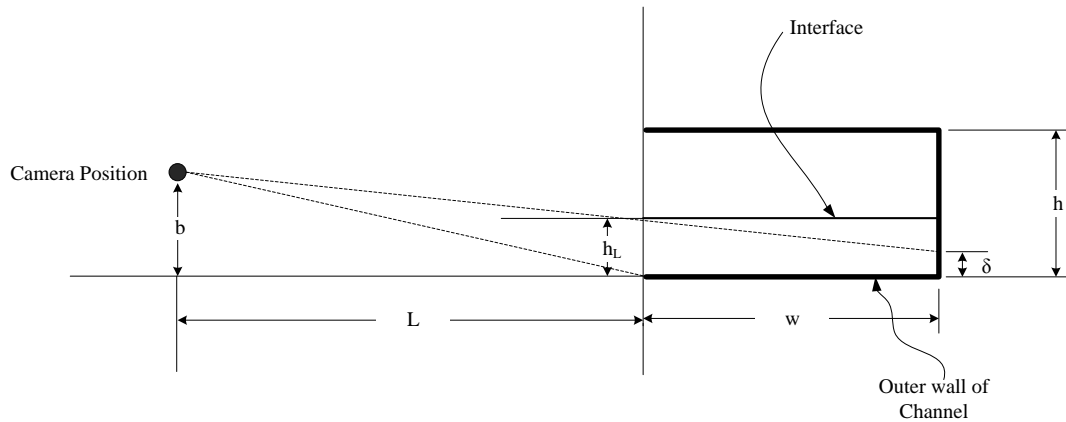


Figure 5.14: The interface is parallel to the wall and camera position too far inward the channel wall.

So the measurement of liquid layer thickness, h_L , will not be affected by misalignment of this kind. However, the background contrast is lost as the width of visible background layer, δ , approaches zero as b increases. The bottom of the channel will not be visible for:

$$\frac{b - h_L}{h_L} \geq \frac{L}{w} \quad (5.3)$$

Since $L/w = 50$ (as before) the offset in this direction can become quite large before the background is obscured and any difficulty arises.

The two cases above do not take into account the influence of the actual shape of the interface which includes curving at either end to the menisci that form and tilting relative to the outer wall due to gravity. These effects are considered next.

5.3.2 Interface affected by menisci and tilt

5.3.2.1 Camera position too far outward

The effects of meniscus curvature and interface tilt are illustrated in Figure 5.15 for the case of outward displacement of the camera. In this case the minimum interface position (where the liquid layer is thinnest) occurs near the bottom of the channel at a distance δ_L from the bottom wall.

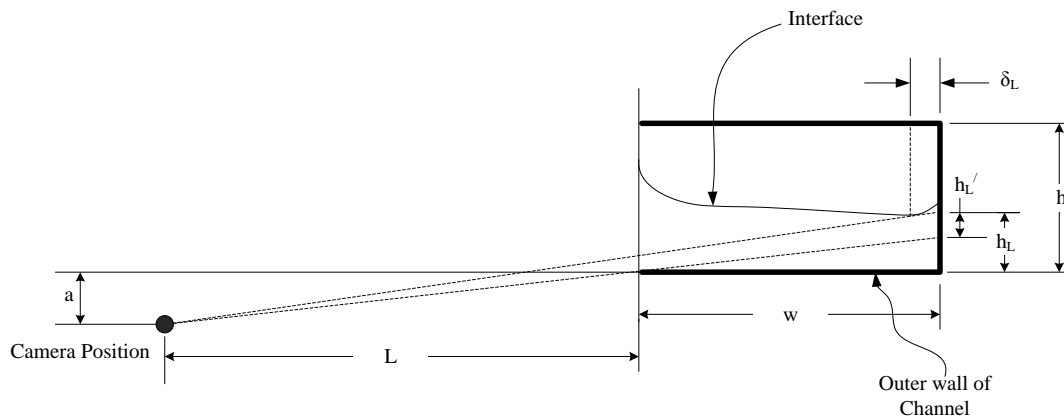


Figure 5.15: The interface affected by meniscus and gravity with the camera position too far outward.

The effect of menisci and tilt simply reduce the error estimated previously for the flat interface by the factor $(w - \delta_L)/w$ and the relative error is given by:

$$\frac{h'_L - h_L}{h_L} = -\frac{(w - \delta_L)}{L} \frac{a}{h_L} \quad (5.4)$$

Thus, the flat-interface result (Equation 5.1) provides a conservative estimate of the actual error.

5.3.2.2 Camera position too far inward

The tilt of the interface is affected directly by the rotation rate and radial position and therefore the allowed distance b needs to be decreased with increasing $R\Omega^2$ and there is a critical value of b which must be defined in order to proceed:

$$b_c = \frac{g}{R\Omega^2}(L + w - \delta_L) + h_L \quad (5.5)$$

For $b < b_c$,

The situation is as shown in Figure 5.16 where the interface position at which the minimum liquid layer thickness occurs is nearly visible to the camera.

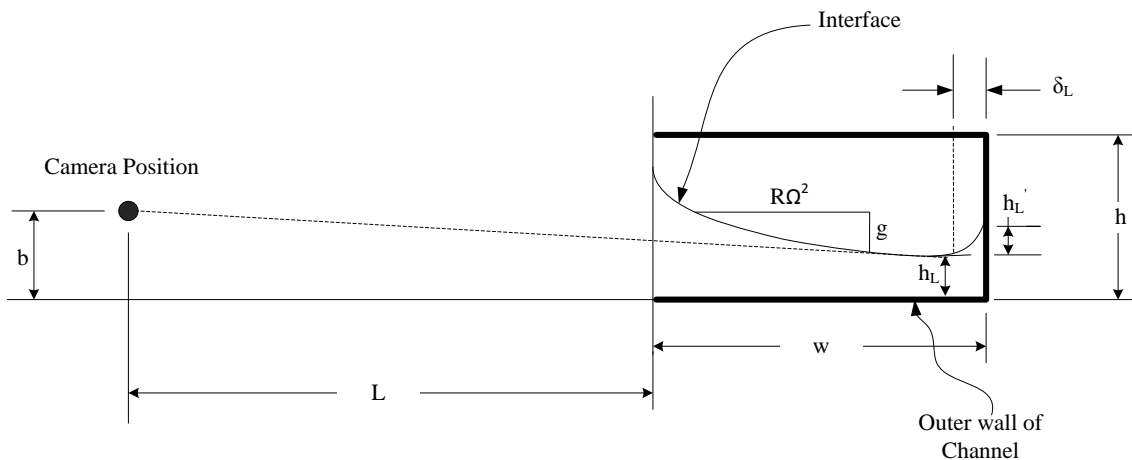


Figure 5.16: The interface is affected by meniscus and gravity and camera position is too far inward.

In this situation there is a negligible error in determining, h_L , this being smaller than the projection error considered in connection with the flat interface.

For $b > b_c$

The situation is as depicted in Figure 5.17 and the minimum point on the interface is clearly not visible to the camera and the height h'_L becomes the measurement of minimum layer thickness.

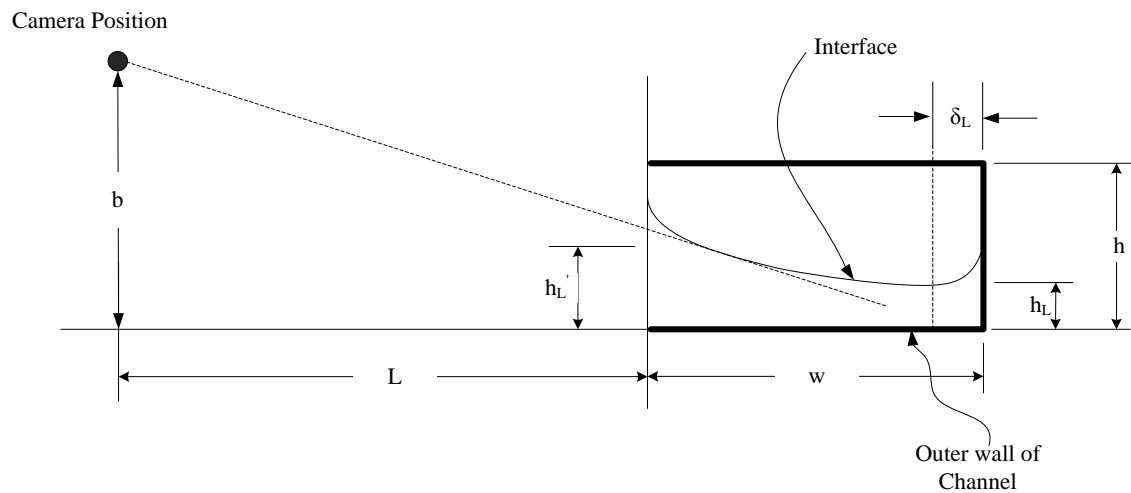


Figure 5.17: The interface is affected by meniscus and gravity and the camera position too far inward

Thus, the error in this case is given approximately by:

$$\frac{h'_L - h_L}{h_L} = \frac{(w - \delta_L)}{h_L} \frac{g}{R\Omega^2} \quad (5.6)$$

This error depends on sufficient misalignment ($b > b_c$) and the tilt of the interface. For the range of rotation rate and radial position in the experiments, the critical offset will remain greater than about 0.5 mm which in practice will not be exceeded and therefore

this case will not arise. This type of misalignment will, however, cause the background contrast surface to disappear from the camera view when $b \geq h_L \left(\frac{L}{w} + 1 \right)$ (with $L/w = 50$).

But again, in practice it is easy to align the camera so this is avoided. For example, for a 20 μm layer thickness b must remain smaller than 1.0 mm.

The criteria and consequences for the error resulting from misalignment of the camera reduce to two simple points:

- For offset to the outer channel direction, the relative error in h_L measurement of the minimum liquid layer thickness, h_L , will have a relative error given conservatively by Equation 5.1. The error is less than 2.0% provided the alignment is within the value of liquid layer thickness ($a < h_L$).
- For offset to the inner channel direction, provided the offset remains within about 1 mm the error is negligible. However, the height measured reflects the layer thickness at the camera side of the layer giving a measure that reflects the maximum layer thickness.

5.4 Image analysis

The previous sections of this chapter have shown that achieving a clear image of the interface and the contact line on the glass side is possible. The gravity test (water in vial) to image the interface and trying different materials and colours as backgrounds has shown that the image of the phase interface is a reflection of the background. For the channel, the reflected light near the outline of the interface originates from the channel bottom which is indistinguishable from the light travelling directly from the channel bottom. Thus, it will be difficult to detect the silhouette of the interface. Use of the yellow tape applied to the channel bottom gives good contrast between the bottom and PEEK side wall and this can be detected reliably in the reflection from the interface surface. The true position of the interface minimum, and hence the minimum thickness of liquid layer, can then be determined from the geometries of the channel and the interface.

The interpretation of the photographic image of the liquid layer is introduced in this section and can be discussed in terms of the concepts and notation introduced in Figure 5.18. The figure shows details of a typical image and associated intensity profiles for an air-water layer. As can be seen in the intensity profiles (shown below the image) five positions are associated with the liquid layer, the meniscus and the air layer. Two of these positions locate the channel walls, i.e. the outer channel wall is to the right and the inner channel wall is to the left. The other three positions are the locations of the reflected channel corner, the meniscus contact line on the glass side and the position on the interface where the interface is such that light travelling to the camera leaves the interface at the critical refraction angle.

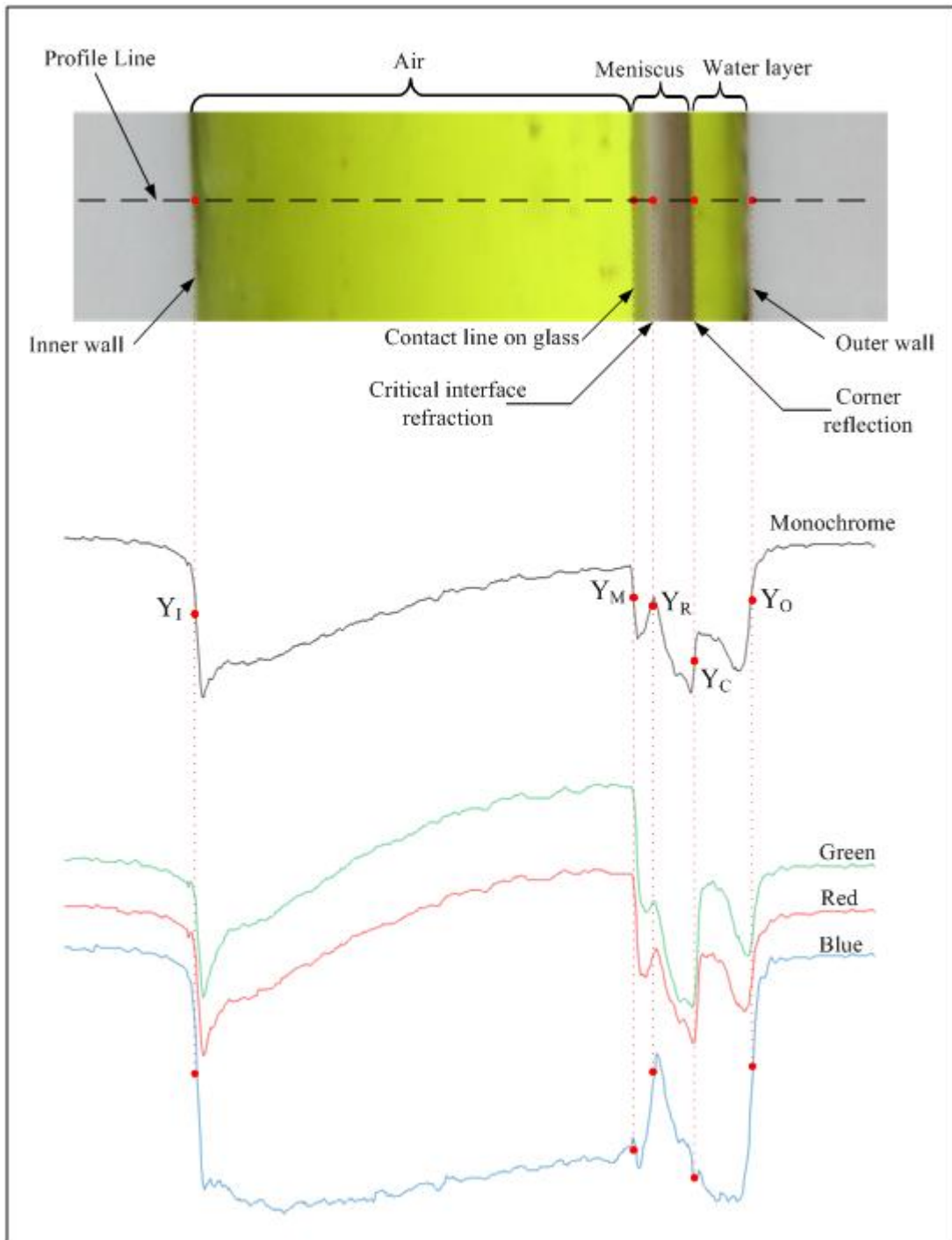


Figure 5.18: Image details and profile lines for air-water contact system.

The intensity profiles taken from the dashed line shown in the image produce red, blue, and green. The fourth profile shown is ‘monochrome’ intensity, calculated as the average of the three colour intensities. The choice of considering the monochrome intensity profile for the analysis comes from the difficulty of identifying some of the points mentioned above using any one colour. For example, looking at the blue intensity profile it can be difficult to identify the point related to contact line (Y_M) or the point related to the reflected light from the corner (Y_C) because there is no blue in the yellow colour. On the other hand, the position of the critical refraction point on the interface (Y_R) can be easily identified using the blue intensity in comparison with the other two colours (red and green). The monochrome intensity profile allows these points to be identified as it includes a contribution from all three colours.

On the intensity profile of any given image, positions Y_I , Y_M , Y_R , Y_C and Y_O are determined by finding the position of maximum absolute value of the slope in the vicinity of a particular position. The slope of intensity I at a given pixel i in the profile is calculated using the central difference approximation $I_{i+1} - I_{i-1}$. Figure 5.19 shows an example print-out of the central differences used to identify the various positions from a given profile. For example, from the left to the right on the photo of Figure 5.18, the inner wall position, Y_I , was characterised by a sharp drop in the intensity at -471 pixels, as was the position of the contact line on the glass at -128 pixels. However, the position of the reflected light from the corner of the channel, Y_C , is characterised by sharp rise in the intensity, at -68 pixels. The outer wall of the channel is found from a rise in intensity, at -40 pixels, and the refraction point by a rise in intensity, at -104 pixels.

i	I _i	i	I _i	i	I _i	i	I _i	i	I _i
-480	-2.3	-133	1.7	-113	0.3	-73	-6.0	-47	0.0
-479	-2.3	-132	0.0	-112	-1.3	-72	-8.7	-46	7.7
-478	-3.0	-131	2.0	-111	1.0	-71	5.0	-45	7.3
-477	-8.7	-130	-3.7	-110	4.0	-70	22.0	-44	9.7
-476	-16.0	-129	-17.3	-109	3.0	-69	25.7	-43	15.3
-475	-20.3	-128	-24.7	-108	2.0	-68	38.7	-42	17.0
-474	-31.0	-127	-18.3	-107	3.7	-67	31.3	-41	22.0
-473	-36.7	-126	-4.0	-106	6.3	-66	6.7	-40	25.0
-472	-36.0	-125	-0.3	-105	10.0	-65	-4.3	-39	25.0
-471	-39.7	-124	-3.0	-104	10.7	-64	-5.3	-38	21.3
-470	-22.3	-123	-1.7	-103	5.7	-63	-5.0	-37	15.7
-469	1.0	-122	0.0	-102	5.7	-62	-3.0	-36	9.3
-468	6.7	-121	-2.0	-101	6.3	-61	1.0	-35	4.0
-467	9.0	-120	-7.7	-100	5.3	-60	0.0	-34	2.3
-466	8.0	-119	-8.3	-99	2.3	-59	-5.0	-33	4.7

$Y_I = -471$ $Y_M = -128$ $Y_R = -104$ $Y_C = -68$ $Y_O = -40$

Figure 5.19: Example print-out showing location of positions of maximum central differences of monochrome intensity.

The use of these values in a calculation sheet and use the scaling value of the channel height, $h = 1.5$ mm, will not give the minimum thickness of liquid layer; it will give the minimum dimension of the corner reflection, Y_C (which can be measured in the image). Consequently, to determine the minimum thickness of liquid layer, h_L , a model for the interface shape would be helpful. Figure 5.20 shows the light paths received by the camera and highlights the relationship between the position of the corner position, Y_C , and the simplest physical measure of liquid layer thickness: its minimum position.

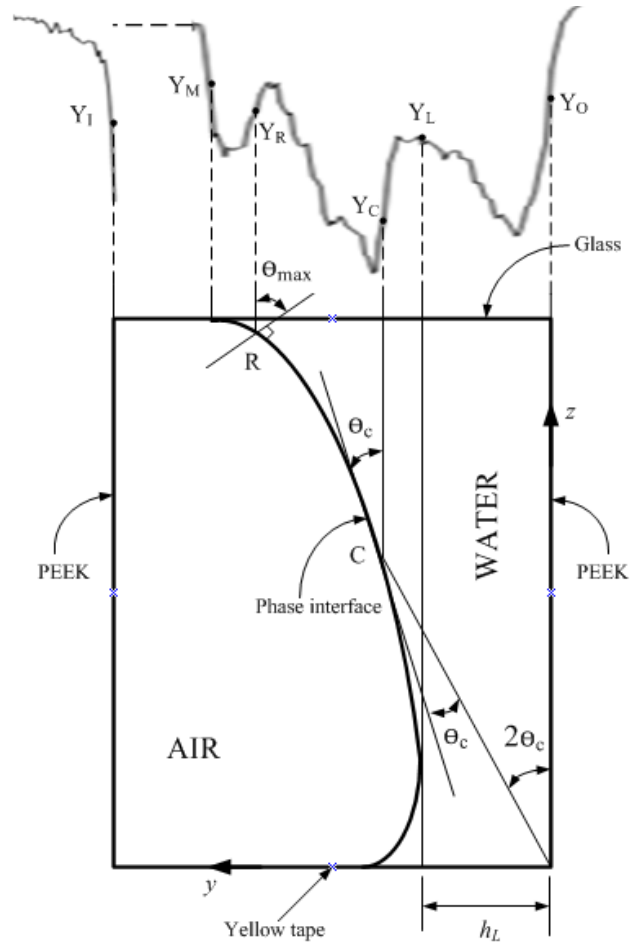


Figure 5.20: Identified positions on image associated with light paths.

5.5 Interface model

It is tempting to accept the position of the corner reflection as a rough measure of liquid layer thickness. However, the differences between this and the true liquid layer thickness can be quite large, can vary with conditions and, therefore, can give a rather misleading account of layer thickness behaviour. Instead, a model for the interface shape can be used to relate the measurable positions in the layer with meaningful physical quantities. This model is described here along with the method for transforming positions of the meniscus contact line, the channel walls and the corner reflection into minimum liquid layer thickness and meniscus height on the camera side of the channel.

In rotating spiral contacting, MacInnes and Zambri (2014) have noted that only hydrodynamic variations in pressure affect the interface shape since the stresses associated with flows are negligible. This is because the spiral angle is small and consequently the component of centrifugal force along the channel (which determines the flow) is small compared to the lateral component that determines the interface shape.

The Young–Laplace equation in the two dimensional section of the spiral channel governs the shape of the interface by linking the radius of curvature, R , at each point along the interface and the pressure difference across it.

$$P_V - P_L = \frac{\sigma}{R_1} \quad (5.7)$$

Using the coordinate system provided in Figure 5.21, the pressure difference at the phase interface between the heavy phase and the light phase appears in equation 5.7 is given by:

$$P_V - P_L = \Delta P_o + (\rho_L - \rho_V) [R_o \Omega^2 y - \mathbf{g} \cdot \mathbf{k} z] \quad (5.8)$$

R_o is the radius to the rotation axis from the outer wall of the channel. Strictly, this should be the radial position of the phase interface at the position considered but the correction has a negligible effect. Similarly, interface curvature in the direction of the channel is far smaller than that in the transverse section and has been dropped.

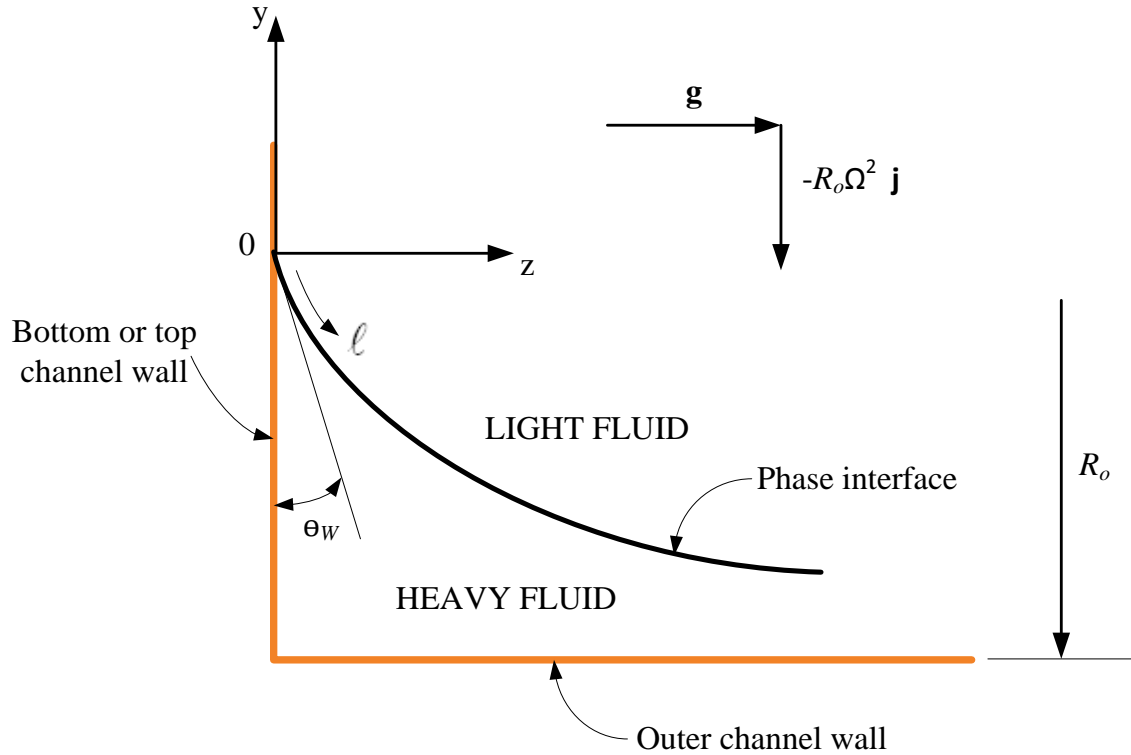


Figure 5.21: Geometry of the interface. R_o is the radial distance from the rotation axis to the outer channel wall. θ_w is the contact angle at the channel wall surface and represents either θ_G at the glass wall surface or θ_p at the plastic wall surface (PEEK or yellow tape) (MacInnes and Zambri, 2014).

Parametric equations for the coordinates of the phase interface which satisfy the Young–Laplace equation can be written in terms of arc length, ℓ , along the interface. Scaling with channel height, h , the parametric equations can be written in non-dimensional form as:

$$\frac{d^2 y^*}{d\ell^{*2}} = \left\{ \Delta P_o^* + \left(\frac{h}{\delta_C} \right)^2 [y^* - \lambda z^*] \right\} \frac{dz^*}{d\ell^*} \quad (5.9)$$

$$\frac{dz^*}{d\ell^*} = \left[1 - \left(\frac{dy^*}{d\ell^*} \right)^2 \right]^{1/2} \quad (5.10)$$

In the above relations the normalisations are $y^* = y/h$, $z^* = z/h$, $\ell^* = \ell/h$ and the pressure difference across the interface has been normalised by the value at $z = y = 0$ is $\Delta P_o^* = h\Delta P_o / \sigma$. Two dynamic parameters arise in the equations: the characteristic capillary height, δ_c (Hunter, 1989), and the non-dimensional gravity, λ .

$$\delta_c = \left(\frac{\sigma}{(\rho_L - \rho_V) R_o \Omega^2} \right)^{1/2} \quad \text{and} \quad \lambda = \frac{g \cdot k}{R_o \Omega^2} \quad (5.11)$$

As can be seen from these definitions both characteristics depend on the centrifugal force. For given interface and fluid properties and gravitational acceleration one can conclude that the interface shape depends on just $R_o \Omega^2$ and the contact angle at the two solid surfaces where the interface meets the top and the bottom channel walls. The contact angles at the channel walls will be referred to as θ_p for the bottom (plastic) wall and θ_G for the top (glass) wall. A final geometric parameter is the ratio between the channel width and height, w/h .

The calculations of the interface profile come from the integration of equations 5.9 and 5.10 where the start points are the contact points at both end of the channel (glass or plastic). From the contact angles at those ends the slopes of the interface are known. The initial pressure difference (ΔP_o^*) at each end wall is adjusted so the integrated profiles extended from the two end walls meet at a central position having identical slope and pressure difference.

The integration step gives approximately 1000 intervals spanning the interface length and the resulting solution is estimated to determine position to within about 0.1 μm (MacInnes and Zambri, 2014). Again for given phase properties (densities and surface tension) and contact angle at both ends the interface shape depends only on the rotation

rate and the channel radial position. Thus, the solution of the interface equation is independent of both the phase flow rates and the liquid layer thickness.

Applying this model to the experimental contact system (air – water) and over the same range of operating conditions as in the experiments will give useful information about interface shape and meniscus height. But it will also allow determination of the minimum thickness of liquid layer, h_L , from measured corner reflection position.

Table 5.1 shows example results for interface shape parameters for different values of rotation rate at the radial position $R_o = 34$ mm, which is in the outer revolution of the spiral. For the same calculations, interface shapes are shown plotted in Figure 5.22 with an arbitrary minimum layer thickness of 100 μm imposed for reference. The effect of rotation rate on the capillary height is clearly seen in both the table and the figure with a factor of 6 reduction in capillary height (and meniscus height) when the rotation rate is increased from 600 rpm to 3840 rpm. The force ratio is decreasing over that same range which produces an increasingly less tilted layer as can be seen most clearly in the enlarged inset plot.

Table 5.1: Dynamic parameters for the computed interface profiles (MacInnes and Zambri, 2014).

Rotation rate, Ω (rpm)	600	960	1480	2400	3840
Capillary height, δ_c (mm)	0.74	0.45	0.30	0.18	0.12
Force ratio, λ	0.074	0.029	0.012	0.005	0.002

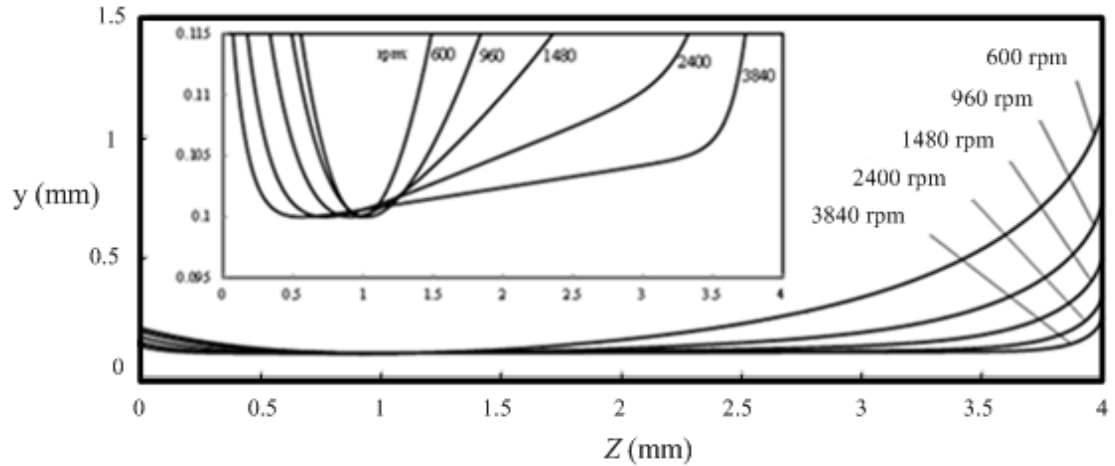


Figure 5.22: Computed interface profiles at various values of rotation rate for conditions typical of the experiments. $z = 0$ corresponds to the plastic surface and $z = 4$ mm to the glass surface. The conditions are as follows: $\theta_G = 15^\circ$, $\theta_p = 75^\circ$; $\rho_L = 995 \text{ kg/m}^3$, $\rho_V = 2.4 \text{ kg/m}^3$ and $\sigma = 0.07 \text{ N/m}$; $h = 1.5 \text{ mm}$, $w = 4.0 \text{ mm}$ and $R_o = 34 \text{ mm}$. The inset plot shows the same curves with an expanded y coordinate scale, revealing both the simple tilting of the interface in the central region at high rotation rate and full penetration of the menisci regions at low rotation rate (MacInnes and Zambri, 2014).

At high rotation rate the capillary height is small and the meniscus penetrates only a short distance from the wall, leaving the majority of the channel width unaffected by surface forces with central region simply tilted by the action of gravity. On the other hand, low rotation rate leads to the menisci affecting entire width of the interface, although the skewing of the interface due to gravity continues to be noticeable except perhaps at the lowest rotation rate of 600 rpm. It is very clear that for rotation rate greater than about 2400 rpm the liquid layer thickness is closely uniform over the channel width for the $100 \text{ }\mu\text{m}$ layer represented in the figure. For rotation rates less than this value we can see a clear effect of the menisci on the thickness of liquid layer, thickening near the walls for this case of a wetting liquid.

Finally, it can be said that the interface shape model calculation presents powerful information that allows us to make an accurate estimation of the minimum thickness of liquid layer and also to clarify the results of liquid layer thickness in relation to the wide channel model as will be seen in a later section and in the results chapter.

5.6 Contact angle and surface tension measurements

In order to apply the interface model it is necessary to have reliable information concerning surface tension and contact angles on the walls of the channel. In this section, measurements of these two key parameters are presented. The contact angle on a specific surface is easily measured by putting a droplet on a flow specimen of that surface. The shape of that droplet depends on the interaction of the fluid and the solid surface and depends not only on the material of the solid but also on the surface finish and chemical state of the surface. Surfaces can be hydrophobic, where the contact angle is large (Figure 5.23a), or hydrophilic, where it is small (Figure 5.23b). The contact angle is defined to be the angle between the surface and the tangent line at the point where the droplet contact with the surface (Sumner et al., 2004).

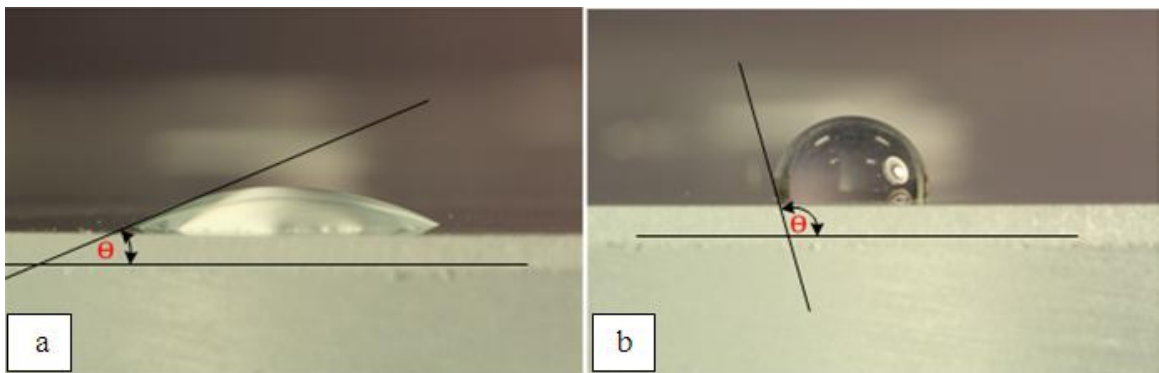


Figure 5.23: Contact angle measurements for one droplet of water on (a) hydrophilic surface and (b) hydrophobic surface.

Tests have been performed manually, using a spare glass window in place of the actual glass window used in the experiment and the yellow tape (on a flat solid support), i.e. the two surfaces which the interface contacts in the channel. The photos have been taken using a digital camera (Canon EOS D550) with a macro lens and analysed using Corel Draw X4 software. The results were confirmed using a commercial device available in the lab (FTA200 Dynamic Contact Angle Analyser) which can measure both the contact angle and the surface tension for liquids in contact with air. Figure 5.24 shows the two arrangements for contact angle measurements.

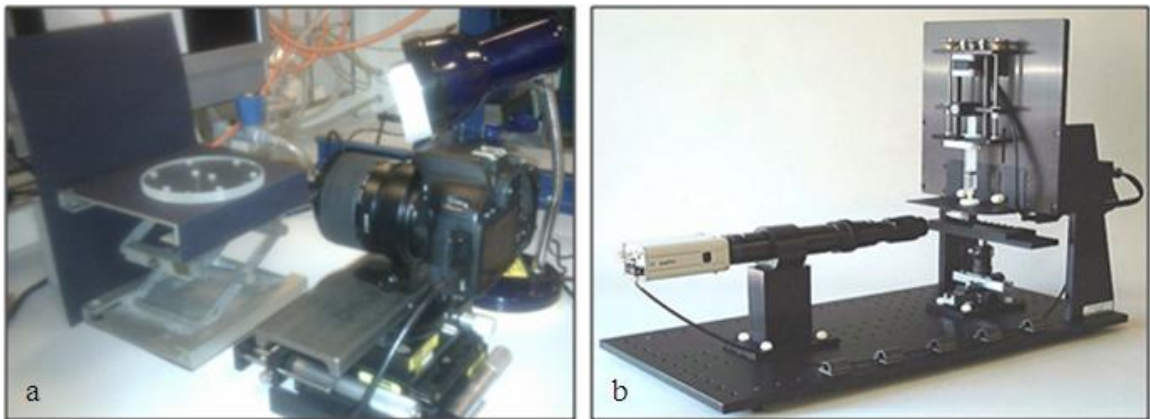


Figure 5.24: Contact angle measurements using (a) Digital camera using 1X magnification and (b) FTA200 Dynamic contact angle analyser.

The tests were performed with two different treatments of the surfaces. In one the surface was cleaned with tap water and surfactant and then dried with a paper lab towel. In the second, the surface was ‘conditioned’ by leaving it in a tap water bath for one week then drying it at room temperature without wiping it in any way (so leaving any residue. The latter is meant to mimic the conditions in the spiral channel for tests with tap water. Table 5.2 presents a summary of the measured angles for the experimental liquids and solid surfaces. The results in the table are averages of three separate drops measured for each liquid and surface combination. The standard deviation of the three determinations is listed in the table following each average value. Clearly the contact

angles were highly repeatable for the data obtained and the procedure used. It can be noted that the measurement of each drop actually included two measurements as the left and right contact regions in the photograph are equally valid and were used.

The surface tension for all fluids included in the experimental work has been obtained using the FTA200 Dynamic contact angle analyser presented above and the results are listed in Table 5.2.

Table 5.2: Summary of measured contact angles for the experimental liquids and solid surfaces.

Fluid Type	Glass		Tape	
	Cleaned	Conditioned	Cleaned	Conditioned
Tap water	$27.7^\circ \pm 2.9^\circ$	$45.0^\circ \pm 3.0^\circ$	$70.0^\circ \pm 0.4^\circ$	$74.0^\circ \pm 2.0^\circ$
Glycerol 88%	$52.0^\circ \pm 2.0^\circ$	$45.0^\circ \pm 1.3^\circ$	$76.0^\circ \pm 1.0^\circ$	$74.5^\circ \pm 1.0^\circ$
Glycerol 60%	$42.0^\circ \pm 3.0^\circ$	$40.0^\circ \pm 3.3^\circ$	$73.0^\circ \pm 2.0^\circ$	$70.5^\circ \pm 1.0^\circ$
Ionic Liquid (Emim EtSO ₄)	$61.0^\circ \pm 1.7^\circ$	$51.3^\circ \pm 1.7^\circ$	$63.0^\circ \pm 2.0^\circ$	$60.6^\circ \pm 1.6^\circ$
Surfactant solution	$7.1^\circ \pm 0.7^\circ$	$11.0^\circ \pm 0.6^\circ$	$8.6^\circ \pm 0.7^\circ$	$18.0^\circ \pm 0.9^\circ$

Table 5.3: Summary of surface tension measurements.

Fluid Type	Surface tension, σ (N/m)
Water	0.070
60% Glycerol solution	0.064
88% Glycerol solution	0.068
Ionic liquid [Emim][EtSO ₄]	0.046
Water – Surfactant solution	0.024

5.7 Minimum liquid layer thickness

Returning to Figure 5.20 and with the interface shape now determined for a given liquid, radial position and rotation rate, it is now possible to determine the minimum position of the liquid layer, Y_L , from the measurement of the corner reflection position, Y_C . For the coordinate system in Figure 5.20, it can be noted that Y_L and h_L will have exactly the same value and the meniscus height on the glass side, defined as the height from the layer minimum to the contact line, can be calculated as $h_M = Y_M - Y_L$. Y_L is important as clearly defined measure of liquid layer thickness that can be compared with the uniform layer thickness which the wide channel model predicts.

Now the method of determining h_L from the measured Y_C and the theoretical interface shape relies on the predicted interface shape being a true representation of the experimental shape. This can be tested by using the theoretical interface shape to also predict both the position of meniscus contact point on the glass wall, Y_M , and of the critical refraction position, Y_R , each of which can be measured along with Y_C . In particular, the theoretical position of the critical refraction point (Y_R) can be compared with the position measured as a check of the consistency of the interface model.

Independently, the profile of the interface has been determined from the experimental points related to the conditions applied such as the radial position, rotation rate, and the fluids properties. Thus, calculating $\Delta Y = Y_C - Y_L$ using the theoretical profile, will lead to calculating the experimental position of the minimum layer thickness, $Y_L = Y_C - \Delta Y$.

For a given measurement of Y_C the conditions of that measurement allow the interface shape to be determined using the interface model. Now Y_L can be found using this theoretical interface shape by adjusting the offset of the minimum position in the profile from the outer wall of the channel until the light ray from the channel corner reflects off the theoretical profile to the camera at a position that agrees with that measured. Figure 5.20 shows the geometry of this light path and the correct minimum layer thickness satisfies the relation between the local slope of the interface and the geometry relative to

the corner position: $(dY/dZ)_C = \tan \theta_c$ and $\tan 2\theta_c = Y_C/Z_C$. Similarly, the critical refraction position, Y_R , is then determined by identifying the interface position point (Z_R, Y_R) such that the slope there corresponds to maximum refraction angle for light coming from the light-phase side: $(dY/dZ)_R = \tan(\pi/2 - \theta_{\max})$, where θ_{\max} is the maximum refraction angle for the interface. For the air-water contacting system the maximum refraction angle $\theta_{\max} = 48.8^\circ$ (the index of refraction of water is 1.33 for a mid-wavelength of visible light in the temperature range of our experiments 30 - 40°C).

Depending on the operating conditions, the difference between the actual position of the minimum liquid layer thickness, Y_L , and the corner reflection position, Y_C , can be large. Figure 5.25 shows this error as a function of rotation rate and layer thickness. It has been mentioned before that at low values of rotation rate the interface becomes more highly curved in the vicinity of the layer minimum. This will cause the corner reflection position to be close to the minimum position and the percentage difference is small. Increasing the rotation rate will lead initially to increasing difference between the two positions until, at sufficiently high rotation rate, the profile becomes sufficiently parallel to the outer wall that the difference necessarily tends to zero. A thicker liquid layer at a given rotation rate increases the difference since the point of reflection must move up the meniscus surface to reflect in the correct angle to reach the camera. The peak difference is substantial, reaching about 30% for the 50 μm layer thickness and this may rise for the yet smaller layer thicknesses measured in the results.

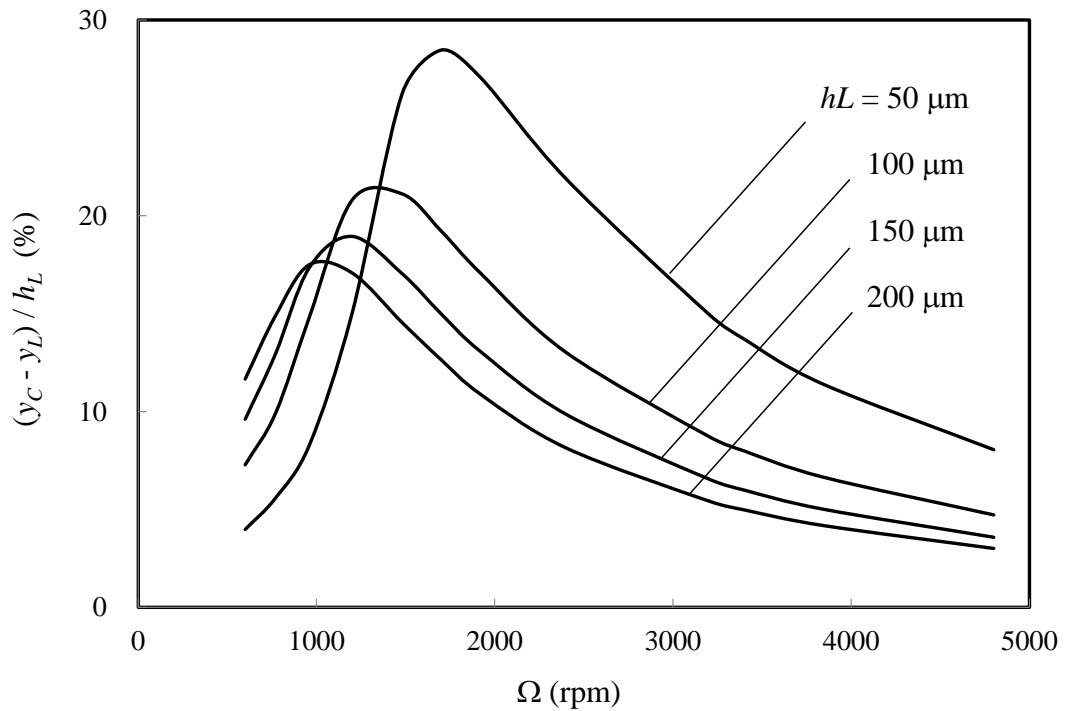


Figure 5.25: The calculated differences between y_C and y_L relative to liquid layer thickness as a function of rotation rate and layer thickness for $R_o = 34$ mm (MacInnes and Zambri, 2014).

5.8 Interface model verification

The procedure for determining a physically meaningful liquid layer thickness relies on the model for interface shape to relate the directly measured corner reflection position to that of the minimum interface position. If the interface shape predicted by the model is reliable it should also predict the position of the critical refraction point on the interface, which is also measured as part of the procedure.

Figure 5.26 shows measured values of the critical refraction position relative to the minimum layer position ($Y_R - Y_L$) plotted against the capillary height (δ_C , Eq. 5.11) for the entire collection of data for the air-water system presented later in the results chapter. The data include ranges in rotation rate, radial position, flow rates and densities. The

solid line on the plot is the prediction of the interface model and clearly follows the data correctly (the lower set of data and curve on the plot). This suggests that the use of the interface shape model to determine the liquid layer thickness from the measured Y_C is accurate.

In principle the measured contact line position, where the interface meets the glass, can serve as a further test of the interface model. However, that position is much more sensitive to the variability in the contact angle at each solid end wall. Indeed the measured $Y_M - Y_L$ (also plotted in Figure 5.26) shows a more gradual increase with δ_C than that given by the interface model for given contact angles. The model calculations for the two glass contact angles 15° (black line) and 30° (grey line) show levels of $Y_M - Y_L$ that are in agreement for different ranges of δ_C . But these values are significantly lower than the 45° angle reported in Table 5.2. Fortunately the interface model prediction for the critical refraction position is insensitive to these changes in contact angle suggesting that the use of the theoretical interface shape is accurate in the central region which is used to find minimum layer position from the measured corner reflection position.

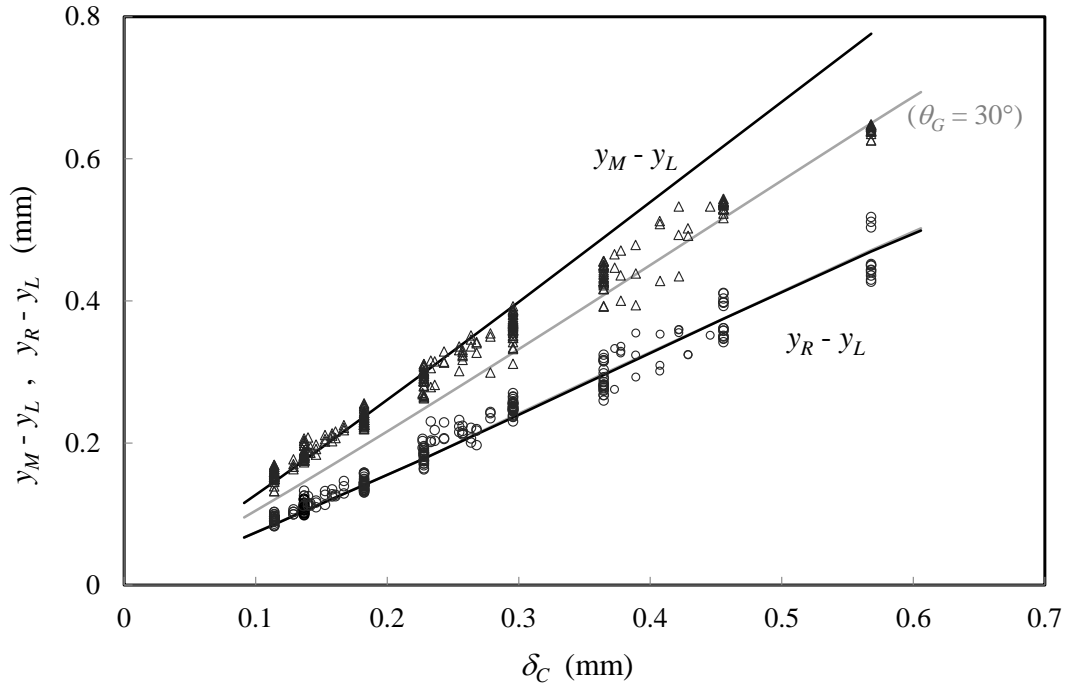


Figure 5.26: Comparison between the calculated and measured height parameters as functions of the capillary height using two values of contact angles on the glass ($\theta_G = 15^\circ$ and $\theta_G = 30^\circ$) and the measured value for the PEEK ($\theta_p = 75^\circ$) (MacInnes and Zambri, 2014).

Chapter 6

6. Results and Discussion

This chapter presents the results obtained using the rotating spiral apparatus described in chapter 4 over a wide range of conditions and compares these with wide-channel model predictions. The experimentally measured values consist of the minimum liquid layer thickness (described in chapter 5), the rotation rate, the flow rate of each phase and the temperature and pressure in the spiral (appendix B). The temperature and pressure are needed to determine fluid properties so the experimental conditions affecting the spiral flow are fully known. Results are obtained for the air-water system over a wide range air flow rate, water flow rate, rotation rate and spiral pressure (gas density). Further tests are conducted using glycerol-water mixtures and an ionic liquid [Emim] [EtSO₄] to examine the effect of liquid phase viscosity. Finally, results of a successful attempt to run an experiment for liquid-liquid contact (1- octanol-water) are also presented.

The experiments have been performed using the approach of varying one of the operating conditions with all others remaining fixed. For example, in the initial tests presented the gas flow rate is varied at fixed values of water, rotation rate and spiral pressure.

6.1 Water and air

6.1.1 Variation of Q_v

In this part of the experiments three constant values of water flow rate have been considered, $Q_L = 9.6, 3.49$ and 1.10 mL/min, covering the full range of the installed rotameter. At each fixed value of water flow rate, the full range of rotation rate allowed by the inverter, motor and seal torque is documented, in addition to the full range of air flow rate allowed by the gas rotameter. As rotation rate increases so does the hydrostatic pressure rise in the liquid outlet passage, as has been mentioned. In order to maintain a fixed spiral pressure, this pressure rise is calculated for each tests rotation rate and the back pressure is set so all tests are at the same spiral pressure. Unless indicated otherwise all tests are carried out at 2.1 bar absolute pressure. Thus to keep the pressure in spiral approximately constant (2.1 bar absolute) the back pressure need to be maintained with changing the rotation rate. Table 6.1 gives the values used for back pressure at each rotation rate tested.

Table 6.1: Rotation rate values and back pressure.

Ω (rpm)	770	960	1200	1480	1920	2400	3200	3840
Pressure, barg	1.05	1.02	0.99	0.93	0.82	0.67	0.33	0.00

Figure 6.1 shows the results of liquid layer measurements when air flow rate is varied at each of the test rotation rates at the highest water flow rate, $Q_L = 9.6$ mL/min. It can be seen that there is generally good agreement between the measured values of minimum layer thickness and those predicted by the wide channel model at high rotation rate. Good agreement is perhaps expected at high rotation rate since centrifugal acceleration is large and the interface will be flat and parallel to the outer wall, as assumed in the wide channel model. Moving up through the figure toward lower values of rotation rate, there is increasingly poor agreement with the model; centrifugal acceleration is weakening and the menisci at the channel walls are growing.

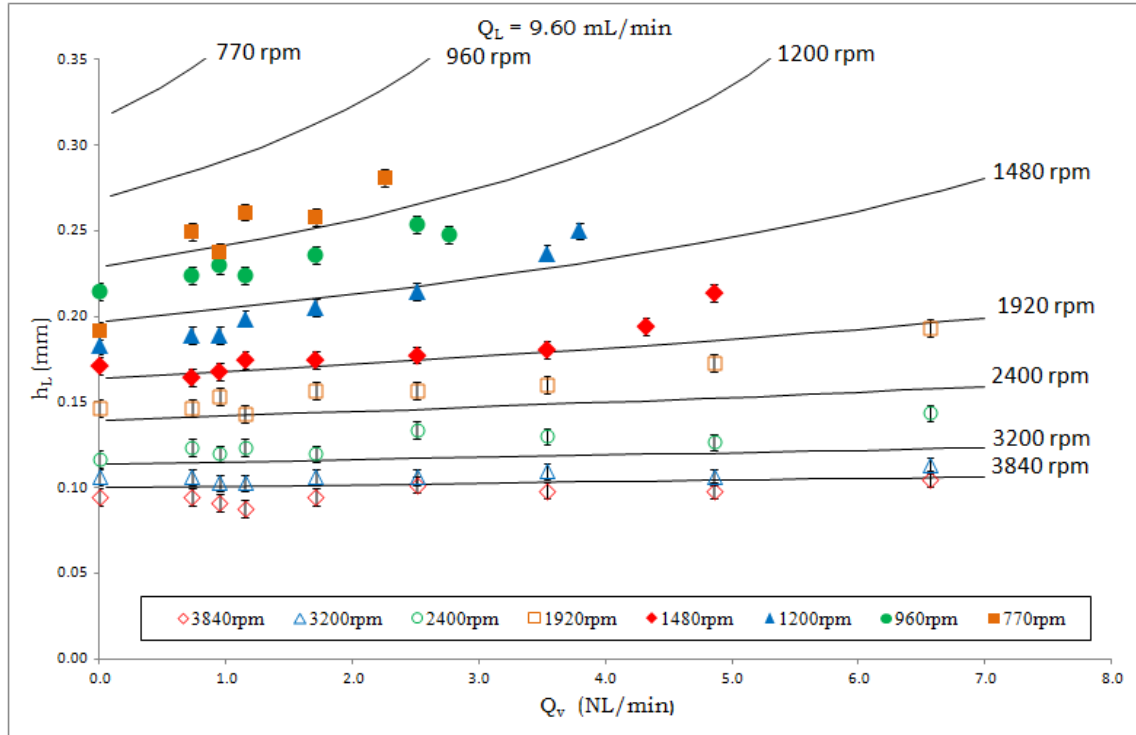


Figure 6.1: The comparison results between liquid layer measurements and wide channel model for varying Q_v at constant $Q_L = 9.6$ mL/min at range of rotation rates.

It can be noted that varying the vapour flow rate has only a slight effect on the liquid layer thickness, except perhaps at very low rotation rate. For example, at 3840 rpm there is an overall increase in the liquid layer thickness of just 12% (from 100 μ m to 112 μ m). However, at low values of rotation rate the effect of varying the vapour flow rate is more pronounced. The thicker liquid layer at lower rotation rate allows small flow section area for the air and both air velocity is increased and air passage height is decreased, each increasing the shear stress retarding the water flow. The wide channel model captures this effect precisely, for the case of uniform layer thickness. Images taken at several of the air flow rates at the highest rotation rate are shown in Figure 6.2. The increase in liquid layer thickness is perceptible but only slight. So, in general, it can be said that both increasing Q_v and decreasing rotation rate cause the water layer thickness to increase. Thus, at low rotation rate and high vapour flow rate there is the possibility of

producing a very thick liquid layer (Figure 6.3). At some point the shear stress exerted by the gas flow will become sufficient to force liquid to flow out the gas outlet. In Figure 6.1 the data can be seen to extend to progressively smaller values of air flow rate as the rotation rate decreases (and the water layer thickness increases). Thus, data for 770 rpm extend only up to about 2.1 mL/min water flow rate, while those at 1480 rpm extend up to about 4.8 mL/min. It was not possible to operate beyond those flow rates as control of the layers was lost.

The rotation rate and the radial position should be the only factors controlling the height of the meniscus. Figure 6.4 shows measured values of meniscus height (glass surface) as water flow rate is varied (at constant $Q_v = 3.54$ NL/min) and for different rotation rates. The measurements give approximately constant meniscus height at each rotation rate as expected.

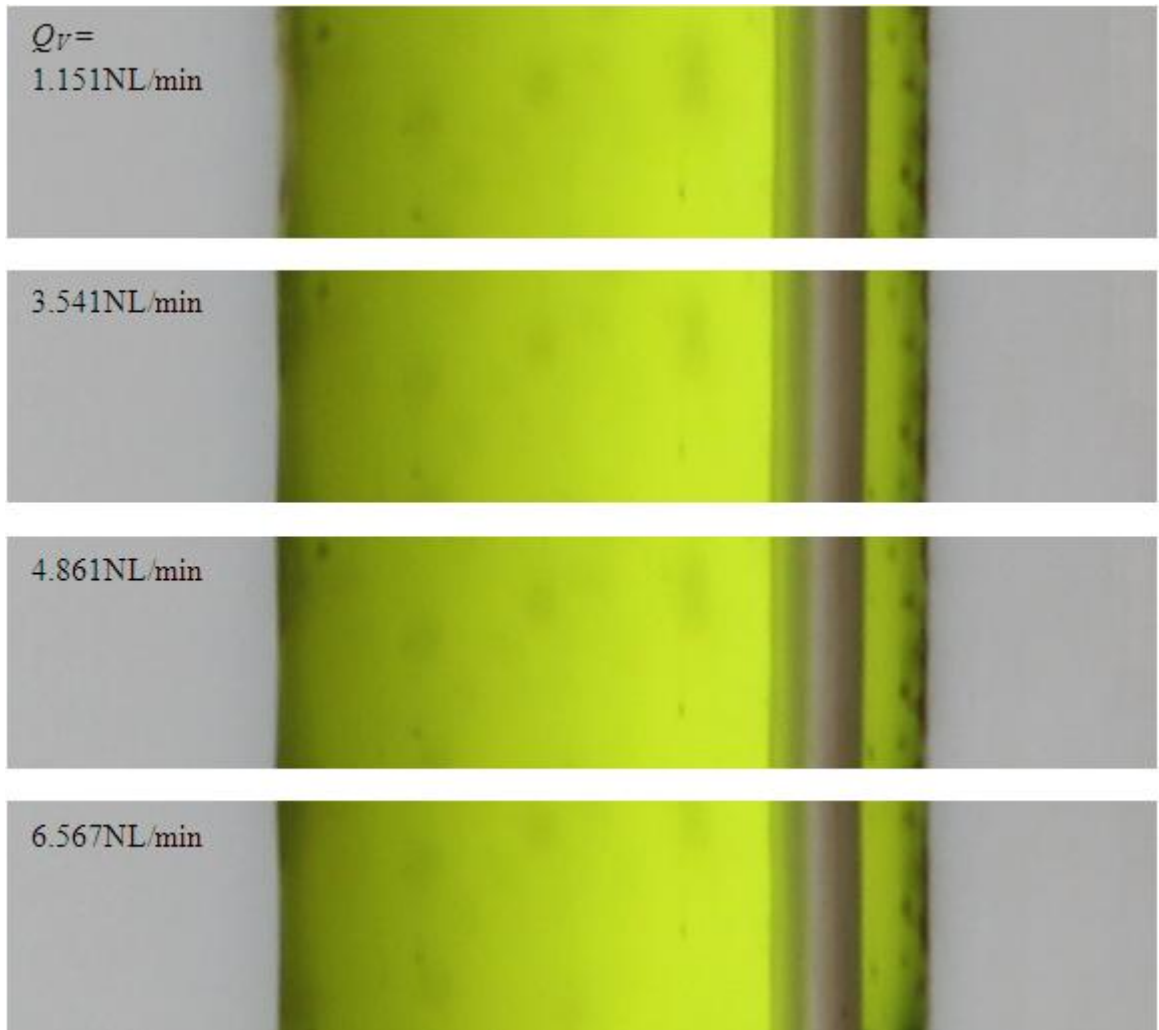


Figure 6.2: Liquid layer thickness variation with gas flow rate, meniscus size remains approximately constant. Conditions are $Q_L = 9.6 \text{ mL/min}$, $P_S = 2.1 \text{ bar absolute}$ and 3840 rpm .

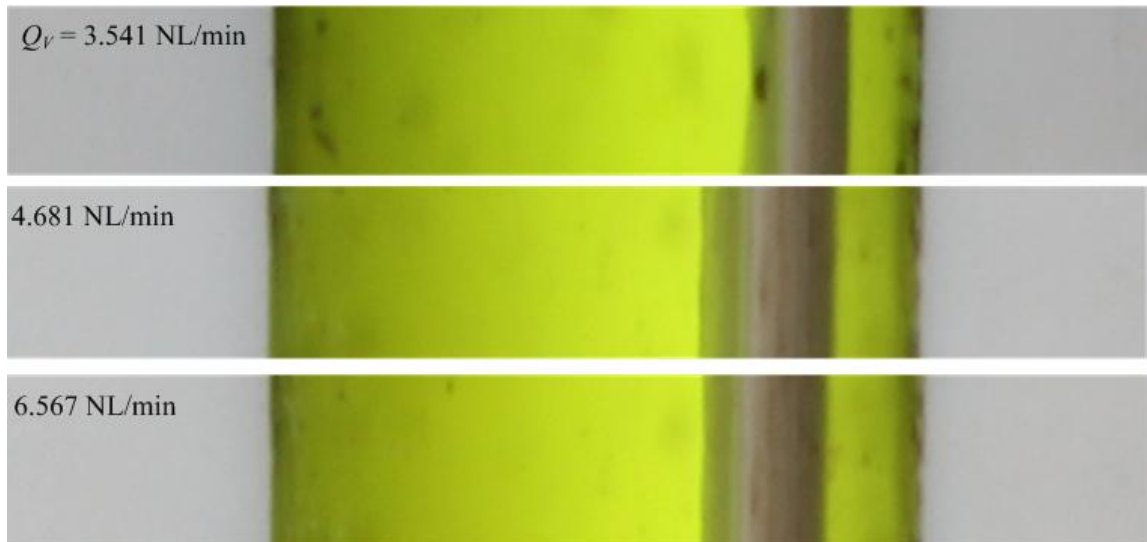


Figure 6.3: Liquid layer thickness variation with gas flow rate meniscus size remains approximately constant. Conditions are $Q_L = 9.6 \text{ mL/min}$, $P_S = 2.1 \text{ bar absolute}$ and 1480 rpm .

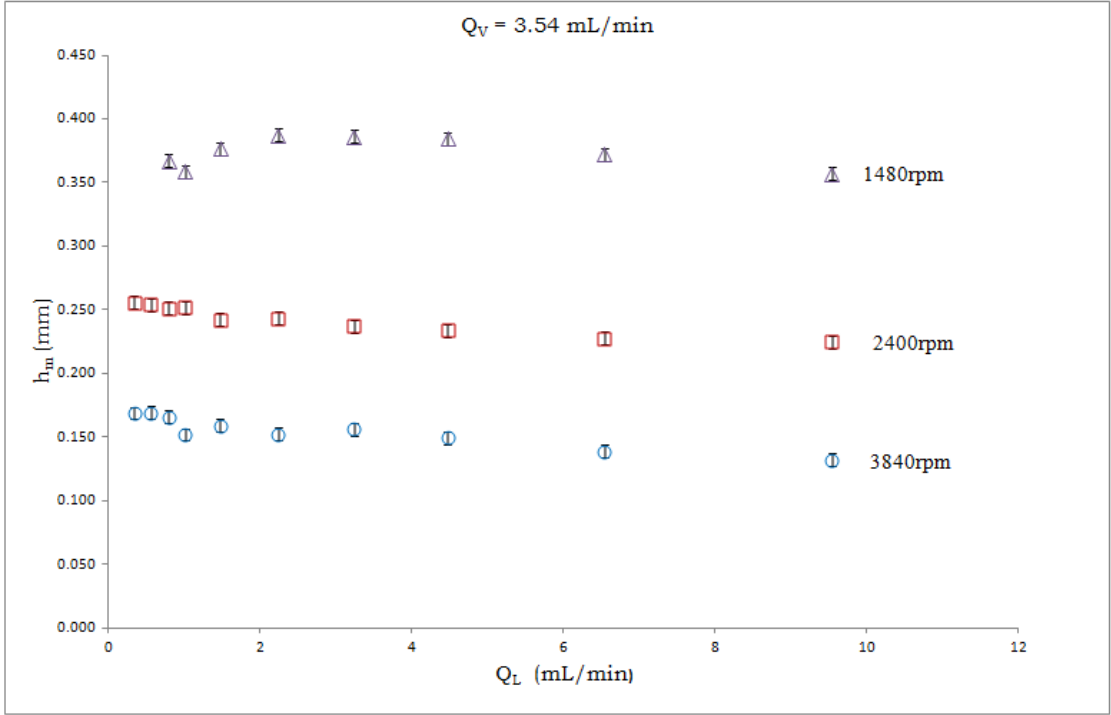


Figure 6.4: The results of meniscus height measurement for varying Q_L at constant $Q_V = 3.54 \text{ NL/min}$ and several rotation rate values over the range.

At this stage there are two points that should be mentioned. These relate to the deviations found for the data in relation to the wide channel model at lower rotation rate. The liquid layer thickness, h_L , is represented in the wide channel model as constant across the layer width while the measurements correspond to layers that are both curved by the menisci and tilted by gravity. The flow rates in the wide channel model are per unit width and to compare the experimental results with the model the experimental flow rates are divided by the channel width ($w = 4.0$ mm) to determine the flow rate condition for the wide-channel model prediction.

Thus, the model considers an infinite width channel of constant layer thickness while the liquid layer has variable thickness in the actual channel (Figure 6.5).

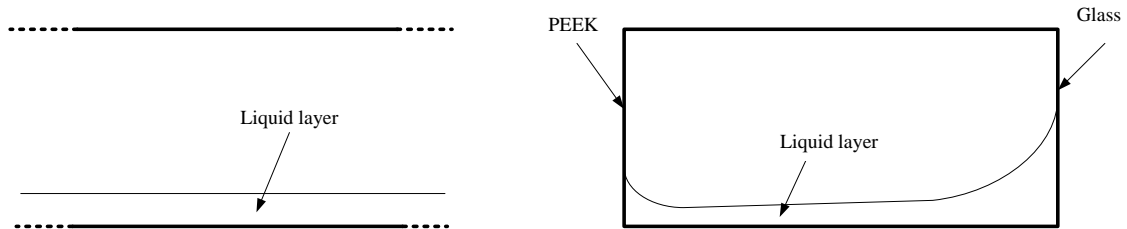


Figure 6.5: Shape of liquid layer for infinite (left) and finite (right) width channel

The poor agreement with the wide channel model is related to the height of the meniscus, h_m , which produces larger section area for flow at the ends of the layer than in the middle section. The interface shape discussed in chapter 5 showed that meniscus height depends on rotation rate and radial position (Eq. 5.11). Disagreement with the wide channel model may be expected to occur when $h_m \gg h_L$, that is when the end areas under the menisci become a significant fraction of the overall section area for liquid flow. This situation will arise for low rotation rate where h_m is large, and low liquid flow rate, where h_L is small. Figure 6.6 shows that for the same value of rotation rate (meniscus height) decreasing the liquid flow rate will increase h_m/h_L and poor agreement will be found. Also, if Q_L is adjusted to maintain constant layer thickness,

increasing the rotation rate will reduce the meniscus size and closer agreement with the wide channel model will be found (Figure 6.7). Since the menisci area promotes larger flow rate per channel width in the end regions than in the thin central region of the liquid layer, the experimental layer will be thinner than predicted by the wide channel model. So in the results of Figure 6.1 the measurement falls furthest below the model prediction and low rotation rate (h_m is large) and at low air flow rate (h_L is small). It is expected, when different water flow rates are next tested, that agreement will be poorest at small water flow rate since layer thickness is small, and that is what is found.

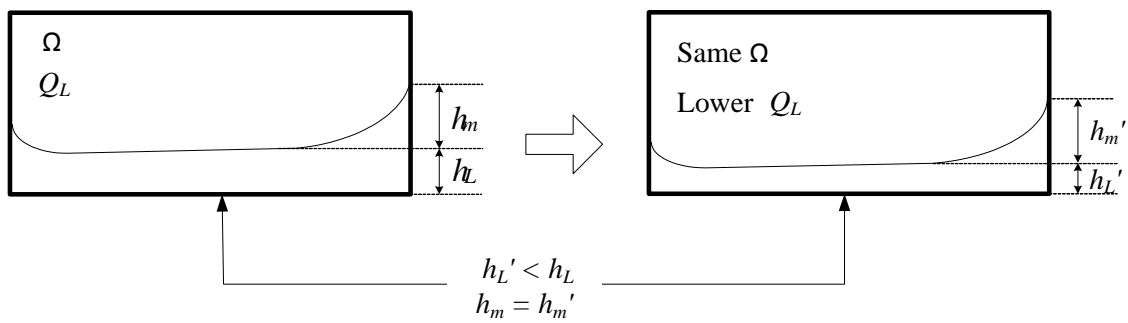


Figure 6.6: The effect of reducing the liquid flow rate on the meniscus size.

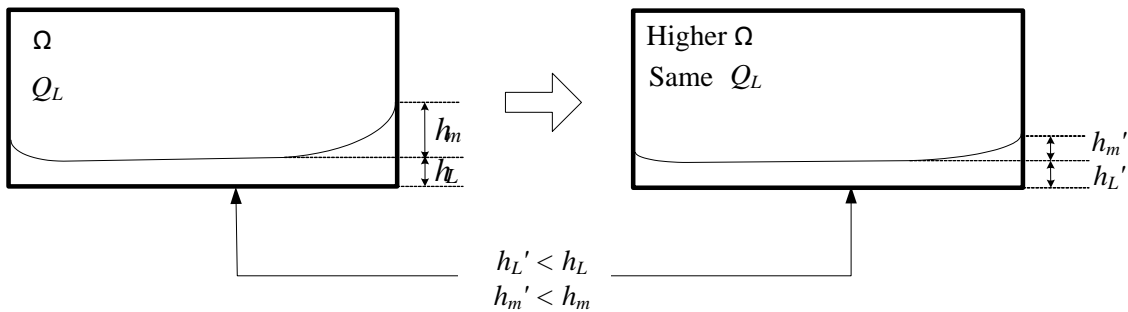


Figure 6.7: The effect of increasing the rotation rate on the meniscus size.

Figure 6.8 and Figure 6.9 present results for two lower values of water flow rate (3.49 mL/min and 1.10 mL/min) for the same ranges of vapour flow rate and rotation rate as before. It is clear that for these lower liquid flow rates that agreement with the wide channel model is generally worsened as expected. For 3.49 L/min water flow rate, only the highest rotation rate remains near the model prediction and for the yet lower flow rate the measured layer thickness falls significantly below the model result even at the highest rotation rate.

Again at low rotation rate, beyond certain vapour flow rate it is not possible to control the layer flows. For example, for 1480 rpm in Figure 6.8 it can be seen that there are no data beyond $Q_v = 4.0$ NL/min. Increasing the flow after this point thickens the water layer to the extent that the gas flow carries the liquid out the air outlet, as illustrated in Figure 6.10. The interface shape and position at the liquid inlet for different liquid layer thickness due to the effect of rotation rate are shown in Figure 6.11 where the increasing layer thickness with rotation rate can be seen. No detailed study of this process of ejection has yet been carried out, but the gas flow rate producing ejection at each rotation and water flow rate combination was reproducible. It can be noted that this ejection appears to require layer thickness in excess of 150 μm and that optimum contacting is achieved for layer thickness well below 100 μm for this 1.5 mm high channel size (MacInnes et al., 2012).

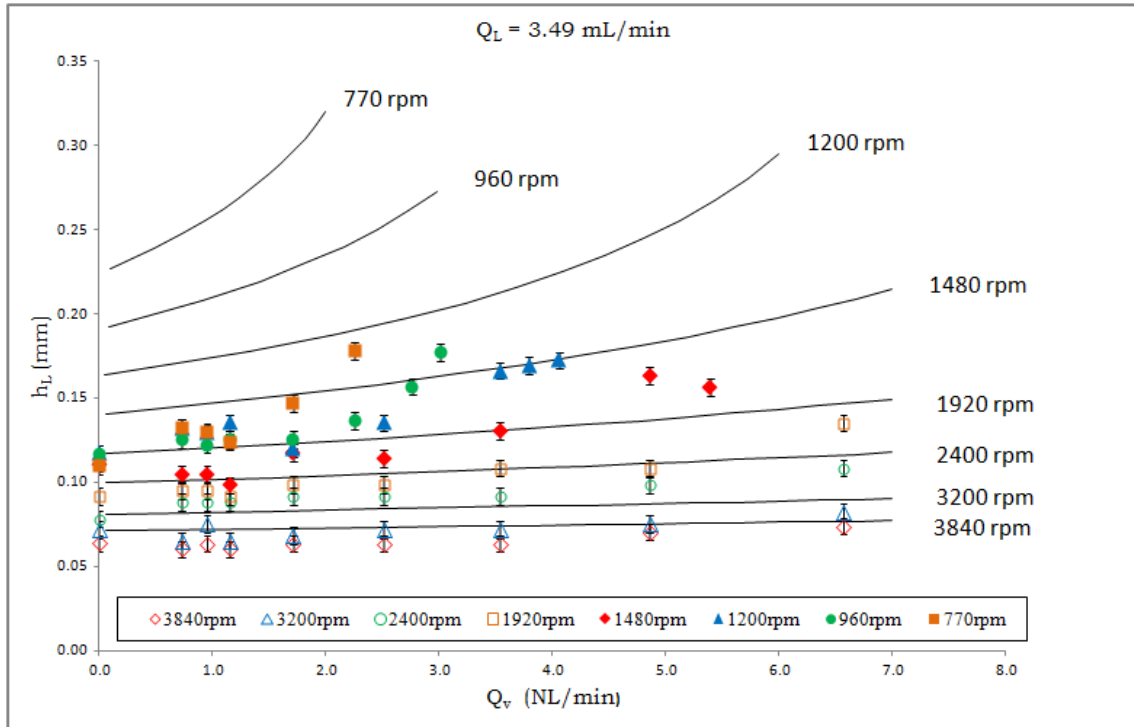


Figure 6.8: The results of liquid layer measurements compared with wide channel model for varying Q_V at constant $Q_L = 3.49 \text{ mL/min}$ at range of rotation rates.

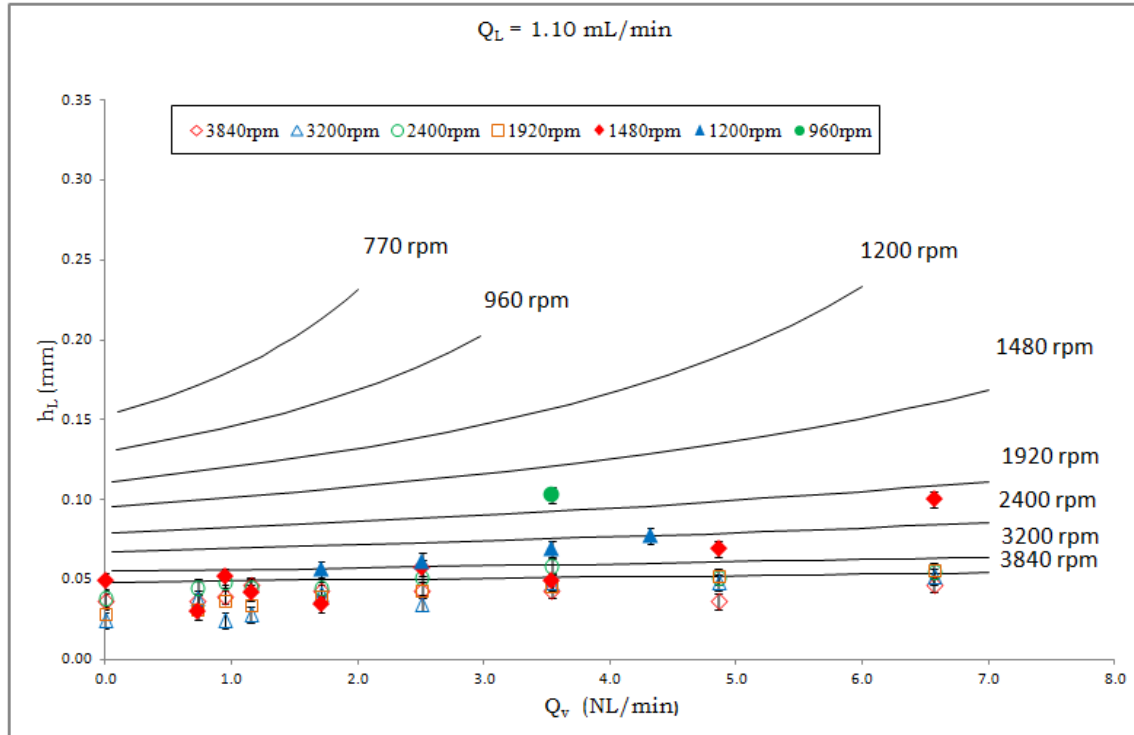


Figure 6.9: The results of liquid layer measurements compared with wide channel model for varying Q_V at constant $Q_L = 1.10 \text{ mL/min}$ at range of rotation rates.

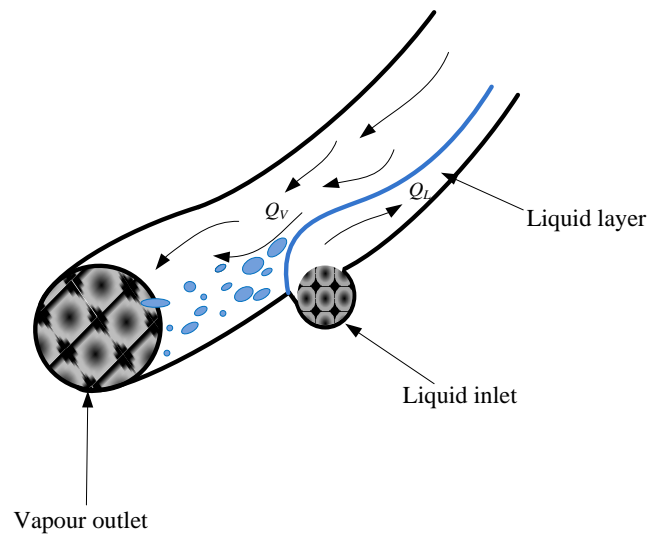


Figure 6.10: Thick liquid layer at liquid inlet due to low rotation rate and high vapour flow rate.

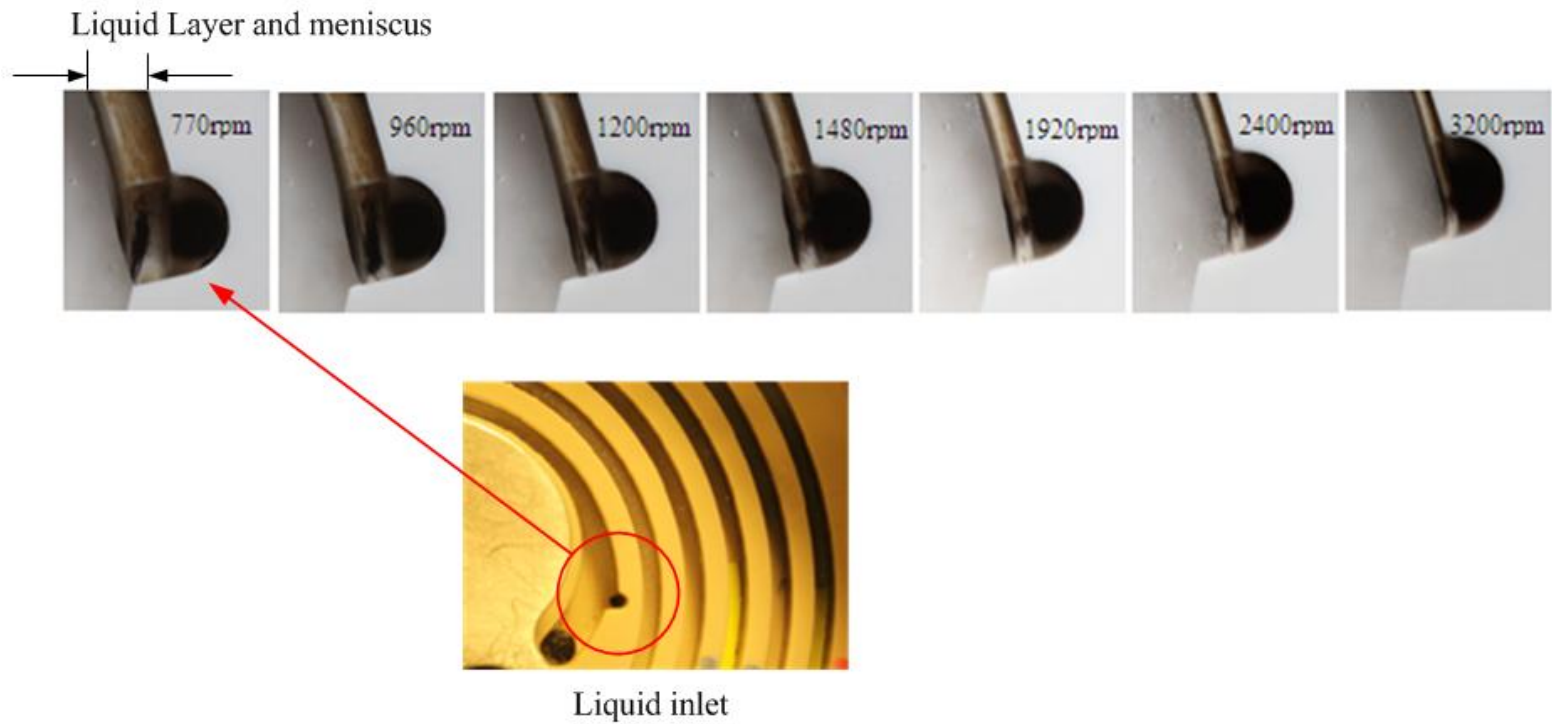


Figure 6.11: Interface position and shape at liquid inlet for different liquid layer thickness (rotation rate). Conditions are $Q_V = 3.54$ NL/min, $Q_L = 3.49$ mL/min and $P_S = 2.1$ bar absolute.

6.1.2 Variation of Q_L

In the following tests Q_V is held constant and the water flow rate is varied to examine more directly the strong effect of Q_L on water layer thickness revealed in the previous results. The water flow rate is varied over the widest range that can be measured using the existing water rotameter from around 0.3 up to over 10.0 mL/min. Experiments using $Q_V = 3.54$ NL/min and at the three values of rotation rate 1480, 2400 and 3840 rpm were carried out. The results are plotted in Figure 6.12 and show the expected deviation at low rotation rate and water flow rate. At the highest rotation rate agreement is good except at the very lowest liquid flow rates where layer thickness falls below about 40 μm . Interestingly, while the model prediction remains in strictly increasing layer thickness order with decreasing rotation rate, as water flow rate approaches zero the order inverts: the highest rotation rate case remains closest to the model prediction with the lower rotation results falling sharply away from the prediction. The large effect of the liquid flow rate on liquid layer thickness can be seen in the series of photographs for this case shown in Figure 6.13.

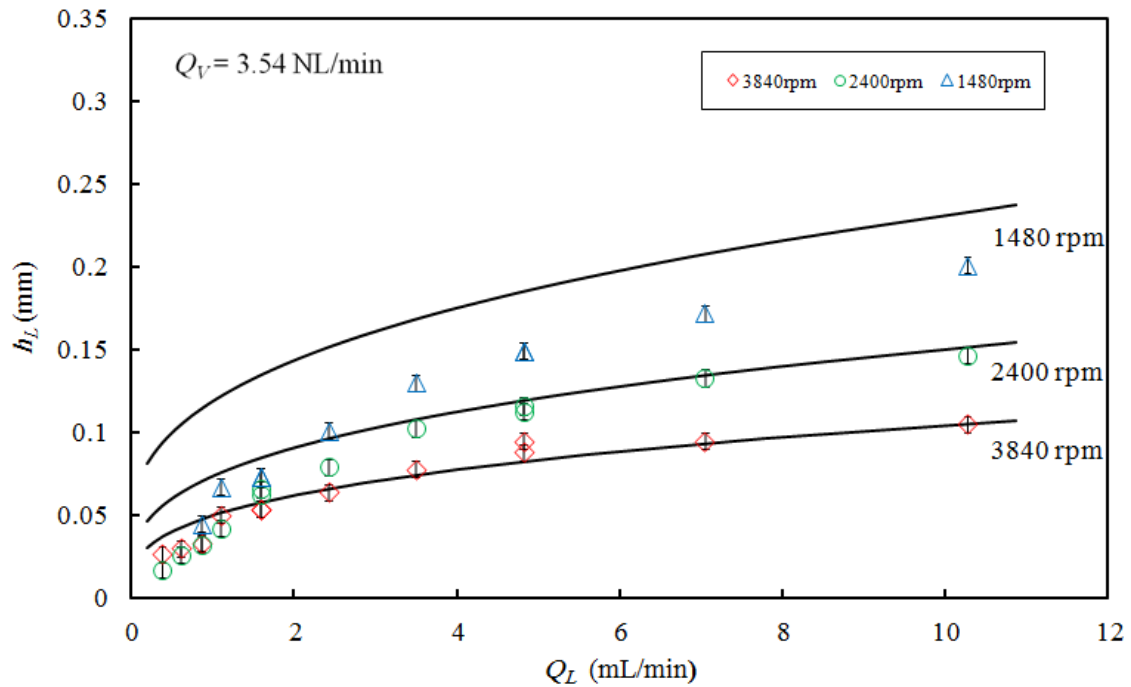


Figure 6.12: The results of liquid layer measurements compared with wide channel model for varying Q_L at constant $Q_V = 3.54$ NL/min at range of rotation rates.

It is important to note that liquid layers as thin as $17\ \mu\text{m}$ have been recorded. Achieving such thin layers was believed to be beyond practical feasibility due to limitations in fabrication tolerances (MacInnes et al., 2012). Such thin liquid layers can correspond to optimum interface placement according to the model so successfully producing them supports the idea that the rotating spiral can allow optimum conditions regardless of flow rate ratio required for a particular phase and solute system. In fact the wide channel model (MacInnes et al., 2012) suggests that over a wide range of phase and solute systems the optimum layer thickness is in the range of 12 to $90\ \mu\text{m}$ for a channel height of $h = 1.5$ mm.

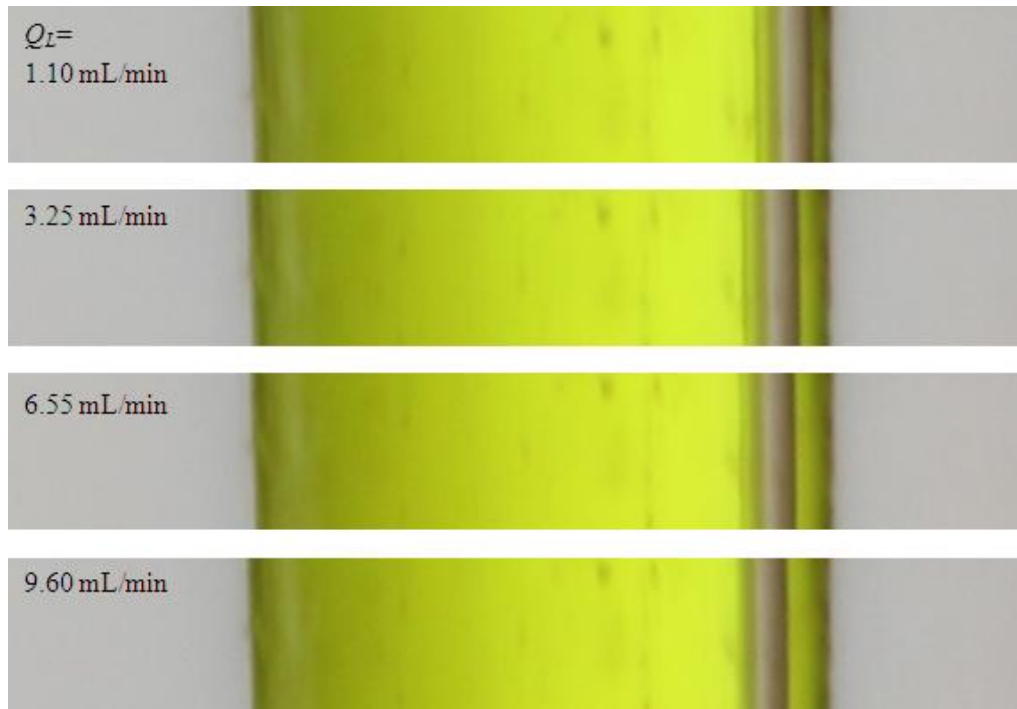


Figure 6.13: Liquid layer thickness variation with liquid flow rate. The meniscus size remains approximately constant. Conditions are $Q_v = 3.54$ NL/min, $P_s = 2.1$ bar absolute and 3840 rpm.

A further test has been done to support the idea that meniscus rise is primarily responsible for the difference in liquid layer thickness between model and experiment. Figure 6.14 shows the effect of adding a surfactant solution to the water. For the test 73 g/L of Fairy Liquid solution with water was delivered using a 1 mL syringe into the water flow. The water and Fairy Liquid flow rates were selected to maintain 0.5 g/L Fairy Liquid. Adding the surfactant solution reduces the interfacial surface tension (Eq. 5.11) and hence the capillary height. This reduces the deviation from the model prediction as is clear from comparison of Figure 6.12 (without surfactant) and Figure 6.14 in which the surfactant has been used. Figure 6.15 highlights the effect of surfactant at 1480 rpm.

Figure 6.16 compares typical images taken with and without the surfactant at the same conditions otherwise. The surfactant clearly reduces the height of the meniscus, but also thickens the central liquid layer as less area is available for flow under the meniscus.

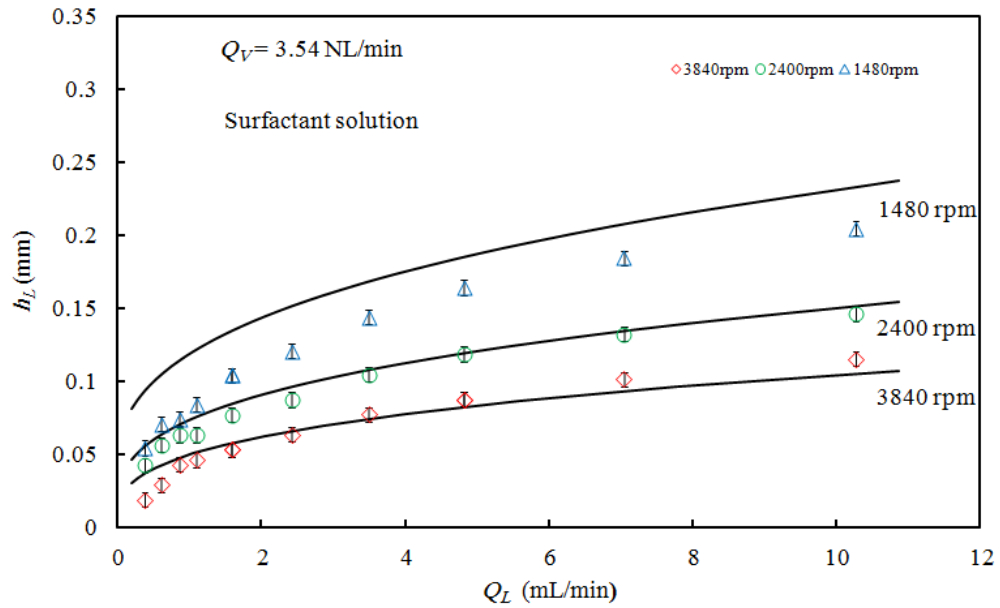


Figure 6.14: The results of liquid layer measurements compared to the wide channel model when a surfactant solution is added to water flow; $Q_V = 3.54$ NL/min.

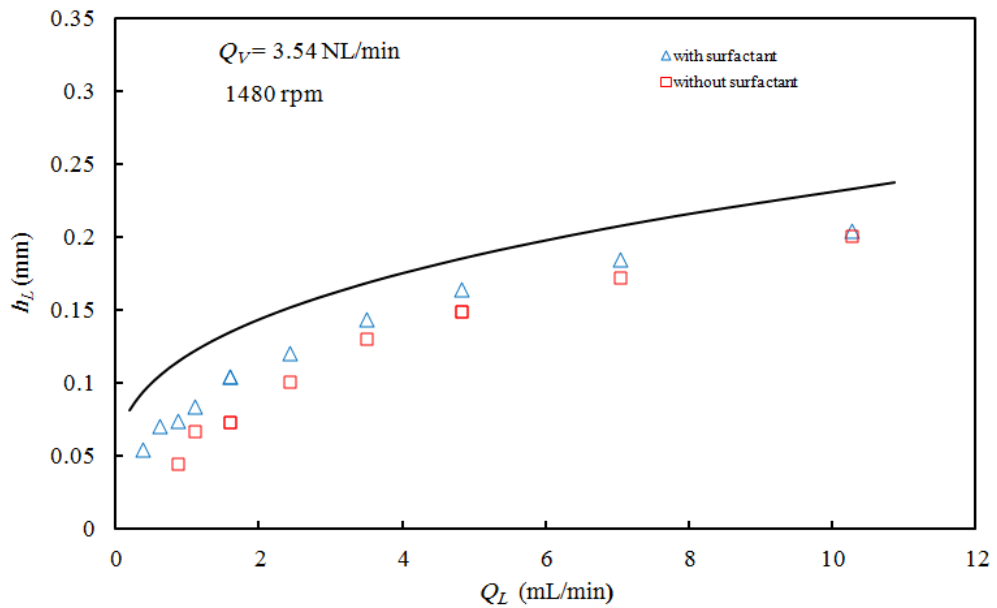


Figure 6.15: A comparison for the liquid layer measurements with and without surfactant at 1480 rpm.

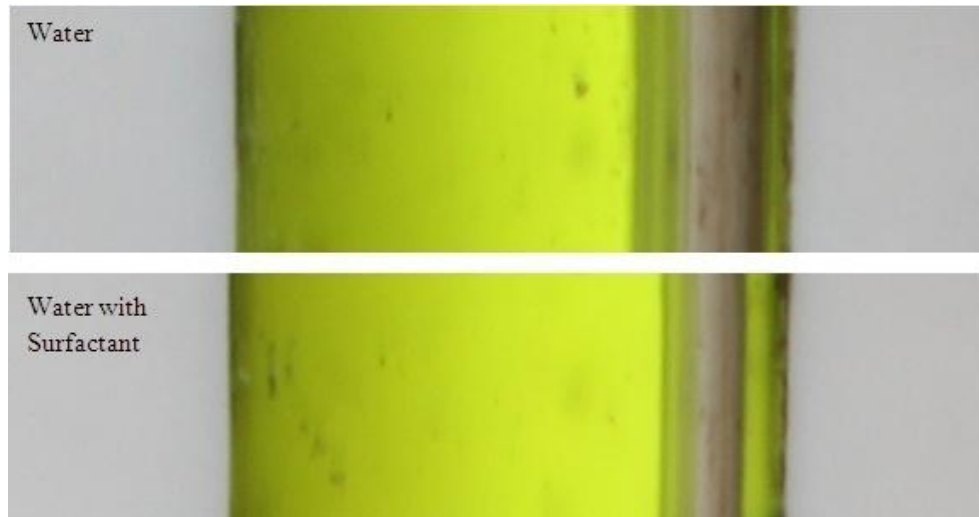


Figure 6.16: Effect of surfactant on liquid layer thickness and meniscus size. Conditions are $Q_v = 3.54 \text{ NL/min}$, $Q_L = 1.10 \text{ mL/min}$, $P_s = 2.1 \text{ bar absolute}$ and 1480 rpm .

Figure 6.17 shows the dramatic effect of rotation rate on liquid layer thickness and meniscus size. These effects are as expected since each depends directly on the centrifugal acceleration $R\Omega^2$ (Eq. 5.11). The meniscus is controlled by the component transverse to the channel ($R\Omega^2 \cos \alpha$) and the layer thickness by the component along the channel ($R\Omega^2 \sin \alpha$) which is the principal force driving the liquid flow in the spiral against viscosity stress. Thus, as rotation rate increases the meniscus size and the liquid layer thickness decrease.

(Further images at other conditions of flow rates and rotation rate are included as appendix D.1.)

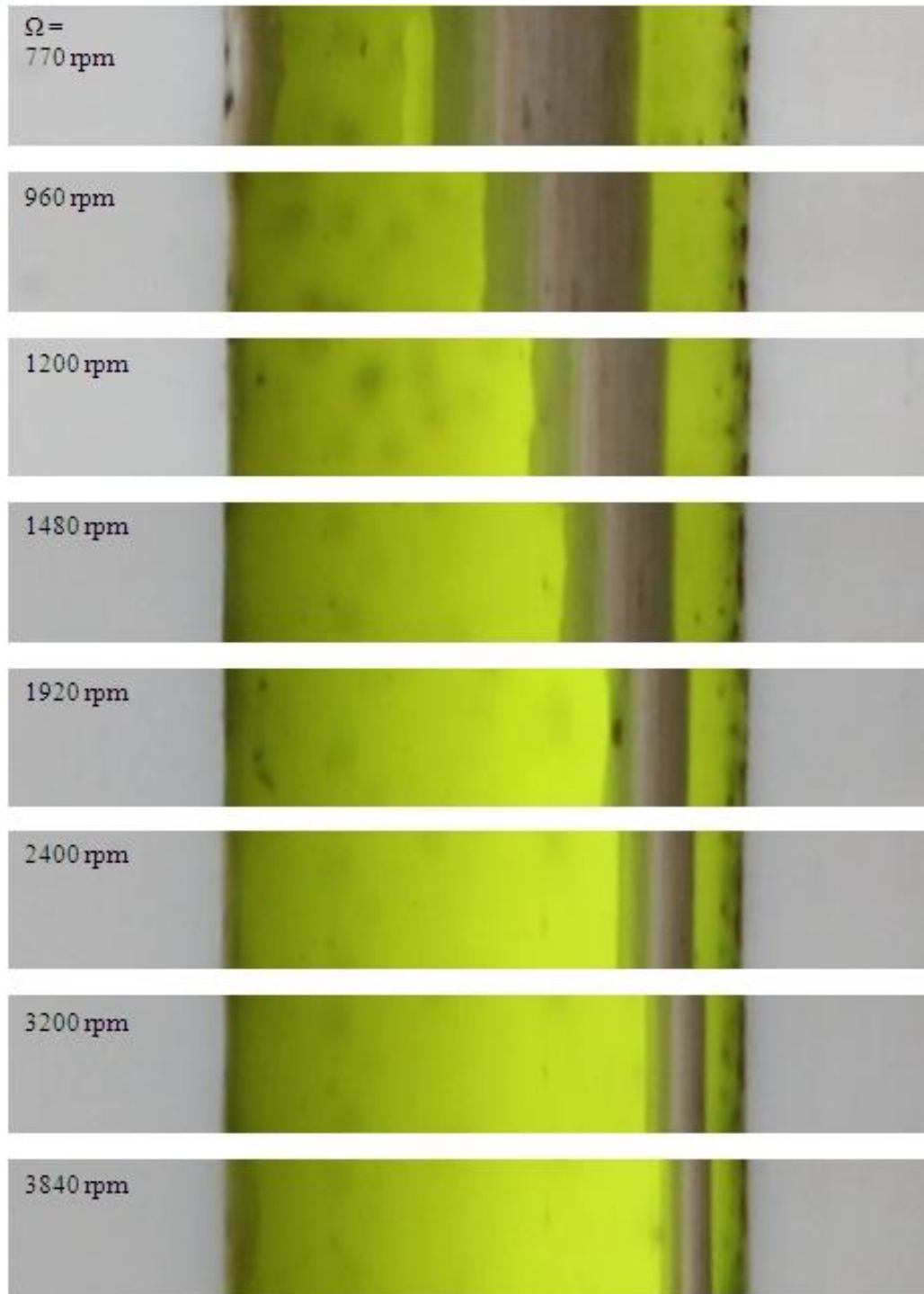


Figure 6.17: Effect of rotation rate on liquid layer thickness and meniscus size. Conditions are $Q_v = 1.71$ NL/min, $Q_L = 9.6$ mL/min and $P_s = 2.1$ bar absolute.

6.1.3 Effect of pressure

The pressure in the spiral channel has an effect on the flows by changing gas-phase density. Operating under constant mass flow rate of gas, increasing the pressure, and hence the gas density, will result in a lower gas volume flow rate in the spiral channel. Since gas viscosity is insensitive to pressure, this lowering of flow rate also lowers the shear stress exerted on the liquid and thus should be roughly equivalent to reducing the gas flow rate at constant spiral pressure. Thus, a slight decrease in h_L with spiral pressure is expected. In this part of the experiments, spiral pressure is varied over the range allowed by the seal pressure limit.

The measurements of liquid layer thickness in Figure 6.18 show changing the spiral pressure has little effect on the liquid layer thickness. The model shows the slight decrease in layer thickness as pressure increases and the measurements perhaps just pick up the decrease. Again agreement with the model is best at high rotation rate and becomes less good as rotation rate decreases. However, agreement is less good than expected for the higher rotation rates. Operating at these higher pressures leads to greater seal friction and more heat generation. Thus the temperature in the spiral (T_s) may have been higher than value used for model calculations (taken from Eq. B.17), which means the actual viscosity of the liquid may have been lower in which case the model prediction drops to smaller liquid layer thickness.

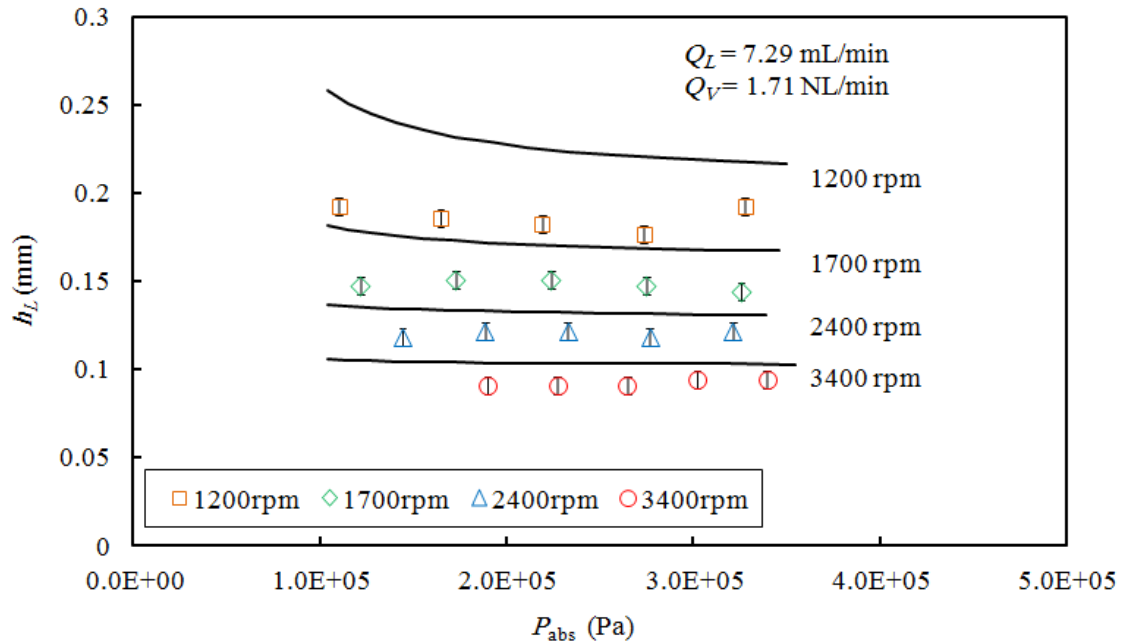


Figure 6.18: The results of liquid layer measurements compared with the wide channel model for variation of spiral pressure at several values of rotation rate.

6.2 Radial position test

The results of experiments presented so far were all taken at the outer radial position ($R = 34.0$ mm) where the centrifugal force is greatest. It is important to consider other positions along the spiral channel to test the expectation that liquid layer thickness should remain constant with radial position. Of course, it has been established that the meniscus size has an important effect and, since meniscus size depends on radial position, the effect of meniscus size will grow as radial position decreases. Eight positions were chosen to span nearly the entire length of spiral channel and therefore allow data from a full range of radial positions. Table 6.2 lists the positions used and the radial position of each one. Figure 6.19 indicates the positions on a photograph of the spiral channel. The yellow tape was applied at each position to allow layer thickness measurements. Obtaining the results was tedious since correct alignment of the camera

is required at each position. For this reason, the data at each radial position (three different liquid flow rates at three different rotation rates) were collected together, before moving on to the next radial position.

Table 6.2: Radial positions values.

Position	R (mm)
1	34.00
2	31.80
3	30.97
4	29.22
5	26.60
6	24.85
7	23.97
8	22.22

Tests were performed for the rotation rates 1200, 1920 and 3200rpm and water flow rates 1.10, 3.49, 9.60 mL/min. The effect of radial position most directly affects the liquid flow and this is insensitive to gas flow rate as has been shown. Thus, variation in air flow is not considered and runs used the same air flow rate of 3.45 NL/min.

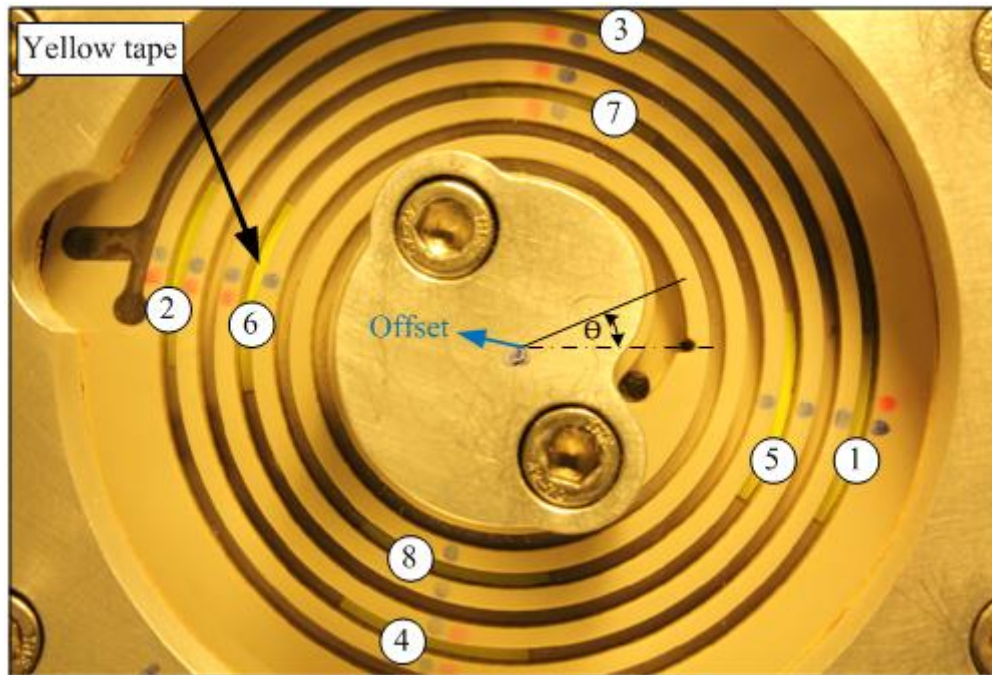


Figure 6.19: Selected radial positions along the spiral channel.

The results for water layer thickness at the intermediate rotation rate are shown in Figure 6.20 and it is immediately clear that there is considerable scatter, although the agreement of the average with the wide channel model prediction (solid lines) are as before. The layer thickness at any given water flow rate is expected to remain constant as radial position increases, or possibly to increase gradually as the meniscus size decreases. No increase in thickness is evident, though this may be masked by the scatter. However, the measurements at the three different flow rates follow an apparently systematic pattern with radial position. Also, this systematic variation can be seen in the layer images at a sequence of radial positions shown in Figure 6.21.

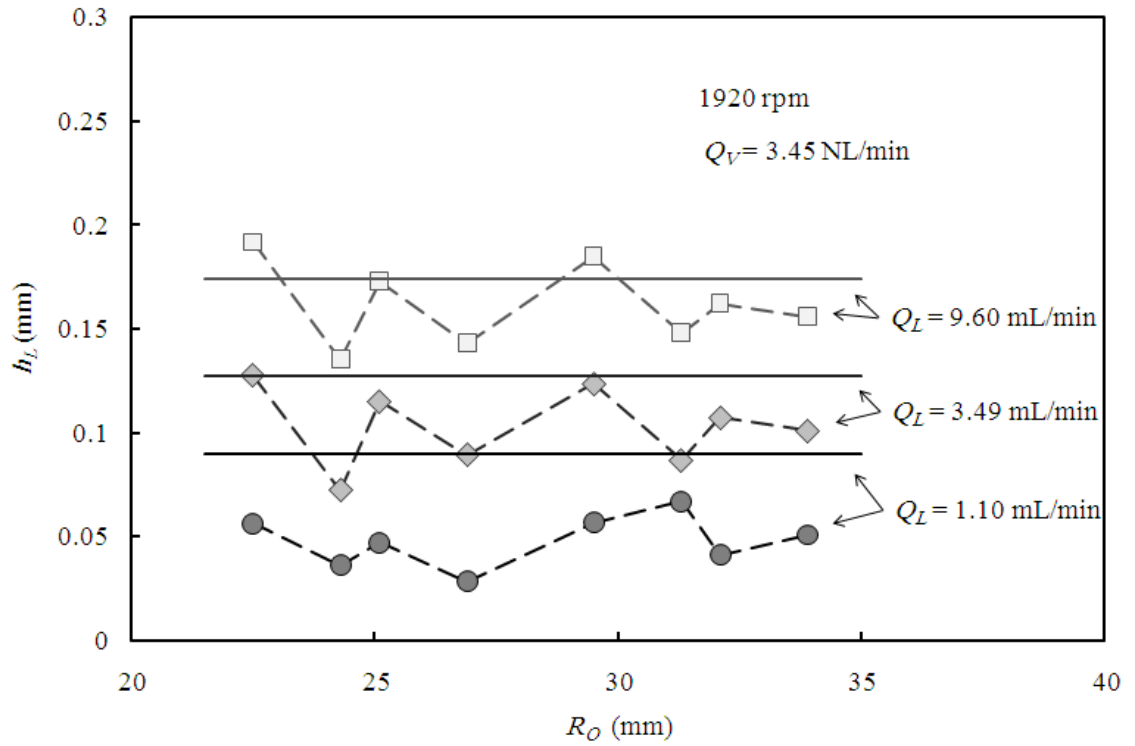


Figure 6.20: Liquid layer measurements along the spiral channel compared to the wide channel model. Conditions are 1920 rpm, $Q_V = 3.54 \text{ NL/min}$, and range of Q_L .

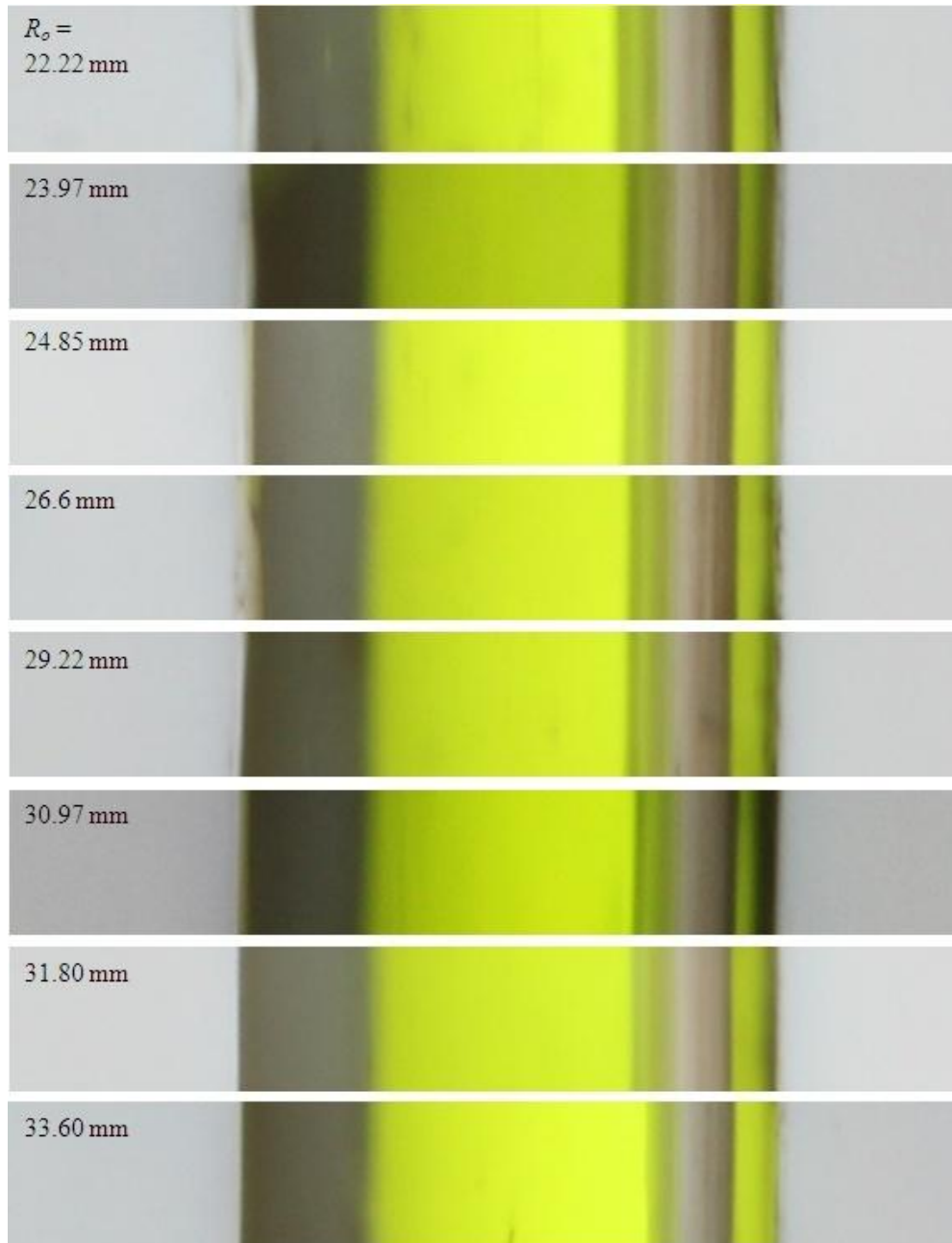


Figure 6.21: Liquid layer variation and meniscus size with the effect of radial position. Conditions are $Q_v = 3.54$ NL/min, $Q_L = 3.49$ mL/min, and 1920 rpm.

Investigation of this issue showed that the centre of the spiral was significantly misaligned from the rotation axis. This offset was determined by comparing a photograph taken from below of the spiral while rotating with one taken from the same position while not rotating. The first procedure resulted in a precise circle being produced on the image for suitably long exposure with a distinct mark drawn on part of the clamp, from which the centre of rotation could be determined. The second was used to locate the spiral centre by fitting the known spiral pattern to the image. The offset was found to be $304\ \mu\text{m}$ in the direction $\theta = 174^\circ$ (angle definition in Figure 6.19) relative to the rotation axis. This degree of offset was much greater than planned as the fabrication machining work was expected to produce an offset of at most about $100\ \mu\text{m}$. The fact that sub $20\ \mu\text{m}$ liquid layers were produced with such large offset error suggests that yet thinner liquid layers may be produced as a matter of routine.

With the offset determined, the variation in $R_o \sin \alpha$ with position along the channel can be determined and this can be used in the wide channel model to predict the resulting h_L variation with position. For purposes of comparison, it was helpful to devise a way to inspect all of the data on a single plot, allowing systematic variation due to offset to be highlighted. Subtracting the average level of h_L for each set of data or for the model prediction proved effective as shown in Figure 6.22. The figure includes the prediction (with offset) of the wide channel model as dashed lines. It is clear that the data correlate well with the periodic undulations in the model results which are due to the varying effect of the offset on successive revolutions of the channel as it spirals around. The much higher peak in the model is again the over-prediction at very low rotation rate. The data presented up to this section has all been taken at $34\ \text{mm}$ radial position which happens to be at a neutral point along the channel, i.e. where the effect of the offset is zero. This same position is used for all subsequent measurements reported here.

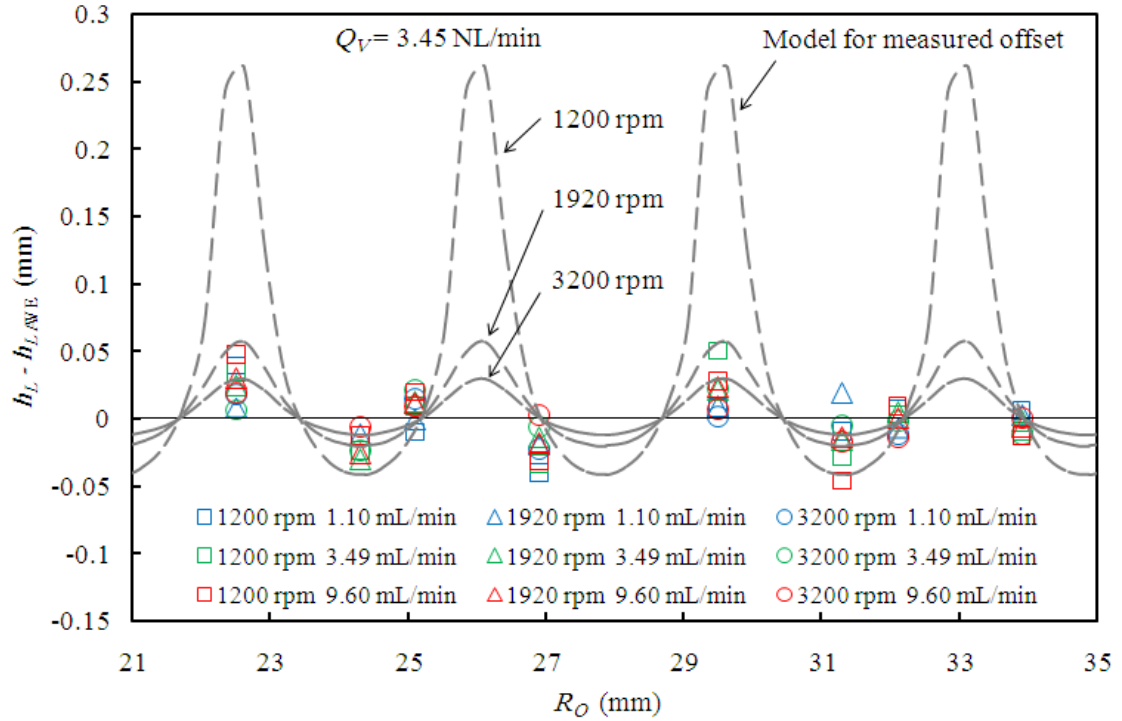


Figure 6.22: Liquid layer measurements (relative to the average) for range of rotation rate and range of liquid flow rate compared to the model results when offset is included.

6.3 Other phase systems

The current rotating spiral apparatus has been designed to suit the widest possible range of contacting system types. A theoretical study based on the wide channel model (MacInnes, 2014) has shown that, using a single device, this technique has the ability to handle the entire range of flow rate ratios and phase properties that may arise from all possible phase and solute systems, using simple changes in the operating conditions. Handling a range of flow rate ratios has been demonstrated in the proceeding tests where, for the air-water system, q ranged from 10^{-2} to 10^2 (the theoretical exploration suggests this can be extended to the much broader range of $10^{-4} < q < 10^4$). For gas-liquid contacting systems the liquid phase viscosity is the property having greatest influence. In this section the effect of viscosity in the range from about 1 to 100 cP is examined experimentally and compared with wide channel model prediction. Also one case of

liquid-liquid contacting is demonstrated, thus introducing a far greater variation in both the density ratio and viscosity ratio of the contacting phases.

6.3.1 Viscous liquids and air

Viscous liquids are common and here two examples are considered. Glycerol-water mixtures will be used to give a range of liquid viscosities by adjusting the amount of glycerol in the mixture. Additionally, an ionic liquid ([Emim] [EtSO₄]) is tested. Ionic liquids are of increasing interest due to their widely adjustable properties and commonly they have viscosities from around 10 to 1000 cP at 20°C (Marsh et al., 2004, Karadas et al., 2010).

6.3.1.1 Glycerol solutions

The glycerol-water solutions have been selected to cover a range of viscosity since they are easily available in the laboratory and safe to deal with. Two concentrations have been prepared 60% and 88% by mass. The viscosity of these solutions were measured using a capillary method (5.49×10^{-3} Pa s and 6.2×10^{-2} Pa s respectively at 20°C) higher than the viscosity of water by ten times for 60% and hundred times for 88% (Weast, 2003). Viscosity values used in the model comparison are estimates based on measurements at lab temperature (28°C for glycerol mixtures and at 23°C for the ionic liquid [Emim] [EtSO₄]). The syringe pump procedure described previously was followed; the flow rates selected from Table 4.1 presented in chapter 4 and several different sizes of syringe were used to span required flow rate ranges. Running such viscous liquids required significant time before recording data to allow the liquid layer to settle down to its steady state thickness. The waiting time was determined by taking an image every two minutes and checking the resulting series of photos to detect the point at which change could no longer be detected. Increasing or decreasing the liquid flow rate required the same procedure, where in some cases taking one point of

measurement of liquid layer thickness required waiting for more than one hour, e.g. for thin layers of 88% glycerol.

Figure 6.23 shows the liquid layer measurements for glycerol solutions compared to the wide channel model where good agreement with the model has again been obtained. At a given flow rate, it can be seen that increasing the viscosity increases the liquid layer thickness. Since the rotation rate and radial position are constant and the liquid density is nearly constant, the centrifugal body force is the same for the results shown. Consequently the countering force from shear stress at the channel wall must also remain approximately the same. Since the shear stress force is proportional to viscosity and the inverse layer thickness squared (at constant liquid flow rate) and the centrifugal force is proportional to the layer thickness, it follows that the layer thickness should increase as the one third power of the viscosity. Thus the approximate factor of one hundred in viscosity between water and the 88% Glycerol solution is expected to give about a five-fold increase in layer thickness, which is just about what is observed. The figure also presents some repeated measurements to confirm that waiting longer time to allow the liquid layer to settle does not change the results.

Only three points were obtained using [Emim] [EtSO₄] as there was only a limited quantity available. These results along with the water results show a consistent relationship with the model prediction over the entire range of viscosity. Agreement is good for large layer thickness with the experimental layers falling away from the model prediction beginning at about 60 μm thickness. The logarithmic flow rate scale is necessary to present on the same plot the factor of one thousand range in flow rates represented. Clearly, a flow rate penalty accompanies high liquid viscosity and this can only be altered by either increasing temperature to reduce the viscosity or by increasing the centrifugal driving force (either by increasing spiral angle or rotation rate).

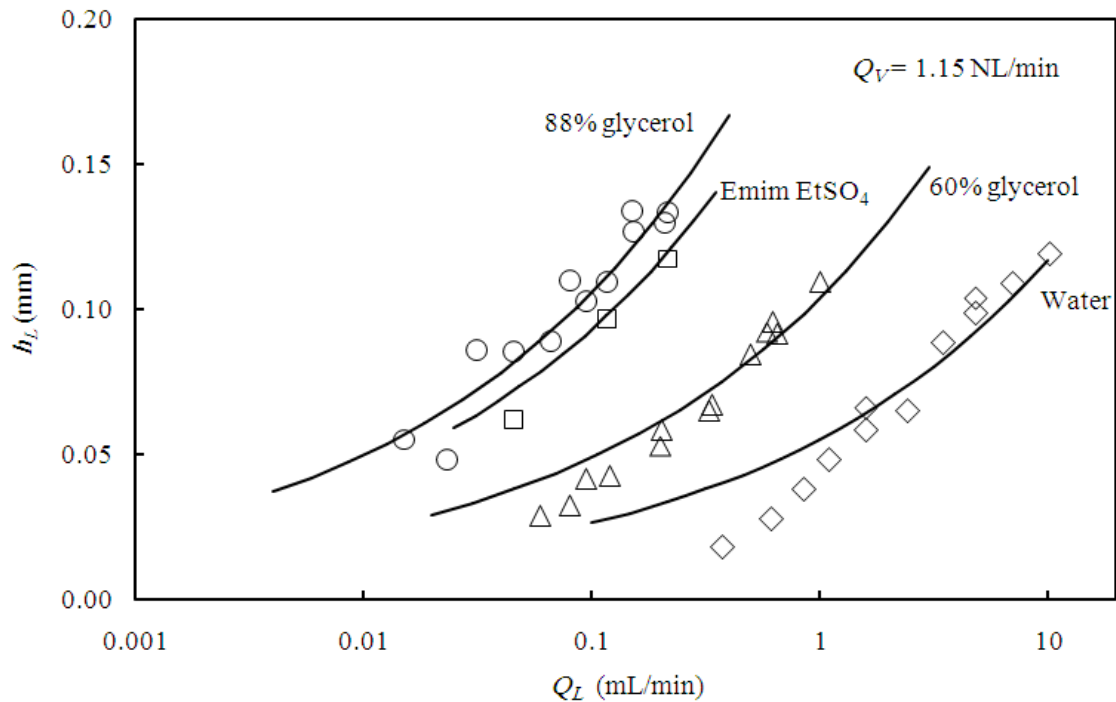


Figure 6.23: Liquid layer measurements for viscous liquids and water contacting with air and compared to the wide channel model. Conditions are: $Q_V = 1.15$ NL/min, 3200 rpm, and $P_s = 1.81$ bar absolute.

6.3.2 A liquid-liquid system

After the promising results obtained from the experiments performed on gas-liquid systems, it was decided to test the device with a liquid-liquid system. MacInnes et al. (2012) stated in a theoretical study the expectation that it is possible to use the same spiral channel for both liquid-liquid and gas-liquid systems. Because the spiral channel has been designed for gas-liquid contact system, however, the heavy-phase inlet has been designed with thin layers in mind and the typical situation of layers of similar thickness that are optimum for liquid-liquid contacting cannot be achieved. It was found using the wide channel model that using a light phase liquid that was about ten times more viscous than the heavy liquid would allow convenient operation with a thin heavy phase liquid layer. Octanol contacting with water produced a suitable immiscible pair of

liquids. The tests were performed using syringe pumps for both liquids, with the octanol flow rate fixed ($Q_v = 0.23$ mL/min) and a range of water flow rate used. Photos for the liquid layer could be analysed in the same way as for the gas-liquid systems, although since the refractive index of the octanol is much larger than that of air, and larger than that of water, refracted light passed much more intensely through the interface. This meant that no point of critical refraction was present and also that it was not possible to detect the contact line of the meniscus. The reflection of the corner was still present and the interface model could be used as before to determine minimum layer thickness from the measured corner position. The results of the measurements of the liquid layer thickness are shown with corresponding wide-channel model prediction in Figure 6.24. They show similar agreement between the model and experiment to the results obtained the gas-liquid tests (see figures in section 6.1). That is, agreement is better for thicker heavy phase layer, falling increasingly below the model as layer thickness decreases.

Figure 6.25 shows the image on which the measurements are based. The layer (corner reflection) can be seen but the meniscus contact line on the glass is indistinct and cannot be seen well or measured.

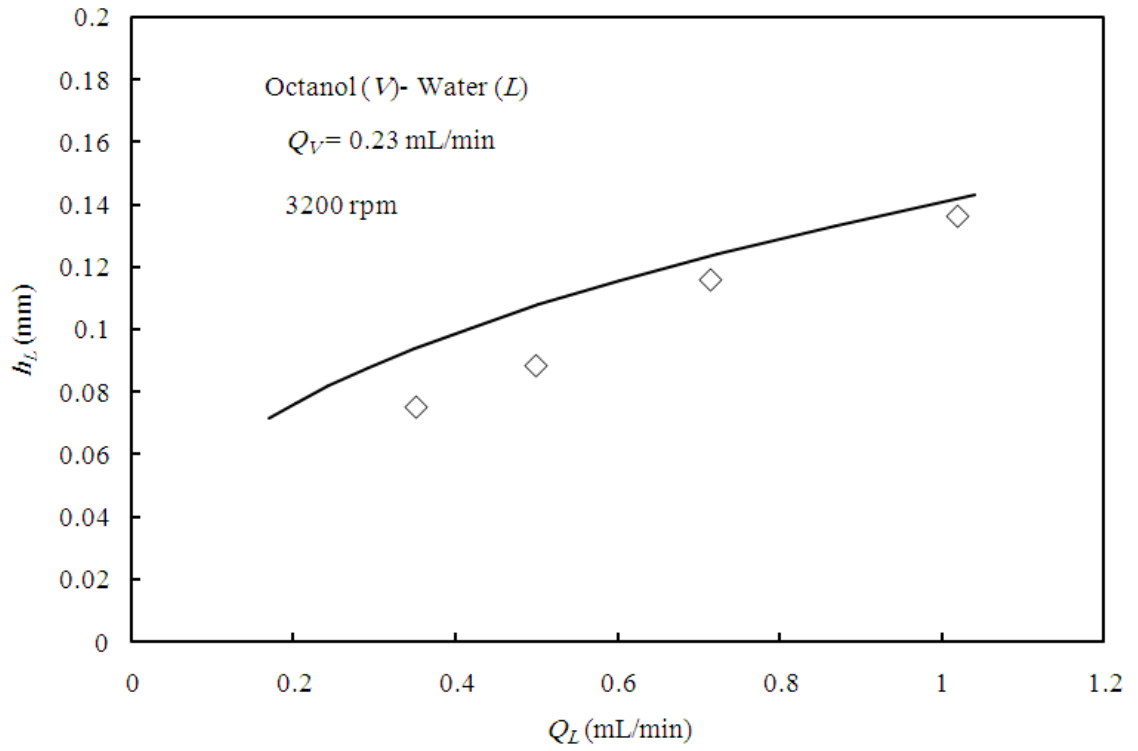


Figure 6.24: Liquid layer measurements compared to the wide channel model for octanol-water contact system. Conditions include a range of water flow rate but fixed octanol flow rate ($Q_V = 0.23$ mL/min); all are at a rotation rate of 3200 rpm.

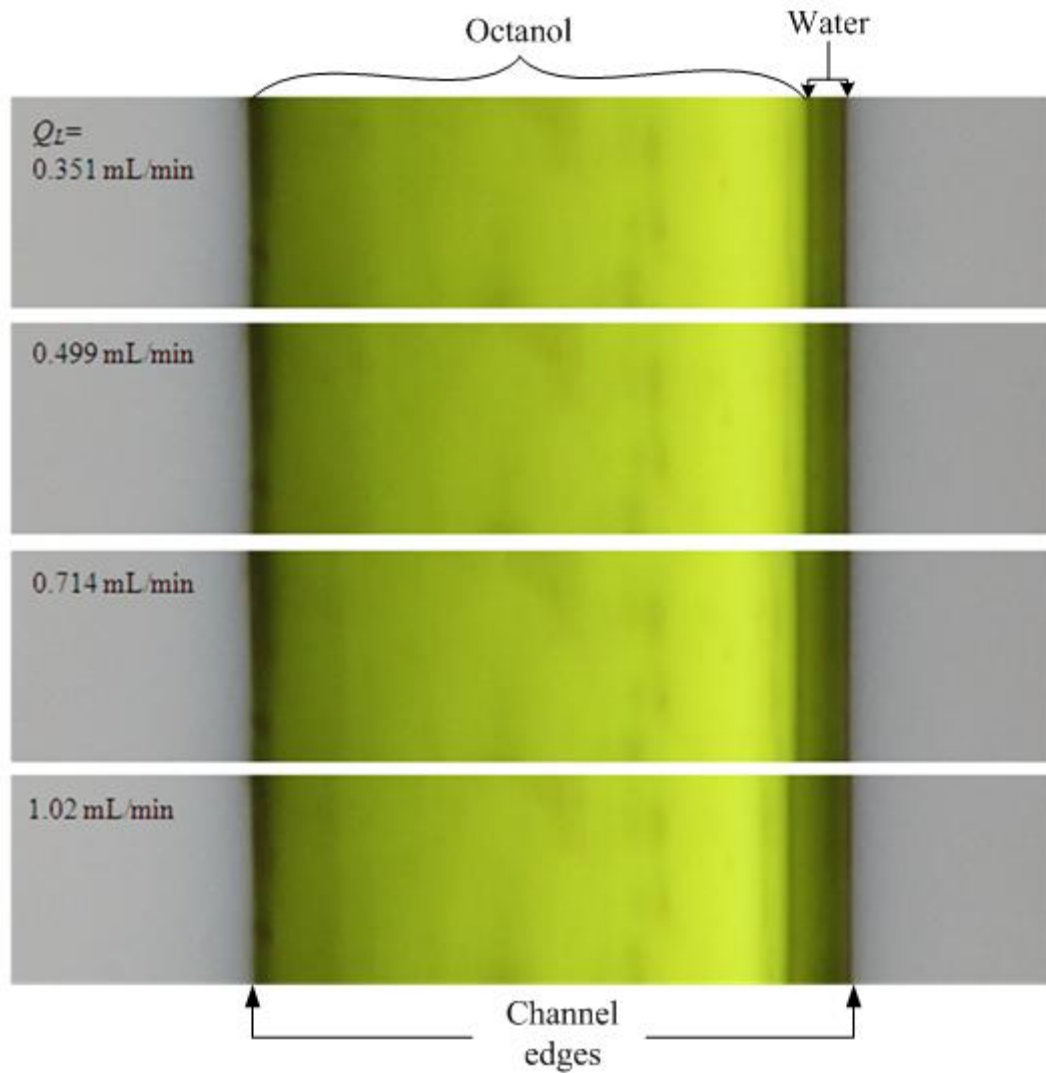


Figure 6.25: Liquid layer thickness variation with water flow rate for water-octanol contact system. Conditions are as for Figure 6.24.

Chapter 7

7. Conclusion

Continuous counter-current flow in a rotating spiral prototype device has been achieved and investigated. The work in this research started with a theoretical study of the wide channel model. The model has both revealed the important characteristics of spiral channel design and shown the expected behaviour for a wide range of operating conditions. The rotating spiral apparatus was designed, developed and tested for different operating conditions and different phase systems in the course of the research.

7.1 Tests conducted

The apparatus has shown the ability of a rotating spiral channel to handle a wide range of operating conditions. Experiments using the air-water system were conducted over a range of liquid flow rate, vapour flow rate, rotation rate and spiral pressure. Also, liquid viscosity, which is the most significant phase property affecting flow, has been varied by orders of magnitude by using alternative liquids to water, including the ionic liquid [Emim][EtSO₄] and glycerol solutions. In all cases measurements of flow rates, spiral temperature and spiral pressure were recorded and measurements of the minimum liquid layer thickness and the meniscus height were performed and compared to the wide channel model prediction. Finally, measurements of the minimum liquid layer thickness at different positions along the spiral channel, hence at different radial positions, for the air-water system were performed and compared to the wide channel model prediction.

7.2 General behaviour

The results of the measurements of minimum liquid layer thickness were as expected from the theory where increasing either the liquid or vapour flow rate leads to increasing the layer thickness. This increase was most noticeable in case of varying the liquid flow rate with generally small effect due to changes in vapour flow rate. Increasing the rotation rate causes the liquid layer thickness to decrease because the corresponding increase in centrifugal body force leads to a thinner layer to produce the required increase in shear stress. With regard to the meniscus height, increasing both the rotation rate and the radial position leads to a decrease in the height of the meniscus. A slight effect was observed from varying the spiral pressure where increasing the pressure in spiral led to slight decrease in the liquid layer thickness for fixed gas and liquid flow rates. In the theoretical study it was assumed that 100 μm was practically the minimum liquid layer thickness but liquid layer thicknesses as small as 17 μm were recorded. The repeatability of the data collected was confirmed when running the experiments both by increasing and decreasing the flow rate and by taking data at the same conditions on two separate occasions. Further, the entire collection of data displayed consistent and explainable behaviour in relation to the wide channel model prediction.

7.3 Wide channel model prediction

The wide channel model gives an accurate prediction of the experiments layer thickness for thick liquid layers and small meniscus size. In other words, the results of the comparison between the predictions of liquid layer thickness using the wide channel model and the actual experimental measurements for all experiments has shown good agreement at high flow rates and high rotation rates. Less good agreement with the model is found at low liquid flow rate for all experiments. To demonstrate the influence of meniscus size, a water experiment was repeated by using a surfactant solution. A clear increase in the liquid layer thickness was observed as expected, since the surfactant reduces surface tension and hence meniscus height so some of the liquid flowing in the channel end regions under the menisci is forced to flow in the central layer region

thereby causing the liquid layer thickness to increase. Thus the disagreement with the model was due to the formation of meniscus regions at the end walls of the channel. The wide channel model considers an infinite-width channel while the results obtained experimentally are for a finite channel width. It is possible to extend the model to account for the experimental effects due to the end walls, but this requires numerical solution and considerable effort. The wide channel model has captured all of the trends in the data and predicts the experimental data well provided the ratio between meniscus height and liquid layer thickness is small ($h_m/h_L \ll 1$). Regarding the radial position a systematic variation in the liquid layer thickness was observed and the investigation of this issue has shown that the spiral element was misaligned from the rotation axis by 304 μm in the direction $\theta = 174^\circ$. Putting all the data obtained from the tests at different radial positions together on one plot and comparing them to the wide channel model taking into account the offset geometry showed the measured variation in layer thickness correlated with the variations predicted by the model.

7.4 Future work

The design and performance of the rotating spiral device presented in this research has shown a successful continuous counter-current flow in the spiral channel with a high level of control the flow and the ability to produce a very thin and uniform liquid layer. For the same device there is much additional experimental work, modelling analysis and device development that can be carried out.

7.4.1 Experimental work

A wide range of experiments can be performed for different phase and solute systems using the same apparatus including absorption, desorption, and extraction. The results of the liquid layer measurements along the spiral have shown a varied thickness along the channel due to the misalignment of the spiral element from the rotation axis. To ensure

good results for mass transfer experiments some work on the spiral element alignment is required. As well as running such experiments, the installation of equipment for concentration measurements at the inlets and outlets is needed. The design of this apparatus was based on assumed values of the stability parameters, thus experiments to investigate and identify the true stability limits are required. The existing spiral element was designed to suit gas-liquid contacting, so running experiments with liquid-liquid systems will require some changes to the spiral channel. These changes include different design to the heavy phase inlet (to produce a thicker layer) and longer channel to ensure a high level of purification. Finally, running such experiments will require adding instruments of concentration measurements at the inlets and outlets of the phases.

7.4.2 Different applications

Rotating spiral contacting technology was demonstrated experimentally by MacInnes et al. (2010) by producing a successful counter-current flow for gas-liquid contacting in a rotating spiral channel to produce multistage distillation. Now with this device that produces a continuous counter-current flow, experiments of continuous distillation can be performed. The design of the spiral channel will need to include heating and cooling processes and, thus, instrumentation to control and measure the temperature long the spiral channel is essential. Also, experiments including reactions in the rotating spiral channel can be performed. The current work has been entirely in the laminar flow region, which requires millimetre-size channels and consequently low flow rate per channel. An avenue of investigation that may open the technology to higher flow rates is operation in the turbulent flow regime, although it is not clear whether the layer flow can continue to be controlled. In this case a theoretical analysis using turbulence modelling with the wide channel assumption would be needed to develop a prediction of mass transfer coefficients and the relation between flow rates, rotation rates and layer thicknesses.

7.4.3 Device development

The present work lays the foundation for application of rotating spiral contacting and there remain many directions to explore and technical to be improved. The high level of control of the phase layers and the interface regardless of phase and solute properties has been demonstrated. Some of the main challenges that now need to be addressed are as follows:

1- Instrumentation: potentially the device can be automated to allow computer control and optimisation during operation. The addition of control valves, flow controllers and digital instrumentation would allow adjustment of rotation rate and flow rates to give exactly the target purification at lowest energy input. Also, with computer control the device could adapt seamlessly to changes in inlet compositions or changes in the phase and solute system being processed with the same device.

2- Increasing the throughput: the description of the apparatus design in chapter 4 has shown a glass window was fixed on the spiral element. The aim of glass window was just to take photos in order to measure the thickness of liquid layer which was achieved successfully. Now there is no need to take photos as we know there is a layer and how thick it is from the operating conditions and thus replacing the glass window with a stack of spiral elements (Figure 7.1) can be used to increase the throughput. Stacking, for example, 25 channels would give a convenient unit handling up to 1 tonne/day. In this case development of liquid inlet orifices that allow uniform distribution of flow to all channels in the stack is needed. It can be noted that the liquid level in the reservoir will move in radially as one moves down the stack and this variation will need to be accommodated in the design.

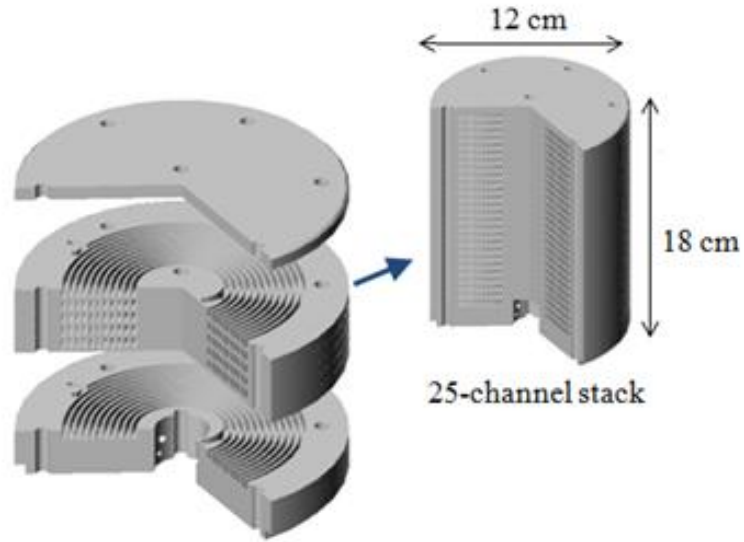


Figure 7.1: Stacking of channels to increase the throughput.

3- Seals: even though the rotating seal has done the job properly, it has some drawbacks that may be unacceptable. These include heat generation, energy dissipation, blockage due debris from normal seal wear and, perhaps most importantly, seal life. It is not clear how long seals can be made to last, but subsequent to this work the seals failed after a total of 325 hours of operation. Based on automotive experience, seal life of around 2000 hours may be considered typical of well-engineered surfaces and seals. For continuously operating equipment this represents only about 3 months and seal replacement would be required four times a year. It is possible to run a rotating spiral with no seals at all and this route would appear to be important for production processing applications and needs to be developed.

References

- AKITA, K. & YOSHIDA, F. 1974. Bubble Size, Interfacial Area, and Liquid-Phase Mass Transfer Coefficient in Bubble Columns. *Industrial & Engineering Chemistry Process Design and Development*, 13, 84-91.
- AL-ASWAD, K. K. M. 1982. *Liquid-liquid extraction in a pilot scale Rotating Disk Contactor*. PhD, ASTON.
- ARAVAMUDAN, K. 1995. *Back-mixing Studies in the Presence of an Unstable Density Gradient in a Reciprocating Plate Extraction Column*. Thesis, McMaster University.
- BARSON, N. & BEYER, G. H. 1953. CHARACTERISTICS OF A PODBIELNIAK CENTRIFUGAL EXTRACTOR. *Chemical Engineering Progress*, 49, 243-252.
- BOODHOO, K. V. K. & Al-Hengari, S. R. 2012. Micromixing Characteristics in a Small-Scale Spinning Disk Reactor. *CEAT Chemical Engineering & Technology*, 35, 1229-1237.
- BURNS, J. R., JAMIL, J. N. & RAMSHAW, C. 2000. Process intensification: operating characteristics of rotating packed beds - determination of liquid hold-up for a high-voidage structured packing. *Chemical Engineering Science*, 55, 2401-2415.
- CARVALHO, J. R. F. G. & COSTA, J. M. C. P. 2006. Effect of gas density on countercurrent flow limitation in wetted wall column. *AIChE Journal*, 52, 3375-3382.
- CASIMIR, D. J. & CRAIG., A. J. 1990. *Engineering and Food*, vol. 3, 106 -117.
- CAZES, J. 2004. *Encyclopedia of Chromatography 2004 Update Supplement*. Hoboken: Taylor & Francis.

- CHANDRA, A., GOSWAMI, P. S. & RAO, D. P. 2005. Characteristics of Flow in a Rotating Packed Bed (HIGEE) with Split Packing. *Industrial & Engineering Chemistry Research*, 44, 4051-4060.
- COULSON, J. M., F., R. J. & H., H. J. 2002a. *practical technology and separation processes*, Oxford, Butterworth-Heinemann.
- COULSON, J. M., RICHARDSON, J. F., BACKHURST, J. R. & HARKER, J. H. 2002b. *Particle Technology and Separation Processes*, Pergamon Press.
- COULSON, J. M., RICHARDSON, J. F., BACKHURST, J. R. & HARKER, J. H. 2003. *Fluid flow, heat transfer, and mass transfer*, Bath, UK, The Bath Press.
- COULSON, J. M. S. R. K. 1991. *introduction to chemical engineering design*, Oxford; Frankfurt, Pergamon Pr.
- DOBIE, C. G., MARIJAVICEVIC & BOODHOO, K. V. K. 2013. An evaluation of the effectiveness of continuous thin film processing in a spinning disc reactor for bulk free-radical photo-copolymerisation. *Chemical Engineering and Processing: Process Intensification*, 71, 97-106.
- GILLILAND, E. R. S. T. K. 1934. Diffusion of Vapors into Air Streams. *Ind. Eng. Chem. Industrial & Engineering Chemistry*, 26, 516-523.
- GUO, K., GUO, F., FENG, Y., CHEN, J., ZHENG, C. & GARDNER, N. C. 2000. Synchronous visual and RTD study on liquid flow in rotating packed-bed contactor. *Chemical Engineering Science*, 55, 1699-1706.
- HETHERINGTON, P. 2006. *Process intensification : a study of calcium carbonate precipitation methods on a spinning disc reactor*. University of Newcastle upon Tyne.
- HUFFMAN, J. R. & UREY, H. C. 1937. Separation of Oxygen Isotopes by a Fractionating Column. *Industrial & Engineering Chemistry*, 29, 531-535.

HUGHMARK, G. A. 1980. Mass Transfer and Flooding in Wetted-Wall and Packed Columns. *Industrial & Engineering Chemistry Fundamentals*, 19, 385-389.

HUNTER, R. J. 1989. *Foundations of colloid science* Oxford, Clarendon Pr.

INTERNET-1

https://www.google.co.uk/search?q=rotating+disk+contactor&espv=2&biw=1366&bih=667&tbm=isch&imgil=fPrhahZsP1O1rM%253A%253BfDLSRUVzXae3oM%253Bhttp%25253A%#tbm=isch&q=rotating+paked+bed&facrc=&imgdi=i=&imgrc=bntrqZnJkN4NxM%253A%3BEKwA1o_v7SJztM%3Bhttp%253A%252F%252Fwww.fvt.bci.tu-dortmund.de%252Fcms%252F. *Google Images*, accessed on 15/04/2014.

INTERNET-2

<https://www.google.co.uk/search?q=rotating+disk+contactor&espv=2&biw=1366&bih=667&tbm=isch&imgil=fPrhahZsP1O1rM%253A%253BfDLSRUVzXae3oM%253Bhttp%25253A%252F%252Fwww.fvt.bci.tu-dortmund.de%252Fcms%252F>. *Google Images*, accessed on 26/04/2014.

INTERNET-3

<https://www.google.co.uk/search?q=karr+reciprocating+plate+extraction+column&espv=2&biw=1366&bih=667&source=lnms&tbm=isch&sa=X&ei=bh4YVJyzD8GI7AaWmoHAAw&ved=>. *Google Images*, accessed on 20/04/2014.

ITO, Y. 1980. Toroidal coil planet centrifuge for counter-current chromatography. *Journal of Chromatography A*, 192, 75-87.

ITO, Y. 2005. Golden rules and pitfalls in selecting optimum conditions for high-speed counter-current chromatography. *Journal of Chromatography A*, 1065, 145-168.

ITO, Y. & BOWMAN, R. L. 1977. Horizontal flow-through coil planet centrifuge without rotating seals. *Analytical Biochemistry*, 82, 63-68.

JACOBSEN, F. M. & BEYER, G. H. 1956. OPERATING CHARACTERISTICS OF A CENTRIFUGAL EXTRACTOR. *Aiche Journal*, 2, 283-289.

- JASSIM, M. S., ROCHELLE, G., EIMER, D. & RAMSHAW, C. 2007. Carbon Dioxide Absorption and Desorption in Aqueous Monoethanolamine Solutions in a Rotating Packed Bed. *Industrial & Engineering Chemistry Research*, 46, 2823-2833.
- JERZY, M. 2010. *Fluid Dynamics of Packed Columns*, Berlin Heidelberg, Springer-Verlag.
- KAFAROV, V. V. & ALEKSANDROVSKII, A. A. 1965. Mass transfer in rotating-disk contactors. *Chemical and Petroleum Engineering*, 1, 23-29.
- KAISER, H. R. 1965. Advances in centrifugal extraction. *Chemical Engineering Progress*, 65, 69-73.
- KARADAS, F., ATILHAN, M. & APARICIO, S. 2010. Review on the Use of Ionic Liquids (ILs) as Alternative Fluids for CO₂ Capture and Natural Gas Sweetening. *Energy & Fuels*, 24, 5817-5828.
- KELLEHER, T. & FAIR, J. R. 1996. Distillation studies in a high-gravity contactor. *Industrial & Engineering Chemistry Research*, 35, 4646-4655.
- KEYVANI, M. 1989. OPERATING CHARACTERISTICS OF ROTATING BEDS. *Chemical Engineering Progress*, 85, 48-52.
- KNIGHT, M., FINN, T. M., ZEHMER, J., CLAYTON, A. & PILON, A. 2011. Spiral counter-current chromatography of small molecules, peptides and proteins using the spiral tubing support rotor. *Journal of Chromatography A*, 1218, 6148-6155.
- KOHL, A. L. N. R. 1997. *Gas purification* [Online]. Houston, Tex.: Gulf Pub. Available: <http://public.ebib.com/choice/publicfullrecord.aspx?p=404356> [Accessed].
- MACINNES, J. M. 2005. Fluid Film Stability in a Spinning Micro-Channel Multiphase Contactor. *7th World Congress of Chemical Engineering*. Glasgow.

- MACINNES, J. M. 2014. Prototype Channel Design Operation range for Rotating Spiral Phase Contacting. *To be submitted*.
- MACINNES, J. M., ORTIZ-OSORIO, J., JORDAN, P. J., PRIESTMAN, G. H. & ALLEN, R. W. K. 2010. Experimental demonstration of rotating spiral microchannel distillation. *Chemical Engineering Journal*, 159, 159-169.
- MACINNES, J. M., PITT, M. J., PRIESTMAN, G. H. & ALLEN, R. W. K. 2012. Analysis of two-phase contacting in a rotating spiral channel. *Chemical Engineering Science*, 69, 304-315.
- MACINNES, J. M. & ZAMBRI, M., K. 2014. Hydrodynamic Characteristics of a Rotating Spiral Fluid-Phase Contactor. *Submitted to Chemical Engineering Science, Sept. 2014*.
- MAKARYTCHEV, S. V., LANGRISH, T. A. G. & FLETCHER, D. F. 2004. Mass Transfer Analysis of Spinning Cone Columns Using CFD. *Chemical Engineering Research and Design*, 82, 752-761.
- MAKARYTCHEV, S. V., LANGRISH, T. A. G. & FLETCHER, D. F. 2005. Exploration of Spinning Cone Column Capacity and Mass Transfer Performance Using CFD. *Chemical Engineering Research and Design*, 83, 1372-1380.
- MAKARYTCHEV, S. V., LANGRISH, T. A. G. & PRINCE, R. G. H. 1998. Structure and regimes of liquid film flow in spinning cone columns. *Chemical Engineering Science*, 53, 1541-1550.
- MARSH, K. N., BOXALL, J. A. & LICHTENTHALER, R. 2004. Room temperature ionic liquids and their mixtures—a review. *Fluid Phase Equilibria*, 219, 93-98.
- MCCABE, W. L., SMITH, J. C. & HARRIOTT, P. 1985. *Unit Operations of Chemical Engineering*, McGraw-Hill.
- MCCABE, W. L. S. J. C. 1985. *Unit operations of chemical engineering*, New York, McGraw-Hill.

- MEEUWSE, M. 2011. *Rotor-stator Spinning Disc Reactor*, Eindhoven University of Technology.
- MEEUWSE, M., HAMMING, E., VAN DER SCHAAF, J. & SCHOUTEN, J. C. 2011. Effect of rotor–stator distance and rotor radius on the rate of gas–liquid mass transfer in a rotor–stator spinning disc reactor. *Chemical Engineering and Processing: Process Intensification*, 50, 1095-1107.
- MEEUWSE, M., VAN DER SCHAAF, J., KUSTER, B. F. M. & SCHOUTEN, J. C. 2010. Gas–liquid mass transfer in a rotor–stator spinning disc reactor. *Chemical Engineering Science*, 65, 466-471.
- MUNJAL, S., DUDUKOVIC, M. P. & RAMACHANDRAN, P. 1989. MASS-TRANSFER IN ROTATING PACKED-BEDS .2. EXPERIMENTAL RESULTS AND COMPARISON WITH THEORY AND GRAVITY FLOW. *Chemical Engineering Science*, 44, 2257-2268.
- MUROYAMA, K., IMAI, K., OKA, Y. & HAYASHI, J. I. 2013. Mass transfer properties in a bubble column associated with micro-bubble dispersions. *Chemical Engineering Science*, 100, 464-473.
- OCHOWIAK, M. & BRONIARZ-PRESS, L. 2011. The flow resistance and aeration in modified spray tower. *Chemical Engineering and Processing: Process Intensification*, 50, 345-350.
- ORTIZ-OSORIO, J., MACINNES, J. M., PRIESTMAN, G. H. & ALLEN, R. W. K. 2009. computations of mass transfer for rotating spiral microchannel distillation. *World congress of Chemical engineering*. Montreal, Canada.
- PARKER HANNIFIN 2006. Rotary Seal Design Guide. *Catalog EPS 5350/USA*.
- PODBIELNIAK, W. 1941. Apparatus and Methods for Precise Fractional-Distillation Analysis: New Design of Adiabatic Fractioning Column and Precision-Spaced Wire Packing for Temperature Range- 190* to 300* C. *Ind. Eng. Chem. Anal. Ed. Industrial & Engineering Chemistry Analytical Edition*, 13, 639-645.

- PODBIELNIAK., W. J. 1935. CENTRIFUGAL FRACTIONATING METHOD AND APPARATUS. *United State Patent Office*, Chigaco, III, CI. 198-202.
- PODBIELNIAK., W. J. 1937. Method and Apprartus of Refining Hydrocarbon Oil. *United State Patent Office*, Chigaco III, CI. 196-40.
- PODBIELNIAK., W. J. 1938. APPARATUS FOR EFFECTINGJCOUNTER CURRENT CONTACT BETWEEN FLUIDS. *United State Patent Office*, Chigaco III, CI. 261-83.
- RAO, D. P., BHOWAL, A. & GOSWAMI, P. S. 2004. Process Intensification in Rotating Packed Beds (HIGEE): An Appraisal. *Industrial & Engineering Chemistry Research*, 43, 1150-1162.
- REISS, L. P. 1967. Cocurrent Gas-Liquid Contacting in Packed Columns. *Industrial & Engineering Chemistry Process Design and Development*, 6, 486-499.
- ROBERSON, J. A. C. C. T. 1997. *Engineering fluid mechanics*, New York, J. Wiley & Sons.
- SHERWOOD, T. K., EVANS, J. E. & LONGCOR, J. V. A. 1939. Extraction in Spray and Packed Columns. *Industrial & Engineering Chemistry*, 31, 1144-1150.
- SHERWOOD, T. K., PIGFORD, R. L. & WILKE, C. R. 1975. *Mass transfer*, New York, McGraw-Hill.
- SMITH, K. H., BOWSER, T. & STEVENS, G. W. 2008. Performance and Scale-up of Karr Reciprocating Plate Extraction Columns. *Industrial & Engineering Chemistry Research*, 47, 8368-8375.
- STELLA, A., MENSFORTH, K. H., BOWSER, T., STEVENS, G. W. & PRATT, H. R. C. 2008. Mass Transfer Performance in Karr Reciprocating Plate Extraction Columns. *Industrial & Engineering Chemistry Research*, 47, 3996-4007.

- STRAND, C. P., OLNEY, R. B. & ACKERMAN, G. H. 1962. FUNDAMENTAL ASPECTS OF ROTATING DISK CONTACTOR PERFORMANCE. *Aiche Journal*, 8, 252-261.
- SUMNER, A. L., MENKE, E. J., DUBOWSKI, Y., NEWBERG, J. T., PENNER, R. M., HEMMINGER, J. C., WINGEN, L. M., BRAUERS, T. & FINLAYSON-PITTS, B. J. 2004. The nature of water on surfaces of laboratory systems and implications for heterogeneous chemistry in the troposphere. *Physical Chemistry Chemical Physics*, 6, 604-613.
- SUN, B.-C., WANG, X.-M., CHEN, J.-M., CHU, G.-W., CHEN, J.-F. & SHAO, L. 2009. Simultaneous Absorption of CO₂ and NH₃ into Water in a Rotating Packed Bed. *Industrial & Engineering Chemistry Research*, 48, 11175-11180.
- THORNTON, J. D. 1956. Spray liquid-liquid extraction columns : : Prediction of limiting holdup and flooding rates. *Chemical Engineering Science*, 5, 201-208.
- TONKOVICH, A. L., JAROSCH, K., ARORA, R., SILVA, L., PERRY, S., MCDANIEL, J., DALY, F. & LITT, B. 2008. Methanol production FPSO plant concept using multiple microchannel unit operations. *Chemical Engineering Journal*, 135, Supplement 1, S2-S8.
- TREYBAL, R. E. 1981a. *Mass-transfer operations*, Tokyo, McGraw-Hill International Book Company.
- TREYBAL, R. E. 1981b. *Mass Transfer Operation, International Operation*, McGraw-Hill.
- VERMIJS, H. J. A. & KRAMERS, H. 1954. Liquid-liquid extraction in a “rotating disc contactor”. *Chemical Engineering Science*, 3, 55-64.
- VIVIAN, J. E. B. P. L. T. K. V. J. 1965. The influence of gravitational force on gas absorption in a packed column. *AIC AIChE Journal*, 11, 1088-1091.

- WEAST, R. C. 2003. *CRC handbook of chemistry and physics*, Boca Raton, FL, CRC Press.
- WHITE, F. M. 1986. *Viscous fluid flow*, New York, McGraw-Hill.
- YANG, Y., GU, D., AISA, H. A. & ITO, Y. 2010a. Evaluation on the performance of four different column models mounted on the compact type-I coil planet centrifuge. *Journal of Chromatography A*, 1217, 7612-7615.
- YANG, Y., GU, D., LIU, Y., AISA, H. A. & ITO, Y. 2010b. Compact type-I coil planet centrifuge for counter-current chromatography. *Journal of Chromatography A*, 1217, 1313-1319.
- ZHANG, Y., KATO, S. & ANAZAWA, T. 2009. Vacuum membrane distillation on a microfluidic chip. *Chemical Communications*, 2750-2752.
- ZHAO, H., SHAO, L. & CHEN, J.-F. 2010. High-gravity process intensification technology and application. *Chemical Engineering Journal*, 156, 588-593.

Appendices

Appendix A

A. Counter Current Phase Contacting

In the separation methods the species have to diffuse from one phase into another phase, and the diffusion rates in both phases affect on the overall mass transfer. In some cases the mass transfer between phases become more complex because of the discontinuity at the interface due to the concentration or the mole fraction of the diffusing solute is barely ever the same on the other side of the interface. For example, in the absorption process it can be found that for a very soluble gas, the mole fraction in the dense phase at the interface would be higher than that in the gas side. Achieving a very thin layer is required to increase the diffusion rate which consequently leads to optimum throughput (Coulson et al., 2002a, McCabe, 1985, Treybal, 1981a). This chapter will present general model equations for counter current flow and discuss the issues affecting on the contacting performance.

A1 Equations for Bulk compositions

An efficient illustration of mass transfer in fluid phase contacting process depends on governing equations in terms of mass transfer coefficients and bulk phase quantities. It has been considered that the process of heat transfer has no significant effect on the transport of species and the scope here is limited to dilute contacting conditions. With regard to the cases that include a negligible rate of mass transfer or where the energy can be changed within the interface a relative simplified analysis can be performed.

Generally other cases also can be considered using the same procedure of analysis has been used in this general model following similar simplifications.

Thus in both cases where the mass transfer rate is negligible or in cases of involving a dilute solute concentrations these simplification are applied. Due to this study is related to the counter-current flow for two immiscible fluids, subscripts V and L will be used to refer to the light phase and heavy phase respectively as one of these simplifications. Also, it has been considered that the flow rate in each phase will not be changed within the passage and the estimation related to mass transfer performance needs to focus on the bulk equations that describe the change in concentration in both cases along the passage.

It does not matter the type of contacting either gas-liquid contacting or liquid-liquid contacting the expressions in terms of the mole fractions in the bulk, molar densities, bulk velocities, and the fraction of liquid layer across the passage occupied by the heavy phase, ξ , can conservative. Consequently, the fluid phase contacting of two phases dominated by differential equations for the change with the flow direction in both the light phase and heavy phase (Y_{VB} and Y_{LB} respectively) (Sherwood et al., 1975, McCabe, 1985, Treybal, 1981a):

$$\text{Light (vapour) phase:} \quad n_V u_{VB} (1 - \xi) \frac{dY_{VB}}{ds} = -k_V a (Y_{VB} - Y_{VI}) \quad (\text{A.1})$$

$$\text{Heavy (liquid) phase:} \quad n_L u_{LB} \xi \frac{dY_{LB}}{ds} = k_L a (Y_{LI} - Y_{LB}) \quad (\text{A.2})$$

The above equations are generally applicable to any kind of processes of contacting including falling film, packed bed, etc where:

n_V, n_L is molar density for light and heavy phase

u_{VB}, u_{LB} the average bulk velocities

k_V, k_L are the mass transfer coefficients

In fluid phase contacting, the parameter a is defined as the interface area per unit flow passage volume.

Selecting the appropriate boundary conditions in the equations above (A.1 and A.2) and by knowing the values of mass transfer coefficients for both phases thus and along the contact direction the variation in mole fraction in each separate phase can be estimated. Consequently, the solute phase equilibrium and the mass balance can be enforced at the interface by the required boundary conditions, thus the interface balance can be defined as:

$$k_V (Y_{VB} - Y_{VI}) = k_L (Y_{LI} - Y_{LB}) \quad (\text{A.3})$$

And the interface equilibrium relation: $Y_{VI} = f(Y_{LI}) \quad (\text{A.4})$

In the usual way the coefficients of mass transfer have to be estimated using the experimental methods. Much straight forward now through the new technology based on rotating spiral channel where these coefficients can be calculated directly from the theoretical analysis presented in the wide channel model since the flow geometry in acceptable (MacInnes et al., 2012).

A2 Mass Transfer Coefficients

When the solute equilibrium concentrating in the two phases are approximately linear related over the length of one equilibrium stage, the overall coefficients K_V and K_L are related to the individual coefficients k_V and k_L and the local slope of the equilibrium curve: $f' = dY_V / dY_L$

$$\frac{1}{K_V} = \frac{1}{k_V} + \frac{f'}{k_L} \quad (\text{A.5})$$

$$\frac{1}{K_L} = \frac{1}{f'k_v} + \frac{1}{k_L} \quad (\text{A.6})$$

Taking in the account the overall bulk mole fraction differences in terms of either vapour or liquid phase quantities the overall mass transfer coefficients can be define as:

$$K_V (Y_{VB} - Y_{VB}^*) = k_V (Y_{VB} - Y_{VI}) \quad K_L (Y_{LB}^* - Y_{LB}) = k_L (Y_{LI} - Y_{LB}) \quad (\text{A.7})$$

Eq. (A.7) explains that using the overall mass transfer coefficients in the usual approach avoids the appearance of interface values, and the jump in concentration at the interface is considered in the account by using Y_{VB}^* and Y_{LB}^* instead of Y_{LI} and Y_{VB} , respectively. Y_{VB}^* is the vapour phase mole fraction that corresponds to equilibrium with the bulk liquid mole fraction, Y_{LB} and Y_{LB}^* the liquid phase mole fraction corresponds to equilibrium with the bulk vapour mole fraction, Y_{VB} .

A3 Mass Transfer Effectiveness

Measures of mass transfer effectiveness are based on the integration of the governing equations which lead to contacting distances required for a given degree of separation. These measures can also represent transfer associated just with the gas phase or liquid phase, or account for the overall effect of transfer in both phases. The two most common measures of the effectiveness are the length of one equilibrium stage ' ℓ_e ' and the length of a transfer unit ' H '. Each of these may be expressed using either gas or liquid phase quantities. Arguably, the equilibrium length is the length of contacting that giving an accurate effect of one stage of equilibrium between the phases.

The length of one equilibrium stage can be expressed in terms of bulk concentration in either vapour or liquid phase bulk mole fraction in terms of vapour coefficient the equilibrium stage length is (Sherwood et al., 1975, MacInnes et al., 2012):

$$\ell_e = - \int_{Y_V(0)}^{Y_V(\ell_e)} \frac{n_V u_V (1-\xi)}{K_V a} \frac{dY_V}{(1-Y_V)(Y_V - Y_V^*)} \quad (\text{A.8})$$

In this case $Y_V(\ell_e)$ corresponds to the vapour mole fraction at equilibrium with $Y_L(0)$. An analytical result for ℓ_e is obtained for the case of dilute concentrations and uniform K_V, K_L, n_V, u_V, a , and ξ over the stage length. This is given by Sherwood et al. (1975) as:

$$\ell_e = \frac{n_V u_V (1-\xi)}{K_V a} \frac{\ln(-f' q_n)}{1 + f' q_n} \quad (\text{A.9})$$

Where, q_n is molar flow rate ratio ($q_n = Q_V / Q_L$).

$$q_n = \frac{n_V u_{VB} (1-\xi)}{n_L u_{LB} \xi} \quad (\text{A.10})$$

The same result is obtained working in terms of liquid in mole fractions Eq. (A.8) since the equilibrium length is a unique physical parameter (Sherwood et al., 1975).

An alternative measure of contacting effectiveness, which is not unique in the same way, is the length of a transfer unit (commonly known as the height of a transfer unit, HTU) but here designated ' H '. This measure is thus somewhat arbitrary and is simply the leading factor of the integral:

$$H_{OV} \equiv - \frac{n_V u_V (1-\xi)}{K_V a} \quad (\text{A.11})$$

The HTU based on liquid phase properties is different by a factor of $-f' q_n$ from HTU based on vapour properties. The liquid-based HTU is given by:

$$H_{OL} \equiv \frac{n_L u_L \xi}{K_L a} = \frac{H_{OV}}{-f' q_n} \quad (\text{A.12})$$

In addition, individual length of transfer units for vapour and liquid can also be represented by the equations below. These may have use where one parameter dominates the mass transfer.

$$H_L = \frac{n_L u_L \xi}{k_L a} \quad (\text{A.13})$$

$$H_V = -\frac{n_V u_V (1 - \xi)}{k_V a} \quad (\text{A.14})$$

The abovementioned equations show that the height of a transfer unit depends on the liquid layer thickness, ξ , and the phase bulk velocity. These definitions together with Eq. (A.5) can be helpful in converting performance represented in terms of individual transfer units to overall transfer units:

$$H_{OV} = H_V - f' q_n H_L \quad (\text{A.15})$$

$$H_{OL} = \frac{-H_V}{f' q_n} + H_L \quad (\text{A.16})$$

Finally, it is sometimes necessary to convert between equilibrium stage length and HTU. Equations, (3.8), (3.15), and (3.16) give the conversion relation:

$$\ell_e = -H_{OV} \frac{\ln(-f' q_n)}{(1 + f' q_n)} = H_{OL} \frac{f' q_n \ln(-f' q_n)}{(1 + f' q_n)} \quad (\text{A.17})$$

Appendix B

Network Modelling

B 1 Developed flow in tube

It is necessary to determine the head loss, h_L , that occurs in the flow in each passage so that the energy equation can be used in the analysis of the flow network. The overall head loss along a given passage consists of the head loss due to viscous developed flow in straight passages which produce the ‘major’ loss, h_{maj} . In addition to this loss, other losses occur in various passage components which called minor losses, h_{min} , and the total loss is the combination of these:

$$h_L = h_{maj} + h_{min} \quad (\text{B.1})$$

B 1.1 Major losses

For developed flow there is a direct connection between the friction losses, the shear stress at the wall, τ_w , and this relation is expressed by the Darcy Weisbach equation in terms of the friction factor.

$$h_L = f \frac{L}{D} \frac{u^2}{2g} \quad (\text{B.2})$$

Where f is the Moody friction factor:

$$f \equiv \frac{8\tau_w}{\rho u^2} \quad (\text{B.3})$$

In order to determine the friction factor, dimensional analysis shows that the friction factor depends only on Reynolds number and a non-dimensional measure of wall roughness. In laminar flow the wall roughness has no effect and the dependency of friction factor on Reynolds number can be derived exactly as:

$$f = \frac{64}{\text{Re}} \quad (\text{B.4})$$
$$\text{Re} = \frac{\rho u D}{\mu}$$

On the other hand turbulent flow does depend on wall roughness and the relation in terms of Reynolds number and wall roughness, k , can be used (Roberson, 1997):

$$f = 0.25 / \left[\log \left(\frac{k/D}{3.7} + \frac{5.74}{\text{Re}^{0.9}} \right) \right]^2 \quad (\text{B.5})$$

B 1.2 Minor losses

The minor losses due to fittings and other flow disruption and transitions must be also included. The interruption of developed flow causes additional loss of energy and the relation for the minor losses associated with these components can be expressed in terms of loss coefficient, K_L , as:

$$h_L = K_L \frac{u^2}{2g} \quad (\text{B.6})$$

K_L , has a particular value for each component and these sums together with the major losses to form the total head loss:

$$h_L = \sum_i f_i \frac{L_i}{D_i} \frac{u_i^2}{2g} + \sum_j K_{L,j} \frac{u_j^2}{2g} \quad (\text{B.7})$$

Due to of lack information about the loss coefficient, K_L , for our design and considering sufficient scale of the network the term related to the minor loss in Eq. (B.7) may be ignored. Thus, the total head loss in the system can be calculated from Eq. (B.8) below:

$$h_L = \sum_i f_i \frac{L_i}{D_i} \frac{u_i^2}{2g} \quad (\text{B.8})$$

B 2 Energy equations

For a steady flow along a passage (non – rotating) the energy equation for single phase flow (gas or liquid) can be expressed as follows:

$$\Delta P + \rho g \Delta z + \frac{\rho}{2} \Delta(u^2) + \rho g h_L = 0 \quad (\text{B.9})$$

Equation (B.9) above shows that loss in pressure can occur due to three factors: elevation, Δz , change in velocity and the friction between the pipe's wall and fluid.

In general for the flow piping system design there are three calculation types encountered

- 1- Calculate the pressure drop, ΔP (or h_L) for given the length, L , diameter, D , and the velocity, u (or flow rate)
- 2- Calculate the velocity, u for given L , D and ΔP
- 3- Calculate the diameter, D for given L , ΔP and u

The first type of calculation can be solved directly using Moody equations above, but types 2 and 3 considered to be more common design problems, for example selection of pipe diameters to minimize the construction and pumping cost. However, iterative approach is required because both the velocity, u , and the diameter, D , are in the Reynolds number. This study focuses on the first type of calculations where the diameter, length and flow rate are known.

Rotating spiral flow system has different passages sections depends on the situation and the position of this part if it is static, rotating and elevated, so the energy equation for each part in the system may have extra terms not in the equation for other part.

The energy equation for single phase flow in rotating ducts (pipes) will be the same factors presented in Eq. B.9 in addition to new term known as centrifugal potential energy. This term has significant consequences for the operating pressure in the main spiral channel where increasing the pressure due to rotation overcomes the pressure loss due to friction.

$$\Delta P + \rho g \Delta Z - \frac{\rho}{2} \Omega^2 \Delta(r^2) + \frac{\rho}{2} \Delta(u^2) + \rho g h_L = 0 \quad (\text{B.10})$$

Where;

$$\Delta(r^2) = r_{out}^2 - r_{in}^2$$

These equations apply to single-phase flow in a passage. This then applies to all passages in the network (Figure 4.12) apart from the spiral channel.

B 3 Phase properties in the spiral channel

It is clear that changes in pressure along the gas passages leads to changes in the gas density. Temperature also affects the fluid properties: the density of the gas and the viscosity of the liquid. Gas density will depend on local temperature and pressure through the ideal gas law.

$$\rho_s = \frac{P_s M_{wt}}{RT_s} \quad (\text{B.11})$$

Where;

ρ_s the density in the spiral

P_s the average pressure in the spiral

T_s the temperature in the spiral

M_{wt} the molecular weight of vapour phase

Experimental work here generally uses water as the liquid. Liquid water density and viscosity variation with temperature will be determined from the empirical relations given by White, (1986) which are as follows (White, 1986):

$$\rho = 1000 - 0.0178|T - 277|^{1.7} \quad (\text{B.12})$$

$$\mu = \mu_o \exp \left\{ -1.704 - 5.306 \left(\frac{273}{T} \right) + 7.003 \left(\frac{273}{T} \right)^2 \right\} \quad (\text{B.13})$$

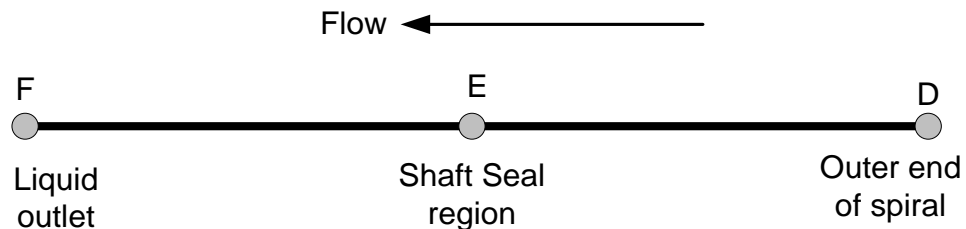
Temperature is in absolute SI units, K

B 4 Applications of network model

B 4.1 Pressure drop estimation

The explanation of how this model works uses the nomenclature presented in Figure 4.12. The procedure of determining the pressure at different positions throughout the flow system of rotating spiral apparatus will start from the liquid outlet (or vapour inlet where the pressure value set by the pressure regulator) to the outer end of the spiral. Pressure drop along the spiral channel can be determined relative to this pressure using the pressure gradient given by the wide channel model.

A part from the flow system (Figure 4.12) to be analyzed is specified in the diagram below:



Calculating the pressure drop in our flow system is a straight forward process following the energy equations presented above. For example, the segment E – F corresponds to

the tube that leads from the rotating seal region to the atmospheric liquid outlet where its length, diameter, and the elevation are known thus Eq. (B.9) can be used to calculate the pressure drop for this part of the system. The segment D – E is belongs to the rotating parts (shaft and spiral element passages) and different radial positions for the inlets and outlets; therefore Eq. (B.10) is suitable to find out the pressure drop in this section. Using similar procedure the pressure drop at all other segments can be found.

B 4.2 Spiral pressure and the selection of network tubing

For gas-liquid contact system the pressure drop within the spiral channel is considered to be small in comparison with the absolute pressure and as a result of this the pressure in the spiral channel can be assumed constant. For the purpose of this and to overcome the friction losses in the flow network tubing the liquid outlet passages have been selected carefully with suitable sizes (1/8" diameter) which allow them to serve as a manometer. As well as for the light phase and starting from the selected dimensions of the spiral channel (4.0 mm width and 1.5 mm height) where the majority ($\approx 90\%$) of the channel was occupied by the light phase the size of the network tubes has been selected to be 1/4" diameter.

Using the value of measured pressure at liquid outlet (P_F), the density of the liquid (ρ_L), the difference in elevation between the point F and the point at the liquid outlet reservoir in spiral channel (Δz), and the difference in radial positions (Δr) which consider the difference from the axis of rotation to the liquid outlet reservoir in spiral channel. From the fact that the losses from friction are negligible the pressure in spiral channel can be given as follows:

$$P_s = P_F + \frac{\rho_L \Omega^2}{2} \Delta(r^2) - \rho_L g \Delta z \quad (\text{B.14})$$

Where; $\Delta z = z_o - z_i$ and $\Delta(r^2) = r_o^2 - r_i^2$

B 4.3 Calculation example

The calculations in this example will present the values of pressure at each point in the flow system considering the schematic flow network presented in Figure 4.12. As well as, in this calculation the extremes flow rates will be used:

The volume flow rate of dense phase, $Q_L = 1.67 \times 10^{-7} \text{ m}^3/\text{s}$ (10 mL/min)

The volume flow rate of light phase, $Q_V = 1.67 \times 10^{-4} \text{ m}^3/\text{s}$ (10 NL/min)

The pressure drop along the spiral channel, $\Delta p_s = 6.214 \times 10^2 \text{ Pa}$

Assumptions:

- 1- The dense phase at point F in Figure 4.12 will be collect in reservoir at atmospheric pressure 1.0 bar.
- 2- All static tubes that connected to the device (L1, L4, V1, and V4) are horizontal and have the same length (1.0 m).
- 3- Constant flow rates within the system.

Following the general approach to calculate the pressure loss at each tube and hole using the energy equations presented in this appendix and the nomenclature in Figure 4.12 starting from point F where the pressure is known, $P_F = 1.0 \text{ bar}$.

The flow system will be divided into two sections depending on the segment in the rotating part or static part. Table B.1 shows the calculations of Reynolds number, elevation and velocity for the static segments and Table B.2 presents the calculation of rotating nodes

Table B.1: Calculations of static segments.

Segment	Length, m	Diameter, m	Area, m ²	Velocity, m/s	Re	Δz m
L1	1.00E+00	3.18E-03	7.92E-06	2.11E-02	6.70E+01	0.00E+00
L4	1.00E+00	3.18E-03	7.92E-06	2.11E-02	6.70E+01	0.00E+00
V1	1.00E+00	6.35E-03	3.17.E-05	5.27E+00	2.23E+03	0.00E+00
V4	1.00E+00	6.35E-03	3.17.E-05	5.27E+00	2.23E+03	0.00E+00

Table B.2: Calculations of rotating nodes.

Segment	Length, m	Diameter, m	Area, m ²	Velocity, m/s	Re	Δz m	Δr^2 m
L2	7.54E-02	1.50E-03	1.77E-06	9.45E-02	1.42E+02	5.00E-02	2.13E-04
L3	9.38E-02	1.50E-03	1.77E-06	9.45E-02	1.42E+02	-8.00E-02	-1.23E-03
V2	1.12E-01	3.00E-03	7.07.E-06	2.36E+01	4.73E+03	1.10E-01	1.23E-03
V3	1.30E-01	3.00E-03	7.07.E-06	2.36E+01	4.73E+03	-1.40E-01	-2.13E-04

Based on the results of calculations above the pressure drop at each segment and the pressure values at the inlets and outlets can be calculated following the energy equations presented in this chapter and the assumptions considered in this example. Table B.3 and Table B.4 present and summarize the calculations of pressure drop and pressure values respectively.

Table B.3: Values of pressure drop in each segment in the flow system.

Static tubes		Shaft nodes	
Tube	ΔP , pa	Node	ΔP , pa
L1	-6.696E+01	L2	-2.393E+03
L4	-6.696E+01	L3	-1.600E+04
V1	-7.533E+01	V2	-1.509E+02
V4	-7.533E+01	V3	-1.989E+02

Table B.4: Values of pressure at each point in the flow system.

Dense Phase		Light Phase	
Point	Pressure, Pa	Point	Pressure, Pa
A	1.130E+05	F	1.000E+05
B	1.130E+05	G	1.170E+05
C	1.154E+05	H	1.160E+05
D	1.161E+05	I	1.150E+05
E	1.000E+05	J	1.150E+05

B 4.4 Spiral temperature

Increasing the temperature in the spiral channel has a direct effect on the liquid viscosity and causes it to decrease. Thus, one of our experimental procedures is to find out a close estimation of the temperature in spiral to find out the accurate values of phase properties and hence accurate prediction by the wide channel model. At high value of rotation rate a heat production will occur from ball bearing side, this heat will be transferred to the spiral element through the shaft head and the metal screws hold all parts together (Figure B.1). The spiral element was designed with no consideration of heat transfer, and in order to achieve a close estimation of the temperature in the spiral, T_s , the following approach was used:

The apparatus design includes a thermocouple fixed in a distance 2 mm from the bearing so the bearing temperature is known, also another thermocouple to record the atmosphere lab temperature. Measuring the glass temperature comes immediately and manually after shut off the flows and the electric motor by using a stop watch and recording the increase in temperature every 10 seconds. We record all these temperature for all different rotation rate, thus each value of rotation rate has its spiral temperature.

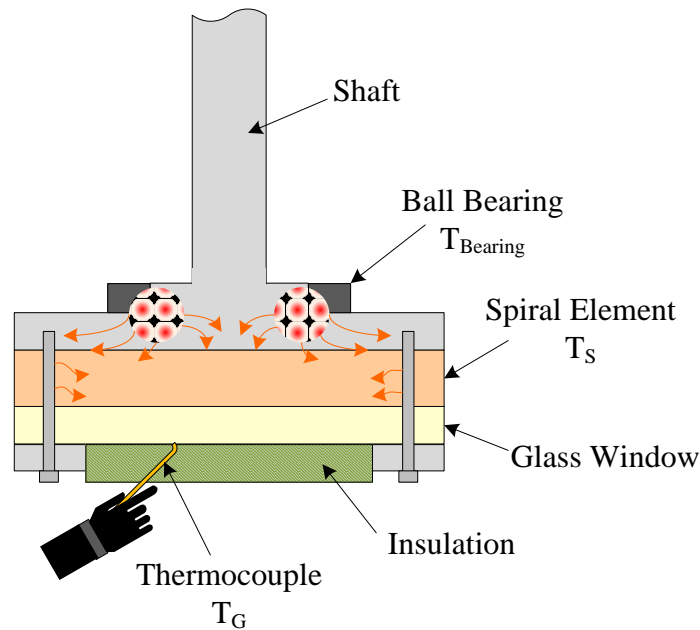


Figure B.1: Measuring of the spiral temperature.

In order to achieve a good comparison with wide channel model, phase properties need to be at conditions very close to the actual conditions of pressure and temperature in spiral channel. Because of both phases pass through the same passages (spiral channel and shaft passages) a single value of temperature for both of them is assumed. This assumed value of temperature comes from the measurement method explained in chapter 5 where determining of the transient temperature at the external side of the glass window occurs immediately after stopping the operation of the device. Stopping the operation includes also shutoff the flows and in this case the PEEK (spiral element) works as insulation for the glass window from inner side. Figure B.2 shows the heat transfer through the glass window is in one direction, the initial temperature of the glass surface (T_o) and the final temperature recorded from the exterior surface also is (T_f) can be fit together in a suitable transient function. The initial temperature is the maximum and the

device cool down to the lowest temperature without the effect of heat transfer from the overall device.

MacInnes and Zambri (2014) state that the final temperature can be the same as the initial mid-thickness value, thus in this case the temperature at the interior glass surface during operation can be found. Taking this as representative of the temperature (T_s) of the fluids within the spiral during operation:

$$T_s = T_o + 2(T_f - T_o) \quad (\text{B.15})$$

A superimposed effect of one-dimensional transfer process can be used to separate the transient by having characteristic time $\delta^2/\alpha = 125$ s ($\delta = 1$ cm and $\alpha = 8 \times 10^{-7}$ m²/s are the glass thickness and thermal diffusivity) as well as the heat transfer at the overall scales of the device and the side heat transfer in the glass region. There is a similar function suggested by Kuvshinov et al. (2010) which related to the measurements of thermal conductivity can be used:

$$T(t) - T_o = (T_f - T_o) \left(1 - \exp \left\{ -\frac{t - t_0}{\tau} \right\} \right) + \gamma(t - t_0) \quad (\text{B.16})$$

Eq. (B.16) above shows that the first term is related to one-dimensional adjustment in the glass and the second term presents the linearization of exponential term for longer time scales. Figure B.3 shows the data fitting of the transient where the temperatures in this case related to the initial and the final are $T_o = 34.8$ °C and $T_f = 36.5$ °C respectively gives an estimation of the spiral temperature of 38.2 °C. (The time constant of $\tau = 21.6$ s is consistent with the characteristic time scale found above, as the time constant is typically around 20% of the characteristic time scale, e.g. MacInnes et al., 2005.)

The results above show the expectation of the spiral temperature using this method can be vary depending on the rotation rate that take in the account the heating from the bearings and the friction of lip seals on rotating shaft.

Figure B.4 shows a range of data were taken for different rotation rate. The solid line related to the power law function that fit to the data that has been used to supply the spiral temperature for property calculations in wide channel model:

$$T_S = 11.7(\Omega_{rpm} - 331)^{0.15} \quad (\text{B.17})$$

This function fits the data with an rms deviation of 1.8 °C (MacInnes and Zambri, 2014)

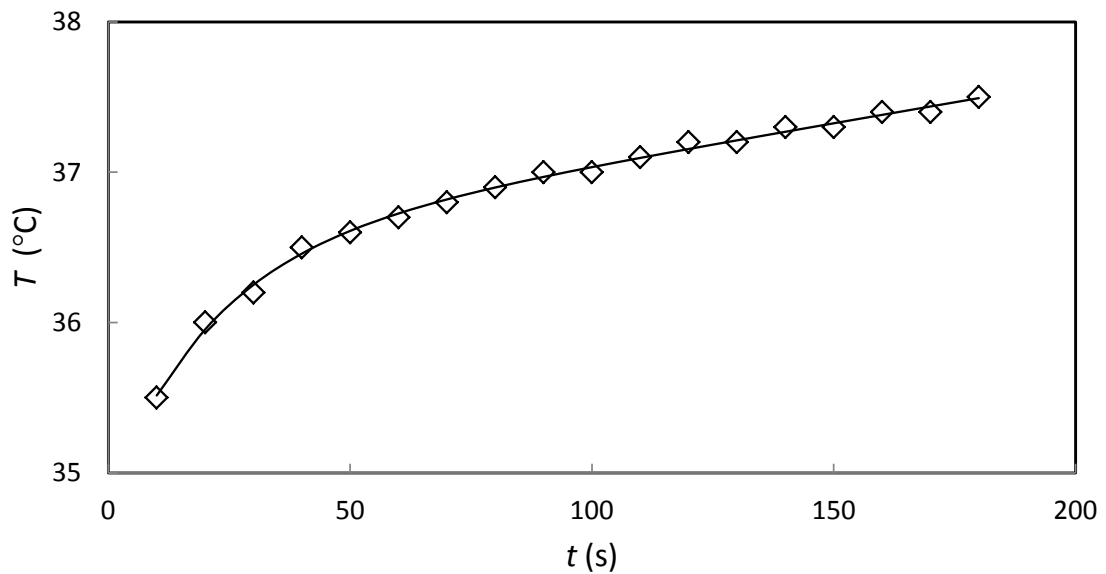


Figure B.2: Transient of glass surface temperature immediately after stopping rotation and the function given by Eq. B.16 (data for 3840 rpm).

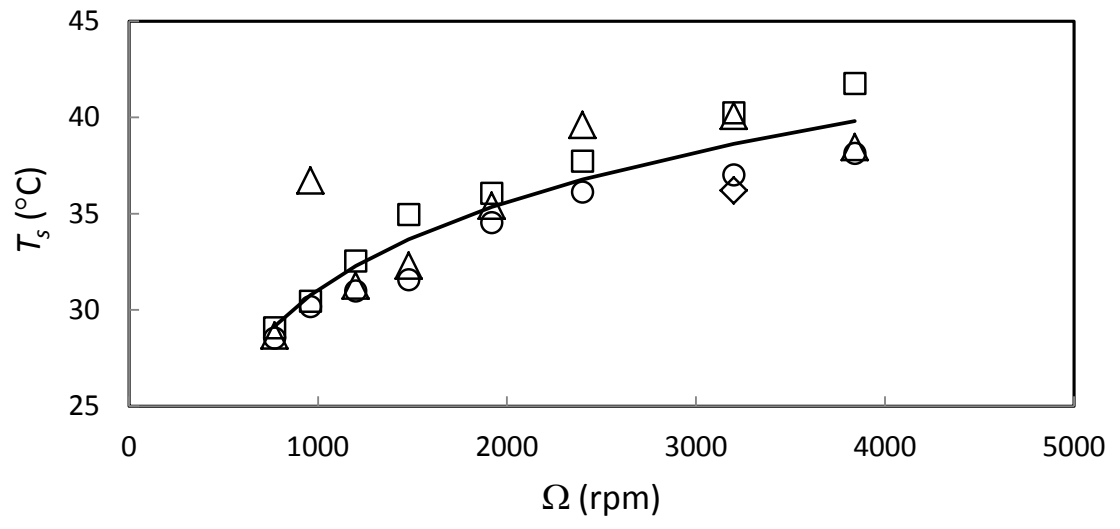


Figure B.3: Correlation of spiral temperature and rotation rate.

Appendix C: Technical drawings

The device concept is a relatively straightforward piece of mechanical design. However, its details may remain unclear to the reader without reference to the formal technical drawings used to make it. This appendix gives these drawings for the principal components associated with the rotation and the flows to and from the spiral. In sections C1 to C4 drawings for the assembled seal unit and individual drawings for its components will be found. Section C4 contains the drawings for the spiral element.

C1 Seal case assembly views

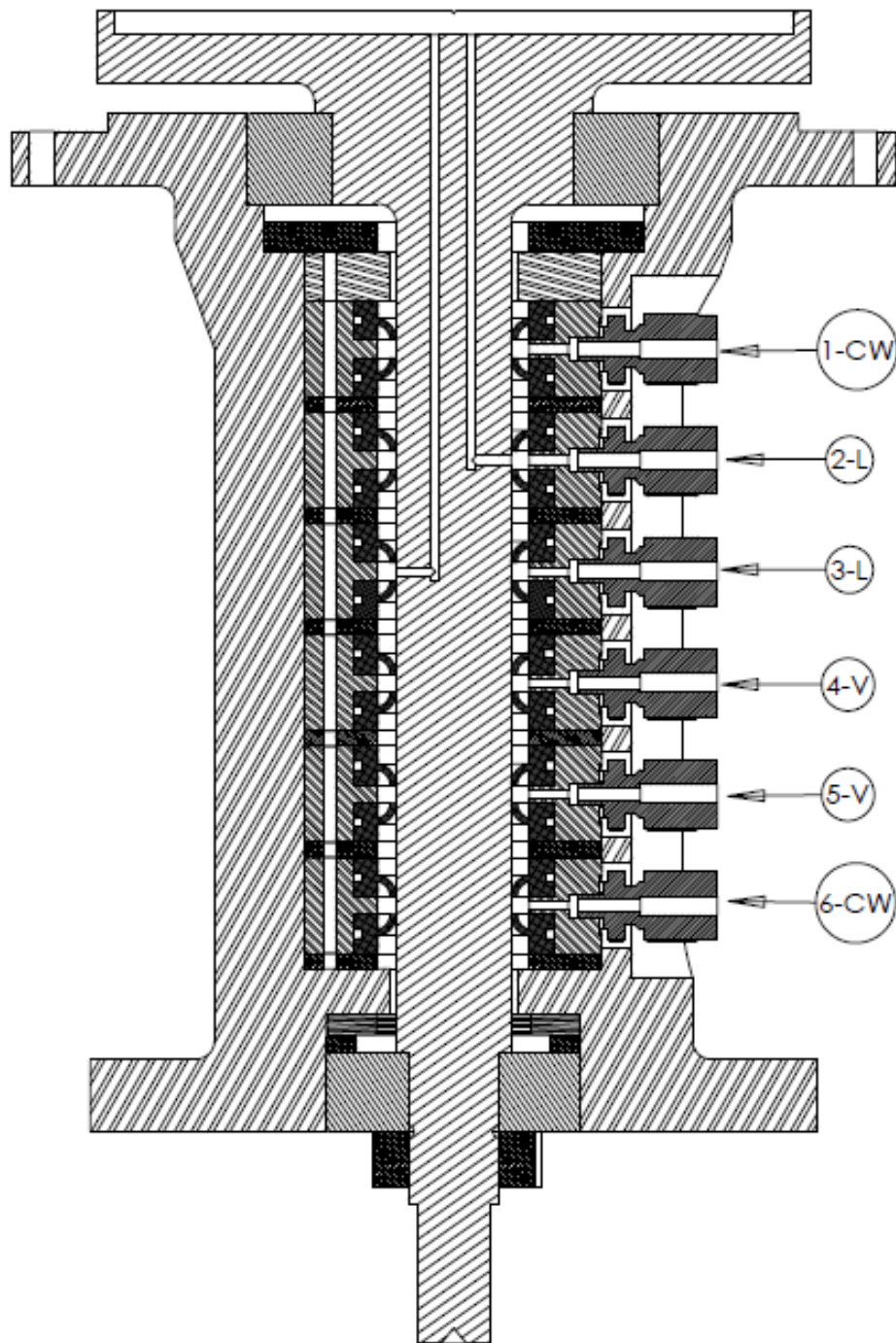


Figure C1. Front section view showing the cooling water and phase flow connections; flow connection numbers used in all drawings are defined.

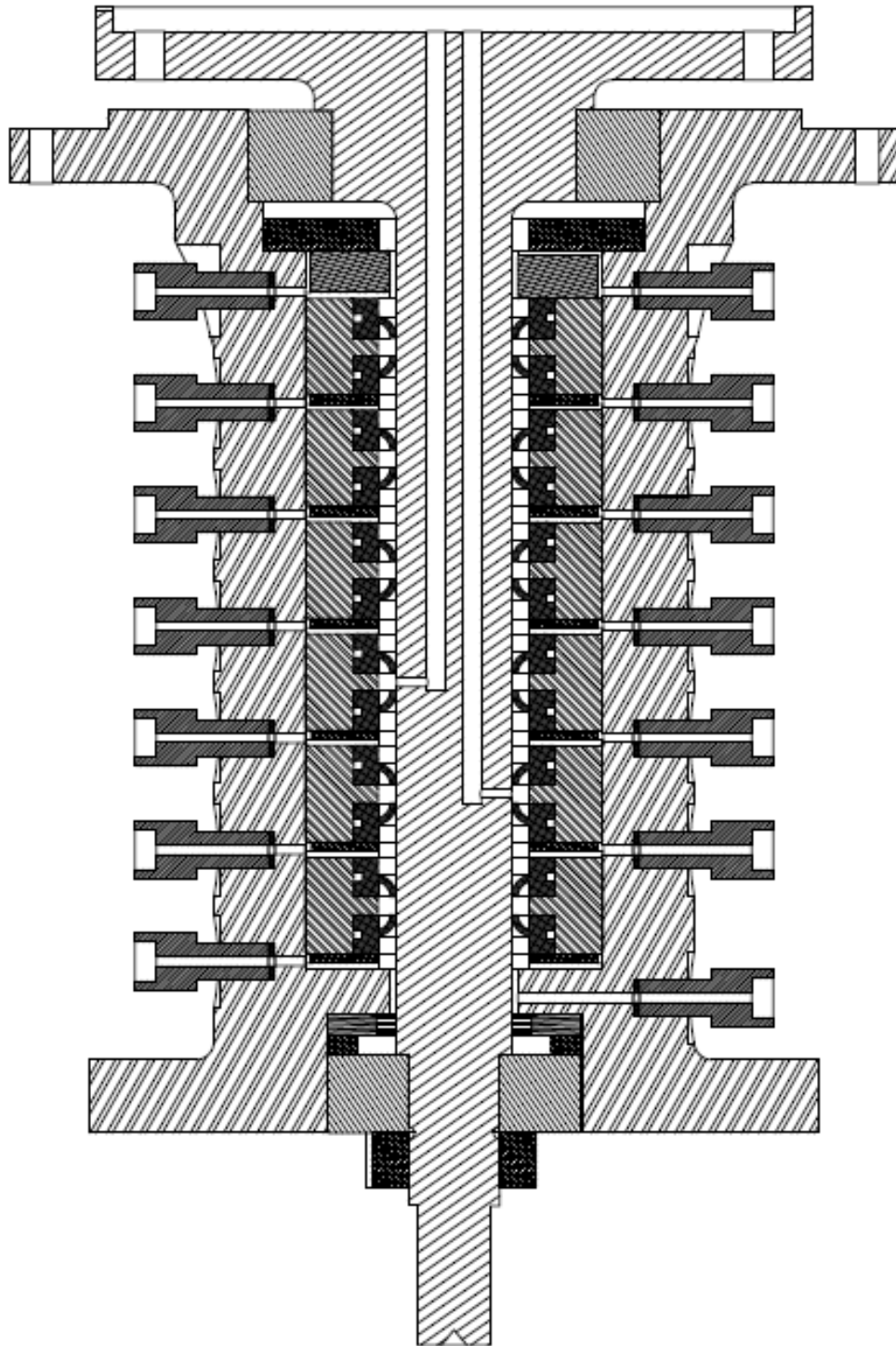


Figure C2. Side section showing the vent connections to the inter-seal spaces.

C2 Seal Case

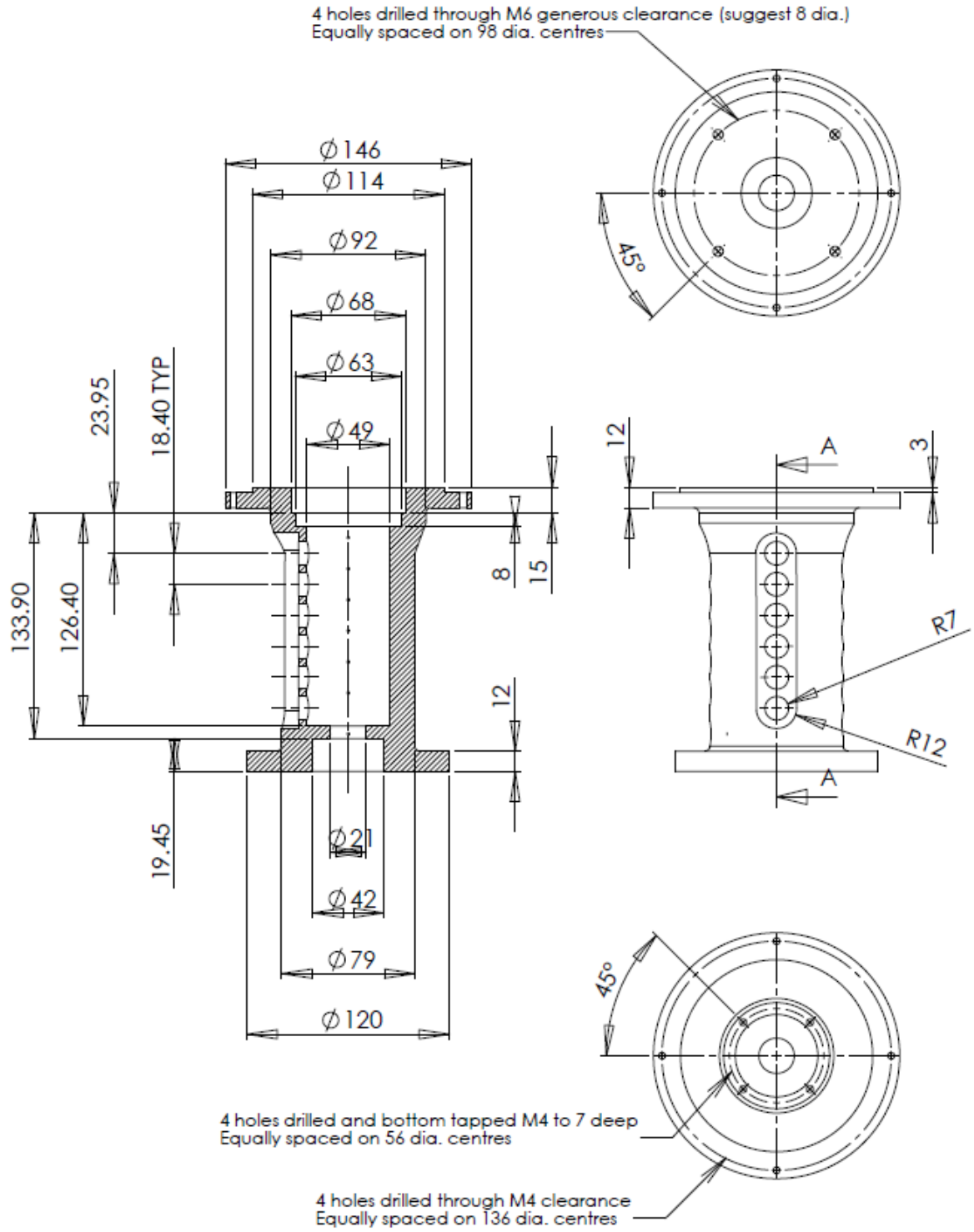


Figure C3. Front section, side and top views.

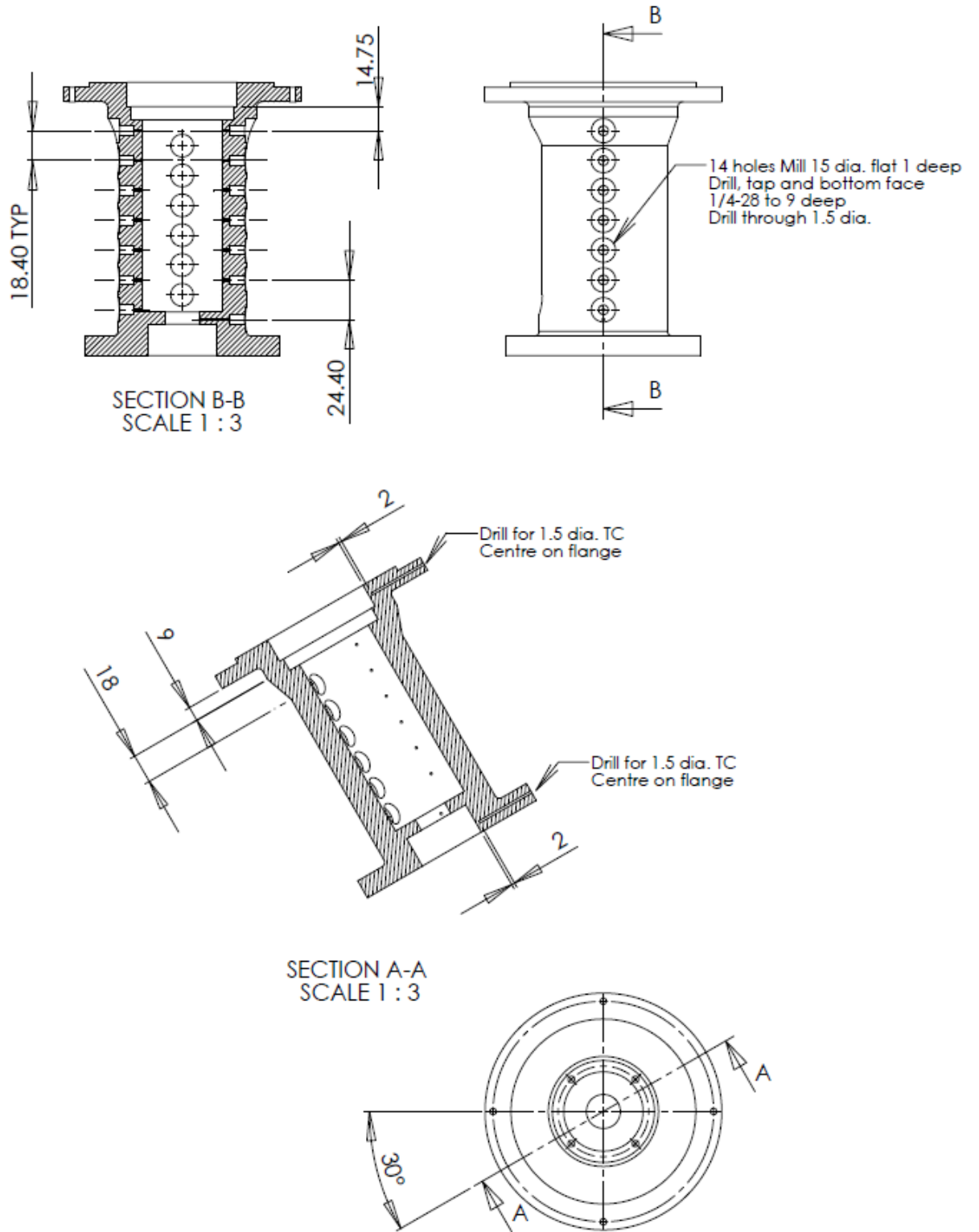


Figure C4. Side section, side and top views.

C3 Shaft

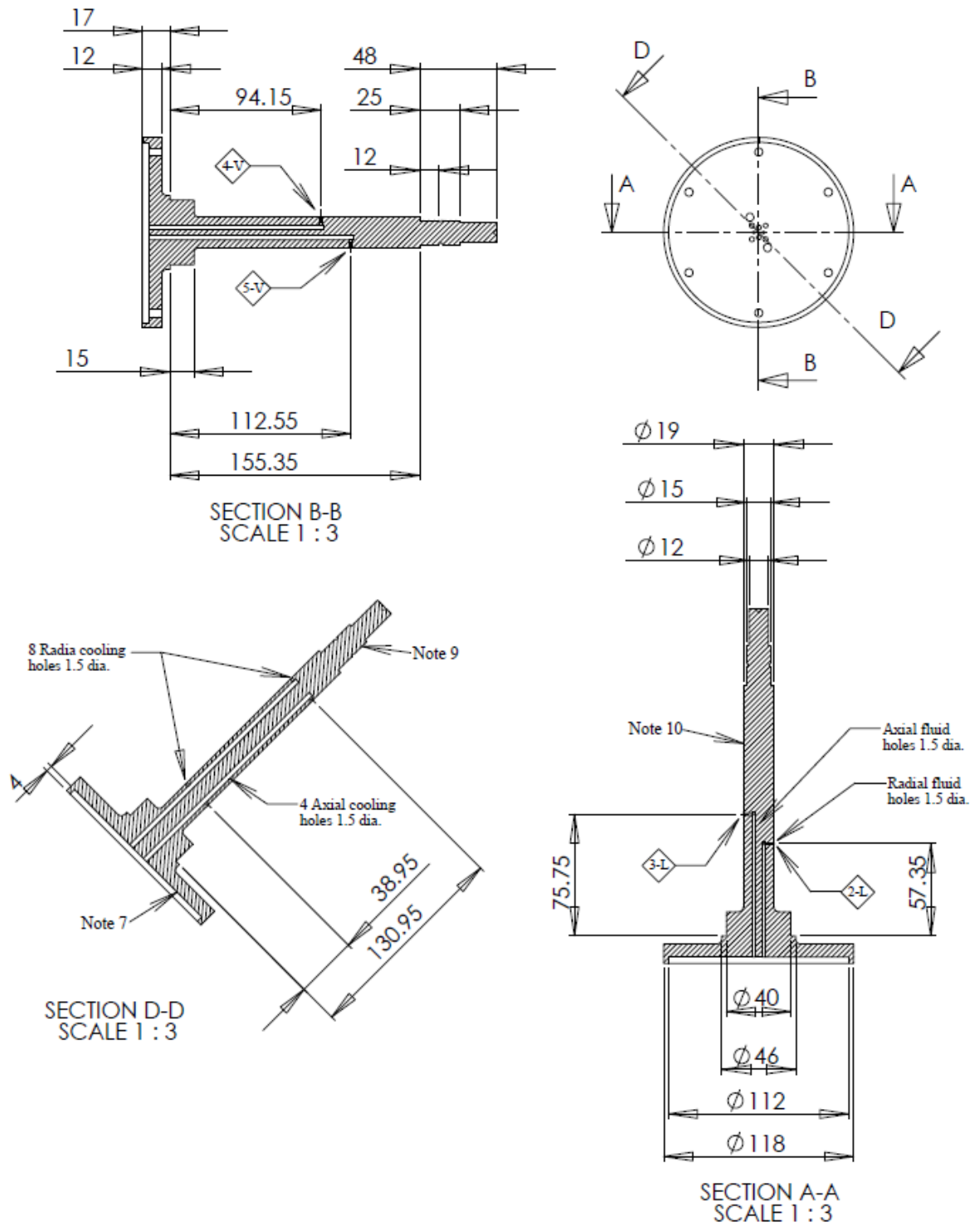


Figure C5. Shaft section views.

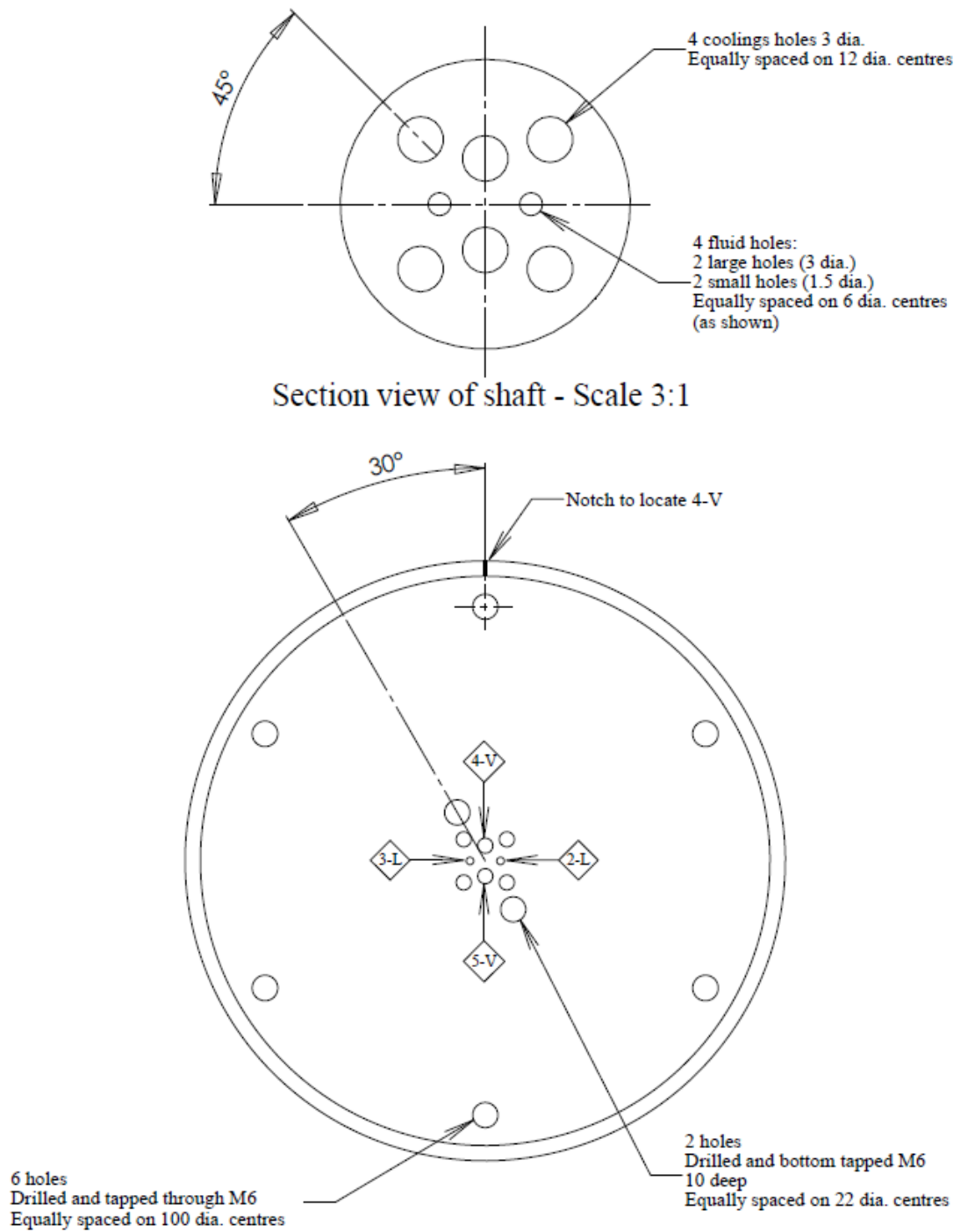


Figure C6. Shaft section and shaft head views showing the hole pattern.

C4 Internal Parts

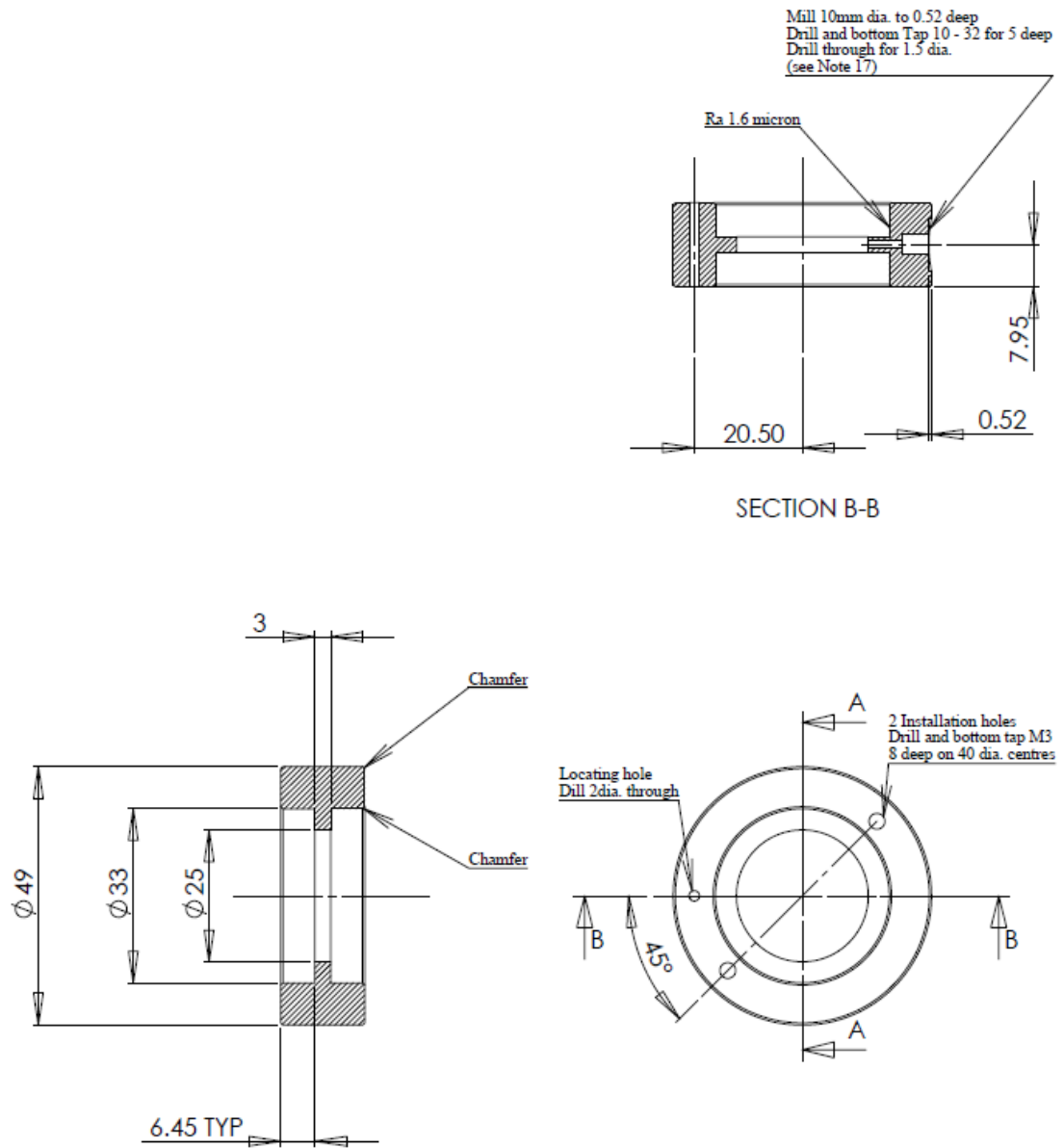
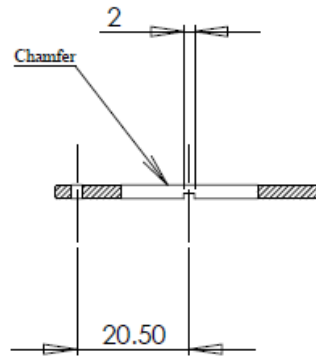
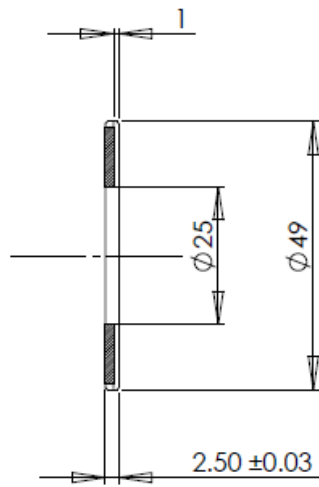


Figure C7. Seal-pair holder



SECTION B-B



SECTION A-A

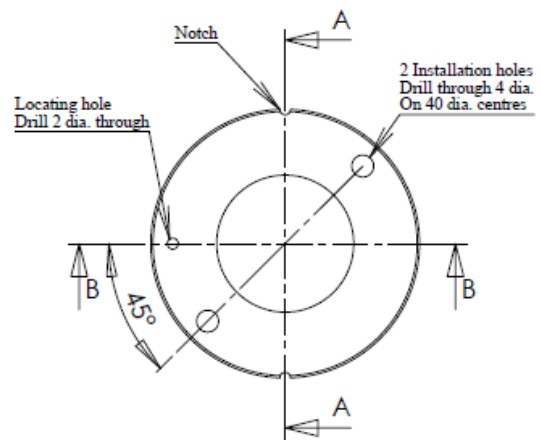
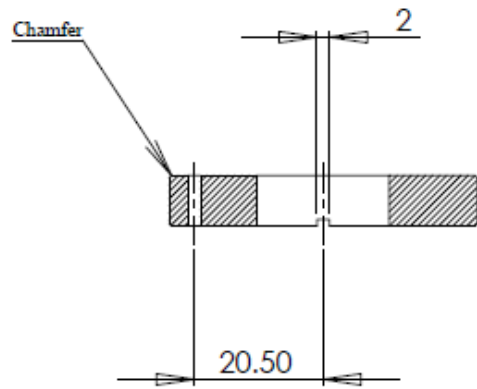
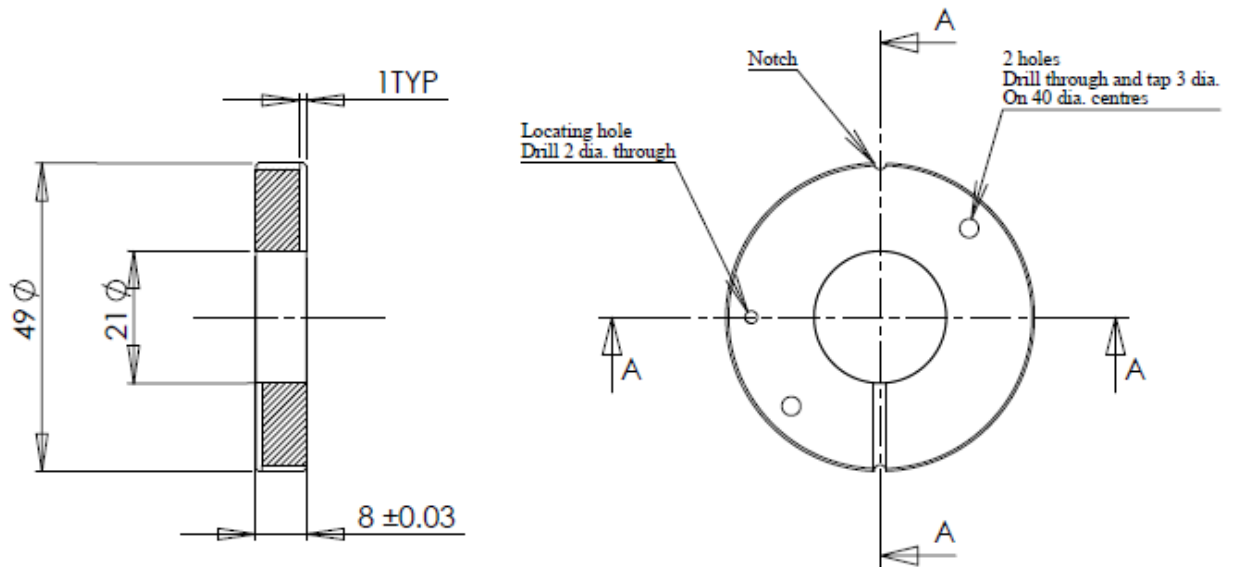


Figure C8. Seal spacers.

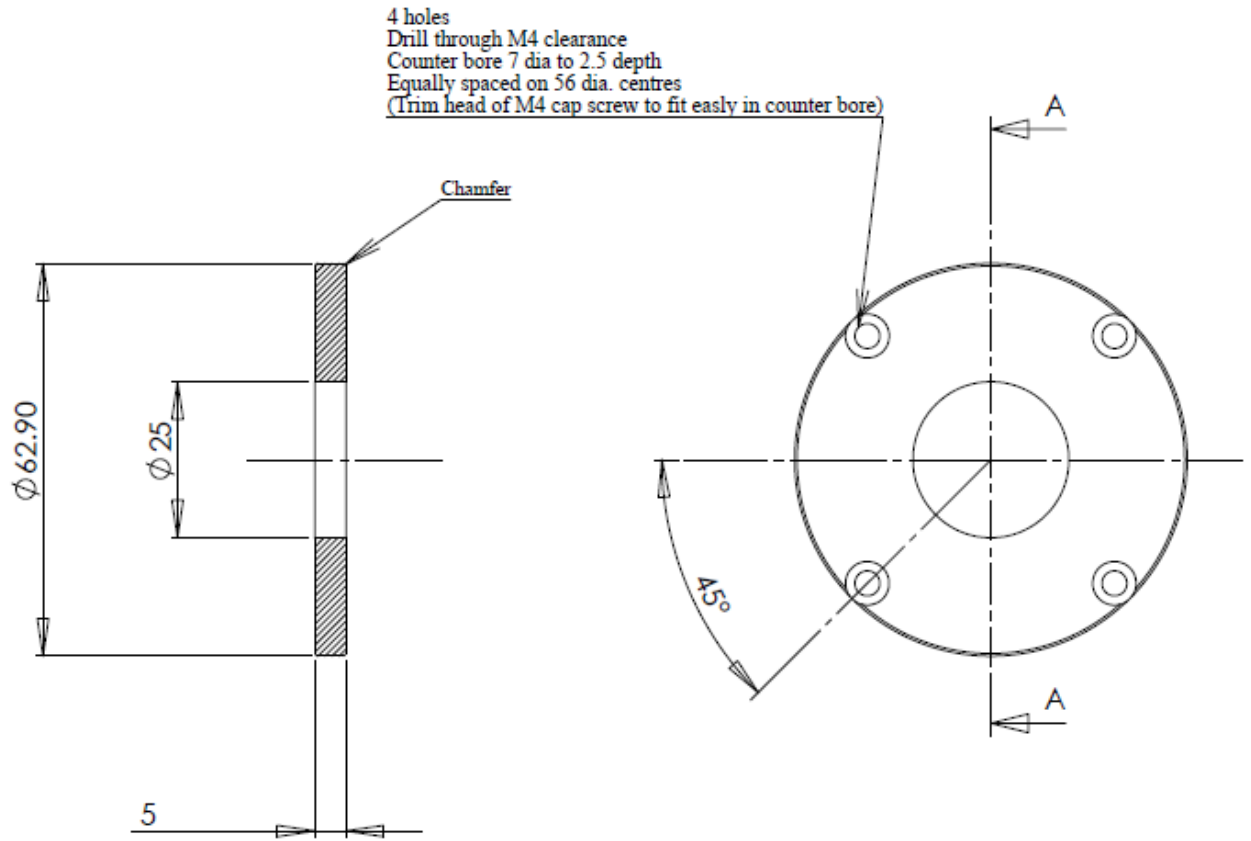


SECTION A-A



SECTION A-A

Figure C9. End spacer.



SECTION A-A
 SCALE 1 : 1

Figure C10. End clamp.

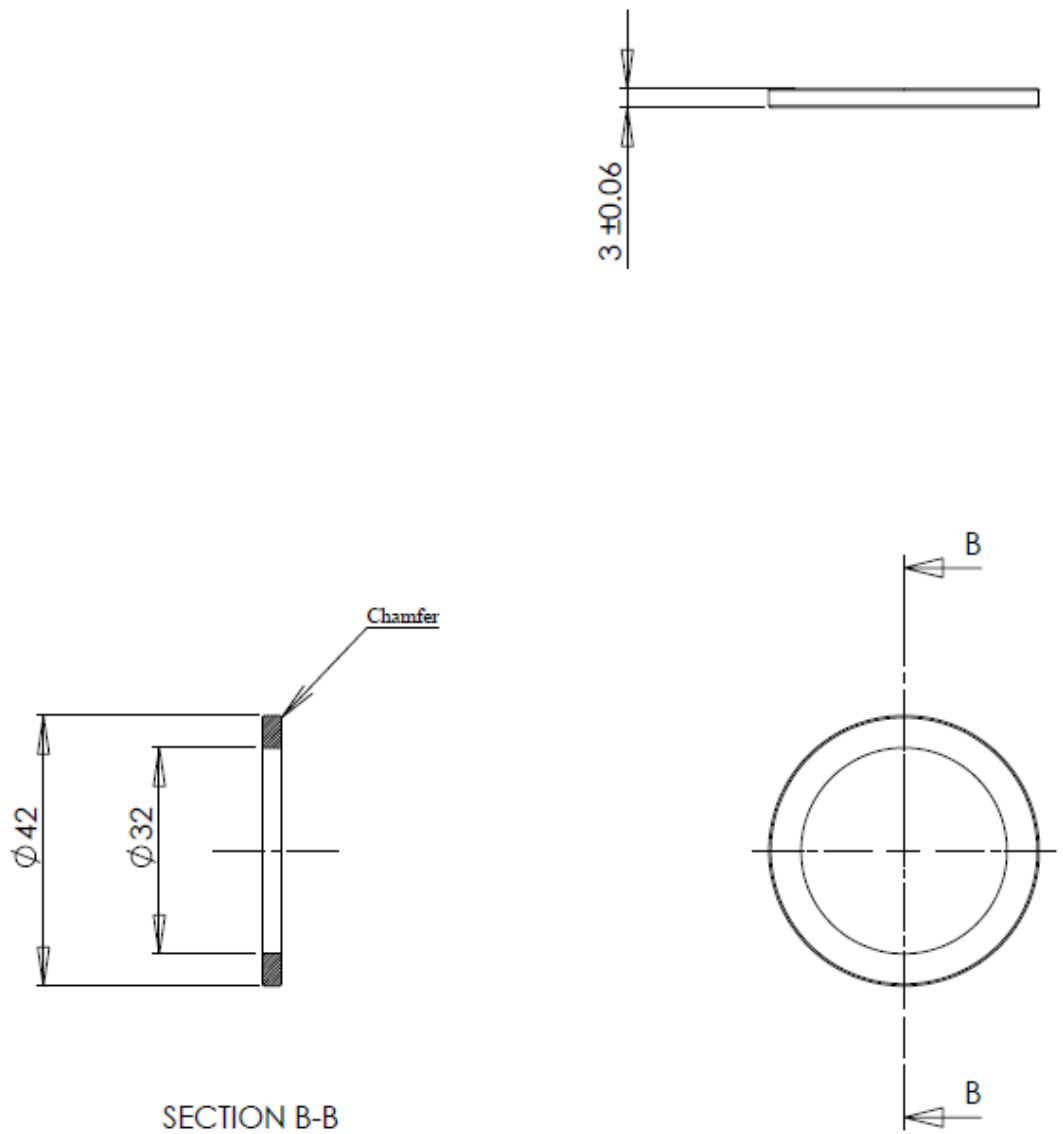


Figure C11. Spring-gauge washer (sets displacement and hence force for the bearing spring washers).

C5 Spiral element

SPIRAL ELEMENT

Make 1 (PEEK)
Dimensions in mm
Scale 1:1 on A4

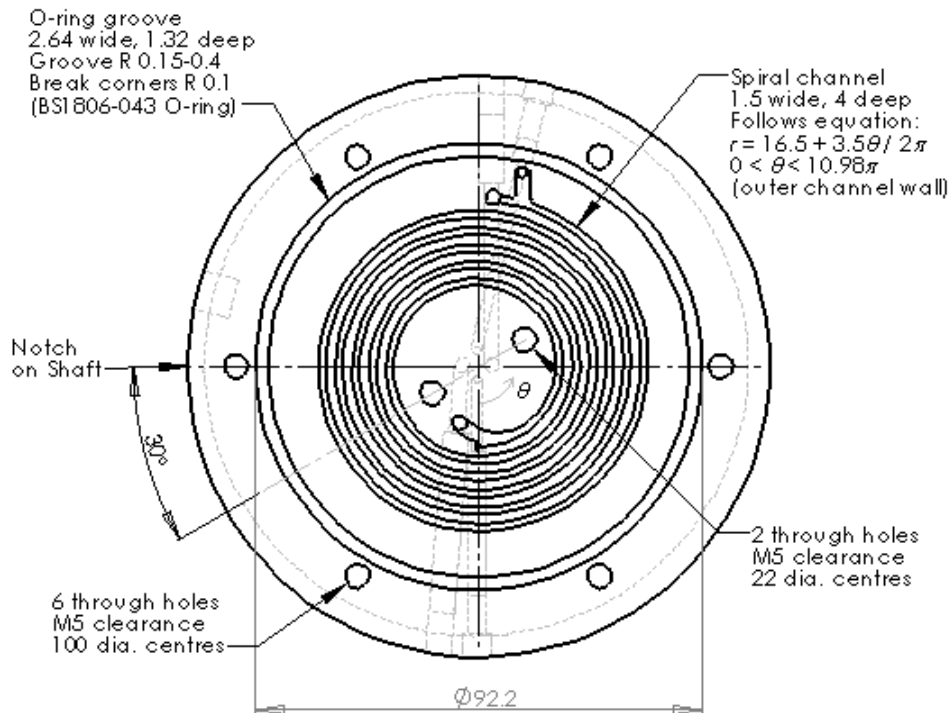
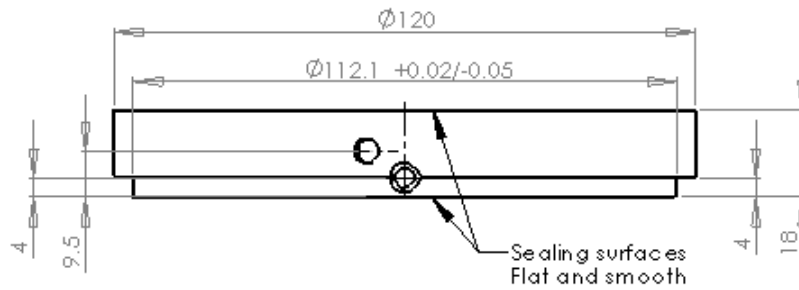
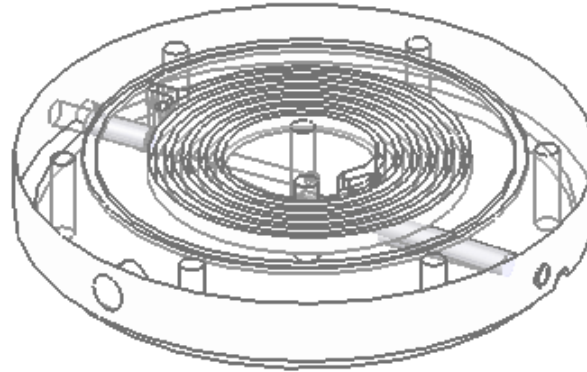


Figure C12. Spiral element with hidden lines showing passages connecting central holes, matching with shaft holes, to the ends of the spiral channel.

Appendix D: Further channel photographs at additional conditions

D1 Influence of Q_L at different rpm

The influence of varying the liquid flow rate at constant value of vapour flow rate and range of rotation rate has been tested. The test has shown that varying the liquid flow rate has direct effect on the liquid layer thickness and has no effect on the height of meniscus. Increasing the liquid flow rate leads to increase the thickness of liquid layer and increasing the rotation rate cause to decrease the thickness. This can be shown in the figures below.

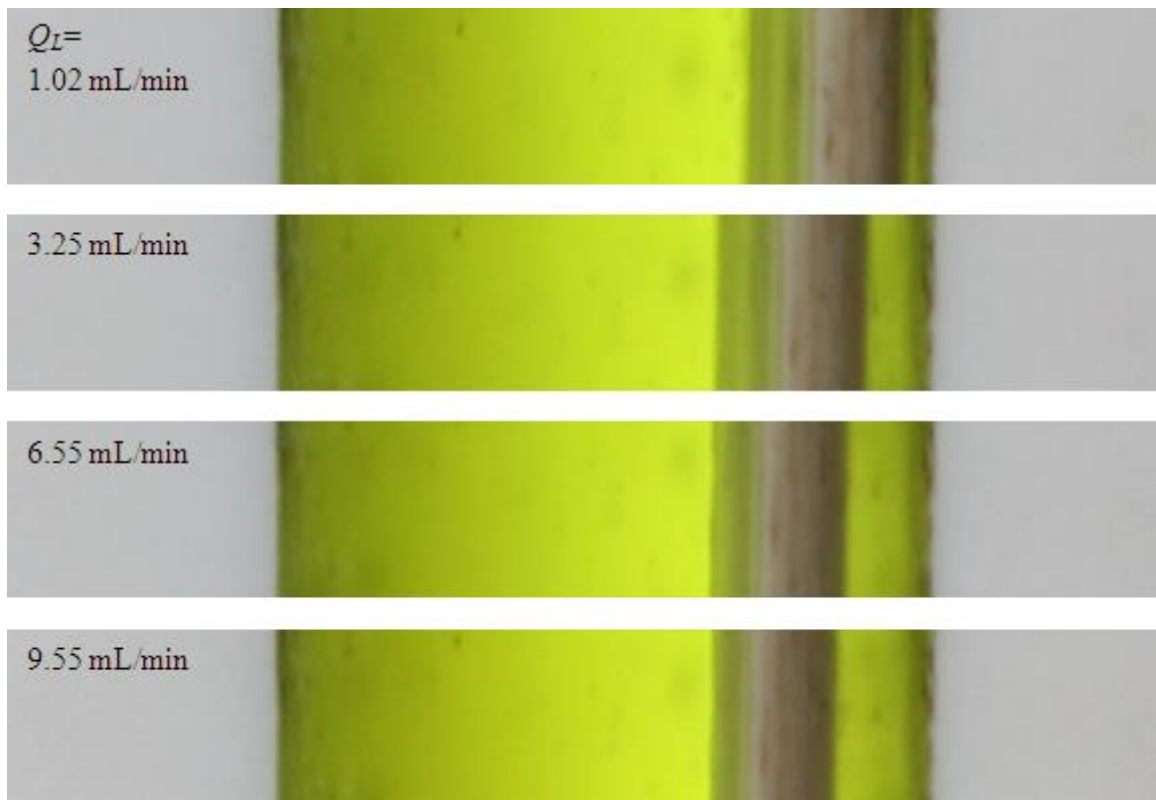


Figure D1.1: Liquid layer thickness variation with liquid flow rate. Meniscus size remains approximately constant. Conditions are $Q_V = 3.54$ NL/min, $P_S = 2.1$ bar absolute and 1480 rpm.

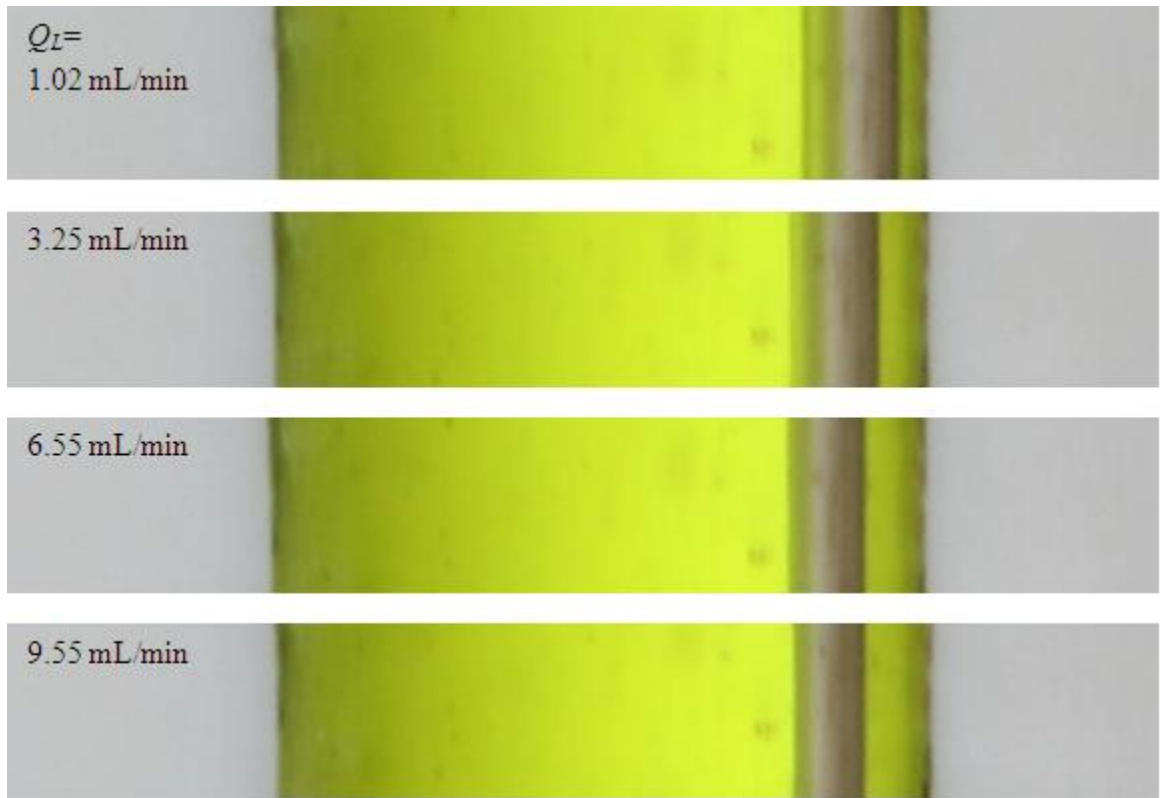


Figure D1.2: Liquid layer thickness variation with liquid flow rate. Meniscus size remains approximately constant. Conditions are $Q_V = 3.54$ NL/min, $P_S = 2.1$ bar absolute and 2400 rpm.

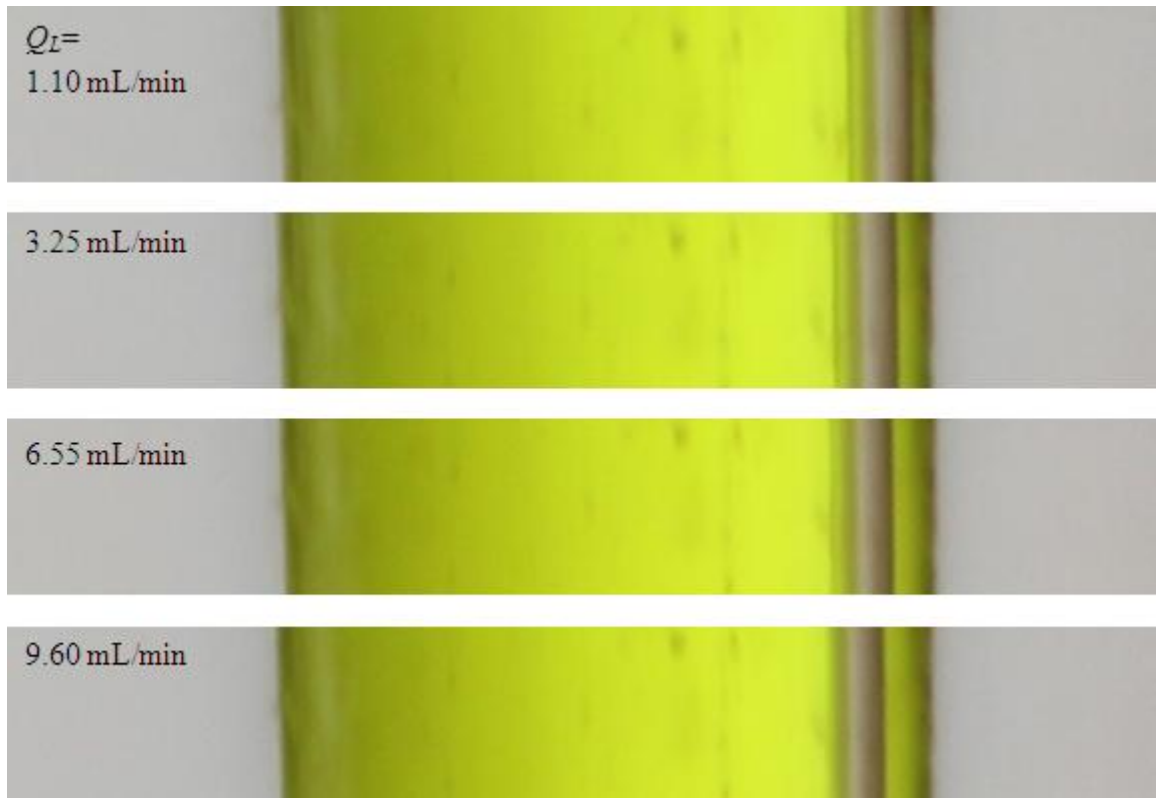


Figure D1.3: Liquid layer thickness variation with liquid flow rate. Meniscus size remains approximately constant. Conditions are $Q_V = 3.54 \text{ NL/min}$, $P_S = 2.1 \text{ bar}$ absolute and 3840 rpm (same as figure 6.12).

D2 Radial position test

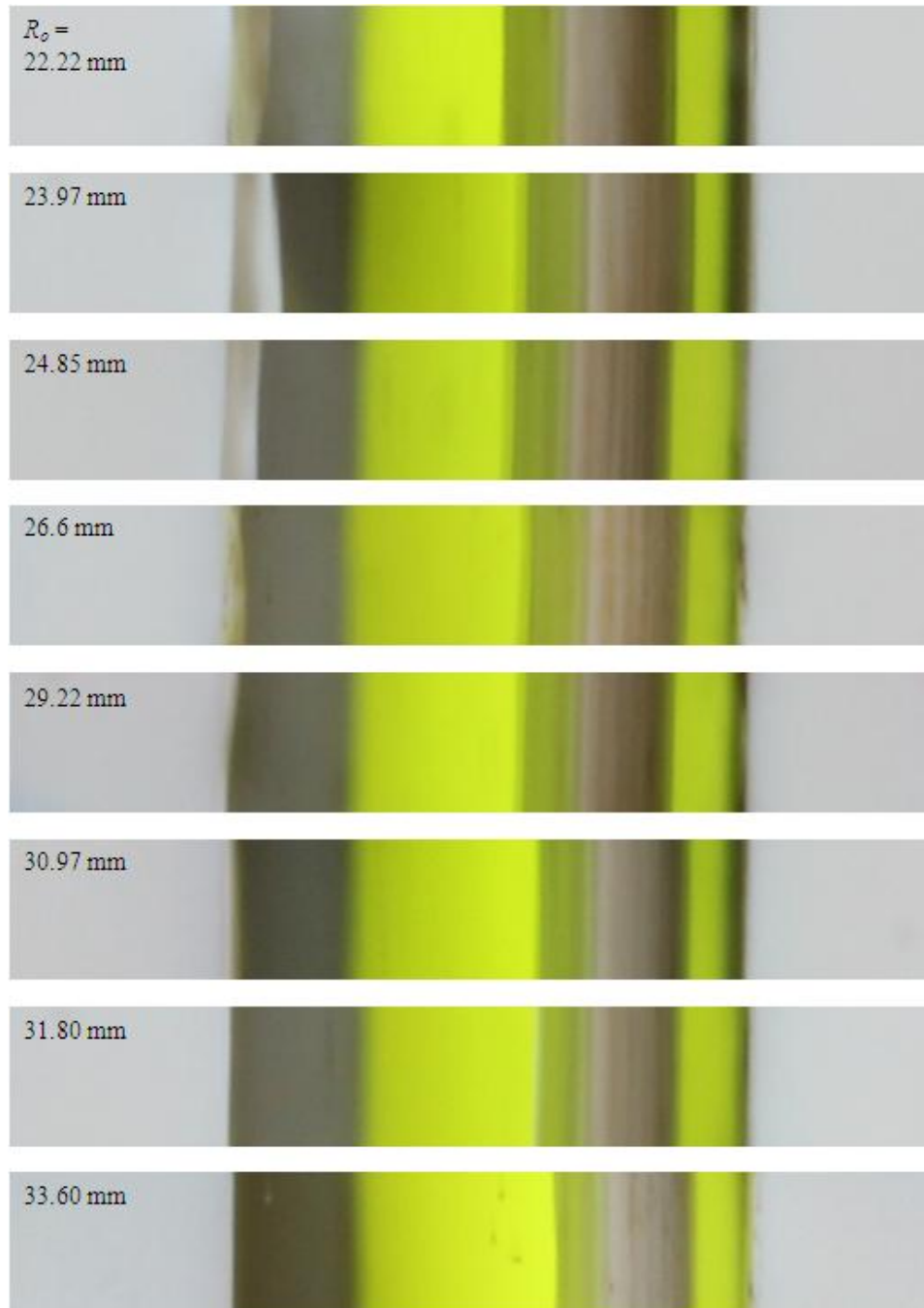


Figure D2.1: Liquid layer thickness variation and Meniscus size with the effect of radial position. Conditions are $Q_V = 3.54$ NL/min, $Q_L = 3.49$ mL/min $P_S = 2.1$ bar absolute and 1200 rpm.

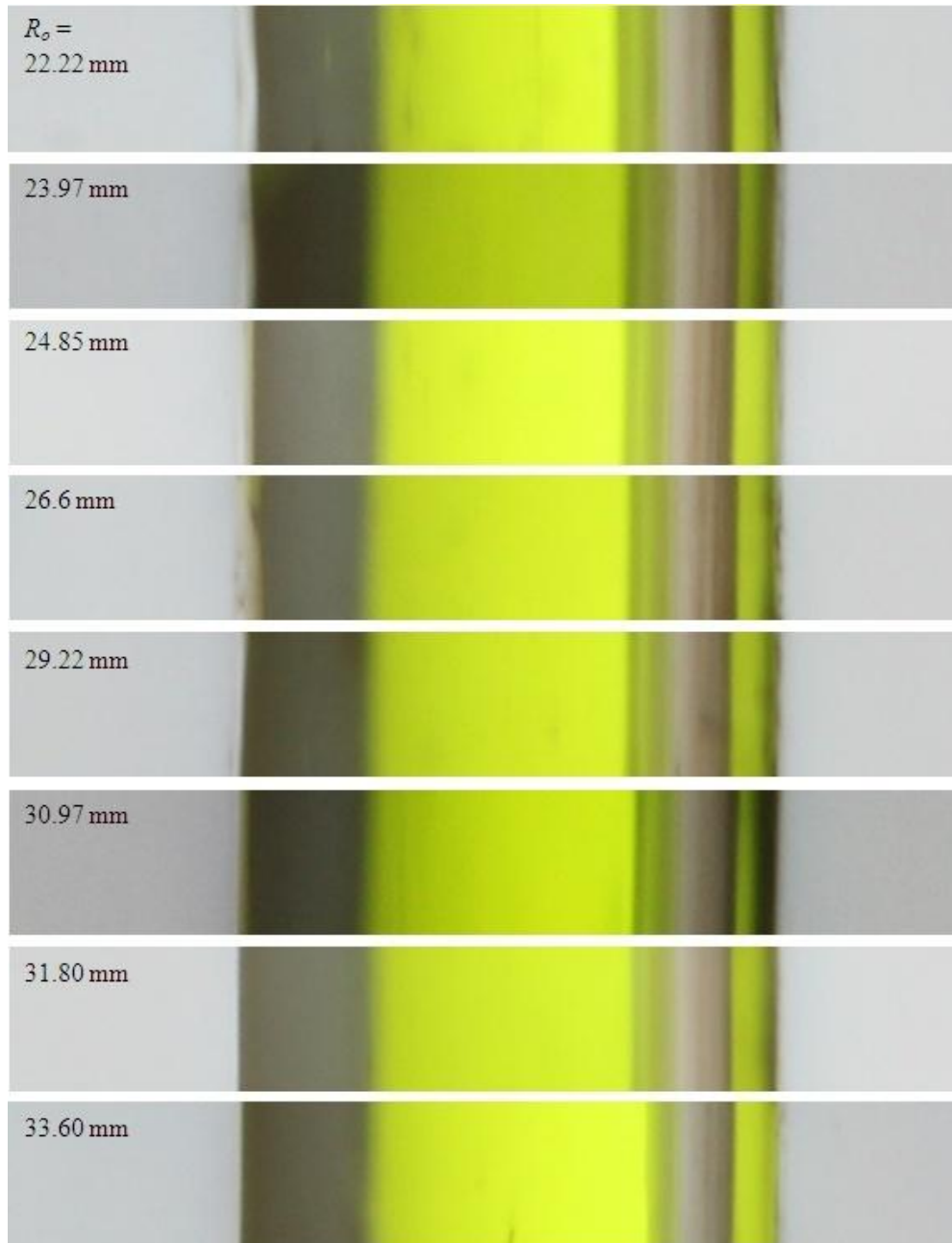


Figure D2.2: Liquid layer variation and meniscus size with the effect of radial position. Conditions are $Q_V = 3.54$ NL/min, $Q_L = 3.49$ mL/min, and 1920 rpm (same as figure 6.19).

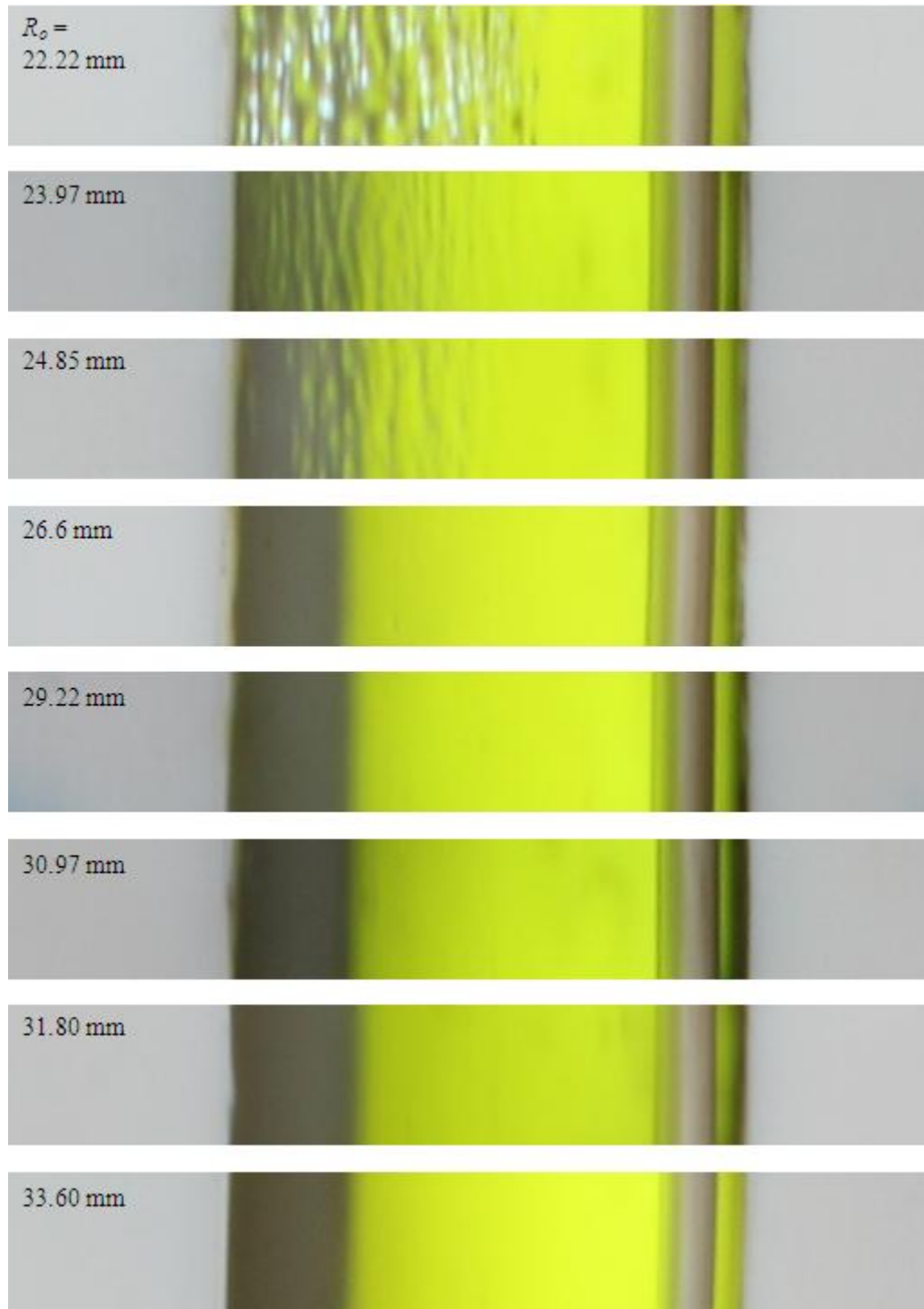


Figure D2.3: Liquid layer thickness variation and Meniscus size with the effect of radial position. Conditions are $Q_V = 3.54$ NL/min, $Q_L = 3.49$ mL/min $P_S = 2.1$ bar absolute and 3200 rpm.

D3 Images for different phase systems at similar h_L

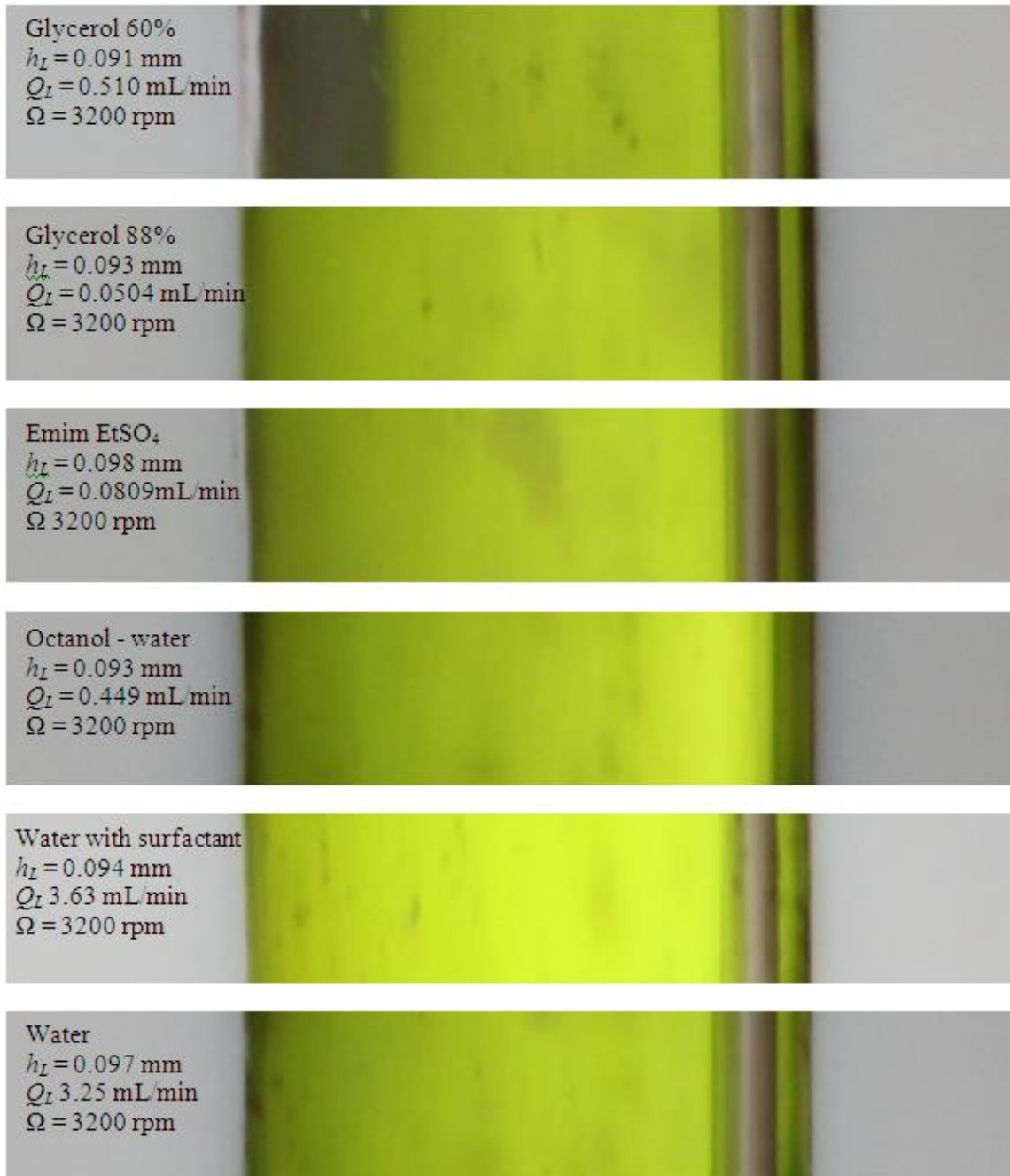


Figure D3.1: The similarity in liquid layer thickness for different phases at different conditions of liquid flow rate. Conditions are, $Q_V = 1.15$ NL/min and 3200rpm.